The nucleation, growth kinetics and mechanism of sulfate scale minerals in the presence and absence of additives as inhibitors

Taher Rabizadeh

Submitted in accordance with the requirements
for the degree of Doctor of Philosophy

The University of Leeds

School of Earth and Environment

November 2016

Declaration

The candidate confirms that the work submitted is his own, except where work which has formed part of jointly-authored publications has been included. The contribution of the candidate and the other authors to this work has been explicitly indicated below. The candidate confirms that appropriate credit has been given within the thesis where reference has been made to the work of others.

Chapter 4 has been published as:

> Rabizadeh, T., Peacock, C. L. and Benning, L. G., 2014. Carboxylic acids: effective inhibitors for calcium sulfate precipitation?, *Mineralogical Magazine*, 78, 1465–1472.

The experiments, analyses, data processing, interpretation and preparation of the manuscript were conducted by the candidate. All co-authors contributed to data interpretation and manuscript preparation.

Chapter 5 has been published as:

> Rabizadeh, T., Stawski, T. M., Morgan D. J., Peacock, C. L. and Benning, L. G., The effects of inorganic additives on the nucleation and growth kinetics of calcium sulfate dihydrate crystals, *Crystal Growth & Design*, 17, 582-589.

The candidate performed the experiments, analyses (except ICP-MS / OES and XPS measurements), data processing (except XPS measurements), interpretation (except XPS measurements) and preparation of the manuscript. XPS analyses, data processing and interpretation were discussed in depth with co-author David J. Morgan at Cardiff University. All co-authors contributed to data interpretation and manuscript preparation.

Chapter 6 is in preparation for submission to the *Journal of Crystal Growth* as:

> Rabizadeh, T., Morgan D. J., Peacock, C. L. and Benning, L. G. Comparative performance of biodegradable *vs.* poly(acrylic acid) antiscalants on calcium sulfate dihydrate crystallisation.

The candidate performed all experiments, analyses, data processing, interpretation and preparation of the manuscript. XPS analyses were performed at Cardiff University together with David J. Morgan. All co-authors contributed to data interpretation and manuscript preparation.

Chapter 7 is in preparation for submission to *Langmuir* as:

> Rabizadeh, T., Morgan D. J., Peacock, C. L. and Benning, L. G., Investigating the effects of phosphonate inhibitors on the nucleation and growth kinetics of calcium sulfate dihydrate crystals.

The candidate performed the experiments, analyses (except ICP-OES and XPS measurements), data processing, interpretation and preparation of the manuscript. XPS analyses were performed at Cardiff University together with David J. Morgan. All co-authors contributed to data interpretation and manuscript preparation.

Dedication

I dedicate this work to my parents for raising me to be the person I am today, and my wife, Azam, who encouraged and supported me in this work from the beginning. I here extend my dedication to my brother as well as my parents-in-law.

Acknowledgements

I would like to take this opportunity to appreciate some people without whom it would not have been possible to do this work.

I would like to express my sincere gratitude to my supervisor, Prof. Liane G. Benning for being supportive, patient, for encouraging me during a difficult time and throughout the development of the project. I really do appreciate all her effort, and without it, I would not be at this stage.

It gives me immense pleasure to thank my co-supervisor, Dr. Caroline L. Peacock for her help, time, advice and patience.

I am also grateful to my research collaborators, Dr. Tomasz M. Stawski, Dr. Davis J. Morgan, and Dr. Adriana Matamoros-Veloza.

I really appreciate the Marie Skłodowska-Curie actions for sponsoring my PhD as part of the MINSC Initial Training Research Network and special thanks to the MINSC project manager, Clare Desplats.

I would also like to thank all the PIs at the University of Leeds, Cohen geochemistry group, MINSC and CO_2 react networks who guided me during my PhD.

Thank you to the scientists at department of geosciences of University of Oslo specially Prof. Bjørn Jamtveit, Prof. Dag Dysthe, Prof. Håkon Olav Austrheim, and Kristina Dunkel for hosting me during my secondment.

A special thank for Clariant Oil Services UK Ltd Company and Dr. Jamie Kerr and Dr. Adam Savin for providing me with an opportunity to have a short collaboration with them.

It is my pleasure to thank the administrative and technical staff, who were always available and helpful. Special thanks to Andy Connelly, Stephen Reid, Fiona Keay, Sam Allshaw, Richard Walshaw, Lesley Neave, Martin Fuller, Stuart Micklethwaite, and Mike Ward.

I also want to thank my friends and colleagues at the University of Leeds, Cohen geochemistry group, MINSC and CO_2 react networks. Thanks to Pilar Ramirez-Garcia, Juan-Diego Rodriguez Blanco, Andy Bray, Ekbal Hussain, Thomas Rinder, Giulia Montanari, Cristina Ruiz-Agudo, Andrea Arale Vidal, Ana Hernandez Rodriguez, Fernando Berro Jimenez, Stefanie Lutz, Jan Prikryl, Diwaker Jha, Deirdre Clark, Romain Guilbaud, and Santosh Narshima Prathap Moola.

Abstract

In this research, I focused on elucidating the crystallisation kinetics and formation mechanism of calcium sulfate phases, specifically gypsum, in the presence and absence of additives as inhibitors. In many industries such as oil production and water desalination, calcium sulfate formation is a problem that causes pipeline and membrane clogging and reduces system efficiency. Thus, different types of additives are added to these systems as inhibitors to tackle the scaling problem. However, their efficiency or effectiveness in terms of calcium sulfate inhibition has not been fully tested and the processes are not well-understood at the mechanistic level. In this thesis, therefore, I investigated the effects of various carboxylic acids, alkali / alkaline earth metal cations, polycarboxylic acids and phosphonates as gypsum inhibitors to fill this knowledge gap.

My results revealed that all additives delayed the crystallisation of gypsum to various degrees and by various pathways. I monitored the change in the time needed for turbidity in a reacting solution to start (induction time) and develop (crystallisation kinetics). I analysed the changes in both solution chemistry and solid characteristics, including surface properties, morphologies as well as composition, to derive a mechanistic understanding of how these additives affect gypsum formation.

The results illustrated that among the tested carboxylic acids (tartaric, maleic and citric), citric acid performed far better than tartaric and maleic (at equivalent concentrations) and using citric acid dramatically increased the induction time (~ 4 fold, to ~ 25 minutes).

Among the tested alkali / alkaline earth metal cations (Li^+, K^+, Na^+ and Mg^{2+}), Mg^{2+} decreased the nucleation and growth kinetics ~ 5 to ~ 10 fold more than Li^+, Na^+ and K^+ even

at low concentrations. Mg^{2+}, Li^{+} and K^{+} only adsorbed to the gypsum crystals surfaces, while ~ 25% of associated Na^{+} became incorporated into the synthesised crystals and Li^{+} and Mg^{2+} also acted as shape and size modifiers.

When I tested the effects of biodegradable polycarboxylic additives (polyaspartic acid; PASP and polyepoxysuccinic acid; PESA) and compared their efficiency with a traditionally used non-biodegradable (polyacrylic acid; PAA) antiscalant, I showed that PASP and PESA had a profound effect on gypsum crystallisation, with PASP having the highest inhibition efficiency. The PAA conformation and molecular weight both played important roles in affecting the crystallisation kinetics because of changes in surface adsorption mechanisms.

Finally, I tested some industrial phosphonate inhibitors and demonstrated that they are indeed strong gypsum inhibitors, but I also showed for the first time that an increase in the number of functional groups affected the efficiency of the additive. Among the tested phosphonates with five phosphonate functional groups, the one with longer molecular chains was the better inhibitor. It is unclear how these additives interacted with the growing gypsum crystals (surface adsorption and / or structural incorporation), but I clearly showed that they affected gypsum growth kinetics and morphologies.

Table of Contents

List of Figures

List of Tables

Chapter 1. Introduction

This chapter gives a general view on mineral scaling. It also details the aims and objectives of the thesis and outlines the thesis layout.

1.1. Background

One of the most common and critical industrial problems is mineral scale formation. Mineral scaling is a crystallisation process during which inorganic salts with low solubilities, nucleate and grow in a supersaturated solution and / or on various surfaces (Figure 1.1) (Amjad and Demadis, 2015).

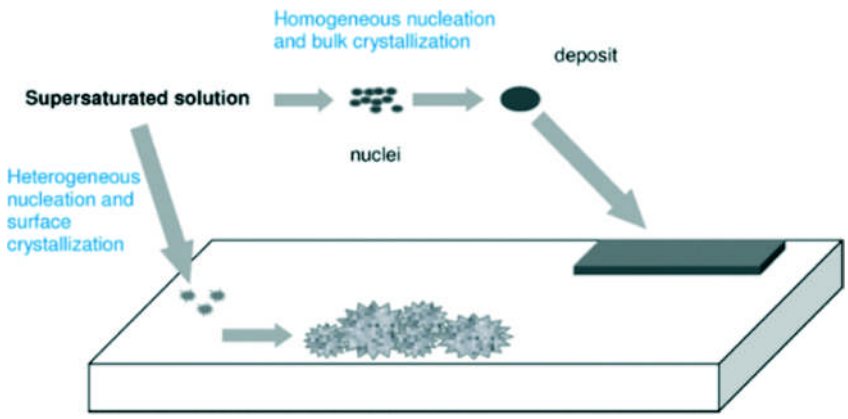

Figure 1.1.Schematic diagram of mineral scale formation in a supersaturated solution and on a surface (from Alabi et al., 2015).

Mineral scaling is governed by both thermodynamics and kinetics (Olajire, 2015). In general, thermodynamics determines which stable phase should precipitate at equilibrium but it does not consider time, whereas kinetics considers the rate at which equilibrium is reached and the rate a scale mineral (or any mineral) precipitates from a supersaturated solution (Safari and

Jamialahmadi, 2014). It is also worth mentioning that, it usually takes a long time for a supersaturated solution to reach equilibrium and therefore, in many cases, because of kinetic factors the first phase to form is not the equilibrium phase but another phase within the same system. For example, although quartz is thermodynamically the most stable silica phase, amorphous silica is the predominant phase that precipitates from geothermal power waters (Brown, 2011). The degree of supersaturation, the pH, the flow rate, or the presence of foreign ions can all to various degrees affect the kinetics of scaling (Brown, 2013). The role and effects that some of these parameters play in the calcium sulfate system will be discussed in detail in chapters 2, and 4-7.

Scaling is observed in different industries such as oil and gas production, water desalination, hydrometallurgy, food processing, and pharmacy. Scaling causes various production problems such as lower efficiency, increased cost, corrosion, etc. (Amjad and Demadis, 2015). For example, in oil industries, to increase oil recovery a solution rich in sulfate ions (e.g., sea water) is injected into a reservoir containing formation water rich in cations (e.g., Ca^{2+}, Ba^{2+}). When these two water bodies meet each other, minerals called scales can form in pipelines and on other production surfaces (Figure 1.2) (Tolaieb, 2014 and references therein).

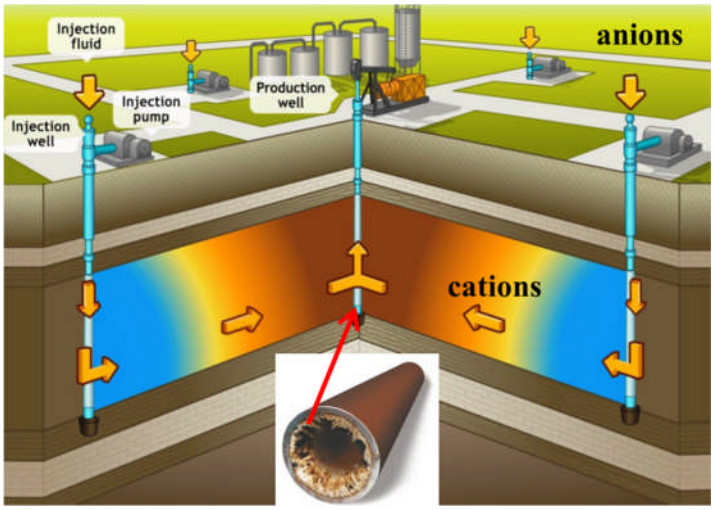

Figure 1.2.Schematic of mineral scaling during oil recovery (modified after Tolaieb, 2014 and references therein).

Among the plethora of mineral scales, calcium sulfate scale formation is one of the most prevailing problems. Calcium sulfate phases can precipitate on any fluid handling surfaces or membranes (e.g., on heat exchanger tubes and water desalination plant membranes) decreasing fluid flow and clogging the membrane, and thus massively reducing production rates (Amjad and Demadis, 2015). Among chemical and physical parameters that effect calcium sulfate formation, temperature is the one that has been most extensively investigated (Freyer and Voigt, 2003). However, there are gaps in our understanding of the effects that, for example, main ions present in seawater or other natural fluids might have on calcium sulfate scale formation.

On the other hand, calcium sulfate formation is not always detrimental, because calcium sulfate phases have some important applications in construction and medical applications (Singh and Middendorf, 2007; Wirsching, 2000). Calcium sulfate phases can occur as different polymorphs with the most important being gypsum (containing two water molecules). This is followed by bassanite (0.5 water molecules in its structure) and anhydrite (obviously anhydrous). Transforming one form into another requires energy but these inter-transformations as well as the formation pathways of these different polymorphs or their importance in mineral scaling are not well-understood.

There are different ways of tackling the scaling problem in different industries. The most common one is using chemicals known as “inhibitors”. These are additives that are injected into a system to reduce scale formation (Olajire, 2015). Different types of inhibitors are available and used but their efficiency or effectiveness has not yet been fully tested and the processes are not understood at the molecular level. Moreover, there is a lack in monitoring of what the effects of inhibitors on the nucleation and growth kinetics of gypsum crystals are by using *in situ* and time resolved techniques. As a result, mineral scaling, and particularly gypsum scaling, although quite often studied, are still a persistent problem that I aim to tackle in my PhD.

It is important, however, to note that the main requirements for an inhibitor to be useful in an industrial process are that (a) the additive has a high efficiency, (b) it is effective at low concentrations (c) its addition will not affect production costs dramatically and (d) it is ideally biodegradable and non-toxic to the environment at concentrations they are used in an industrial process. Therefore, novel biodegradable inhibitors are available but their potential to replace the common industrial antiscalants is not yet well-understood or quantified.

1.2. Aims and objectives

Considering the current knowledge gaps mentioned above, the aims and objectives of my thesis are:

Aim 1: Identify the efficiency of carboxylic acids in hindering gypsum scale formation.

Objective 1.1: Assess the effects of carboxylic acids with different functional groups (citric, maleic and tartaric acids) on the induction time, the growth kinetics and the morphology of gypsum crystals.

Objective 1.2: Assess the influence of carboxylic acids (citric, maleic and tartaric acids) at different concentrations on the crystallisation kinetics of gypsum crystals.

Aim 2: Identify the effect of major ions in, for example, brines or formation waters, on the nucleation and growth kinetics of gypsum.

Objective 2.1: Assess the changes in induction time and gypsum growth kinetics in the presence of major ions in natural fluids (e.g., Li^+, Na^+, K^+ and Mg^{2+}).

Objective 2.2: Identify whether and how these major ions (e.g., Li^+, Na^+, K^+ and Mg^{2+}) associate with gypsum crystals.

Aim 3: Identify the potential of biodegradable polycarboxylic inhibitors to replaced non-biodegradable polycarboxylic inhibitors.

Objective 3.1: Compare the changes in induction time and gypsum growth kinetics in the presence of two “green” antiscalant and two non-biodegradable antiscalant additives and assess the effects that the molecular weight of such inhibitors have on the efficiency of the antiscalant.

Objective 3.2: Identify changes in gypsum morphology in the presence and absence of additives.

Aim 4: Quantify the effects that phosphonate antiscalants have on the crystallisation of gypsum.

Objective 4.1: Test the effects of phosphonate inhibitors that contain different numbers of phosphonate functional groups on gypsum crystallisation kinetics.

Objective 4.2: Identify whether and how phosphonate inhibitors modify the morphology of gypsum crystals.

1.3. Structure of thesis

This thesis consists of the following chapters:

Chapter 1: Introduction; this chapter gives a general overview about the main topic of my thesis (mineral scaling) and outlines the existing research gaps that led me to set up the aims and objectives of my thesis.

Chapter 2: Literature review; in this chapter I review the literature that has proven to be crucial during the development of my research ideas and interpretations. First, I focus on the fundamentals of mineral crystallisation, the crystal chemistry and structural differences between the different phases in the $CaSO_4 – H_2O$ system as the main system I studied, and then I address different types of mineral scales, and discuss scaling mitigation methods.

Chapter 3: Experimental and analytical methods; in this chapter I outline the common analytical techniques that I used in this thesis, and then provide a more in-depth discussion of X-ray photoelectron spectroscopy (XPS) as this is a method less often used in Earth Science research projects.

Chapter 4: Carboxylic acids: effective inhibitors for calcium sulfate precipitation? (published in *Mineralogical Magazine*; Rabizadeh et al., 2014). This chapter is a published paper in which I detail the results from my investigation on the effects of three common carboxylic acid additives with different functional group numbers and structures (tartaric, maleic and citric acids) that have widespread applications in the oil and gas industries on the precipitation of calcium sulfate phases. My data reveals that all additives increased the time needed for gypsum crystals to nucleate and grow and show that citric acid is an effective carboxylic acid inhibitor. The addition of citrate stabilised bassanite and changed the final gypsum habit from typical needle-like crystals in the additive-free system to plates in the citrate additive experiments.

Chapter 5: The effects of inorganic additives on the nucleation and growth kinetics of calcium sulfate dihydrate crystals (published in *Crystal Growth & Design*; Rabizadeh et al., 2017). This chapter is a published paper in which I compare the effects of alkali and alkaline earth metal additives as the major ions in for example brines and formation water (Li^+, Na^+, K^+, Mg^{2+}) on the crystallisation kinetics and mechanisms of gypsum. My results reveal that these additives decreased the crystallisation kinetics in the order of $K^+ < Na^+ < Li^+ < Mg^{2+}$. In all cases, the additives also changed the shapes and sizes of the formed crystals. In addition, I show that, regardless of concentration, Mg^{2+}, Li^+ and K^+ only adsorbed to the newly forming surfaces of the growing gypsum crystals, while ~ 25% of Na^+ became incorporated into the synthesised crystals.

Chapter 6: This chapter summarised the comparative performance of specific biodegradable *vs.* poly(acrylic acid) antiscalants on gypsum crystallisation (to be submitted to the *Journal of*

Crystal Growth). In this chapter, I summarise the findings from an investigation on the effects of 20 ppm of two newly designed and commercialised green scale inhibitors (i.e., poly(epoxysuccinic acid) (PESA), poly(aspartic acid) (PASP)) and 20 ppm of two common industrial non-biodegradable poly(acrylic acid) (PAA) types with molecular weights of ~ 2000 and ~ 100000, on gypsum formation. The results reveal a decrease in gypsum crystallisation kinetics in the presence of these additives. I also discuss the different mechanisms that affect these processes.

Chapter 7: The final results chapter summarises a molecular level insight into the effects of phosphonate antiscalants on the crystallisation of gypsum (in preparation for submission to *Langmuir*). In this chapter, I show how industrial phosphonate antiscalants with a different number of phosphonate functional groups (i.e. from 1 to 5) affect the nucleation and growth kinetics of gypsum. These additives were used in different industrial such as water treatment, oil and gas, etc. However, the mechanisms by which these additives work is not well-understood. My data reveals that an increase in function groups and solution pH is mirrored by a decrease in crystallisation kinetics. Analysing both concentrations of additives in solution during the crystallisation process and solid end-products illustrates that surface adsorption and / or structural incorporation of the antiscalants play important but competing roles. The additives also change the shapes and sizes of the formed crystals.

Chapter 8: In the last chapter, I draw conclusions about the work presented in the previous results chapters and outline some potential knowledge gaps that could be addressed in future studies.

Appendix C: In this part of my thesis, I summarise in brief the findings from the evaluations done on the PbS and ZnS samples provided by Clariant Oil Services UK Ltd.

1.4. References

Alabi, A., Chiesa, M., Garlisi, C. & Palmisano, G., 2015. Advances in anti-scale magnetic water treatment. *Environmental Science: Water Research & Technology,* 1**,** 408-425.

Amjad, Z. & Demadis, K. D., 2015. *Mineral Scales and Deposits: Scientific and Technological Approaches*, Elsevier.

Brown, K., 2011. Thermodynamics and kinetics of silica scaling. *International Workshop on Mineral Scaling.*

Brown, K., 2013. *Mineral scaling in geothermal power production*, United Nations University.

Freyer, D. & Voigt, W., 2003. Crystallization and Phase Stability of CaSO4 and CaSO4 - Based Salts. *Monatshefte fur Chemie / Chemical Monthly,* 134**,** 693-719.

Olajire, A. A., 2015. A review of oilfield scale management technology for oil and gas production. *Journal of Petroleum Science and Engineering,* 135**,** 723-737.

Rabizadeh, T., Peacock, C. L. & Benning, L. G., 2014. Carboxylic acids: effective inhibitors for calcium sulfate precipitation? *Mineralogical Magazine,* 78**,** 1465-1472.

Rabizadeh, T., Stawski, T. M., Morgan, D. J., Peacock, C. L. & Benning, L. G., 2017. The effects of inorganic additives on the nucleation and growth kinetics of calcium sulfate dihydrate crystals. *Crystal Growth & Design,* 17**,** 582-589.

Safari, H. & Jamialahmadi, M., 2014. Thermodynamics, kinetics, and hydrodynamics of mixed salt precipitation in porous media: model development and parameter estimation. *Transport in porous media,* 101**,** 477-505.

Singh, N. & Middendorf, B., 2007. Calcium sulphate hemihydrate hydration leading to gypsum crystallization. *Progress in Crystal Growth and Characterization of Materials,* 53**,** 57-77.

Tolaieb, B. M. A., 2014. *Barium sulphate surface deposition kinetics and inhibition in dynamic flow systems.* PhD, University of Leeds.

Wirsching, F., 2000. Calcium sulfate. *Ullmann's encyclopedia of industrial chemistry,* 6**,** 519-550.

Chapter 2. Literature review

In this chapter, I review the literature that has proven to be crucial during the development of the research ideas and interpretations of the work I have done in my PhD thesis. First, I focus on the fundamentals of mineral crystallisation. Then, I introduce different phases in the $CaSO_4$ – H_2O crystallisation system as the main system I studied, and later I address different types of mineral scales, and discuss scaling mitigation methods.

2.1. Fundamentals of crystallisation

In general, crystallisation can be defined as the transition from a liquid or vapour phase to a solid state (Benning and Waychunas, 2008 and references therein).

The three basic steps that have to happen prior to the formation of a crystal from solution are:

1. Onset of supersaturation
2. Nucleation
3. Growth of the nuclei and their transformation into crystals

These steps will be defined and discussed below.

2.1.1. Supersaturation

To induce crystallisation, one important requirement is to reach a chemical state where supersaturated conditions are achieved. In such a state, the driving force to nucleation and crystallisation is high. It is important, however, to understand that to achieve such a supersaturated state, first we have to be able to determine the thermodynamic solubility product (or solubility constant; K_{sp}) of the mineral system in discussion. Considering that the

solubility of a phase is the ability of a solute to dissolve in a solvent, the K_{sp} is expressed as the propensity of a phase (such as AB) to dissolve in a solvent. By considering equations 2.1 and 2.2 for aqueous systems, we can express the dissociation equilibrium of AB, as the process of one molecule of AB dissociating into x positive ions and y negative ions. For compounds with very low solubility, the K_{sp} values are usually presented in concentration terms rather than their activity, and therefore K_{sp} will be considered as the product of c_+ and c_- ionic concentrations at equilibrium conditions (mol/L) (Mullin, 2001):

$$A_xB_y \Leftrightarrow x\, A^{z+} + y\, B^{z-} \tag{2.1}$$

$$K_{sp} = (c_+)^x (c_-)^y \tag{2.2}$$

where the valencies of the produced ions are represented by z^+ and z^-. For example, dissociation of an AB salt with a 1:1 stoichiometric ratio yields two ions (i.e., x = y = 1). Therefore, the concentration of ions is equal to $c_+ = c_- = c_{eq}$ which c_{eq} is the equilibrium solubility (mol/L) (i.e. dynamic equilibrium occurs when a solid is in equilibrium with chemical solution of that compound) and defined as:

$$c_{eq} = (K_{sp})^{1/2} \tag{2.3}$$

Thus in general,

$$c_{eq} = \left(\frac{K_{sp}}{x^x y^y}\right)^{1/(x+y)} \tag{2.4}$$

Overall, depending on their solubility characteristics, most salts that are important in crystallisation are classified into two groups. Some, which have a very high solubility, are called normal soluble salts and these include sodium chloride (NaCl) or sodium nitrate ($NaNO_3$). Others have lower solubility, and are called sparingly soluble salts such as calcium sulfate ($CaSO_4$) and calcium carbonate ($CaCO_3$) and are the salts of prime interest (Mullin, 2001).

Different physical and chemical parameters affect the solubility of salts in solutions which among them temperature, pressure, mechanical agitation, type of solvent, solution pH, and the presence impurities in solution are the important and common ones (Mullin, 2001).

Supersaturation (SS) also determines how much the solute concentration is higher than the equilibrium solubility and is important because it is considered as driving force for crystallisation processes and are calculated and formulated by different terms. For example, we can consider the concentration driving force as

$$\Delta c = c - c_{eq} \tag{2.5}$$

Therefore, the supersaturation ratio will be

$$SS = c / c_{eq} \tag{2.6}$$

and the relative supersaturation ratio will be

$$\sigma = \Delta c / c_{eq} = SS - 1 \tag{2.7}$$

which are used to report the supersaturation levels of a solution, with c and c_{eq} refer to the solution concentration and the equilibrium solubility (or the concentration at equilibrium) at the specific temperature, respectively (Mullin, 2001).

2.1.2. Nucleation

The nucleation process is classified into two main groups homogeneous or heterogeneous. Heterogeneous nucleation is more common than homogeneous nucleation because always a surface is present in the reaction media (Myerson, 2002).

In a supersaturated solution, ions bind to each other and form clusters. These clusters might become bigger or redissolve until some of the clusters reach a “critical size” (Jackson, 2006; Mullin, 2001).

This process can be considered from the energy variation point of view. During the nucleation of a particle the free energy related to the formation of a new solid volume (ΔG_V) and the free energy from the creation of a new surface (ΔG_s) are varied and the sum of these two terms is expressed as the overall free energy, ΔG, which changes as a function of the nucleation process (Figure 2.1) (Jackson, 2006):

$$\Delta G = \Delta G_S + \Delta G_V \quad (2.8)$$

Simply assuming that the nucleus is spherical with radius r, means that the overall free energy will be:

$$\Delta G = 4\pi r^2\gamma + \frac{4}{3}\pi r^3 \Delta G_\upsilon \quad (2.9)$$

During nucleation, the free energy related to the nucleus formation (per unit volume of the nucleus) and the interfacial tension between the crystallisation medium and the nucleating cluster are changed. This is expressed in equation 2.9 by ΔG_υ and γ, respectively. ΔG_υ has positive value towards nucleation but γ hinders the nucleation. Therefore, there is always a competition between these two terms until the free energy of formation, ΔG, reaches a maximum and the newly formed unit passes a certain maximum value of r^* - i.e., the critical radius (r_c) (Figure 2.1) (Jackson, 2006; Mullin, 2001; Sangwal, 2007).

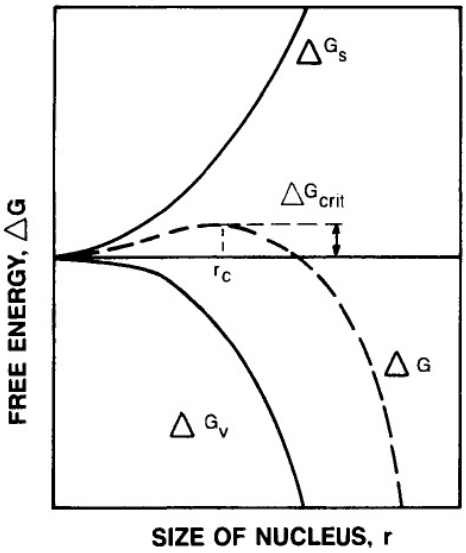

Figure 2.1.Changes in free energy of nucleation as a function of nucleus radius (modified after Myerson, 2002).

The radius of a particle (r_c), can be computed from the minimised free energy function with respect to the nucleus radius, i.e., $\frac{d\Delta G}{dr} = 0$, thus:

$$r_c = \frac{-2\gamma}{\Delta G_\upsilon} \tag{2.10}$$

The free energy for nucleation for this critical nucleus, ΔG_{crit} being expressed as:

$$\Delta G_{crit} = \frac{4\pi\gamma r_c^2}{3} \tag{2.11}$$

Furthermore, the relationship between the solubility of a crystal and its size can be defined by the Gibbs-Thomson relationship (Mullin, 2001; Sangwal, 2007):

$$\ln\left(\frac{c}{c_{eq}}\right) = \ln(SS) = \frac{2\gamma\upsilon}{kTr} \tag{2.12}$$

where υ is the molecular volume (**Å**^{3}), k is the Boltzmann constant ($1.3806488 \times 10^{-23}$ m^2 kg s^{-2} K^{-1}). T is temperature and r is nucleus radius ($r_c < r$). By considering the above equation and the free energy change equations (2.12 and 2.13):

$$-\Delta G_\upsilon = \frac{2\gamma}{r} = KT\frac{\ln(SS)}{\upsilon} \tag{2.13}$$

$$\Delta G_{crit} = \frac{16\pi\gamma^3\upsilon^2}{3[kTln(SS)]^2} \quad (2.14)$$

we can derive the rate of nucleation, J, as per the Arrhenius law (Hong, 2007, Sangwal, 2007):

$$J = A \exp\left(\frac{-\Delta G_{crit}}{kT}\right) \quad (2.15)$$

or

$$J = A \exp\left(-\frac{16\pi\gamma^3\upsilon^2}{3k^3T^3[ln(SS)]^2}\right) \quad (2.16)$$

Equation 2.16 reveals that the temperature, the degree of supersaturation, and the interfacial tension are the main factors affecting the nucleation rate (Myerson, 2002; Sangwal, 2007).

2.1.2.1. Induction period

The time between onset of supersaturation and the formation of the first critical nucleus is called induction period or induction time. The induction time also depends on several factors like temperature, solution composition, supersaturation, agitation, presence of impurities. Induction time invariably depends on the analytical method employed (Myerson, 2002; Sangwal, 2007; Kashchiev and Van Rosmalen, 2003; Sohnel and Mullin, 1988). Techniques applied to measure induction times include: evaluations of the changes in laser light scattering (Prisciandaro et al., 2012), increase in turbidity measured by a turbidity meter (Shih et al., 2004), change in ion selective electrode responses (Shih et al., 2004) or changes in the values measured by conductivity electrodes (Ruiz-Agudo et al., 2014). Some of these that are relevant to my thesis are discussed in detail below.

When turbidity is the parameter used to evaluate the changes in crystallisation process, two different approaches are used to determine the induction time which are (i) the intersection point of the baseline and the line drawn on the linear part of a turbidity curve (Figure 2.2 a; Rashad et al., 2004) or (ii) the point where the baseline deviates from the zero value (Figure 2.2 c; Chen et al., 2004). A turbidity curve is often divided into three regimes (i)

regime in which the turbidity is zero, (ii) nucleation and growth regime where nuclei form and grow; in this regime the turbidity increases fast, and (iii) the stable phase where little to no more change in turbidity values is observed because the degree of supersaturation has changed and the driving force to form new crystals is low and most often in this regime crystals growth has slowed down.

The turbidity can be measured by a spectrophotometer. Vallina et al. (2015) for example used a dual beam UV-vis spectrophotometer to monitor the turbidity variation of a calcium carbonate crystallisation solution inside a cuvette and under a stirring condition. However, when a UV-vis spectrophotometer is used to measure the turbidity variation as a proxy to the crystallisation kinetics, a few concerns should be considered. For example, (i) the Beer-Lambert law is applied to dilute solutions and at concentrated solutions the absorbance plot deviates from linear behaviour (Aulisa and Gilliam, 2015); (ii) any chemical changes during the crystallisation (e.g., dissociation-association) affects the absorbance (Anderson, 2005; Perkampus et al., 1992); (iii) reflection and scattering the light by the surface of the growing crystals may affect the measured absorbance (Jonasz and Fournier, 2011), etc.

When the induction time is derived from changes in solution concentrations measured by ion selective electrode (e.g., Ca^{2+} ion selective electrode to follow $CaSO_4 \cdot 2H_2O$ precipitation) usually the potential *vs.* time is plotted (Figure 2.2 b) and the point where a sharp decrease in calcium ion potential is observed was interpreted as a consequence of calcium ion consumption to form gypsum crystals (Shih et al., 2004).

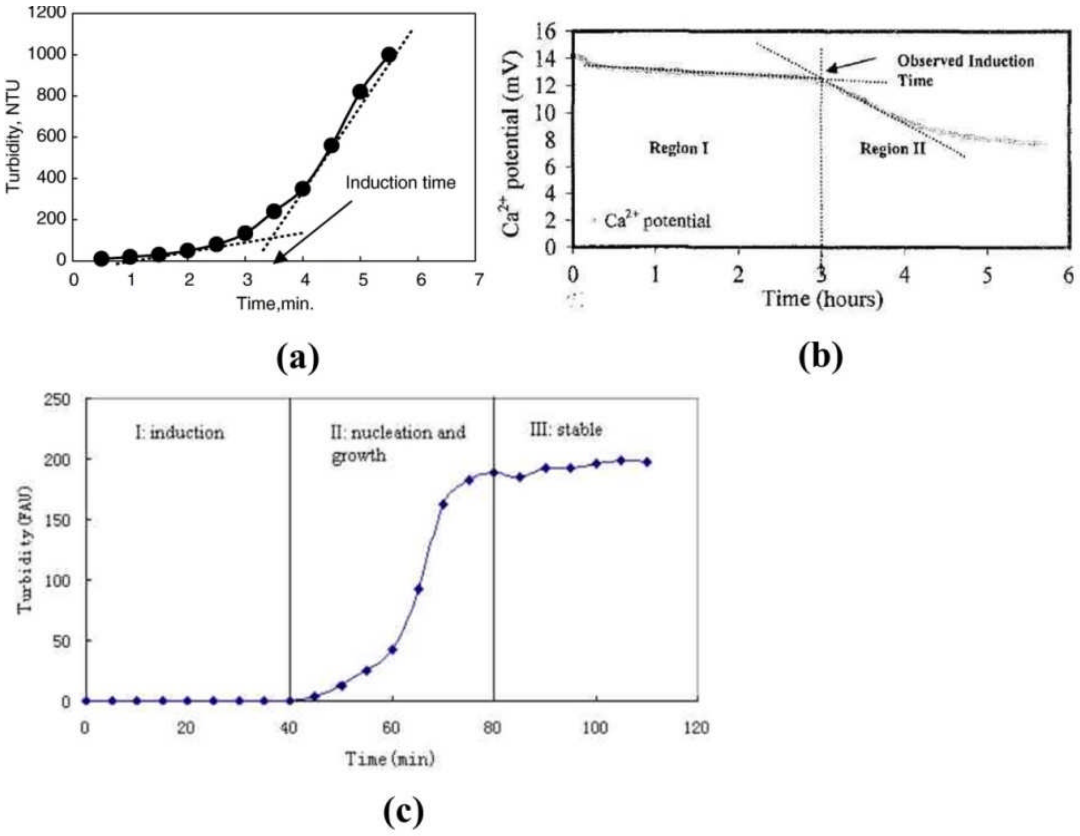

Figure 2.2.(a) Plot of turbidity *vs.* time and the intersection point drawn to determine the induction time from a turbidity curve (from Rashad et al., 2004); (b) induction time determined from a sharp change in a Ca^{2+} ion selective electrode profile (from Shih et al., 2004); (c) three regimes of a turbidity curve and how they are related to the nucleation and growth regimes in a solution (from Chen et al., 2004).

2.1.2.2. Heterogeneous nucleation

In practice, purely homogeneous nucleation is rare and there are always surfaces in experimental or natural systems (e.g., container wall, pipeline, stirrer or impurities). These can act as nucleation sites. This type of nucleation, which occurs at an interface with a surface is called "heterogeneous nucleation". There is a smaller free energy barrier that needs to be surpassed for this type of nucleation to occur compared to homogeneous nucleation, i.e., the overall free energy changes for the heterogeneous nucleation ($\Delta G_{crit,het}$) is smaller than the homogeneous one ($\Delta G_{crit,hom}$) (equation 2.17; Mersmann et al., 1995; Myerson, 2002).

$$\Delta G_{crit,het} = \phi \, \Delta G_{crit,hom} \tag{2.17}$$

where ϕ is less than 1.

As illustrated in Figure 2.3 (a), the contact angle between a newly forming nucleus and a surface is the crucial parameter that decreases the free energy barrier for heterogeneous nucleation. When three phases, for example, a liquid, a newly forming crystal nucleus and a surface are in contact with each other, the interfacial tension between these three entities are the one between surface-liquid (γ_{sl}), crystal-liquid (γ_{cl}) and surface-crystal (γ_{sc}) (De Yoreo and Vekilov, 2003; Mersmann et al., 1995). These three interfacial tensions are related to each through equation 2.18

$$\gamma_{sl} = \gamma_{cs} + \gamma_{cl} \cos\theta \tag{2.18}$$

where θ is the wetting angle

Therefore, parameter ϕ defined in equation 2.17 can be expressed as through equation 2.19:

$$\phi = \frac{(2+\cos\theta)\,(1-\cos\theta)^2}{4} \tag{2.19}$$

Thus, as shown in Figure 2.3 (b), when θ=180˚, crystallisation occurs homogeneously in solution, whereas when θ is between 0˚ and 180˚, the heterogeneous nucleation barrier is reduced because of the wetting of the surface reduced the nucleation barrier. Finally, when θ is 0˚ the surface is completely wetted and the free energy barrier for heterogeneous nucleation is zero (Mersmann et al., 1995).

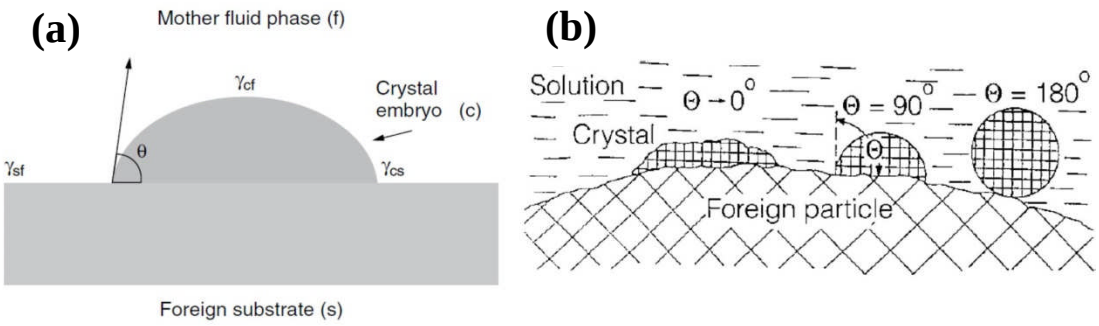

Figure 2.3.(a) Cross section of a crystal formed on a surface with the related interfacial tensions and wetting angle (Sangwal, 2007); (b) the effects of different wetting angles on formation of a crystal on surface (from Mersmann et al., 1995).

2.1.2.3. Classical and non-classical nucleation theories

Nucleation is a complex process and over the last century many theoretical aspects of it have been studied. Currently, there are two theories that are in discussion and each of them has different applications and uses. These are the classical nucleation theory (CNT) and the more recently proposed non-classical nucleation theory. In both theories, by changing the supersaturation of a reacting solution, a new unit precipitates, which gradually transforms into to a solid phase. However, this process can occur via various pathways (Figure 2.4; Stawski and Benning, 2013).

CNT is based on the theoretical knowledge derived from nucleation of water droplets from the vapour phase and it has been transferred to liquid – solid transitions also (e.g., Benning and Waychunas 2008 and references therein). CNT deals with the role and fate of simple monomers such as atoms, ions, molecules in a supersaturated solution during a reaction leading to nucleation and continuing to crystallisation. CNT assumes that such monomers attach to an formed nucleus, which forms in a supersaturated solution. This nucleus is thermodynamically unstable and under its critical size is prone to dissolve. Thus, to have a primary particle, the critical nuclei have to be bigger than a certain size. This theory assumes that nuclei that are formed have the same properties as the final bulk phase (Gebauer and Cölfen, 2011).

However, the more recently proposed, and in part still debated non-classical nucleation theory (Figure 2.4) implies that a reaction in a supersaturated solution first leads to the formation of metastable or stable “pre-nucleation” clusters that then transform, by a so far unknown and not well-defined reaction, into amorphous particles which then, in turn, transform by different pathways to various crystalline phases (Gebauer et al., 2014; Stawski and Benning, 2013; Vallina et al., 2015).

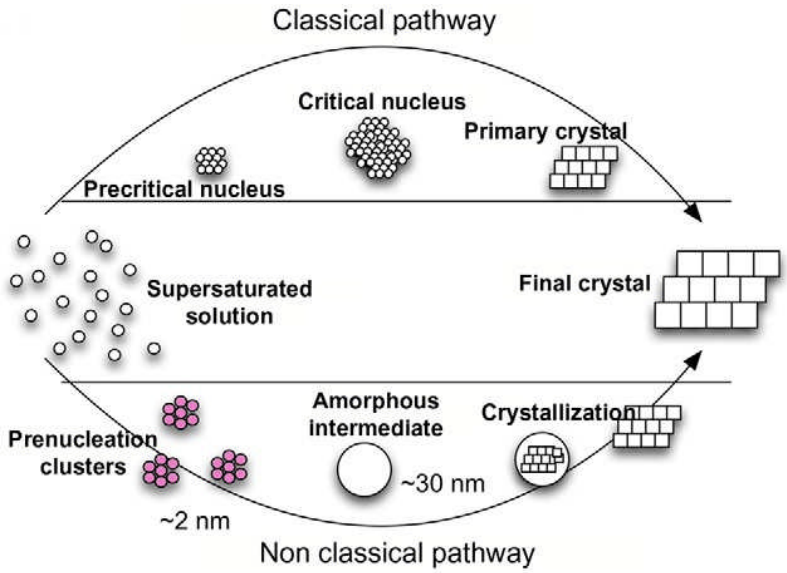

Figure 2.4.Classical and nonclassical pathways describing nucleation and growth of the crystalline materials from solutions (from Stawski and Benning, 2013).

2.1.3. Crystal growth

As long as the system is supersaturated, any nuclei that are stable and larger than the critical size will continue their growth. Various crystal growth theories have been suggested which some of them are discussed here:

(a) **Surface energy theories:** are based on the surface free energy concept and they state that crystal faces grow in such a manner that the total free energy of a phase with a defined volume remains at a minimum. Therefore, the equilibrium crystal shape and the crystal faces growth rates are dependent of the individual free energies of each crystal face (Mullin, 2001 and references therein).

(b) **Adsorption layer theories:** infer that the crystallising units merge into the crystal lattice after loosing one degree of their freedom. Then, they can migrate over the crystal surface by surface diffusion. This process will result in the formation of an adsorption layer at the interface between a crystal face and the bulk solution. (Mullin, 2001 and references therein). It is worth mentioning that it is easier for a crystal unit to incorporate into the kink sites on a crystal surface and this result in kink movement along a step and eventually face growth (Figure 2.5). In several crystal systems and under certain conditions (e.g., barium sulfate)

grow happens through a spiral growth mode because of screw dislocations development on the growing surface (Figure 2.6) (Mullin, 2001 and references therein).

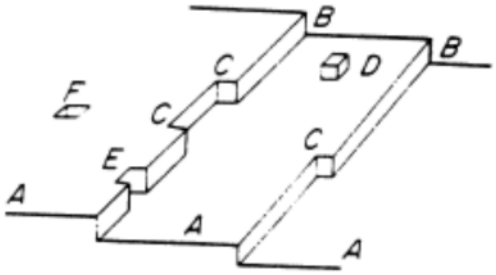

Figure 2.5.Representation of growing crystal surface sites (A) flat surface; (B) steps; (C) kink; (D) surface adsorbed growth unit; (E) edge vacancy; (F) surface vacancy (from Mullin, 2001).

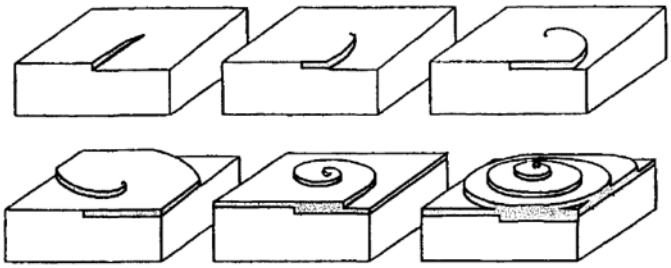

Figure 2.6.Schematic representation of a two dimensional spiral growth by screw dislocations (from Sunagawa, 2001)

2.2. The $CaSO_4 – H_2O$ system

The phases in the $CaSO_4 – H_2O$ system form the most abundant sulfate minerals in nature (Chang et al., 1996). There are three solid phases in the $CaSO_4 – H_2O$ system: calcium sulfate dihydrate (gypsum), calcium sulfate hemihydrate (bassanite), and anhydrite. Bassanite also has two forms α and β, and there are three forms of anhydrites; anhydrite I, anhydrite II, and anhydrite III.

The water content of the various calcium sulfate phases allows inter-transformations between them. Figure 2.7, schematically explains the ideal dehydration and rehydration reactions and the conditions that lead to the different calcium sulfate phases (from Singh and Middendorf, 2007 and references therein).

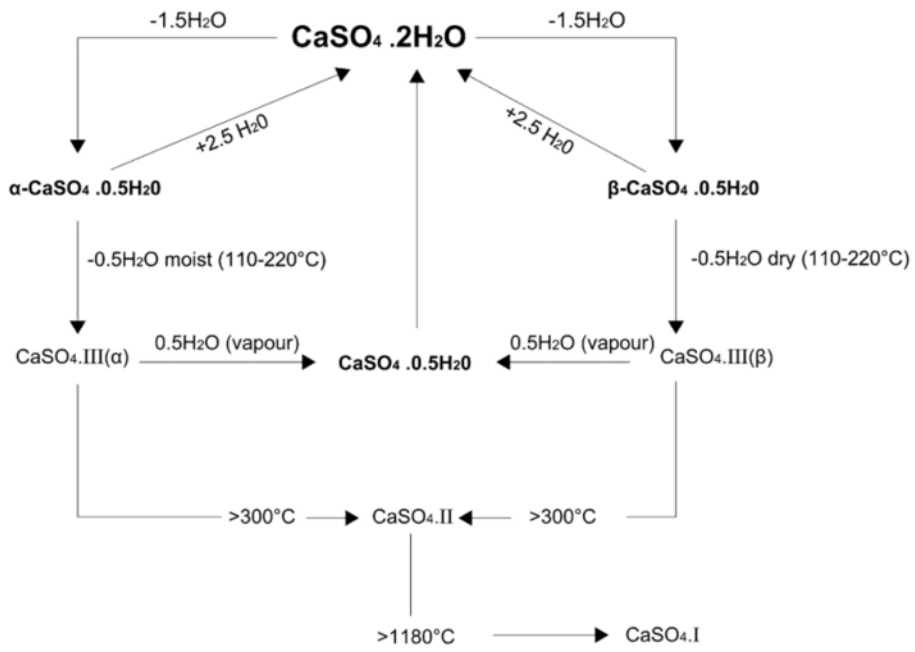

Figure 2.7.Idealised reaction pathways of hydration and dehydration producing different forms of $CaSO_4 \cdot xH_2O$ (x=0.0-2.0) (from Singh and Middendorf, 2007).

2.2.1. Structure of calcium sulfate phases

The crystallographic structure of the crystalline phases in the $CaSO_4 – H_2O$ system (Figure 2.8) has been investigates for many decades as they are important in both natural geochemical cycles (e.g., seawater chemistry) and in many industrial processes (e.g., construction industry). Gypsum has a monoclinic lattice symmetry (Figure 2.8 a) and a space group of I2/a with unit cell parameters of a = 5.6740 Å; b = 15.1049 Å; c = 6.4909 Å and β = 118.513° (Hildyard, 2009 and references therein). In contrast, anhydrite II (Figure 2.8 b) and III have orthorhombic lattice symmetry while anhydrite III is cubic (Wirsching, 2000 and references therein). For anhydrite II, the space group of Amma and unit cell parameters of a = 6.991 Å; b = 6.992 Å; c = 6.238 Å and for anhydrite I, the space group of C222 and unit cell parameters of a = 12.78 Å; b = 6.972 Å; c = 6.304 Å have been suggested (Hildyard, 2009 and references therein).

In contrast a monoclinic bassanite crystal (Figure 2.8 c) has a space group of I121 and unit cell parameters of a = 12.317 Å, b = 6.9269 Å, c = 12.6712 Å and β = 90.27° (Hildyard, 2009 and references therein)

There are lots of contradicting reports about the exact unit cell parameters and lattice symmetries which is primarily due to the large variations in the nature of the samples (impurities or foreign ions in structure), the methods of studies (e.g., neutron or X-ray diffraction), the way used for refining the structures and any changes in temperature, pressure or additive contents in experimentally synthesised crystals (Hildyard, 2009 and references therein).

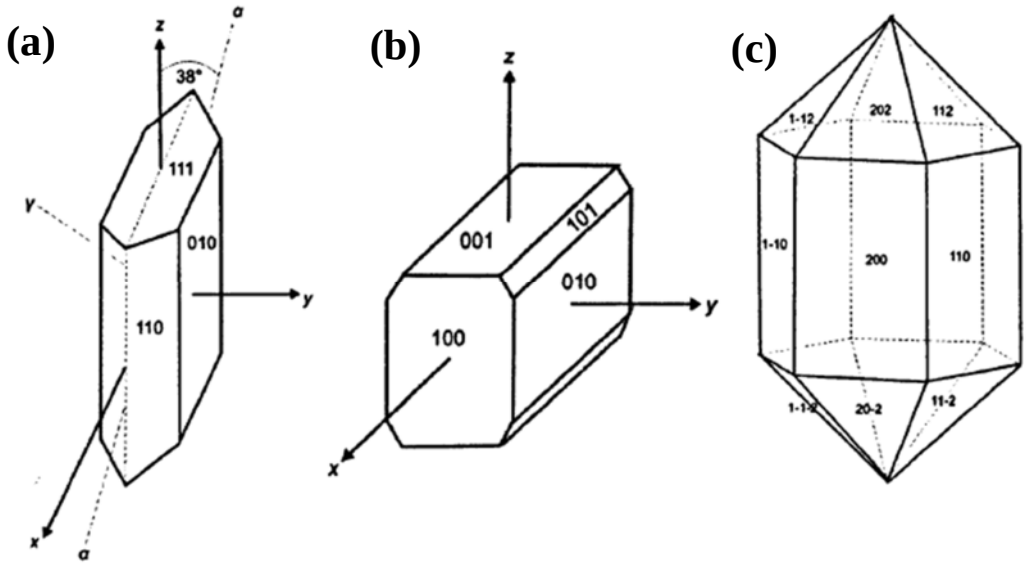

Figure 2.8.Crystallographic unit cell of (a) monoclinic gypsum; (b) orthorhombic anhydrite and (c) monoclinic bassanite (from Hildyard, 2009).

2.2.2. Calcium sulfate dihydrate (gypsum)

Gypsum ($CaSO_4 \cdot 2H_2O$) is an evaporite and sedimentary rock-forming mineral, which is found naturally in both marine and continental regions such as lakes with high salinity, sea water, sabkhas, hot spring and geothermal fluids (Sharpe and Cork, 2006). Gypsum precipitation in the Mediterranean during the Messinian salinity crisis (e.g., ~ 6 million years ago) is a classical example of natural evaporite gypsum formation where gypsum was one of the main calcium salts that formed in the evaporate sequence (Stefano et al., 2010; Testa and Lugli, 2000).

Gypsum precipitation occurs when high proportions (e.g., 66-85 wt. %) of sea water is

evaporated (Lugli, 2008; Sharpe and Cork, 2006). Usually, normal sea water is undersaturated with respect to gypsum but during evaporation, the concentrations of calcium and sulfate ions increase to a level where sea water becomes supersaturated with respect to gypsum. It is worth mentioning that just 75 cm of gypsum would precipitate if 1000 m column of sea water with usual salinity were to evaporate (Sharpe and Cork, 2006 and references therein).

Gypsum can also be a by-product of dolomitisation of carbonate bearing sediments. In that case, during the evaporation of sea water, the activity constant ratio and molar ratio of Mg^{2+}/Ca^{2+} increases and when it reacts with pre-formed carbonate rocks, this can lead to dolomitisations, because the resulting denser brine can sink down through the calcareous sedimental pores and Mg^{2+} replaces Ca^{2+} to form dolomite. As a result, the excess sulfate in the concentrated brine reacts with the released Ca^{2+} to form gypsum (reactions 2.20 and 2.21) (Tucker and Wright, 2009 and references therein).

$$2CaCO_3 + Mg^{2+} \rightarrow CaMg(CO_3)_2 + Ca^{2+} \quad (2.20)$$

$$Ca^{2+} + SO_4^{2-} + 2H_2O \rightarrow CaSO_4.2H_2O \quad (2.21)$$

On Earth, gypsum is also found in gypsiferous and acid sulfate soils (Poch et al., 2010) and recently photographs obtained by rovers together with solid analyses indicated the presence of gypsum even in soils on Mars (Squyres et al., 2012).

There are some unique shapes of gypsum crystals in nature, such as dunes in the White Sands National Monument in New Mexico (Figure 2.9 a) (Langford et al., 2016), and huge crystals in the Naica cave in Mexico (Figure 2.9 b) (García-Ruiz et al., 2007), or rosette shapes (also called desert rose) in arid environments (Figure 2.9 c) (Hope et al., 2015; Jafarzadeh and Burnham, 1992).

Overall, gypsum is a material with hugely diverse applications in various industries such as in construction, cement, soil remediation, or medical usage (Ossorio et al., 2014 and references therein).

Commercial mining is the main way of obtaining gypsum from natural deposits

(Brown, 1990). According to data published by the U.S. Geological Survey, China, the United Sates or America and Iran have the largest resources of gypsum and they were producing a total of 246000 metric tons of gypsum in 2014 (Garbarino et al., 2015).

However, gypsum can also be a by-product as it is formed in industrial processes such as flue gas desulfurization (FGD) (Freyer and Voigt, 2003) or acid production (Sun et al., 2016). In addition, titanogypsum (Zhang et al., 2016), fluorogypsum (Garg and Pundir, 2014) and phosphogypsum (Sun et al., 2016) are produced in different industries. For example, phosphogypsum is obtained during fertiliser or wet phosphoric acid production from phosphate rocks.

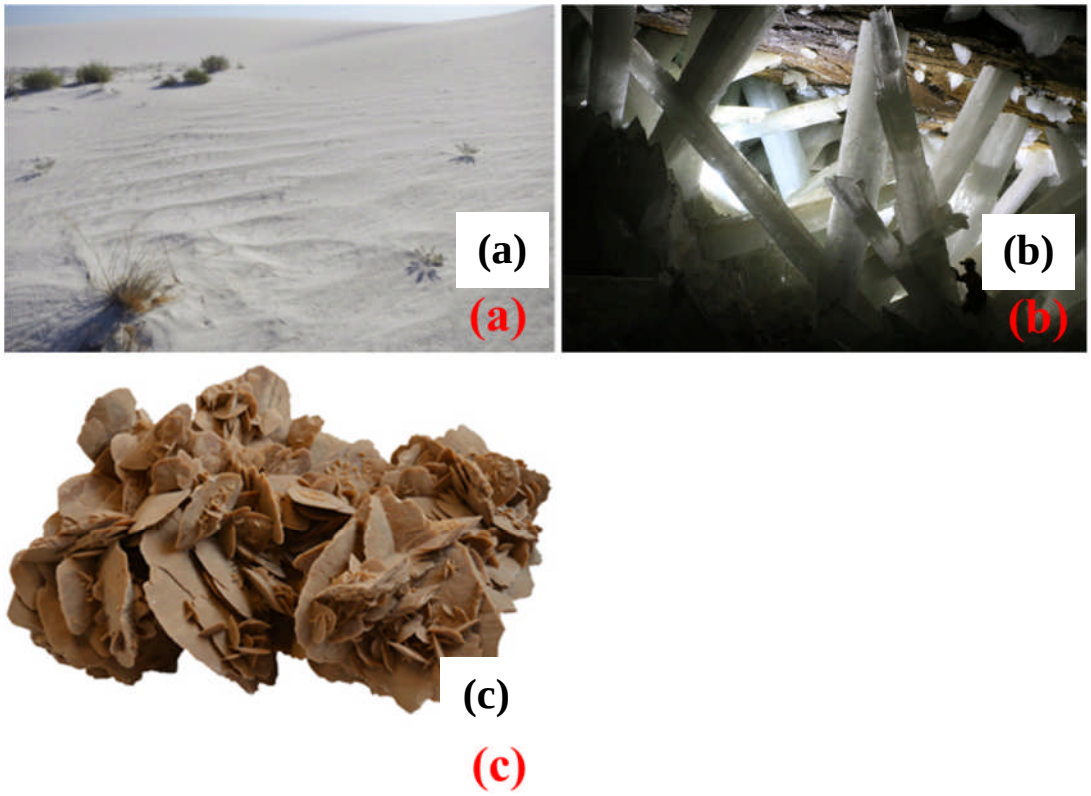

Figure 2.9.Gypsum crystals in nature (a) White Sands National Monument dunes, New Mexico (from Szynkiewicz et al., 2010); (b) huge crystals in the Naica cave in Mexico (from García-Ruiz et al., 2007); (c) rosette shape or desert rose (from Hope et al., 2015).

2.2.3. Calcium sulfate hemihydrate (bassanite)

Bassanite ($CaSO_4 \cdot 0.5H_2O$) has two crystalline forms, α and β. This phase is also hugely important in various industries such as building or construction, ceramics and medical where it

is usually called “Plaster of Paris” (Singh and Middendorf, 2007 and references therein).

Although X-ray diffraction and infrared studies do not show any structural differences between the bassanite α and β forms (Singh and Middendorf, 2007 and references therein), they differ in physical properties (e.g., Feldmann and Demopoulos, 2012; Schmidt et al., 2011). For example, α-bassanite has better mechanical properties which makes it more suitable for construction and medical application (Wang et al., 2008). The α form is usually composed of crystals with a smaller particle size, and therefore less water is required to transform it into a solid and dense mass (Thomas and Puleo, 2009).

Usually bassanite formation requires high temperature and salinity, it is rarely found naturally in soil and rocks except in, for example, dry lake beds in California (Worku and Parker, 1992 and references therein), but surprisingly single crystals of bassanite (up to 60 μm in length and 15 μm in diameter) have been reported to form the statoliths of deep-sea medusae (Becker et al., 2005; Tiemann et al., 2002).

Because it is a hugely important material, bassanite is commercially produced from gypsum via dehydration through an energy consuming procedure. Wet methods (e.g., autoclaving) are used to react gypsum at high temperatures and pressures to produce the α-form, while the β-form is prepared by dry methods (e.g., calcining) (Wirsching, 2000 and references therein). This is also the reason, why many studies in recent years have attempted to synthesise this mineral chemically through less energy demanding methods such as reverse microemulsion (Kong et al., 2012).

2.2.4. Gypsum precipitation pathway

There are still no conclusive studies to fully elucidate the various gypsum formation pathways. Wang et al. (2012) suggested that bassanite particles formed from an amorphous calcium sulfate (ACS) precursor phase through an aggregation procedure. Subsequently, this bassanite transformed to gypsum by an exothermic dissolution-reprecipitation mechanism. They showed that in a barely supersaturated calcium sulfate solution (15 mM) and after 1 minute, an

amorphous calcium sulfate phase formed (Figure 2.10 a) while after 7 days gypsum was the sole phase in the solution. However, when these experiments were carried out in a 50 mM supersaturated calcium sulfate solution and after 1min, there were blocky and rod-like mostly bassanite particles together with a trace amount of gypsum (Figure 2.10 b). The bassanite rods were stable in solution up to 1 hour and finally after 2 hours all of the precipitated materials were gypsum (Figure 2.10 c) (Wang et al., 2012). Furthermore, they suggested that confinement led to stabilisation of the ACS and bassanite with respect to gypsum. The degree of stabilisation depended on the surface separation in the confinement system, i.e., the smaller the surface separation the higher the stabilisation period of the ACS and bassanite because confinement limited the diffusion and aggregation of the precursor particles and the conversion of bassanite to gypsum (Wang et al., 2013).

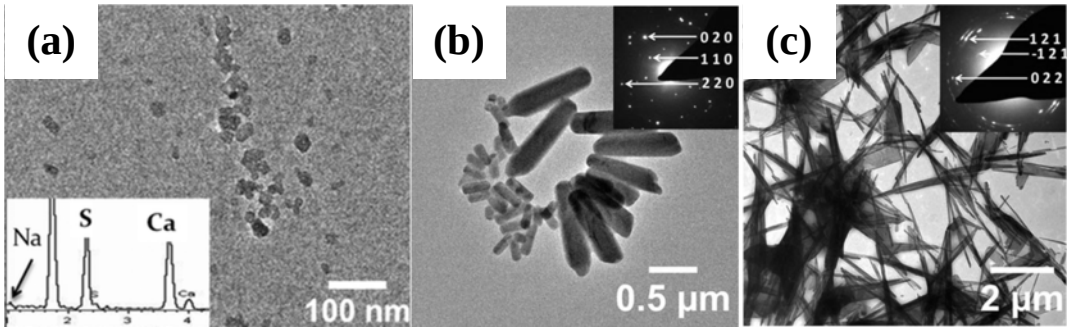

Figure 2.10.Micrographs and elemental analyses or nano-diffraction (insets) of (a) inferred amorphous calcium sulfate particles precipitated from a 15 mM calcium sulfate solution after 1 minute; (b) bassanite particles precipitates from a 50 mM solution after 1 minunte; (c) gypsum crystals formed from a 50 mM solution after 2hours (from Wang et al., 2012).

In the same year, however, Van Driessche et al. (2012) reported that the crystallisation of gypsum does not proceed via ACS but that the first formed phase are nanocrystals of bassanite with 5-15 nm in diameter. With time, these nanocrystals transform into bassanite nanorods that then self-assemble into elongated aggregates which co-oriented along *c*-axis (Figure 2.11) and ultimately these aggregates transformed into gypsum crystals.

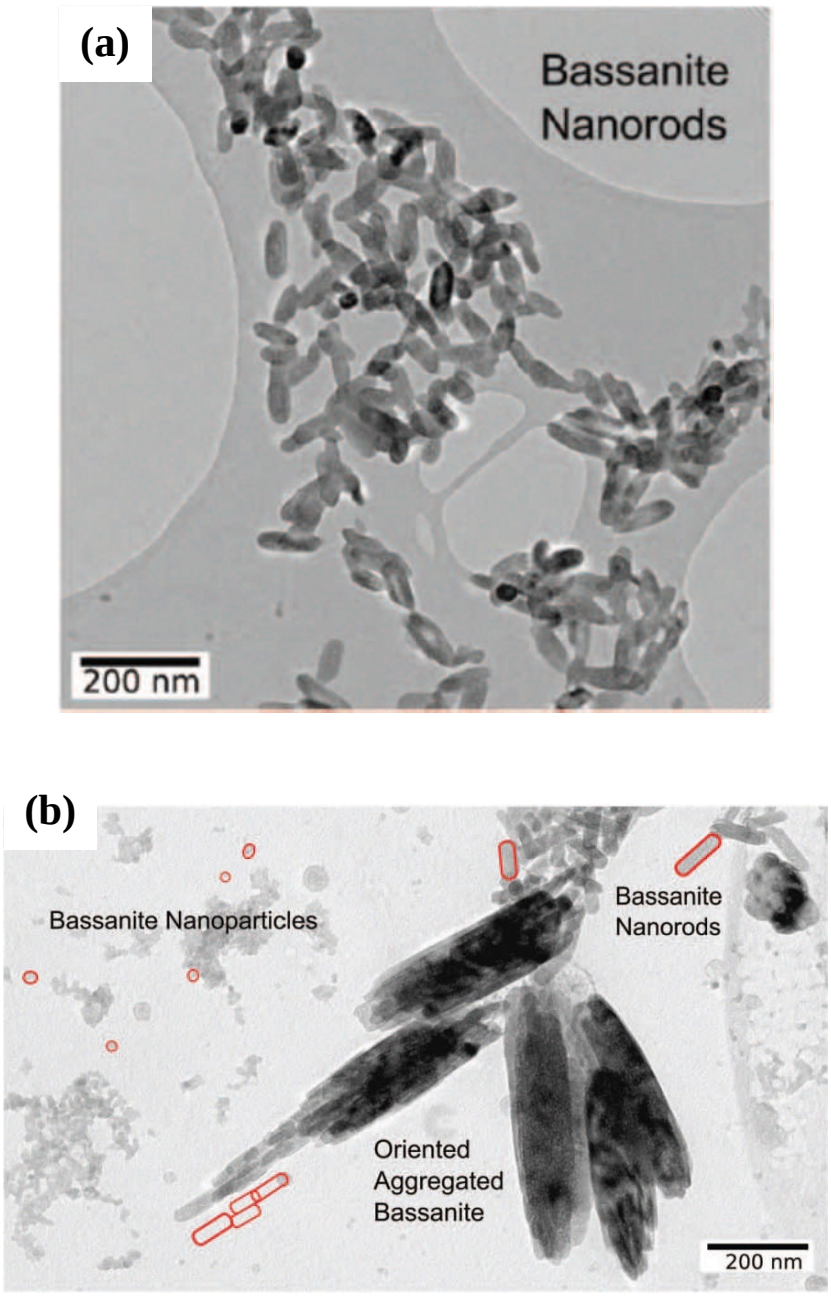

Figure 2.11.Photomicrograph of (a) single bassanite nanoparticles and (b) self-assembled bassanite aggregates (from Van Driessche et al., 2012).

Some studies also suggested that the presence of additives such as poly(acrylic acid) and Mg^{2+} can stabilise both ACS and bassanite at room temperature, and thus delay their transformation into gypsum (Wang and Meldrum, 2012). For example, Saha et al. (2012) proposed that in the presence of citric acid the process progressed through the initial formation of amorphous clusters that transformed to an ACS like phase then it transformed to gypsum crystals (Figure 2.12). Citric acid stabilised the ACS and delayed its transformation to gypsum.

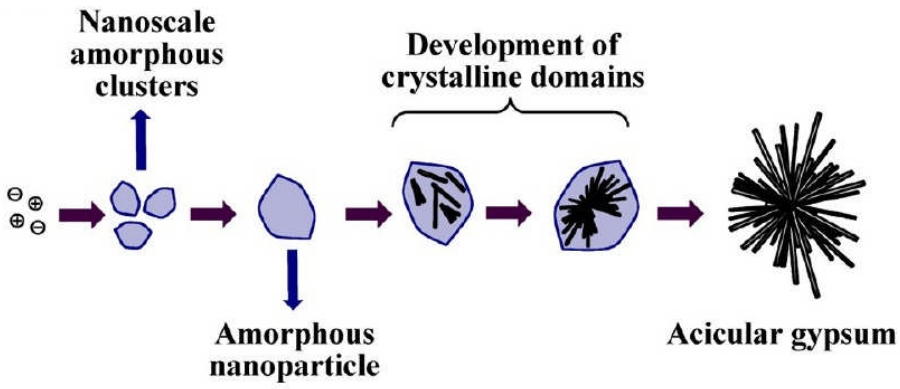

Figure 2.12.A proposed model for the early stages of gypsum formation (from Saha et al., 2012).

2.2.5. Solubility of phases in the $CaSO_4 – H_2O$ system

A number of factors such as temperature, pressure, humidity, and impurities can affect the solubility and phase transformations in the $CaSO_4 – H_2O$ system (Freyer and Voigt, 2003 and references therein).

The solubility curves of different phases in the $CaSO_4 – H_2O$ system at temperature between 0 – 200˚C are shown in Figure 2.13. At low temperatures (< ~ 45 ºC), the phase with the lowest solubility is gypsum, while anhydrite is the stable phase at higher temperatures. At temperatures < ~ 100˚C and at low saturation levels bassanite is metastable and should not be stable. According to Figure 2.13, bassanite should only be stable at high temperatures and rather high saturation levels. This is also the reason why, gypsum and anhydrite are the dominant phases in geological settings while bassanite is rare. The curves intersect showing the transition temperatures between gypsum-anhydrite (at 40 ± 5 ºC), and gypsum-bassanite (99 ± 5ºC) (Azimi et al., 2007; Freyer and Voigt, 2003 and references therein).

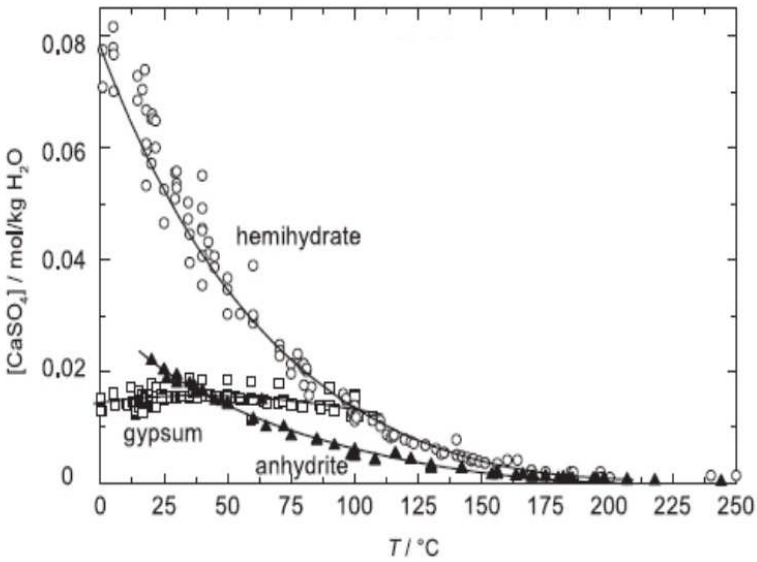

Figure 2.13.Solubility diagram as a function of concentration for gypsum, anhydrite, and bassanite (from Freyer and Voigt, 2003).

In addition, as in all mineral systems, the presence of impurities and specially high concentrations of metallic cations (e.g., Na^+, Mg^{2+}, K^+) affects the solubility of phases in the $CaSO_4 – H_2O$ system. In some cases, this can result in the formation of double salts such as glauberite ($Na_2SO_4.CaSO_4$), syngenite ($K_2SO_4.CaSO_4.H_2O$), polyhalite ($K_2SO_4.MgSO_4.2CaSO_4.2H_2O$), etc. (Spencer, 2000).

The solubility of gypsum in the presence of chloride and sulfate salts has also been examined extensively (e.g., Sverjensky et al., 1997; Zhang et al., 2013). The presence of chloride salts increases the solubility of gypsum (Li and Demopoulos, 2007; Sun et al., 2015a) while with sulfate salts or in the presence of Ca^{2+} the solubility of gypsum decreases (Sun et al., 2015a; Tanji, 1969).

Finally, pressure does not seem to have a large effect and has not been studied, but an increase in the solubility of all $CaSO_4 – H_2O$ phases at high pressure has been reported (Freyer and Voigt, 2003 and references therein).

2.3. Introduction to mineral scaling

Mineral scaling is an undesirable phenomena during which sparingly soluble minerals form from aqueous solutions and deposit onto various surfaces (Kelland, 2014). The formation of mineral scales (e.g., Figure 2.14), leads to industrial problems such as flow reduction or clogging of pipes, valves and other equipments (Amjad and Demadis, 2015).

Figure 2.14.Precipitated mineral scale in an industrial pipe (from Baraka-Lokmane and Sorbie, 2010).

2.3.1. Why is mineral scale formation a problem for industries?

Scale formation is a problem because the deposition of minerals on industrial surfaces used for production usually leads to increased cost due to the need to replace equipment and due to the fact that scale deposition reduces the life time of production wells, etc. Some of these, scaling-related costs for an industrial process include (Bott, 1995):

• Increase in investment, e.g., due to need for replacement of materials (e.g. pipelines, etc.).

• Increase in operational cost, e.g., higher energy consumption due to thermal inefficiencies, pressure drops or clogging. Table 2.1 compares the thermal conductivities of some common mineral scales that often precipitate on heat transfer equipment surfaces and the thermal conductivities of the heat exchanger construction materials. The differences illustrate that even a thin layer of mineral scales can decrease the thermal conductivity and efficiency of a system.

• Higher maintenance cost, e.g., due to local increased corrosion of tubes or pipes and / or the need for additional cleaning systems.

• lower production efficiency, e.g., due to decreasing product quality or due to an inability to meet operational requirements, and / or due to enforced shutdown for cleanup.

• The cost of tackling scaling, such as the need to add some additives that can help reduce scaling and / or of purchasing chemicals to clean scaled surfaces.

Table 2.1.Thermal conductivity of some common mineral scales and metals / alloys (from Bott, 1995)

Material	Thermal conductivity (W/mK)
Calcium sulfate	0.74
Calcium carbonate	2.19
Magnesium carbonate	0.43
Copper	400
Brass	114
Mild steel	27.6

2.3.2. Scale types

The scales discussed here will be primarily the inorganic mineral scales. These are usually divided into groups according to the main anion types (Table 2.2). It is worth mentioning that this table summarises only the main mineral scales occur in industries but it is not a comprehensive list of all possible scales forming in industrial processes and often in different industries the presence of more than one mineral scale type occurs and this multi-scale issue leads to serious problems.

Depending on solution composition and process operational conditions, mineral scales can precipitate on pipe walls, heat exchanger surfaces, pumps, stream generators, boilers, cooling systems, membrane surfaces, etc. (Amjad and Demadis, 2015). These are common in different industries such as oil and gas production (Oddo and Tomson, 1994), water desalination plants (Kostoglou and Karabelas, 2013), geothermal power plants (Pambudi et al.,

2015), sewage and waste water treatment (Doyle and Parsons, 2002), chemical and petrochemical plants (Choi et al., 2002), food (Yu et al., 2003), or in hydrometallurgical processing (Azimi and Papangelakis, 2011).

Table 2.2.Different types of mineral scales

Scale type	Cation	Anion	Example
carbonates	Ca^{2+}, Fe^{2+}	CO_3^{2-}	$CaCO_3$ (Chen et al., 2005); $FeCO_3$ (Figueiredo et al., 2015)
sulfates	Ba^{2+}, Sr^{2+}, Ca^{2+}	SO_4^{2-}	$BaSO_4$ (Xiao et al., 2001); $SrSO_4$ (Safari et al., 2014), $CaSO_4$ (Butt et al., 1997)
sulfides	Fe^{2+}, Pb^{2+}, Zn^{2+}	S^{2-}	FeS (Salman et al., 2007); PbS (Demir et al., 2014); ZnS (Baraka-Lokmane et al., 2015)
chlorides	Na^{+}	Cl^{-}	NaCl (Kan et al., 2003)
fluorides	Ca^{2+}	F^{2-}	CaF_2 (Macdonald and North, 1974)
phosphate	Ca^{2+}	PO_4^{3-}	$Ca_3(PO_4)_2$ (Fu et al., 2012)
oxalate	Ca^{2+}	$C_2O_4^{2-}$	CaC_2O_4 (Doherty et al., 1995)
non-ionic	-	-	SiO_2 (Zarrouk et al., 2014)

2.3.3. Factors affecting mineral scaling

A number of chemical and physical factors affect mineral scale formation.

(a) **Chemical factors**: solution chemistry (water composition), supersaturation and pH are the main chemical factors affecting scale formation. In addition, the presence of impurities (both inorganic and organic) can have also dramatic influences on the crystallisation of undesirable mineral scales and their composition (Amjad and Demadis, 2015).

For example, in order to maintain reservoir pressure and increase oil recovery, in many cases water is injected into reservoirs and mixed with formation waters (Barbot et al., 2013). Table 2.3 illustrates an example from the Forties formation water and North Sea water composition (Moghadasi et al., 2006). Mixing sea water, with high anion concentrations (specially $SO_4^{2-}$and CO_3^{2-}) with the formation water, which usually contains Ca^{2+}, Ba^{2+} and

Sr^{2+} (Abdou et al., 2011) creates problems. This is because upon mixing, the high ion concentrations result in supersaturated conditions and this may cause precipitation of $CaCO_3$, $CaSO_4$, $SrSO_4$ or $BaSO_4$ scales (Crabtree et al., 1999). Scale minerals can also be classified into pH independent (e.g., barium, strontium and calcium sulfates) and pH sensitive mineral scale types (e.g., carbonates, sulfides and SiO_2) (Olajire, 2015).

Table 2.3.Water analysis of North Sea and Forties formation water (from Moghadasi et al., 2006).

Ions (mg/L)	Formation water	Sea water
Cl^-	53000	19800
SO_4^{2-}	-	2480
HCO_3^-	360	135
Mg^{2+}	480	1320
Ca^{2+}	3110	403
Na^+	30200	11000
K^+	430	340
Ba^{2+}	250	-
Sr^{2+}	660	-

(b) **Physical conditions**: any variation in temperature or pressure can lead to changes in supersaturation, and thus can induce scale mineral precipitation. For example, subsurface waters containing calcium bicarbonate and when they reach the surface, because of a reduction in pressure, CO_2 is released and this causes an increase in pH and precipitation of calcium carbonate according to equations 2.22 and 2.23 (Gaur and Abbas, 2013).

$$2HCO_3^- \rightarrow CO_3^{2-} + CO_2 \uparrow + H_2O \quad (2.22)$$

and

$$Ca^{2+} + CO_3^{2-} \rightarrow CaCO_3 \downarrow \quad (2.23)$$

In addition, hydrodynamic factors such as fluid flow velocity (Hasson et al., 1997), pipe diameters (Hoang et al., 2007), Reynolds numbers (Quddus and Al-Hadhrami, 2012) together with the surface roughness (Rankin and Adamson, 1973) and types of surface materials (Zhao

and Liu, 2004) can all affect scale mineral formation. However, comprehensive studies of these effects are lacking, as each of them is very dependent on production conditions in each industry.

2.3.4. Calcium sulfate scales

Calcium sulfate precipitation is one of the most undesirable problems happening in industries such as water desalination plants (Tlili et al., 2007), water distillation (Al-Jaroudi et al., 2010), or oil and gas production (Moghadasi et al., 2003). Calcium sulfate phases can also precipitate as a by-product in hydrometallurgical operations such as sulfuric acid (Adams and Papangelakis, 2007), phosphoric acid (Jamialahmadi and Müller-Steinhagen, 2007) and boric acid (Çetin et al., 2001) production lines.

For example, according to reaction 2.24, gypsum is a by-product of producing boric acid (H_3BO_3) from colemanite ($Ca_2B_6O_{11}.5H_2O$), which is a key boron ore mineral.

$$2CaO.3B_2O_3.5H_2O + 2H_2SO_4 + 6H_2O \rightarrow 2CaSO_4.2H_2O + 6H_3BO_3 \quad (2.24)$$

This type of scale is more stable than the other scales such as calcium carbonate because its formation is pH independent and in this case gypsum precipitates even at a pH as low as 2 (Adams and Papangelakis, 2000). In such systems, calcium sulfate scales can reduce the heat flow when they form on heat exchangers (Kazi et al., 2010), or they can accumulate in pipelines thus clogging the process flow and fouling the reverse osmosis membranes that are commonly used in water desalination systems (Rahardianto et al., 2006). Similar to other scales, various parameters such as temperature, supersaturation, impurities will invariably affect calcium sulfate scale formation (Amjad and Demadis, 2015).

For instance, as described above (section 2.2.5) an increase in temperature reduces the solubility of calcium sulfate phases, and thereby increases their precipitation rates. However, depending on the process temperature, gypsum or anhydrite can form (Amiri et al., 2013). It

has also been reported that impurities such as metal ions (e.g., Cu^{2+}, Cr^{3+}) decrease the calcium sulfate formation (Hamdona and Al Hadad, 2007).

Gypsum as the most prevalent calcium sulfate scale phase has usually a needle shape morphology, and therefore it can easily clog, for example, membranes (Figure 2.15 a). Furthermore, gypsum can have various types of surface growth texture (e.g., bunches of needles or sheaves growing from one point towards the fluid; Figure 2.15 b). These clusters or sheaves can grow on all surfaces of pipeline, for example, and with time they can reach each other in the fluid flow path, and thus clog the pipeline and prevent the fluid flow (Figure 2.15 c, d).

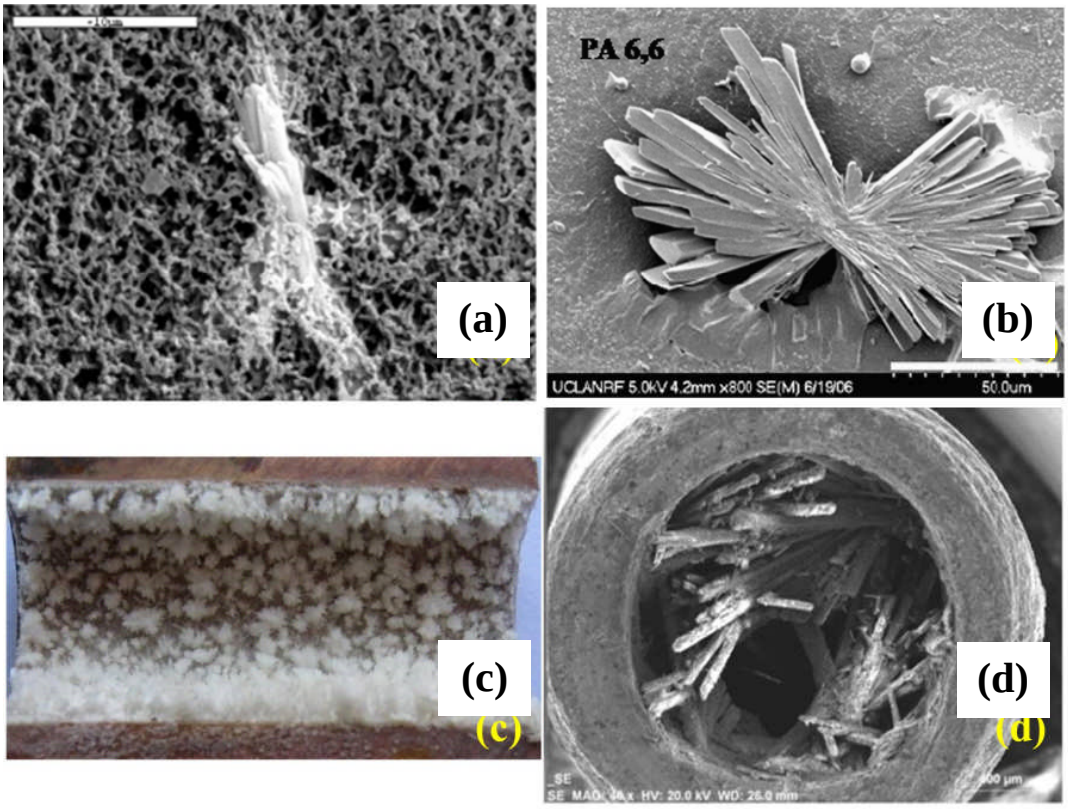

Figure 2.15.(a) Clogging a membrane by needle like gypsum crystals (from Karabelas et al., 2014); (b) growth texture of gypsum crystals forming on a polyacrylic acid modified surface (from Lin et al., 2011); (c) gypsum growth on a semi-annular coupon (from Muryanto et al., 2012); (d) clogging of a steel pipe with an outside diameter of ~ 0.3 cm by gypsum needles (from Al-Roomi and Hussain, 2015).

2.4. Scaling mitigation methods

Mineral scaling reduces the efficiency of industrial processes, so it is crucial to remove the scales after formation or prevent their precipitation. Some of the approaches used to achieve this in industrial processes will be introduced and discussed in this section.

2.4.1. Scale removal methods

There are two different methods to remove precipitated scales: chemical and mechanical (Crabtree et al., 1999). The chemical methods include dissolving the deposited scales such as carbonates and sulfides by acid treatment (Garverick, 1994).

Overall, organic (e.g., citric, formic and sulfamic acids) and inorganic (e.g., HCl) acids are used for acid treatments, but the later acid type is more common in industries due to it slower cost (Kelland, 2014). It is also worth mentioning that these acids are not useful for all mineral scales such as calcium sulfates because of the low solubility of these minerals (e.g., gypsum). Instead EDTA is usually used to dissolve $CaSO_4$ phases (Al-Khaldi et al., 2011).

Although acid treatment is an effective way of removing scales, it has disadvantages too. For examples, hydrochloric acid and sulfuric acids might react with the metals and cause corrosion (Do Carmo Marques and Mainier, 1994). Therefore, it is necessary to add corrosion inhibitors to the acid treatment solutions (Frenier et al., 1989) and choose a suitable acid compatible with base materials which increases costs. Furthermore, some acids such as sulfuric acid might also act as a source of sulfate and can inducing further calcium sulfate precipitation in a system (Delorey et al., 1996).

On the other hand, different mechanical methods such as water jet cleaning, blasting, using a lances are utilised to drill or chip off the scales formed on industrial devices (Thulukkanam, 2013). Most often, a high pressure water jet system with or without sand can be useful to clean both external and internal surfaces (Figure 2.16) (Thulukkanam, 2013).

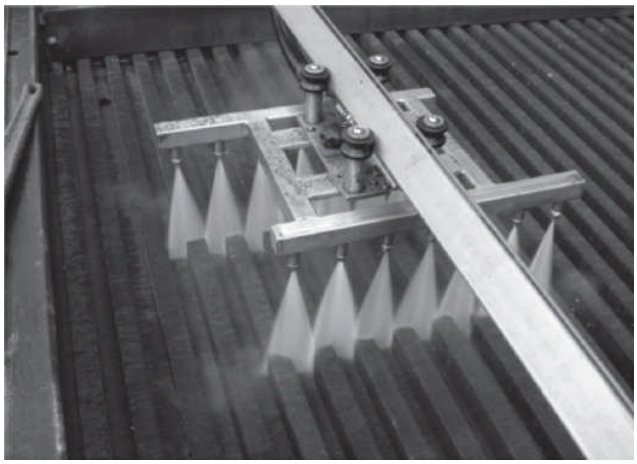

Figure 2.16.Mechanical water jet cleaning a heat exchanger tubes (from Thulukkanam, 2013).

The problem with both chemical and mechanical methods is that usually their implementation in a production unit forces the industrial operations to be shut down whilst scale removal occurs, and this causes a costly downtime. There is also an increased risk of system failure during cleaning. In light of these issues, the prevention or retardation of scale formation is much more appealing than scale removal. At present, however, there is also no single universal method that can be used to prevent scale formation and each scale type requires its own, specific inhibition method.

2.4.2. Scale prevention methods

One way to inhibit scale formation is to treat the water from which the scales are precipitating prior to reaching heat exchangers, boilers, cooling water containers, etc. This method involves either treatment of the water in the system (internal water treatment) or pre-treatment of the water (external water treatment) (Rosmalen, 1983). These classifications are not absolute and sometimes might overlap with each other.

2.4.2.1. External water treatment

External water treatment means treating the source water outside the system and before feeding it into a boiler, heat exchanger, etc. (Rosmalen, 1983). This can include different steps and processes:

- Filtration to remove any rust, sand and corrosion by-products, which might cause pipeline or boiler clogging (Borenstein, 1994).

- Coagulation and flocculation of small suspended particles, which might pass through any filtration set up or through osmotic cartridges (Faust and Aly, 1998). In this process small particles are usually forced to adhere to each other by neutralising their charge using coagulants or by reacting bridged coagulated particles with flocculants. For example, iron and aluminium salts (e.g. $FeCl_3$ and $Al_2(SO_4)_3$) (Gabelich et al., 2002) and some synthetic polymers (Zeng and Park, 2009) are the most common coagulants used in industries.

- Lime-soda and soda-ash softening processes are utilised to reduce the Ca^{2+} and Mg^{2+} concentration in solution. This lead to a sludge that will settled or filtered before feeding the water to the process system (Twort et al., 2000).

- Utilising ion-exchange softening agents and resins such as zeolite is another way to sequestrate metal ions or carbonate, bicarbonate, and sulfates by making complexes and therefore reducing the mineral crystallisation driving force (Antony et al., 2011; Hendricks, 2010);

2.4.2.2. Internal water treatment

Mineral scale prevention by internal treatment can be physical (or mechanical) and chemical. Physical methods include:

- Seeding: this technique is based on introducing a large surface area in the form of the seed materials. These seeds are desirable to induce crystallisation of the undesirable scale precipitate on them (Rosmalen, 1983);

- Ultrasonic treatment: this is performed by positioning an ultrasonic probe or transducer near a surface where scale forms and therefore preventing scaling due to vibrations of the walls and the cavitation and micro-streaming at the surface (Doosti et al., 2012; Rosmalen, 1983).

Ultrasonic treatment also enhances the cross-flow membrane filtration efficiency (Feng et al., 2006; Kyllönen et al., 2006);

- The use of permanent magnets or electromagnets producing a magnetic field within the water passing, for example, through a pipe conduit can inhibit or prevent scale formation. In terms of permanent magnets, the magnets with and without alternating pole arrangements are desirable. Moreover, the number of coils and the thickness of the wire can both affect the field strength of used, and thus efficiency of electromagnets (Figure 2.17). The mechanisms by which the magnetic treatments hinder mineral scaling are still not well-understood and the reported results are often contradictory due to the lack of consistency in experimental procedures (e.g., temperature, exposure time to magnetic field, fluid flow velocity and pipe materials), experimental set-ups and variations in impurity in the to be treated waters (Alabi et al., 2015).

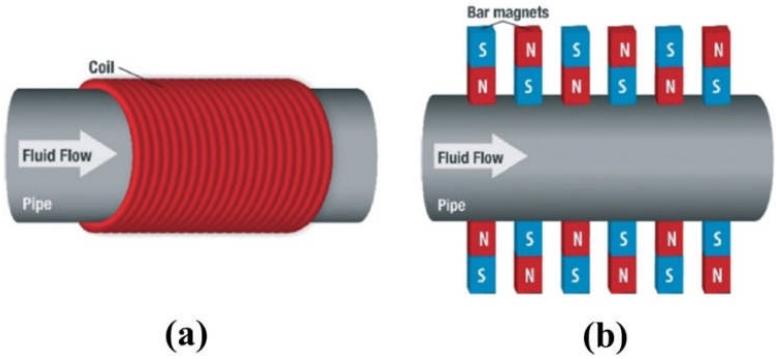

Figure 2.17.Different magnetic field sources utilised for magnetic scaling mitigation (a) coil type; (b) bar magnets (from Alabi et al., 2015).

Utilising chemical antiscalants is the most economical and effective way of mitigating mineral scale formation (Amjad and Demadis, 2015). A few approaches will be discussed in detail below.

2.5. Addition of inhibitors

The term “squeeze treatment” refers to utilising chemicals known as inhibitors or antiscalants with the purpose to prevent or retard the nucleation and / or growth of sparingly soluble minerals both in treated solution and on the surfaces (Amjad and Demadis, 2015; Vazquez et al., 2016).

To date, various polymeric and non-polymeric chemicals have been used and a plethora of research is in progress to synthesise more efficient, economical and environmental friendly inhibitors. Furthermore, it is also important to ideally find antiscalants that can inhibit or retard the formation of more than one mineral scale type.

Although such chemical additives act as antiscalants, they can also act as corrosion inhibitors. They can, for example, adsorb on metal surfaces and create a protective layer against corrosion (Gopi et al., 2007; Marin-Cruz et al., 2006; Shen et al., 2013). This protective layer not only prevents the metal to be corroded but in many cases can also prevent the corrosion products to enter the solution, and thus in turn act as nucleation sites for additional heterogeneous nucleation of mineral scales.

2.5.1. Molecular structures of common antiscalants

Inhibitors are classified according to the functional groups present in their molecular structure. The important anionic groups in inhibitor molecules are (Kelland, 2014):

- phosphate ions ($-OPO_3H^-$)
- phosphonate ions ($-PO_3H^-$)
- phosphinate ions ($-PO_2H^-$)
- carboxylate ions ($-COO^-$)
- sulfonate ions ($-SO_3^-$)

Therefore, the common industrial inhibitors are usually classified into the following groups:

- Phosphates (e.g., sodium triphosphate; Ketrane et al., 2009)

- Phosphonates (e.g., aminotris(methylenephosphonic acid, Zieba et al., 1996)
- Polycarboxylates (e.g., polyacrylic acid, Brinis and Samar, 2014)
- Polysulfonates (e.g., polyvinyl sulfonate, Dyer and Graham, 2003)

It is worth noting, however, that there are inhibitors which contain combinations of these functional groups, and therefore such inhibitors can be considered in more than one classification group. For example, 2-phosphonobutane-1,2,4-tricarboxylic acid (PBTCA) contains one phosphonic acid group and several carboxylic acid groups. Figure 2.18 illustrates the molecular structure of some important industrial inhibitors.

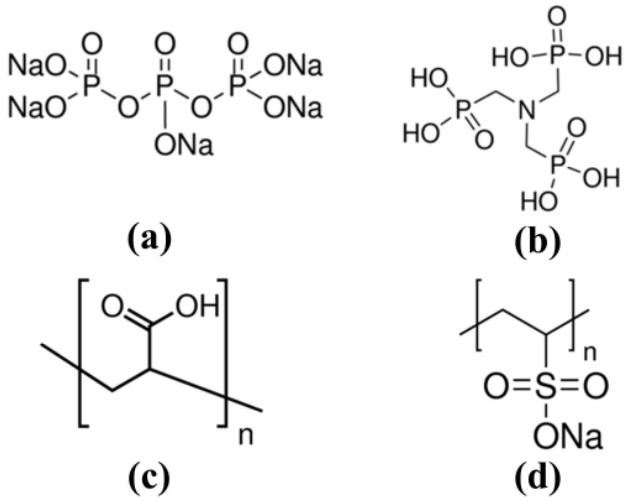

Figure 2.18.Chemical structure of some common industrial antiscalants (a) sodium triphosphate; (b) aminotris(methylenephosphonic acid; (c) polyacrylic acid; (d) polyvinyl sulfonate sodium salt (from Sigma-Aldrich).

2.5.2. Inhibition mechanisms

Scale formation can be reduced or inhibited through a series of mechanisms that are still poorly understood despite the plethora of studies addressing this issue. The proposed mechanisms are classified into the following categories:

(a) Sequestration or chelation: Inhibitors can prevent the crystallisation of mineral scales by making soluble complexes with structure building cations (e.g., Ca^{2+}, Mg^{2+}) present in the

solution. This usually decreases the activity of the cations and prevents ion pair formation and in extreme cases even crystal nucleation (Figure 2.19) (Amjad and Demadis, 2015).

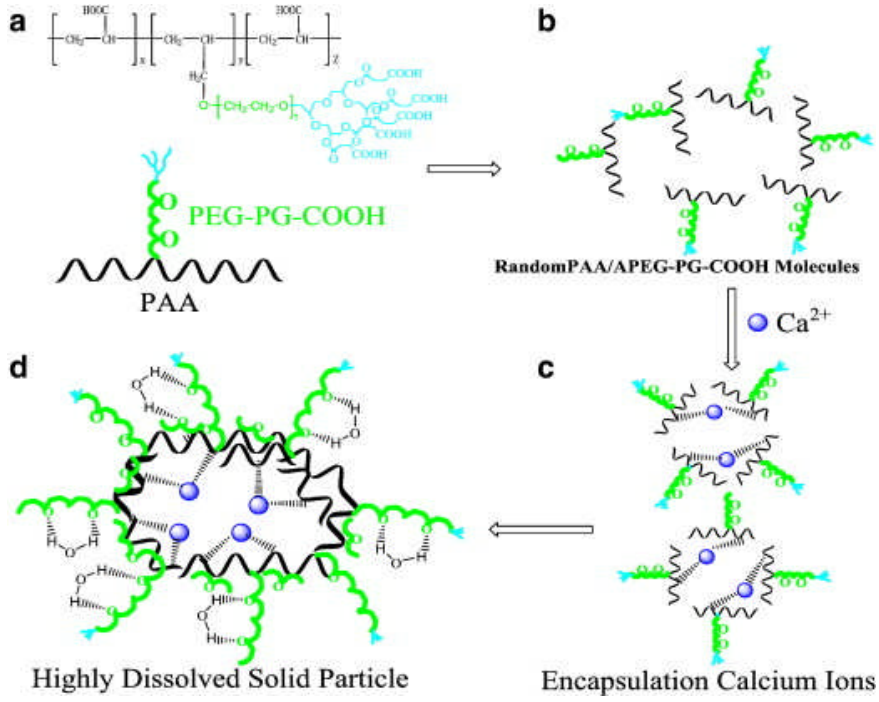

Figure 2.19.Schematic of chelation for an acrylic acid (AA)-allyloxy poly(ethylene glycol) polyglycerol carboxylate (APEG-PG-COOH) copolymer binding to a Ca^{2+} ion; (a) copolymer main chain; (b) random distribution of copolymer in solution; (c) interaction between Ca^{2+} ions and carboxyl groups of the copolymer; (d) distribution of the polymer-Ca^{2+} complexes in solution (from Ling et al., 2012).

(b) Threshold effect: Efficient inhibitors change the crystallisation process at concentrations far below the stoichiometric ratio with reactive cations (usually below 20 ppm) (Amjad and Demadis, 2015; Chen et al., 2015a). Below 20 ppm, by increasing the inhibitor concentration in the solution, its efficiency increases but does not exceed beyond a certain level (threshold concentration). For example, for calcium carbonate inhibition, by increasing the concentration of a phosphonate-terminated poly(maleic-co-sulfonate) inhibitor from 2 ppm to 8 ppm, the calcium carbonate scale inhibition increased from ~ 25% to 90% but beyond this concentration and up to 20 ppm, and scale inhibition does not change significantly (Figure 2.20) (Wang et al., 2009). Although the exact mechanism behind the threshold effect is still unclear, the adsorption of inhibitors on the newly formed nuclei, keeping the nuclei at subcritical size and dissolving them before their growth are the most common suggested

mechanism (Amjad and Demadis, 2015). Therefore, after the disappearance of the nuclei, the inhibitors are available for a repeated adsorption (Liu and Nancollas, 1975).

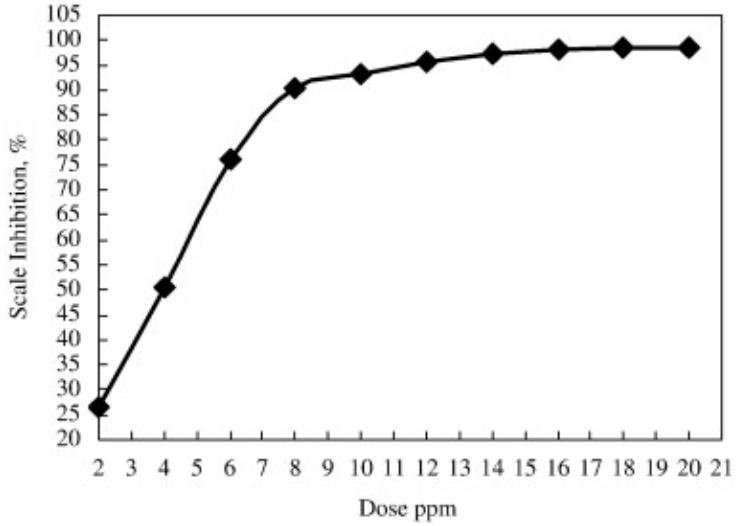

Figure 2.20.The calcium carbonate inhibition by a phosphonate-terminated poly(maleic-co-sulfonate) polymeric inhibitor (from Wang et al., 2009).

(c) Surface adsorption: Inhibitors can adsorb onto growing active sites of mineral scales which can be, for example, crystal defects (kink, step, and terrace). Therefore, they will affect crystal growth by blocking or occupying such growth sites. This process can happen just after the nucleation onset, and thus possibly prevent further diffusion of the scaling forming ions onto a crystal growth site (Amjad and Demadis, 2015).

Among crystal defects, because of lower binding energy required for the adsorption of inhibitors to kink sites compared to terrace sites, inhibitors tend to adsorb more readily to kink sites (Figure 2.21) (Davey and Mullin, 1974; Weijnen et al., 1987). However, beside inhibiting growth, such inhibitors can also act as nucleation inhibitors by absorbing on a newly formed nucleus, and thus preventing its further growth and causing its dissolution (Graham et al., 1997).

It has been reported that to prevent mineral scaling, specially for carbonate and sulfate scales, inhibitors need to cover just between 3-5% of a growing mineral surface (e.g., 5%

coverage of barium sulfate by nitrilotri methylenephosphonic acid) to effectively inhibit its further growth (Leung and Nancollas, 1978).

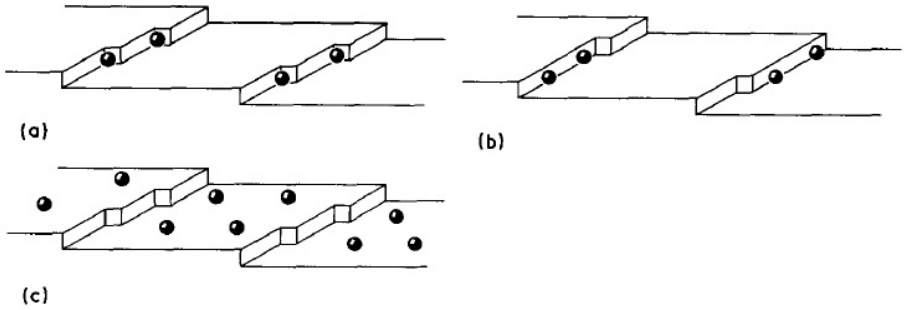

Figure 2.21.Surface defects that inhibitor molecules can adsorb to (a) kink; (b) steps; (c) terrace (Davey and Mullin, 1974).

The selectively adsorption of inhibitors onto a growing sites and the subsequent induced changes in surface properties do also often result in crystal shape modifications (Figure 2.22) (Jones et al., 2002).

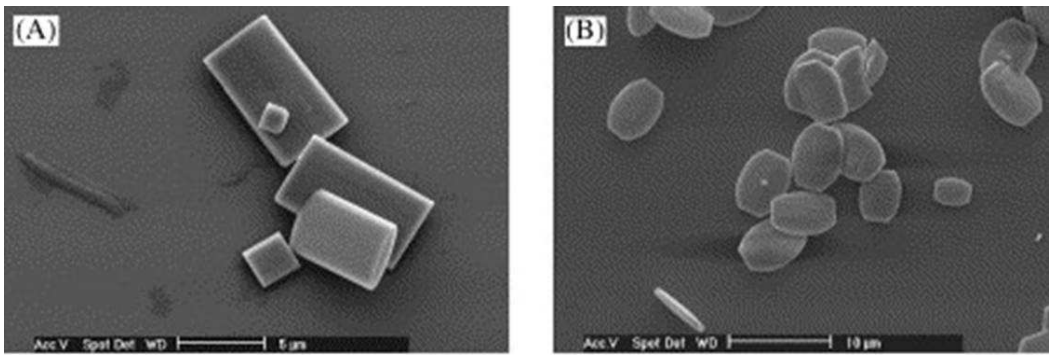

Figure 2.22.Photomicrographs of barium sulfate crystals formed in the presence of the phosphonate molecules at pH 5.6: (a) Control; (b) 10 ppm nitrilodimethylenephosphonic acid (from Jones et al., 2002).

(d) Dispersion: Adsorption of the inhibitors onto crystals can also affects the zeta potential of mineral scales (e.g., silica; Demadis, 2008). Such an effect can cause electrostatic and steric repulsions between newly formed entities (regardless if amorphous or crystalline), and thus this often prevents agglomeration and / or surface deposition of the forming mineral phase and thus the newly formed material remains dispersed in solution and does not form real mineral

scales (Bassioni, 2010). As shown in Figure 2.23, the electrostatic interaction between and adipic acid/amine-terminated polyethers/amine-terminatedpolyethers D230/diethylenetriamine inhibitor and a silica solution prevents the polymerisation of silica and the formation of scales (Zhang et al., 2012).

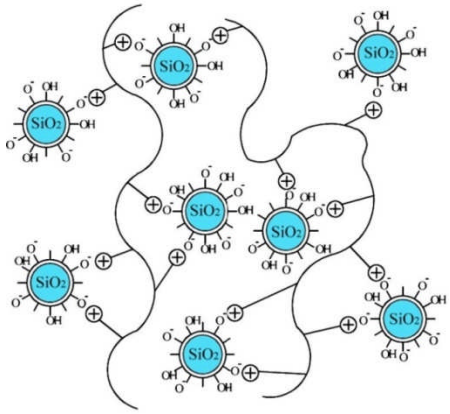

Figure 2.23.Schematic of possible electrostatic interaction between an adipic acid/amine-terminated polyethers/amine-terminated polyethers D230/diethylenetriamine inhibitor and silica (from Zhang et al., 2012).

2.5.3. Green inhibitors

The 1960s are usually considered the trigger point where widespread international concern about environmental pollution and ecosystem devastations caused by industries were becoming a global issue (Grieger, 2012). This was the time that the concepts of “green” chemistry and inhibitors were born yet even today this is not an easy feat to achieve.

Industrial inhibitors used as antiscalants were among the main chemicals that were flushed into the waterways following water treatments, or post use in the oil and gas industries, etc. At the time (and sadly even in part today) inhibitors containing nitrogen, inorganic phosphates and organic phosphorous were released and these caused widespread eutrophication (algae blooming) and massive problems for aquatic live in lakes, rivers and our oceans (Hasson et al., 2011).

Phosphorous and nitrogen are prime metabolic nutrients, but they also result in unfavourable growth of algae and aquatic weeds. Death and decomposition of these plants in

turn will results in oxygen depletion and thereby fish and aquatic organism (Figure 2.24; Khan and Mohammad, 2014; Knockaert, 2014).

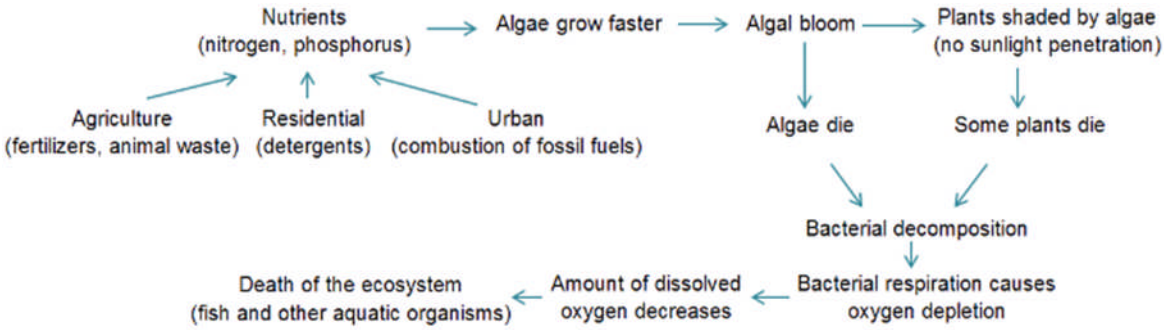

Figure 2.24.An overview on the eutrophication process and its causes and consequences (from Knockaert, 2014).

Finally, an important factor that determines the ability of an inhibitor to be classed as a green inhibitor is its biodegradability. Biodegradability is defined as the decomposition propensity of organic substances by microorganisms into simpler organic compounds that are ideally non-toxic and re-usable in other metabolic processes. The biodegradability of a substance depends on its chemical composition and bonding structure, but also on the presence of right microorganisms, temperature, pH, electrolytes of the medium in which the microbes should degrade the substance (Bastioli, 2005).

Following these criteria, a green chemical inhibitor is defined as one that has to meet three prime criteria: be non-toxic, be easily biodegradable and be non-bioaccumulative (Bastioli, 2005; Martinod et al., 2009).

2.5.3.1. Commonly used green inhibitors

Polyepoxysuccinic acid (PESA) (Shi et al., 2012), polyaspartic acid (PASP) (Sun et al., 2015b), and carboxymethyl inulin (CMI) (Boels and Witkamp, 2011) are the most common green scale inhibitors used in industrial applications. This is because of their excellent biodegradability, their non-toxic nature, their ability to chelate metal ions, and their

dispersibility (Figure 2.25). These green inhibitors are not just environmentally friendly scale inhibitors but they are also green corrosion inhibitors (Cui et al., 2011; Gu et al., 2013)

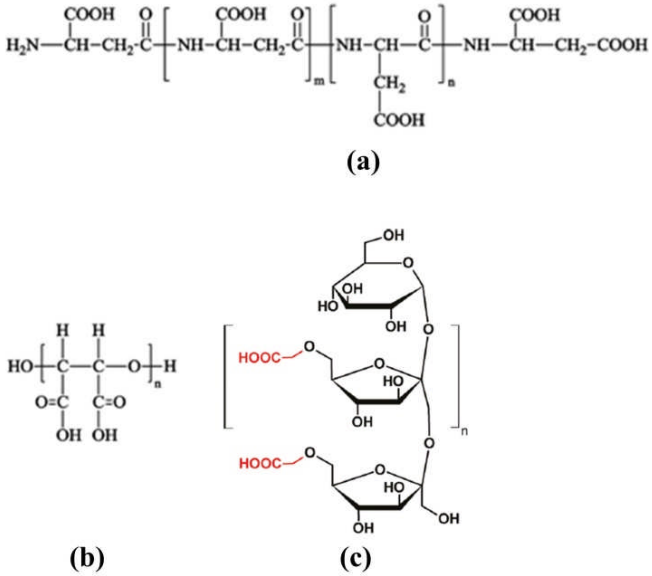

Figure 2.25.(a) Polyaspartic acid (from Xiao et al., 2011); (b) polyepoxysuccinic acid (from Xiao et al., 2011); (c) carboxymethyl inulin (from Boels and Witkamp, 2011).

2.5.4. Factors affecting the efficiency of an inhibitor

There are several factors that can affect the efficiency of an inhibitor, and these have to be taken into account in the process of choosing a suitable inhibitor for a specific system. These factors are temperature, pH, solution hardness and inhibitor molecular structure. For example, as deep oil or gas production wells have a high temperatures (150-250 ˚C), pressures (1000-2000 psi) and todal dissolved solids (> 300,000 mg/L) a selected antiscalant has to be one that has a high efficiency to inhibit the specific scale formation at these conditions and not just at ambient conditions that are usually used for laboratory tests (Sorbie and Laing, 2004).

2.5.4.1. Temperature

Temperature is an important factor affecting the efficiency of an inhibitor. This is because mineral scales usually precipitate at high-temperature conditions such as on deep well pipe

walls or on heat exchanger surfaces. Therefore, a suitable inhibitor should not decompose as this would decreases the surface adsorption and / or chelation capability and eventually the inhibitor efficiency (Amjad and Demadis, 2015).

Although decomposition of the inhibitors is the main reason, a decrease in the solubility of the sparingly soluble salts with temperature is the other factor which declines the efficiency of inhibitors at high temperature (Amjad and Demadis, 2015).

For example, El Dahan and Hegazy, 2000) showed that a 96% calcium sulfate inhibition was possible in the presence of 10 ppm phosphate ester inhibitor at 40 ˚C (Figure 2.26), but at 70 ˚C, the efficiency decreased and 20 ppm were needed to reach a 95% scale inhibition. Further increasing the solution temperature to 90 ˚C dramatically decreased the inhibitor performance and a high concentration of 75 ppm was needed to reach a 97% inhibition (El Dahan and Hegazy, 2000).

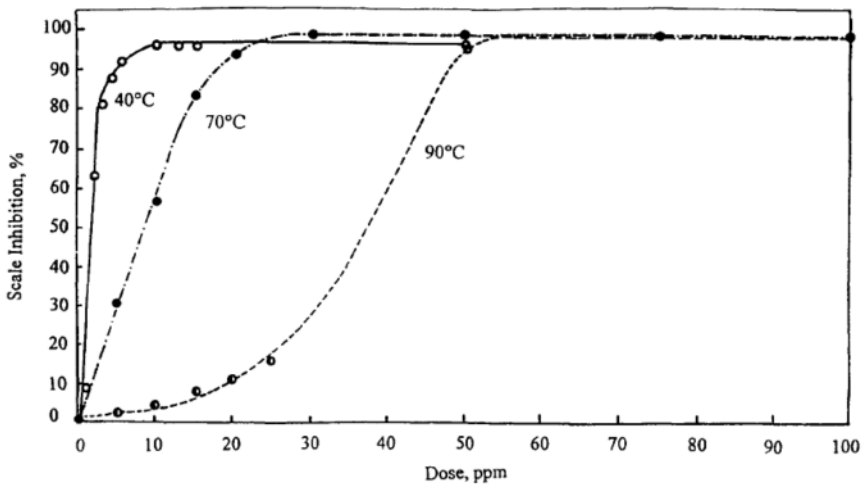

Figure 2.26.Effect of solution temperature on the efficiency of calcium sulfate inhibitor (from El Dahan and Hegazy, 2000).

Similar temperature dependent efficiency have been observed for calcium carbonate (Li et al., 2015) and barium sulfate (Yuan, 2002) inhibitors. To overcome this issue, in some cases polymers with complex structures (such as acrylic acid-allylpolyethoxy maleic carboxylate), which have excellent thermal stabilities up to 700 ˚C have been synthesised and these are more suitable for used in cooling water systems, boilers, etc (Cao et al., 2014).

2.5.4.2. pH

It is well-known that the protonation degree of many inhibitors is pH sensitive (Amjad and Demadis, 2015). It has also been confirmed that inhibitors can bind to cations in a crystallisation solution or that they can attach onto a growing crystal through their deprotonated functional groups and these all depend on the pH of the solution (Amjad and Demadis, 2015).

For example, Figure 2.27 illustrates the dissociation of 1-hydroxyethane-1,1′-diphosphonic acid (HEDP) and nitrilotris(methylenephosphonic acid) (NTMP) over the full pH range. With increasing pH, both inhibitors dissociates and thus form stronger complexes with cations in the solution (Zenobi et al., 2008). At a constant pH of 8, NTMP dissociates more than HEDP making NTMP a stronger antiscalant than HEDP.

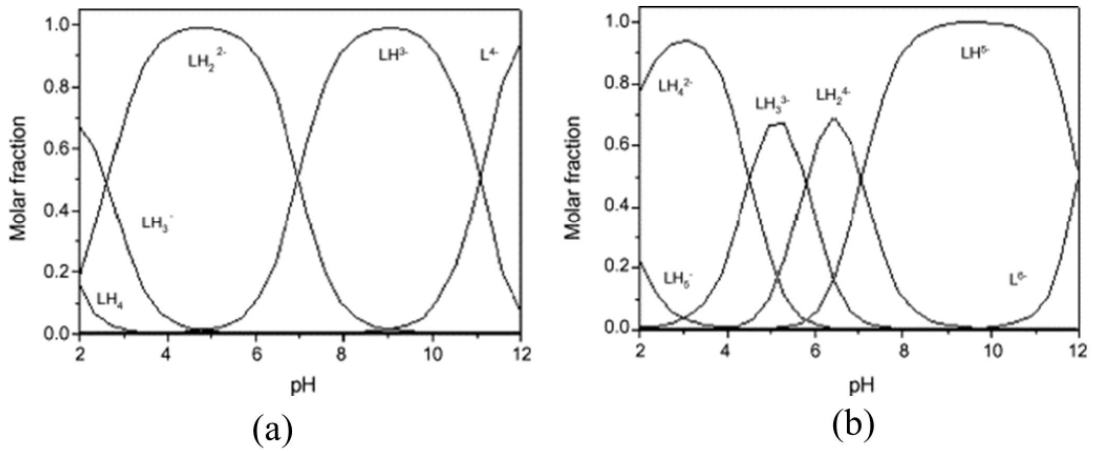

Figure 2.27.Dissociation plots for (a) HEDP and (b) NTMP as a function of pH (from Zenobi et al., 2008).

2.5.4.3. Chemical structure

The effects that an antiscalant's chemical structure can have on its efficiency of scale reduction can be evaluated by analysing the characteristic functional groups on each antiscalant compound, including their type, number and their position in an inhibitor structure (Kelland, 2014).

(a) Functional group type: Inhibitors with phosphonate functional group have higher efficiencies than inhibitors with carboxylic functional groups. For instance, nitrilotris(methylenephosphonic acid) (NTMP) which has 3 phosphonate functional groups, inhibited the growth of gypsum stronger than nitrilotriacetic acid (NTA) with three carboxylic acid functional groups (Hoang et al., 2009).

(b) Number of functional groups: Usually inhibitors with higher numbers of functional groups are more efficient. Thus, to increase the efficiency of a polymeric inhibitor, co-, ter- or quadri-polymers with higher numbers of functional groups have been synthesised through a process called graft polymerisation (Figure 2.28) (Xu et al., 2012). The reason for this increase in efficiency is usually attributed to the presence of multifunctional groups in the additive structure which lead to stronger complexation with cations in the reacting solution as well as likely higher degrees of dispersion of the macromolecule (Liu et al., 2012). For example, it was observed that at the equal concentration of 4 ppm and at 50 ˚C, a poly(aspartic acid)–tryptophan copolymer, has 20% greater calcium carbonate and calcium sulfate inhibition efficiencies than poly(aspartic acid) alone (Sun et al., 2015b).

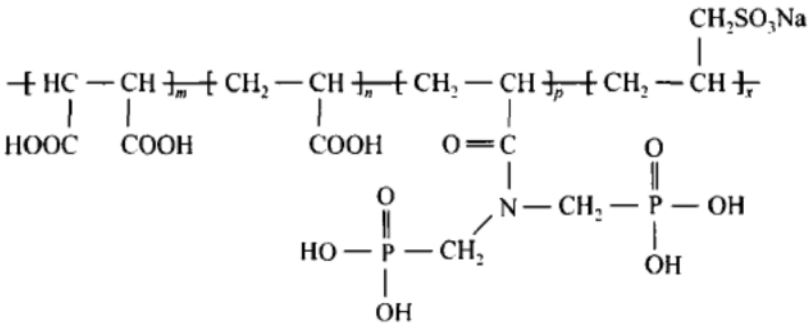

Figure 2.28.Molecular structure of complex quadripolymer inhibitor structure (poly-maleic anhydride-acrylic acid-acrylamide-sodium methallyl sulfonate (from Zhang et al., 2007) that acts as an efficient antiscalant in calcium carbonate and calcium sulfate mineral systems.

Even more complex polymers like acrylic acid-maleic acid copolymer [P(AA-co-MA)] (Shi et al., 2012), acrylic acid-allylpolyethoxy carboxylate-2-acrylamido-2-methyl-propanesulfonic acid [P(AA-APEY-AMPS)] (Bu et al., 2016), and poly-maleic anhydride-acrylic acid-acrylamide-sodium methallyl sulfonate (Zhang et al., 2007) are also examples of co-, ter- and

quadri-polymers, that have been tested and applied as antiscalant additives with high degrees of success. However, further research is needed to fully clarify the effects that such complex additives have on scale reduction.

Finally, the molar ratios between the functional groups present in an inhibitor also affect the efficiency of the antiscalants. As listed in table 2.4, copolymers synthesised with an acrylic acid (AA) to allylpolyethoxy carboxylate (APEY) molar ratio of 3:1 had the highest inhibitor efficiency when used in the $CaSO_4$ system to inhibit gypsum formation. When just 3 ppm were used a 98% calcium sulfate inhibition efficiencies was achieved at 70 ˚C (Cao et al., 2014).

Table 2.4.Effects of functional group molar ratio on the efficiency of the inhibitor (in the presence of 13600 ppm Ca^{2+}, 14.200 ppm SO_4^{2-} at 70 ˚C after 6 h) (from Cao et al., 2014)

AA/APEY molar ratio	maximum gypsum inhibition (%)	minimum dosage (ppm)
5:1	89.3	5
3:1	98.4	3
1:1	94.3	4
1:3	84.5	7
1:5	78.9	9

(C) Chain length: Spacing between the moieties of an antiscalant backbone (or chain length) is also playing a significant role in defining its efficiency. For example, Barouda et al. (2007) documented that ethylenediamine-N,N,N′,N′-tetra(methylenephosphonic acid) (EDTMP) and hexamethylenediamine-N,N,N′,N′-tetra(methylenephosphonic acid) (HDTMP) both with four phosphonate functional groups, have strong barium sulfate inhibition effects but EDTMP is slightly stronger. On the other hand, when the adsorption of polyether polyamino methylene phosphonates (PAPEMP) on anhydrite was investigated by molecular dynamic simulation approach, the results indicated that an PAPEMP type inhibitor with a short chain length ($n \leq$

3) adsorbed well, while at n ≥ 3 the stereo-hindrance effects decreased its efficiency (Shi et al., 2013).

2.5.5. Phase stabilisation effects

The last major effect discussed is the fact that inhibitors can stabilise metastable phases of some scaling minerals. However, the mechanism through which this occurs are still not well-understood.

In the calcium carbonate system, amorphous calcium carbonate and vaterite are metastable phases with respect to the thermodynamically stable phase calcite but 4 ppm of acrylic acid-allylpolyethoxy carboxylate-2-acrylamido-2-methyl-propanesulfonic acid P(AA-APEY-AMPS) stabilised vaterite (Bu et al., 2016). A similar effect was with acrylic acid-oxalic acid-allypolyethoxy carboxylate phosphorous acid (AA-APEM-H_3PO_3) terpolymer (Figure 2.30) (Chen et al., 2015b). In a similar way in the calcium oxalate system, in the presence of PESA, instead of the thermodynamically stable monoclinic calcium oxalate monohydrate, the metastable tetragonal calcium oxalate dihydrate phase was stabilised (Zhang et al., 2015). Again, however, a mechanistic understanding of this observation is still lacking.

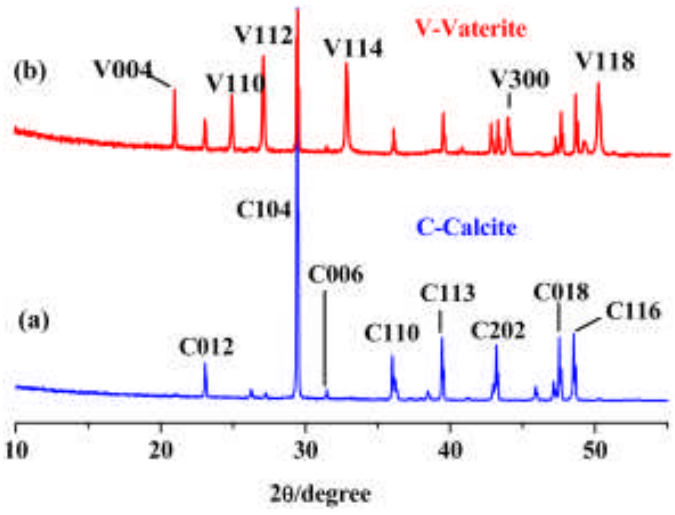

Figure 2.29.XRD pattern of calcium carbonate (a) without AA-APEM-H_3PO_3 terpolymer and (b) with AA-APEM-H_3PO_3 terpolymer (from Chen et al., 2015b).

2.6. Summary of the literature and state-of-the-art

Mineral scaling, and with respect to this PhD specifically gypsum precipitation, is an important problem in many industries dealing with fluid handling. Applying antiscalants is a common and somewhat economical way among scale removing or mitigating methods. This review highlighted in part the plethora of studies that address gypsum scaling and the trials to tackle unwanted gypsum precipitation, but it also revealed that gypsum scaling is still a persistent problem that is not fully understood at a fundamental level. There are still lots of debates and controversial laboratory results which are not applicable in a systematic way to gypsum scale prevention or reduction. This is primarily due to a lack of systematic research on the fundamentals of gypsum crystallisation and the mechanisms by which efficient antiscalants change (inhibit or reduce) gypsum precipitation. Open questions include, for example:

- Do carboxylic acids with different function groups affect the crystallisation pathway of gypsum crystals?

- What are the mechanisms by which the main ions in sea water or ground water (e.g., Li^+, Na^+, K^+ and Mg^{2+}) affect the nucleation and growth kinetics of gypsum crystals?

- What is the potential of common non-biodegradable industrial polycarboxylic antiscalants to be replaced by novel biodegradable green inhibitors with supportive mechanistic reasons?

- What is a good and efficient comparison between the common phosphonate industrial antiscalants and what are the mechanisms by which they affect gypsum scaling?

With these questions in mind, in the following chapters I detail the research I have done to address these knowledge gaps, by investigating the crystallisation pathway of gypsum as a scale mineral, and generating a new molecular-level insight into the effects of different types of inhibitors on gypsum crystallisation and growth kinetics.

2.7. References

Abdou, M., Carnegie, A., Mathews, S. G., McCarthy, K., O'Keefe, M., Raghuraman, B., Wei, W. & Xian, C., 2011. Finding value in formation water. *Oilfield Review,* 23**,** 24-35.

Adams, J. F. & Papangelakis, V. G., 2000. Gypsum scale formation in continuous neutralization reactors. *Canadian metallurgical quarterly,* 39**,** 421-432.

Adams, J. F. & Papangelakis, V. G., 2007. Optimum reactor configuration for prevention of gypsum scaling during continuous sulphuric acid neutralization. *Hydrometallurgy,* 89**,** 269-278.

Al-Jaroudi, S. S., Ul-Hamid, A. & Al-Matar, J. A., 2010. Prevention of failure in a distillation unit exhibiting extensive scale formation. *Desalination,* 260**,** 119-128.

Al-Khaldi, M. H., AlJuhani, A., Al-Mutairi, S. H. & Gurmen, M. N., New insights into the removal of calcium sulfate scale. SPE European Formation Damage Conference, 2011. Society of Petroleum Engineers.

Al-Roomi, Y. M. & Hussain, K. F., 2015. Application and evaluation of novel acrylic based CaSO 4 inhibitors for pipes. *Desalination,* 355**,** 33-44.

Alabi, A., Chiesa, M., Garlisi, C. & Palmisano, G., 2015. Advances in anti-scale magnetic water treatment. *Environmental Science: Water Research & Technology,* 1**,** 408-425.

Amiri, M., Moghadasi, J. & Jamialahmadi, M., 2013. The Effect of Temperature on Calcium Sulfate Scale Tendency in an Iranian Oil Reservoir and Production Equipment During Water Injection. *Energy Sources, Part A: Recovery, Utilization, and Environmental Effects,* 35**,** 2264-2273.

Amjad, Z. & Demadis, K. D., 2015. *Mineral Scales and Deposits: Scientific and Technological Approaches*, Elsevier.

Anderson, C., 2005. Turbidity 6.7 Ver. 2.1. *US Geological Survey Techniques of Water Resources Investigations Book,* 9**,** 55.

Antony, A., Low, J. H., Gray, S., Childress, A. E., Le-Clech, P. & Leslie, G., 2011. Scale formation and control in high pressure membrane water treatment systems: a review. *Journal of membrane science,* 383**,** 1-16.

Aulisa, E. & Gilliam, D., 2015. *A practical guide to geometric regulation for distributed parameter systems*, CRC Press.

Azimi, G. & Papangelakis, V. G., 2011. Mechanism and kinetics of gypsum–anhydrite transformation in aqueous electrolyte solutions. *Hydrometallurgy,* 108**,** 122-129.

Azimi, G., Papangelakis, V. G. & Dutrizac, J. E., 2007. Modelling of calcium sulphate solubility in concentrated multi-component sulphate solutions. *Fluid Phase Equilibria,* 260**,** 300-315.

Baraka-Lokmane, S., Hurtevent, C., Tillement, O., Simpson, C. & Graham, G., Development and Qualification of New Zinc and Lead Sulphide Scale Inhibitors for Application

under Harsh Conditions. SPE International Symposium on Oilfield Chemistry, 2015. Society of Petroleum Engineers.

Baraka-Lokmane, S. & Sorbie, K., 2010. Effect of pH and scale inhibitor concentration on phosphonate–carbonate interaction. *Journal of Petroleum Science and Engineering,* 70**,** 10-27.

Barbot, E., Vidic, N. S., Gregory, K. B. & Vidic, R. D., 2013. Spatial and temporal correlation of water quality parameters of produced waters from Devonian-age shale following hydraulic fracturing. *Environmental science & technology,* 47**,** 2562-2569.

Barouda, E., Demadis, K. D., Freeman, S. R., Jones, F. & Ogden, M. I., 2007. Barium sulfate crystallization in the presence of variable chain length aminomethylenetetraphosphonates and cations (Na+ or Zn2+). *Crystal growth & design,* 7**,** 321-327.

Bassioni, G., 2010. Mechanistic aspects on the influence of inorganic anion adsorption on oilfield scale inhibition by citrate. *Journal of Petroleum Science and Engineering,* 70**,** 298-301.

Bastioli, C., 2005. *Handbook of biodegradable polymers*, iSmithers Rapra Publishing.

Becker, A., Sötje, I., Paulmann, C., Beckmann, F., Donath, T., Boese, R., Prymak, O., Tiemann, H. & Epple, M., 2005. Calcium sulfate hemihydrate is the inorganic mineral in statoliths of scyphozoan medusae (cnidaria). *Dalton Transactions,* 21**,** 1545-1550.

Benning, L. G. & Waychunas, G. A., 2008. Nucleation, growth, and aggregation of mineral phases: Mechanisms and kinetic controls. *In:* Brantley, S., Kubicki, J. & White, A. (eds.) *Kinetics of Water-Rock Interaction.* Springer, pp. 259-333.

Boels, L. & Witkamp, G. J., 2011. Carboxymethyl inulin biopolymers: a green alternative for phosphonate calcium carbonate growth inhibitors. *Crystal Growth & Design,* 11**,** 4155-4165.

Borenstein, S. W., 1994. *Microbiologically influenced corrosion handbook*, Woodhead Publishing Limited.

Bott, T. R., 1995. *Fouling of heat exchangers*, Elsevier.

Brinis, H. & Samar, M. E. H., 2014. A method for inhibiting scale formation and corrosion in a cooling water system. *Desalination and water treatment,* 52**,** 2609-2619.

Brown, R. L., 1990. Exploration and geology techniques. *In:* Kennedy, B. A. (ed.) *Surface mining.* Society for Mining, Metallurgy, and Exploration (SME), pp. 173-181.

Bu, Y., Zhou, Y., Yao, Q., Chen, Y., Sun, W. & Wu, W., 2016. Inhibition of calcium carbonate and sulfate scales by a non-phosphorus terpolymer AA-APEY-AMPS. *Desalination and Water Treatment,* 57**,** 1977-1987.

Butt, F., Rahman, F. & Baduruthamal, U., 1997. Evaluation of SHMP and advanced scale inhibitors for control of CaSO4, SrSO4, and CaCO3 scales in RO desalination. *Desalination,* 109**,** 323-332.

Cao, K., Zhou, Y., Liu, G., Wang, H. & Sun, W., 2014. Preparation and properties of a polyether- based polycarboxylate as an antiscalant for gypsum. *Journal of Applied Polymer Science,* 131**,** 1-9.

Çetin, E., Eroğlu, İ. & Özkar, S., 2001. Kinetics of gypsum formation and growth during the dissolution of colemanite in sulfuric acid. *Journal of Crystal Growth,* 231**,** 559-567.

Chang, L. L., Deer, W. A., Howie, R. A. & Zussman, J., 1996. *Rock-forming minerals. 5B: Non-silicates. Sulphates, carbonates, phosphates, halides*, Geological Society.

Chen, T., Neville, A. & Yuan, M., Effect of PPCA and DETPMP inhibitor blends on CaCO3 scale formation. SPE International Symposium on Oilfield Scale, 2004. Society of Petroleum Engineers.

Chen, T., Neville, A. & Yuan, M., 2005. Calcium carbonate scale formation—assessing the initial stages of precipitation and deposition. *Journal of Petroleum Science and Engineering,* 46**,** 185-194.

Chen, Y., Zhou, Y., Yao, Q., Bu, Y., Wang, H., Wu, W. & Sun, W., 2015a. Evaluation of a low-phosphorus terpolymer as calcium scales inhibitor in cooling water. *Desalination and Water Treatment,* 55**,** 945-955.

Chen, Y., Zhou, Y., Yao, Q., Bu, Y., Wang, H., Wu, W. & Sun, W., 2015b. Preparation of a low- phosphorous terpolymer as a scale, corrosion inhibitor, and dispersant for ferric oxide. *Journal of Applied Polymer Science,* 132**,** 1-10.

Choi, D.-J., You, S.-J. & Kim, J.-G., 2002. Development of an environmentally safe corrosion, scale, and microorganism inhibitor for open recirculating cooling systems. *Materials Science and Engineering: A,* 335**,** 228-235.

Crabtree, M., Eslinger, D., Fletcher, P., Miller, M., Johnson, A. & King, G., 1999. Fighting scale—removal and prevention. *Oilfield Review,* 11**,** 30-45.

Cui, R., Gu, N. & Li, C., 2011. Polyaspartic acid as a green corrosion inhibitor for carbon steel. *Materials and Corrosion,* 62**,** 362-369.

Davey, R. & Mullin, J., 1974. Growth of the {100} faces of ammonium dihydrogen phosphate crystals in the presence of ionic species. *Journal of Crystal Growth,* 26**,** 45-51.

De Yoreo, J. J. & Vekilov, P. G., 2003. Principles of crystal nucleation and growth. *Reviews in mineralogy and geochemistry,* 54**,** 57-93.

Delorey, J., Allen, S. & McMaster, L., Precipitation of calcium sulphate during carbonate acidizing: Minimizing the risk. Annual Technical Meeting, 1996. Petroleum Society of Canada.

Demadis, K. D., 2008. Silica scale inhibition relevant to desalination technologies: Progress and recent developments. *In:* Delgado, D. J. & Moreno, P. (eds.) *Desalination Research Progress.* Nova Science Publishers, Inc.: New York, pp. 249-259.

Demir, M. M., Baba, A., Atilla, V. & İnanlı, M., 2014. Types of the scaling in hyper saline geothermal system in northwest Turkey. *Geothermics,* 50**,** 1-9.

Do Carmo Marques, L. & Mainier, F., 1994. Corrosion Problems Associated with the Use of Copper-Based Corrosion Inhibitor Intensifier in Acid Stimulation Treatments. *SPE Advanced Technology Series,* 2**,** 58-62.

Doherty, W., Crees, O. & Senogles, E., 1995. Polymeric Additives' Effect on Crystallization of Calcium Oxalate Scales. *Crystal Research and Technology,* 30**,** 791-800.

Doosti, M., Kargar, R. & Sayadi, M., 2012. Water treatment using ultrasonic assistance: A review. *Proceedings of the International Academy of Ecology and Environmental Sciences,* 2**,** 96-110.

Doyle, J. D. & Parsons, S. A., 2002. Struvite formation, control and recovery. *Water research,* 36**,** 3925-3940.

Dyer, S. & Graham, G., 2003. Thermal stability of generic barium sulphate scale inhibitor species under static and dynamic conditions. *Journal of Petroleum Science and Engineering,* 37**,** 171-181.

El Dahan, H. & Hegazy, H., 2000. Gypsum scale control by phosphate ester. *Desalination,* 127**,** 111-118.

Faust, S. D. & Aly, O. M., 1998. *Chemistry of water treatment,* CRC Press.

Feldmann, T. & Demopoulos, G. P., 2012. The crystal growth kinetics of alpha calcium sulfate hemihydrate in concentrated CaCl2–HCl solutions. *Journal of Crystal Growth,* 351**,** 9-18.

Feng, D., Van Deventer, J. & Aldrich, C., 2006. Ultrasonic defouling of reverse osmosis membranes used to treat wastewater effluents. *Separation and Purification Technology,* 50**,** 318-323.

Figueiredo, C. M. S., Junior, A. G. B., Flaten, E. M., Beck, R. & Seiersten, M., 2015. Crystal growth of FeCO3 in mixed monoethylene glycol and water solvent. *Crystal Research and Technology,* 50**,** 354-361.

Frenier, W., Hill, D. & Jasinski, R., 1989. Corrosion inhibitors for acid jobs. *Oilfield Review,* 1**,** 15-21.

Freyer, D. & Voigt, W., 2003. Crystallization and Phase Stability of CaSO4 and CaSO4 - Based Salts. *Monatshefte fur Chemie / Chemical Monthly,* 134**,** 693-719.

Fu, C., Zhou, Y., Liu, G., Huang, J., Wu, W. & Sun, W., 2012. Carboxylate-ended poly (ethylene glycol) macromonomers and their copolymers as inhibitors for calcium phosphate and calcium sulfate. *International Journal of Polymeric Materials,* 61**,** 341-356.

Gabelich, C. J., Yun, T. I. & Coffey, B. M., 2002. Effects of aluminum sulfate and ferric chloride coagulant residuals on polyamide membrane performance. *Desalination,* 150**,** 15-30.

Garbarino, R., Struzeski, T. M. & Casadevall, T. J., 2015. US Geological Survey.

García-Ruiz, J. M., Villasuso, R., Ayora, C., Canals, A. & Otálora, F., 2007. Formation of natural gypsum megacrystals in Naica, Mexico. *Geology,* 35**,** 327-330.

Garg, M. & Pundir, A., 2014. Investigation of properties of fluorogypsum-slag composite binders–Hydration, strength and microstructure. *Cement and Concrete Composites,* 45**,** 227-233.

Garverick, L., 1994. *Corrosion in the petrochemical industry*, ASM international.

Gaur, R. P. S. & Abbas, N. M., 2013. Oil-Field Calcium Carbonate Scales. *In:* Amjad, Z. (ed.) *Mineral Scales in Biological and Industrial Systems.* CRC Press, pp. 407-422

Gebauer, D. & Cölfen, H., 2011. Prenucleation clusters and non-classical nucleation. *Nano Today,* 6**,** 564-584.

Gebauer, D., Kellermeier, M., Gale, J. D., Bergstrom, L. & Colfen, H., 2014. Pre-nucleation clusters as solute precursors in crystallisation. *Chem Soc Rev,* 43**,** 2348-71.

Gopi, D., Manimozhi, S., Govindaraju, K., Manisankar, P. & Rajeswari, S., 2007. Surface and electrochemical characterization of pitting corrosion behaviour of 304 stainless steel in ground water media. *Journal of Applied electrochemistry,* 37**,** 439-449.

Graham, G., Boak, L. & Sorbie, K., The influence of formation calcium on the effectiveness of generically different barium sulphate oilfield scale inhibitors. International Symposium on Oilfield Chemistry, 1997. Society of Petroleum Engineers.

Grieger, A., 2012. *Only One Earth: Stockholm and the Beginning of Modern Environmental Diplomacy* [Online]. Available: http://www.environmentandsociety.org/node/3867.

Gu, T., Su, P., Liu, X., Zou, J., Zhang, X. & Hu, Y., 2013. A composite inhibitor used in oilfield: MA-AMPS and imidazoline. *Journal of Petroleum Science and Engineering,* 102**,** 41-46.

Hamdona, S. K. & Al Hadad, U. A., 2007. Crystallization of calcium sulfate dihydrate in the presence of some metal ions. *Journal of Crystal Growth,* 299**,** 146-151.

Hasson, D., Bramson, D., Limoni-Relis, B. & Semiat, R., 1997. Influence of the flow system on the inhibitory action of CaCO 3 scale prevention additives. *Desalination,* 108**,** 67-79.

Hasson, D., Shemer, H. & Sher, A., 2011. State of the art of friendly "green" scale control inhibitors: a review article. *Industrial & Engineering Chemistry Research,* 50**,** 7601-7607.

Hendricks, D., 2010. *Fundamentals of water treatment unit processes: physical, chemical, and biological*, CRC Press.

Hildyard, R. C., 2009. *The Textures and Microstructures of the Calcium Sulphate Minerals Anhydrite Gypsum and Bassanite.* PhD, University of Liverpool.

Hoang, T. A., Ang, H. M. & Rohl, A. L., 2007. Effects of temperature on the scaling of calcium sulphate in pipes. *Powder Technology,* 179**,** 31-37.

Hoang, T. A., Ang, H. M. & Rohl, A. L., 2009. Effects of organic additives on calcium sulfate scaling in pipes. *Australian journal of chemistry,* 62**,** 927-933.

Hong, Y., 2007. *Composite fouling on heat exchanger surfaces,* Nova Publishers.

Hope, S. M., Kundu, S., Roy, C., Manna, S. S. & Hansen, A., 2015. Network topology of the desert rose. *Frontiers in Physics,* 3**,** 1-7.

Jackson, K. A., 2006. *Kinetic Processes: Crystal Growth, Diffusion, and Phase Transformations in Materials*, John Wiley & Sons.

Jafarzadeh, A. & Burnham, C., 1992. Gypsum crystals in soils. *Journal of soil science,* 43**,** 409-420.

Jamialahmadi, M. & Müller-Steinhagen, H., 2007. Heat exchanger fouling and cleaning in the dihydrate process for the production of phosphoric acid. *Chemical Engineering Research and Design,* 85**,** 245-255.

Jonasz, M. & Fournier, G., 2011. *Light scattering by particles in water: theoretical and experimental foundations*, Academic Press.

Jones, F., Oliveira, A., Rohl, A., Parkinson, G., Ogden, M. & Reyhani, M., 2002. Investigation into the effect of phosphonate inhibitors on barium sulfate precipitation. *Journal of crystal growth,* 237**,** 424-429.

Kan, A. T., Fu, G. & Tomson, M. B., 2003. Effect of methanol and ethylene glycol on sulfates and halite scale formation. *Industrial & engineering chemistry research,* 42**,** 2399-2408.

Karabelas, A., Karanasiou, A. & Mitrouli, S., 2014. Incipient membrane scaling by calcium sulfate during desalination in narrow spacer-filled channels. *Desalination,* 345**,** 146-157.

Kashchiev, D. & Van Rosmalen, G., 2003. Review: nucleation in solutions revisited. *Crystal Research and Technology,* 38**,** 555-574.

Kazi, S. N., Duffy, G. G. & Chen, X. D., 2010. Mineral scale formation and mitigation on metals and a polymeric heat exchanger surface. *Applied Thermal Engineering,* 30**,** 2236-2242.

Kelland, M. A., 2014. Production chemicals for the oil and gas industry. 2 ed.: CRC press.

Ketrane, R., Saidani, B., Gil, O., Leleyter, L. & Baraud, F., 2009. Efficiency of five scale inhibitors on calcium carbonate precipitation from hard water: effect of temperature and concentration. *Desalination,* 249**,** 1397-1404.

Khan, M. N. & Mohammad, F., 2014. Eutrophication: challenges and solutions. *In:* Ansari, A. A. & Singh Gill, S. (eds.) *Eutrophication: Causes, Consequences and Control.* Springer, pp. 1-15.

Knockaert, C., 2014. *Possible consequences of eutrophication.* [Online]. Available: http://www.coastalwiki.org/wiki/Possible_consequences_of_eutrophication.

Kong, B., Yu, J., Savino, K., Zhu, Y. & Guan, B., 2012. Synthesis of α-calcium sulfate hemihydrate submicron-rods in water/n-hexanol/CTAB reverse microemulsion. *Colloids and Surfaces A: Physicochemical and Engineering Aspects,* 409**,** 88-93.

Kostoglou, M. & Karabelas, A. J., 2013. Modeling scale formation in flat- sheet membrane modules during water desalination. *AIChE Journal,* 59**,** 2917-2927.

Kyllönen, H., Pirkonen, P., Nyström, M., Nuortila-Jokinen, J. & Grönroos, A., 2006. Experimental aspects of ultrasonically enhanced cross-flow membrane filtration of industrial wastewater. *Ultrasonics sonochemistry,* 13**,** 295-302.

Langford, R. P., Gill, T. E. & Jones, S. B., 2016. Transport and mixing of eolian sand from local sources resulting in variations in grain size in a gypsum dune field, White Sands, New Mexico, USA. *Sedimentary Geology,* 333**,** 184-197.

Leung, W. H. & Nancollas, G. H., 1978. Nitrilotri (methylenephosphonic acid) adsorption on Barium Sulfate crystals and its influence on crystal growth. *Journal of Crystal Growth,* 44**,** 163-167.

Li, X., Gao, B., Yue, Q., Ma, D., Rong, H., Zhao, P. & Teng, P., 2015. Effect of six kinds of scale inhibitors on calcium carbonate precipitation in high salinity wastewater at high temperatures. *Journal of Environmental Sciences,* 29**,** 124-130.

Li, Z. & Demopoulos, G. P., 2007. Speciation-based chemical equilibrium model of CaSO4 solubility in the H+ Na+ Ca+ Mg+ Al+ Fe (II)+ Cl+ SO4+ H2O system. *Industrial & Engineering Chemistry Research,* 46**,** 6385-6392.

Lin, N. H., Shih, W.-Y., Lyster, E. & Cohen, Y., 2011. Crystallization of calcium sulfate on polymeric surfaces. *Journal of colloid and interface science,* 356**,** 790-797.

Ling, L., Zhou, Y., Huang, J., Yao, Q., Liu, G., Zhang, P., Sun, W. & Wu, W., 2012. Carboxylate-terminated double-hydrophilic block copolymer as an effective and environmental inhibitor in cooling water systems. *Desalination,* 304**,** 33-40.

Liu, G., Zhou, Y., Huang, J., Yao, Q., Ling, L., Zhang, P., Zhong, X., Fu, C., Wu, W. & Sun, W., 2012. Carboxylate-terminated double-hydrophilic block copolymer as an effective and environmentally friendly inhibitor for carbonate and sulfate scales in cooling water systems. *Water, Air, & Soil Pollution,* 223**,** 3601-3609.

Liu, S. & Nancollas, G., 1975. A kinetic and morphological study of the seeded growth of calcium sulfate dihydrate in the presence of additives. *Journal of Colloid and Interface Science,* 52**,** 593-601.

Lugli, S., 2008. Evaporites. *In:* Gornitz, V. (ed.) *Encyclopedia of paleoclimatology and ancient environments.* Springer Science & Business Media, pp. 321-325.

Macdonald, R. W. & North, N. A., 1974. The effect of pressure on the solubility of CaCO3, CaF2, and SrS04 in water. *Canadian Journal of Chemistry,* 52**,** 3181-3186.

Marin-Cruz, J., Cabrera-Sierra, R., Pech-Canul, M. & Gonzalez, I., 2006. EIS study on corrosion and scale processes and their inhibition in cooling system media. *Electrochimica acta,* 51**,** 1847-1854.

Martinod, A., Neville, A., Euvrad, M. & Sorbie, K., 2009. Electrodeposition of a calcareous layer: Effects of green inhibitors. *Chemical Engineering Science,* 64**,** 2413-2421.

Mersmann, A., Heyer, C. & Eble, A., 1995. Activated nucleation. *In:* Mersmann, A. (ed.) *Crystallization technology handbook, pp. 45-81.*

Moghadasi, J., Jamialahmadi, M., Müller-Steinhagen, H., Sharif, A., Ghalambor, A., Izadpanah, M. & Motaie, E., Scale formation in Iranian oil reservoir and production

equipment during water injection. International Symposium on Oilfield Scale, 2003. Society of Petroleum Engineers.

Moghadasi, J., Sharif, A., Müuller- Steinhagen, H. & Jamialahmadi, M., 2006. Prediction of scale formation problems in oil reservoirs and production equipment due to injection of incompatible waters. *Developments in Chemical Engineering and Mineral Processing,* 14**,** 545-566.

Mullin, J. W., 2001. *Crystallization,* Butterworth-Heinemann.

Muryanto, S., Bayuseno, A., Sediono, W. & Mangestiyono, W., 2012. Development of a versatile laboratory project for scale formation and control. *Education for Chemical Engineers,* 7**,** 78-84.

Myerson, A., 2002. *Handbook of industrial crystallization,* Butterworth-Heinemann.

Oddo, J. & Tomson, M., 1994. Why scale forms in the oil field and methods to predict it. *SPE Production & Facilities,* 9**,** 47-54.

Olajire, A. A., 2015. A review of oilfield scale management technology for oil and gas production. *Journal of Petroleum Science and Engineering,* 135**,** 723-737.

Ossorio, M., Van Driessche, A., Pérez, P. & García-Ruiz, J., 2014. The gypsum–anhydrite paradox revisited. *Chemical Geology,* 386**,** 16-21.

Pambudi, N. A., Itoi, R., Yamashiro, R., Alam, B. Y. C. S., Tusara, L., Jalilinasrabady, S. & Khasani, J., 2015. The behavior of silica in geothermal brine from Dieng geothermal power plant, Indonesia. *Geothermics,* 54**,** 109-114.

Perkampus, H. H., Grinter, H. C. & Threlfall, T. L., 1992. *UV-VIS Spectroscopy and its Applications,* Springer.

Poch, R. M., Artieda, O., Herrero, J. & Lebedeva-Verba, M. P., 2010. Gypsic Features. *In:* Stoops, G., Marcelino, V. & Mees, F. (eds.) *Interpretation of micromorphological features of soils and regoliths.* Elsevier, pp. 195-216.

Prisciandaro, M., Olivieri, E., Lancia, A. & Musmarra, D., 2012. PBTC as an Antiscalant for Gypsum Precipitation: Interfacial Tension and Activation Energy Estimation. *Industrial & Engineering Chemistry Research,* 51**,** 12844-12851.

Quddus, A. & Al-Hadhrami, L. M., 2012. Impact of solution hydrodynamics on the deposition of CaSO4 on brass. *Desalination and Water Treatment,* 50**,** 285-293.

Rahardianto, A., Shih, W.-Y., Lee, R.-W. & Cohen, Y., 2006. Diagnostic characterization of gypsum scale formation and control in RO membrane desalination of brackish water. *Journal of Membrane Science,* 279**,** 655-668.

Rankin, B. & Adamson, W., 1973. Scale formation as related to evaporator surface conditions. *Desalination,* 13**,** 63-87.

Rashad, M. M., Mahmoud, M. H. H., Ibrahim, I. A. & Abdel-Aal, E. A., 2004. Crystallization of calcium sulfate dihydrate under simulated conditions of phosphoric acid production in the presence of aluminum and magnesium ions. *Journal of Crystal Growth,* 267**,** 372-379.

Rosmalen, G. v., 1983. Scale prevention with special reference to threshold treatment *Chemical Engineering Communications,* 20**,** 209-233.

Ruiz-Agudo, C., Putnis, C. V. & Putnis, A., 2014. The effect of a copolymer inhibitor on baryte precipitation. *Mineralogical Magazine,* 78**,** 1423-1430.

Safari, H., Shokrollahi, A., Moslemizadeh, A., Jamialahmadi, M. & Ghazanfari, M. H., 2014. Predicting the solubility of SrSO 4 in Na–Ca–Mg–Sr–Cl–SO4–H2O system at elevated temperatures and pressures. *Fluid Phase Equilibria,* 374**,** 86-101.

Saha, A., Lee, J., Pancera, S. M., Braeu, M. F., Kempter, A., Tripathi, A. & Bose, A., 2012. New insights into the transformation of calcium sulfate hemihydrate to gypsum using time-resolved cryogenic transmission electron microscopy. *Langmuir,* 28**,** 11182-7.

Salman, M., Qabazard, H. & Moshfeghian, M., 2007. Water scaling case studies in a Kuwaiti oil field. *Journal of Petroleum science and engineering,* 55**,** 48-55.

Sangwal, K., 2007. *Additives and crystallization processes: from fundamentals to applications*, John Wiley & Sons.

Schmidt, H., Paschke, I., Freyer, D. & Voigt, W., 2011. Water channel structure of bassanite at high air humidity: crystal structure of CaSO4· 0.625 H2O. *Acta Crystallographica Section B: Structural Science,* 67**,** 467-475.

Sharpe, R. & Cork, G., 2006. Gypsum and anhydrite. *In:* Kogel, J. E., Trivedi, N. C., Barker, J. M. & Krukowski, S. T. (eds.) *Industrial Minerals & Rocks: Commodities, Markets, and Uses.* 7 ed.: Society for Mining Metallurgy & Exploration, pp. 519-541.

Shen, Z., Ren, H., Xu, K., Geng, J. & Ding, L., 2013. Inhibition effect of phosphorus-based chemicals on corrosion of carbon steel in secondary-treated municipal wastewater. *Water Science & Technology,* 67**,** 2412-2417.

Shi, W.-Y., Ding, C., Yan, J.-L., Han, X.-Y., Lv, Z.-M., Lei, W., Xia, M.-Z. & Wang, F.-Y., 2012. Molecular dynamics simulation for interaction of PESA and acrylic copolymers with calcite crystal surfaces. *Desalination,* 291**,** 8-14.

Shi, W., Xia, M., Lei, W. & Wang, F., 2013. Molecular dynamics study of polyether polyamino methylene phosphonates as an inhibitor of anhydrite crystal. *Desalination,* 322**,** 137-143.

Shih, W.-Y., Albrecht, K., Glater, J. & Cohen, Y., 2004. A dual-probe approach for evaluation of gypsum crystallization in response to antiscalant treatment. *Desalination,* 169**,** 213-221.

Sigma-Aldrich. Available: http://www.sigmaaldrich.com/united-kingdom.html.

Singh, N. B. & Middendorf, B., 2007. Calcium sulphate hemihydrate hydration leading to gypsum crystallization. *Progress in Crystal Growth and Characterization of Materials,* 53**,** 57-77.

Sohnel, O. & Mullin, J. W., 1988. Interpretation of Crystallization Induction Periods. *Journal of Colloid and Interface Science,* 123**,** 43-50.

Sorbie, K. & Laing, N., 2004. How scale inhibitors work: Mechanisms of selected barium sulphate scale inhibitors across a wide temperature range. *SPE International Symposium on Oilfield Scale.* Aberdeen, United Kingdom: Society of Petroleum Engineers.

Spencer, R. J., 2000. Sulfate minerals in evaporite deposits. *In:* Alpers, C. N., Jambor, J. L. & Nordstrom, K. (eds.) *Reviews in Mineralogy and Geochemistry.* Mineralogical Society of America, pp.173-192.

Squyres, S. W., Arvidson, R. E., Bell, J., Calef, F., Clark, B., Cohen, B., Crumpler, L., De Souza, P., Farrand, W. & Gellert, R., 2012. Ancient impact and aqueous processes at Endeavour Crater, Mars. *Science,* 336**,** 570-576.

Stawski, T. M. & Benning, L. G., 2013. SAXS in Inorganic and Bioinspired Research. *In:* Yoreo, J. J. D. (ed.) *Research Methods in Biomineralization Science (Methods in Enzymology).* Elsevier, pp. 95-127.

Stefano, L., Vinicio, M., Marco, R. & Charlotte, S. B., 2010. The Primary Lower Gypsum in the Mediterranean: a new facies interpretation for the first stage of the Messinian salinity crisis. *Palaeogeography, Palaeoclimatology, Palaeoecology,* 297**,** 83-99.

Sun, J., Liu, W., Wang, W., Hu, Y., Yang, X., Chen, H., Zhang, Y., Li, X. & Xu, M., 2016. Optimizing Synergy between Phosphogypsum Disposal and Cement Plant CO2 Capture by the Calcium Looping Process. *Energy & Fuels,* 30**,** 1256-1265.

Sun, J., Wang, L. & Yu, G., 2015a. Effects of Na, Ca, Mg, and Al Chloride Salts on Dissolution and Phase Stability of Calcium Sulfate Dihydrate in Aqueous Solutions at 278.15 K to 308.15 K. *Journal of Chemical & Engineering Data,* 60**,** 2559-2566.

Sun, X., Zhang, J., Yin, C., Zhang, J. & Han, J., 2015b. Poly (aspartic acid)–tryptophan grafted copolymer and its scale- inhibition performance. *Journal of Applied Polymer Science,* 132**,** 1-8.

Sunagawa, I., 2001. Crystal growth—Its significance for modern science and technology and its possible future applications. *In:* Sato, K., Furukawa, Y. & Nakajima, K. (eds.) *Advances in crystal growth research.* Elsevier, pp. 1-21.

Sverjensky, D., Shock, E. & Helgeson, H., 1997. Prediction of the thermodynamic properties of aqueous metal complexes to 1000 C and 5 kb. *Geochimica et Cosmochimica Acta,* 61**,** 1359-1412.

Szynkiewicz, A., Ewing, R. C., Moore, C. H., Glamoclija, M., Bustos, D. & Pratt, L. M., 2010. Origin of terrestrial gypsum dunes—Implications for Martian gypsum-rich dunes of Olympia Undae. *Geomorphology,* 121**,** 69-83.

Tanji, K. K., 1969. Solubility of gypsum in aqueous electrolytes as affected by ion association and ionic strengths up to 0.15 M and at 25. deg. *Environmental Science & Technology,* 3**,** 656-661.

Testa, G. & Lugli, S., 2000. Gypsum–anhydrite transformations in Messinian evaporites of central Tuscany (Italy). *Sedimentary Geology,* 130**,** 249-268.

Thomas, M. V. & Puleo, D. A., 2009. Calcium sulfate: properties and clinical applications. *Journal of Biomedical Materials Research Part B: Applied Biomaterials,* 88**,** 597-610.

Thulukkanam, K., 2013. *Heat exchanger design handbook*, CRC Press.

Tiemann, H., Sötje, I., Jarms, G., Paulmann, C., Epple, M. & Hasse, B., 2002. Calcium sulfate hemihydrate in statoliths of deep-sea medusae. *Journal of the Chemical Society, Dalton Transactions,* 7**,** 1266-1268.

Tlili, M. M., Korchef, A. & Ben Amor, M., 2007. Effect of scalant and antiscalant concentrations on fouling in a solar desalination unit. *Chemical Engineering and Processing: Process Intensification,* 46**,** 1243-1250.

Tucker, M. E. & Wright, V. P., 2009. *Carbonate sedimentology*, John Wiley & Sons.

Twort, A. C., Ratnayaka, D. D. & Brandt, M. J., 2000. *Water supply*, Butterworth-Heinemann.

Vallina, B., Rodriguez-Blanco, J. D., Brown, A. P., Blanco, J. A. & Benning, L. G., 2015. The role of amorphous precursors in the crystallization of La and Nd carbonates. *Nanoscale,* 7**,** 12166-12179.

Van Driessche, A., Benning, L., Rodriguez-Blanco, J., Ossorio, M., Bots, P. & García-Ruiz, J., 2012. The role and implications of bassanite as a stable precursor phase to gypsum precipitation. *Science,* 336**,** 69-72.

Vazquez, O., Herrero, P., Mackay, E. & Jordan, M., 2016. Non-aqueous vs aqueous overflush scale inhibitor squeeze treatment in an oilfield offshore Norway. *Journal of Petroleum Science and Engineering,* 138**,** 1-10.

Wang, C., Li, S.-p. & Li, T.-d., 2009. Calcium carbonate inhibition by a phosphonate-terminated poly (maleic-co-sulfonate) polymeric inhibitor. *Desalination,* 249**,** 1-4.

Wang, P., Lee, E. J., Park, C. S., Yoon, B. H., Shin, D. S., Kim, H. E., Koh, Y. H. & Park, S. H., 2008. Calcium sulfate hemihydrate powders with a controlled morphology for use as bone cement. *Journal of the American Ceramic Society,* 91**,** 2039-2042.

Wang, Y. W., Christenson, H. K. & Meldrum, F. C., 2013. Confinement leads to control over calcium sulfate polymorph. *Advanced Functional Materials,* 23**,** 5615-5623.

Wang, Y. W., Kim, Y.-Y., Christenson, H. K. & Meldrum, F. C., 2012. A new precipitation pathway for calcium sulfate dihydrate (gypsum) via amorphous and hemihydrate intermediates. *Chemical Communications,* 48**,** 504-506.

Wang, Y. W. & Meldrum, F. C., 2012. Additives stabilize calcium sulfate hemihydrate (bassanite) in solution. *Journal of Materials Chemistry,* 22**,** 22055-22062.

Weijnen, M., Van Rosmalen, G. & Bennema, P., 1987. The adsorption of additives at the gypsum crystal surface: A theoretical approach: II. Determination of the surface coverage required for growth inhibition. *Journal of crystal growth,* 82**,** 528-542.

Wirsching, F., 2000. Calcium sulfate. *Ullmann's encyclopedia of industrial chemistry,* 6**,** 519-550.

Worku, T. & Parker, A., 1992. Occurrence of bassanite in Lower Lias rocks of the Lyme Regis area, England. *Mineralogical magazine,* 56**,** 258-260.

Xiao, C., Chen, H., Yu, X., Gao, L. & Guo, L., 2011. Dispersion of aqueous alumina suspensions with biodegradable polymers. *Journal of the American Ceramic Society,* 94**,** 3276-3281.

Xiao, J., Kan, A. & Tomson, M., 2001. Prediction of BaSO4 precipitation in the presence and absence of a polymeric inhibitor: Phosphino-polycarboxylic acid. *Langmuir,* 17**,** 4668-4673.

Xu, Y., Zhao, L., Wang, L., Xu, S. & Cui, Y., 2012. Synthesis of polyaspartic acid–melamine grafted copolymer and evaluation of its scale inhibition performance and dispersion capacity for ferric oxide. *Desalination,* 286**,** 285-289.

Yu, H., Sheikholeslami, R. & Doherty, W. O., 2003. Composite fouling of calcium oxalate and amorphous silica in sugar solutions. *Industrial & engineering chemistry research,* 42**,** 904-910.

Yuan, M., 2002. Effect of Temperature on Barium Sulfate Scale Inhibition of Diethylene Triamine Penta (Methylene Phosphonic Acid). *In:* Amjad, Z. (ed.) *Advances in Crystal Growth Inhibition Technologies.* New York: Kluwer Academic/Plenum Publishers. pp. 151-163.

Zarrouk, S. J., Woodhurst, B. C. & Morris, C., 2014. Silica scaling in geothermal heat exchangers and its impact on pressure drop and performance: Wairakei binary plant, New Zealand. *Geothermics,* 51**,** 445-459.

Zeng, Y. & Park, J., 2009. Characterization and coagulation performance of a novel inorganic polymer coagulant—Poly-zinc-silicate-sulfate. *Colloids and Surfaces A: physicochemical and engineering aspects,* 334**,** 147-154.

Zenobi, M. C., Luengo, C. V., Avena, M. J. & Rueda, E. H., 2008. An ATR-FTIR study of different phosphonic acids in aqueous solution. *Spectrochimica Acta Part A: Molecular and Biomolecular Spectroscopy,* 70**,** 270-276.

Zhang, B., Xin, S., Chen, Y. & Li, F., 2012. Synergistic effect of polycation and polyanion on silica polymerization. *Journal of colloid and interface science,* 368**,** 181-190.

Zhang, Y., Jihuai, W., Sancun, H. & Minghua, L., 2007. Synthesis and inhibition efficiency of a novel quadripolymer inhibitor. *Chinese Journal of Chemical Engineering,* 15**,** 600-605.

Zhang, Y., Tang, Y., Xu, J., Zhang, D., Lu, G. & Jing, W., 2015. Modulation of polyepoxysuccinic acid on crystallization of calcium oxalate. *Journal of Solid State Chemistry,* 231**,** 7-12.

Zhang, Y., Wang, F., Huang, H., Guo, Y., Li, B., Liu, Y. & Chu, P. K., 2016. Gypsum blocks produced from TiO2 production by-products. *Environmental technology,* 37**,** 1094-1100.

Zhang, Y., Yang, Z., Guo, D., Geng, H. & Dong, C., 2013. Effect of chloride salts and bicarbonate on solubility of CaSO 4 in aqueous solutions at 37 C. *Procedia Environmental Sciences,* 18**,** 84-91.

Zhao, Q. & Liu, Y., 2004. Investigation of graded Ni–Cu–P–PTFE composite coatings with antiscaling properties. *Applied surface science,* 229**,** 56-62.

Zieba, A., Sethuraman, G., Perez, F., Nancollas, G. & Cameron, D., 1996. Influence of organic phosphonates on hydroxyapatite crystal growth kinetics. *Langmuir*, 12**,** 2853-2858.

Chapter 3. Experimental methods

The full details of all experimental procedures and sample preparation and handling methods are described separately in each results chapter. In this chapter, at first the common analytical techniques utilised in this thesis are briefly introduced, while X-ray photoelectron spectroscopy (XPS) is described in more detail as it is a method less often used in Earth science research projects.

3.1. Ultraviolet and visible (UV-Vis) absorption spectroscopy

This technique was used to measure the change in light (as a result of adsorption) after passing through a solution. It works at the ultraviolet and rainbow portion of the electromagnetic spectrum (e.g., λ = 180-900 nm). Equation 3.1 (Beer-Lambert law) shows the fundamental relationship used to evaluate changes in light absorbance:

$$A = \log_{10} \frac{I_0}{I} \quad (3.1)$$

where I_0 is the intensity of incident beam (W/cm^2) and a given wavelength (λ; nm), I is the intensity of beam after transmission (Perkampus et al., 1992). I used this method to study the effects of additives on the crystallisation induction time and crystal growth kinetics. I monitored changes in the mixed solutions using a Uvikon XL system and following the changes at a wavelength λ = 520 nm with an angle between the incident beam and detector of 180˚.

3.2. X-ray diffraction (XRD)

XRD is a non-destructive technique used to identify and quantify the mineralogical phases present in a sample based on the fact that they diffract X-rays. When samples are irradiated by a monochromatic X-ray beam (with wavelength λ; nm), atoms of crystals present in the sample elastically scatter the incident electromagnetic X-ray and the constructive scattered X-ray cause diffraction. According to Bragg's law (equation 3.2) diffracted rays reveal the lattice spacing (d; nm) in a crystalline sample and the detector processes and counts the diffracted rays. Recording the intensity of the diffracted rays (in counts) as a function of 2 times the incident angle of the beam to the samples (θ; degrees) yields the XRD pattern. From this, it is possible to either directly or by applying some refinement techniques derive information on the crystallinity, crystal structure, unit cell parameters, etc. (Waseda et al., 2011).

$$n\lambda = 2d \sin\theta \quad (3.2)$$

In my PhD, I analysed all my mineral powders using a Bruker D8 diffractometer that was run using a CuKα1 source and using the following parameters: 2θ range 5 - 35°; resolution 0.105° / step; counting time 1s / step. The resulting XRD patterns were analysed with the EVA software (version 3).

3.3. Inductively coupled plasma mass spectrometry (ICP-MS) and inductively coupled plasma optical emission spectroscopy (ICP-OES)

Inductively coupled plasma mass spectrometry (ICP-MS) and inductively coupled plasma optical emission spectroscopy (ICP-OES) were both used to analyse the concentrations of elements in my reacting or digested solution. In both techniques, the solution containing cations or anions after they are fed into the instrument are nebulised into a spray that gets ionised or excited after meeting the plasma and heating up to a high temperature of 6000 °K –

8000 ˚K. The elements are detected and separated according to light emission by elements (ICP-OES) or differences in mass to charge (m/z) ratio (ICP-MS) (Lee, 2012; Thomas, 2013).

In my work, depending on the concentration of the interested elements the samples were analysed for their Na, Mg, Li, K, P and Ca contents by ICP-MS using a Thermo Scientific iCAPQc instrument or by ICP-OES using a Thermo Scientific iCAP 7400 instrument. At concentrations higher than 10 ppb, ICP-OES was used for Li, Na, K, Mg, P, and Ca at wavelength of 670.784 nm, 589.592 nm, 766.490 nm, 279.553 nm, 213.617 nm, and 184.006 nm respectively. At concentration below 10 ppb, ICP-MS was utilised to analyse the Li, Na, Mg, and K with molar mass of 7, 23, 24, and 39, respectively.

3.4. Scanning electron microscopy (SEM)

I used SEM to study the surface morphologies of the crystals synthesised in the presence or absence of additives. SEM works by firing a beam of electrons from an electron gun onto the sample. This beam passes through various condenser lenses (electron magnets) in a vacuum chamber and hits and scans the sample mounted on a stage. Secondary electrons and back scattered electrons are produced and detected. To have a better image quality, the samples should be coated by a thin conductive layer (Reimer, 2000).

In this thesis, the morphology of all samples were imaged using a field emission gun scanning electron microscope (FEG-SEM, FEI Quanta 650) with the samples coated with 15 nm of Pt.

3.5. Transmission electron microscopy (TEM)

TEM works in vacuum with a beam of electrons being transmitted through an ultrathin specimen mounted on a grid. Because of low wavelength of the electron beam, TEM can be used to detect very small objects even atoms (Williams and Carter, 2009).

In this thesis, samples were investigated by transmission electron microscopy (TEM, JEM1400) and imaging occurred at 120k eV after deposition of a droplet of ethanol containing a few crystals onto a carbon coated AGAR copper grid.

3.6. X-ray photoelectron spectroscopy (XPS)

X-ray photoelectron spectroscopy is a method that is usually utilised to determine the elemental composition of the topmost layers (max. 10 nm) of a solid. This techniques is used to identify and quantify (> 0.05 at.%) the presence and chemical environment of all elements (Li-U) except H and He. XPS analysis requires relatively little sample handling and can reveal the depth profile in a sample by Ar^+ sputtering. It is heavily used to determine, for example, the surface contamination, surface treatment, or surface compositions of coatings and thin films, for tribological studies but is also often used in mineralogy, semiconductor, and corrosion science. However, this technique is not cost-effective, and requires samples to be analysed under high vacuum (Van der Heide, 2011).

3.6.1. Historical perspective

In 1887, H. Hertz found out the photoelectric effect which is the basic fundamental of the X-ray photoelectron spectroscopy. Later in 1907, P.D. Innes subjected different surfaces to X-rays and recorded the kinetic energy of the emitted electrons. Finally, the binding energies of the photoelectron peaks were accurately measured by Kai Siegbahn and his research group who developed XPS technique in mid-1960s. He also suggested the application of XPS spectra for various types of chemical analyses and ultimately this led to him being awarded a Noble prize in physics in 1981 (Haasch, 2014; Van der Heide, 2011 and references therein).

3.6.2. The photoemission process

In XPS, the photoelectrons are produced when electrons in a sample are irradiated by photons with defined energy, $h\upsilon$. At reasonable high X-ray energies, the electrons (called

photoelectrons) will be emitted from a sample and their amount and kinetic energy can be measured and calculated (Haasch, 2014).

The kinetic energy (KE) (in eV) and binding energy (BE) (in eV) of the produced photoelectron can be calculated by following equation 3.3:

$$KE = h\upsilon - BE - \Phi_{spectrometer} \quad (3.3)$$

where $h\upsilon$ is the energy of the incident radiation (where h is Planck constant 6.62×10^{-34} J s and υ is frequency of the radiation in Hz), $\Phi_{spectrometer}$ is the work function of spectrometer in electron volts (Figure 3.1) (Haasch, 2014).

During XPS analysis, the interference between the incident photon energy and the sample cause the electron to be ejected from an atom's core level. Thus, XPS spectra are generated by recording the spread of kinetic or binding energies as a function of photoelectron flux (Haasch, 2014).

It is also worth mentioning that emission of a photoelectron results in an exited state ion, which causes an Auger effect. During the XPS process, an excited state is created and during a subsequent relaxation, the created hole is filled by an electron from an upper shell and an X-ray photon is released (Auger electron emission). As the energy is conserved during the relaxation phenomenon, the energy of the Auger electron will be equal to the difference between the energy of the two orbitals. The Auger effects will cause additional peaks in a XPS intensity-binding energy plot (Haasch, 2014).

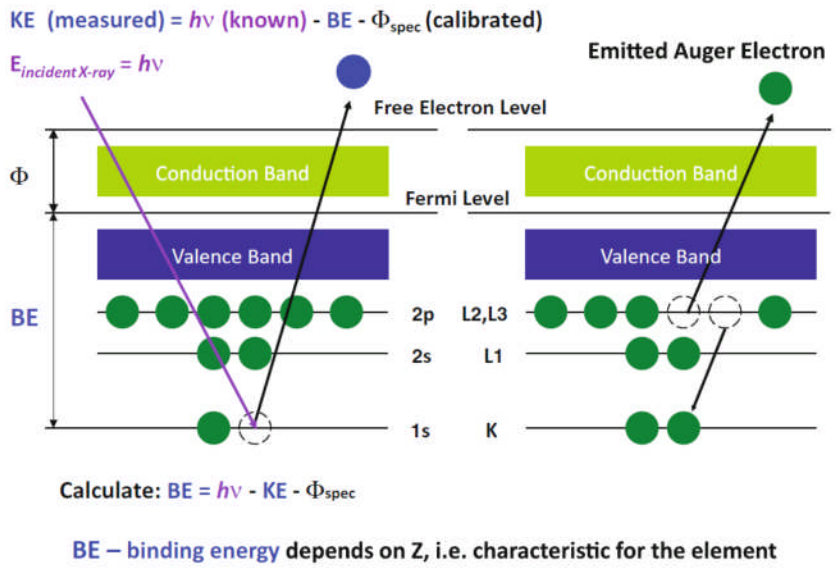

Figure 3.1.Schematic of processes occurring during the photoelectron and Auger electron emission (from Haasch, 2014).

Beside the main photoelectron lines and the Auger peaks, there might be some other lines in an XPS spectrum. These can be caused by multiple effects that are listed below with brief explanation each.

- **Multiplet splitting** happens when an unpaired electron in the core couples with an unpaired electron in the outer shell of an atom. The unpaired electron can be present originally or can be created after relaxation. This phenomenon is usually observed in transition metals and rare earths because the former have unfilled p and d orbitals and the later ones have unfilled f orbitals (Van der Heide, 2011).

- **Spin orbital splitting** is due to splits in orbital energy levels. This happens because of coupling of electron spin momentum with its orbital angular momentum (Figure 3.2a).

- **Plasmon peak:** results from the excitation of an electron in the conduction band.

- **Shake-up peak (satellite peak)** appear together with the main photoelectron peaks but at higher binding energies. They are produced during the photoionisation process of an atom when an electron from a lower level is promoted to the higher level. This results in a decrease in the kinetic energy of the main photoelectron and is equal to the energy required for the transition from the lower level to the higher level (Figure 3.2b).

- Shake-off peak (satellite peak) the excitation of an electron from a valence level into an unbound continuum states (Van der Heide, 2011).

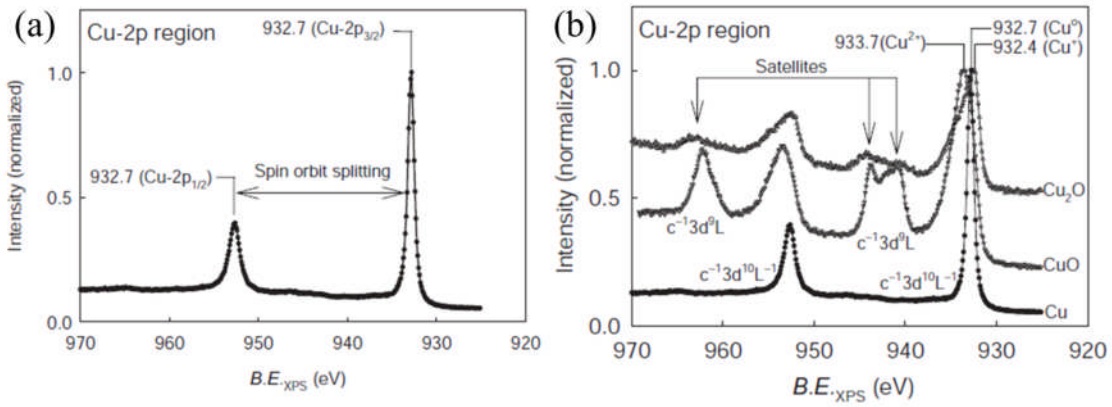

Figure 3.2.(a) schematic of a spin orbit splitting observed in the Cu 2p photoelectrons spectra measured on a copper metal surface; (b) shake-up satellite peaks observed in an XPS spectra over the Cu 2p region of Cu_2O (from Van der Heide, 2011).

3.6.3. Instrumentation

A schematic of a modern high resolution XPS spectrometer showing a monoenergetic X-ray source, an electron energy analyser, and a detector as the basic components is shown in Figure 3.3 (Haasch, 2014).

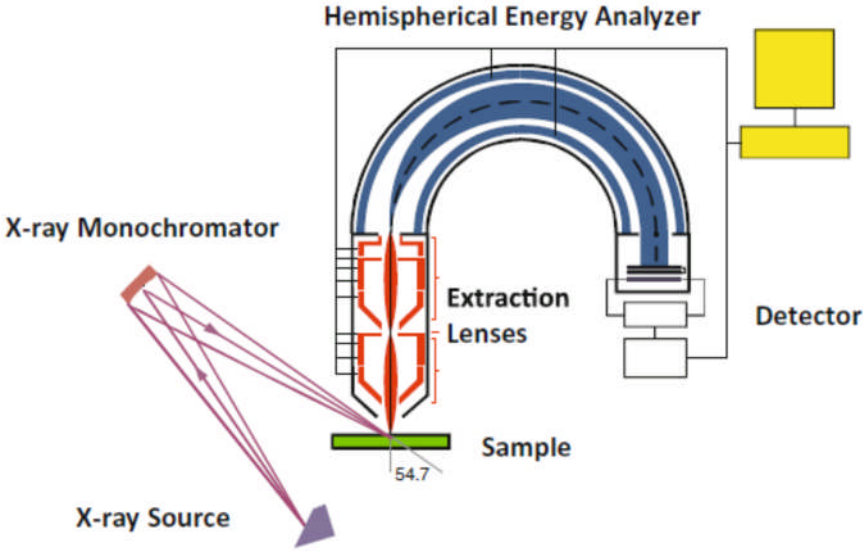

Figure 3.3.Schematic of a modern high resolution XPS spectrometer with its main components (from Haasch, 2014).

The main parts of a XPS instrument are:

- Ultrahigh vacuum system (greater than 1 × 10^{-6} Pa) to prevent any sample surface contamination or loss of photoelectrons because of scattering.

- Sample holder (the stage) a stainless steel plate to mount the samples and introduce them into the instrument.

- X-Ray is generated by impacting an accelerated electron onto a metal anode. Mg Kα or Al Kα with photon energies of 1253.6 eV and 1486.6 eV, respectively are usually utilised as an anode.

- The analyser consists of lenses (knows as extraction lenses) and an energy analyser (usually a hemispherical energy filter) to separate the photoelectrons emitted by a sample. The electrons will be gathered by these lenses, which have two main functions (i) determining the analysis / sample area from which the electrons are collected by combination of electrostatic steering plates and apertures (selected area apertures); (ii) decreasing the photoelectron's kinetic energy by applying a retarding voltage and adjusting the pass energy.

The photoelectrons passing the lenses enter the hemispherical part of the analyser, which is itself usually made of two hemispherical gold plates. A voltage is applied to each hemisphere and thus determines the range and resolution of the targeted kinetic energy of the photoelectrons. The electrons with high kinetic energy passing through the analyser collide with the outer hemisphere, while those with lower kinetic energies collide with the inner hemisphere and disappear. At the end, the remaining electrons are passed onto the detector.

- Detector counts the photoelectrons as they emerge from the analyser (Istone, 1995; Van der Heide, 2011).

3.6.4. Quantification

There are various commercial software packages for processing the XPS data and these are used to manipulate and interpret the XPS spectra, via peak analysis. In my work, I used the software packages Casa XPS.

The software contains an element library and is used to label the peaks automatically and suggest the elements that are most likely to correspond to the peaks in the spectrum. It also automatically fixes and calculates the position, area and atomic percentage of each element but the results can also reviewed manually (Fairley, 2009).

In XPS analysis, the peak areas are used for quantification and calculations of the atomic percentage of each element in a sample. The peak area is calculated by defining a background and integrating the signal above the background. Among various background subtraction methods (Figure 3.4), the Shirley type is the most common and in this procedure the subtraction considers an S-shaped background between the lower and higher part of the binding energy peak (Van der Heide, 2011).

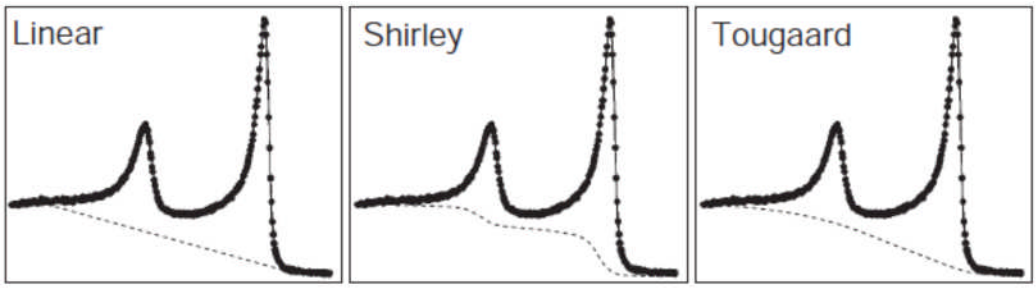

Figure 3.4.Three different primary background subtraction routines used in XPS (from Van der Heide, 2011).

To start the quantification, a peak of the desired element and its quantification region (the peak start and end point) is selected. There are different peak areas for various transition state of each element. For example Cu $2p_{3/2}$ has a double the peak area compared to Cu $2p_{1/2}$ (Figure 3.2 a). Therefore, a scaling factor (called relative sensitivity factor; F) is applied to normalise all peak areas (Van der Heide, 2011). The relative sensitivity factors corresponding to all elements are known (Fairley, 2009) and the atomic percentage of each element can thus be calculated by equation 3.4.

$$c_a = \left(\frac{\left(\frac{I_a}{F_a}\right)}{\left(\frac{I_a}{F_a}\right)+\left(\frac{I_b}{F_b}\right)+\cdots} \right) \times 100 \qquad (3.4)$$

where a and b and so on, represent the elements of interest, I is the intensity (area) of a photoelectron peak and F is the relative intensity factor (Van der Heide, 2011).

In my thesis, the nature of the surface interactions between the various types of additives and the formed precipitates, analysed by XPS could be quantified with a detection limit of 0.1 at.% (which is roughly 1ppth or 10^{19} atoms/cm^3). XPS spectra were acquired from the top 8-10 nm of end-product gypsum crystals using a Kratos Axis Ultra-DLD spectrometer with a monochromatic Al K_α X-ray source (144 W) and analyser pass energies of either 160 eV (survey scans) or 40 eV (high resolution scans). The base pressure during analysis was ca. 6×10^{-7} Pa. All data were referenced to the C (1s) signal at 284.8 eV and quantified as atomic percentage using the CasaXPS™ (Version 2.3.15) software and using elemental sensitivity factors supplied by the manufacturer.

3.7. References

Fairley, N., 2009. *CasaXPS manual 2.3. 15*, Acolyte Science.

Haasch, R. T., 2014. X-Ray Photoelectron Spectroscopy (XPS) and Auger Electron Spectroscopy (AES). *In:* Sardela, M. (ed.) *Practical Materials Characterization.* Springer New York, pp. 93-132.

Istone, W. K., 1995. X-ray photoelectron spectroscopy (XPS). *In:* Conners, T. E. & Banerjee, S. (eds.) *Surface analysis of paper*. CRC Press, pp. 235-268.

Lee, M. S., 2012. *Mass spectrometry handbook*, John Wiley & Sons.

Perkampus, H. H., Grinter, H. C. & Threlfall, T. L., 1992. *UV-VIS Spectroscopy and its Applications*, Springer.

Reimer, L., 2000. Scanning electron microscopy: physics of image formation and microanalysis. IOP Publishing.

Thomas, R., 2013. *Practical guide to ICP-MS: a tutorial for beginners*, CRC press.

Van der Heide, P., 2011. *X-ray photoelectron spectroscopy: an introduction to principles and practices*, John Wiley & Sons.

Waseda, Y., Matsubara, E. & Shinoda, K., 2011. *X-ray diffraction crystallography: introduction, examples and solved problems*, Springer Science & Business Media.

Williams, D. B. & Carter, C. B., 2009. Transmission electron microscopy: a textbook for materials science. *Springer Science+ Business Media, New York, USA*.

This chapter has been published in *Mineralogical Magazine* and has been modified and reformatted for this PhD thesis in the response to the requests from the two thesis examiners.

Chapter 4. Carboxylic acids: effective inhibitors for calcium sulfate precipitation?

Taher Rabizadeh[1,*], Caroline L. Peacock[1], and Liane G. Benning[1,2,*]

1- Cohen Geochemistry Laboratory, School of Earth and Environment, University of Leeds, UK LS2 9JT

2- GFZ German Research Centre for Geosciences, Telegrafenberg, D-14473 Potsdam, Germany

* Correspondence to: Taher Rabizadeh (eetr@leeds.ac.uk) and Liane G. Benning (L.G.Benning@leeds.ac.uk)

Abstract

Results are reported here an investigation into the effects of three carboxylic acid additives (tartaric, maleic and citric acids) on the precipitation of calcium sulfate phases. Precipitation reactions were followed at pH 7 in the pure $CaSO_4$ system and in experiments with 0-20 ppm carboxylic acids added using *in situ* UV-VIS spectrophotometry (turbidity). The solid products were characterized in terms of their mineralogical composition, using X-ray diffraction, during and at the end of each reaction, and in terms of their morphological features, by scanning electron microscopy. All additives increased the time needed for turbidity to develop (induction time, start of precipitation) and the comparison between additive and additive-free experiments showed that at equivalent concentrations citric acid performed far better than the other two carboxylic acids. In all cases bassanite precipitated

first and with time it transformed to gypsum. The addition of citrate stabilized bassanite and changed the final gypsum habit from typical needle-like crystals in the pure $CaSO_4$ system to plates in the citrate-additive experiments.

Keywords: gypsum, bassanite, carboxylic acids, inhibition, crystallization

4.1. Introduction

Calcium sulfates are important rock forming minerals that occur in thick evaporitic deposits throughout geologic history (Kinsman, 1969). In the calcium sulfate system three phases with various degrees of hydration exist: the dihydrate, gypsum ($CaSO_4 \cdot 2H_2O$), the hemihydrate, bassanite ($CaSO_4 \cdot 0.5H_2O$) and the anhydrous anhydrite ($CaSO_4$). The stability and formation of these phases are very temperature- and concentration- dependent (Freyer and Voigt, 2003). Between ambient and ~ 40 °C the most stable phase is gypsum. With increasing ion concentrations and / or temperature, the solubilities of bassanite and anhydrite decreases leading to the dehydration of gypsum and its transformation to less hydrous polymorphs (Freyer and Voigt, 2003). The mechanisms controlling the nucleation and growth of gypsum from aqueous solutions have gained renewed interest recently, however, because gypsum probably does not form directly from solution. One study (Wang et al., 2012) has suggested that gypsum forms through non-classical nucleation via an amorphous calcium sulfate intermediate, while another study (Van Driessche et al., 2012) suggested that gypsum forms not through amorphous precursors but through the initial precipitation of nanocrystalline bassanite particles that self-assemble into larger gypsum crystals through oriented attachment.

The gypsum formation pathway is important because among calcium sulfates, gypsum is mined extensively for use as the crucial component in plasters and cements (e.g., Camarini and De Milito, 2011); to make plasters, gypsum has to be dehydrated to bassanite through the use of large amounts of energy. Equally important however, is the fact that in several industrial processes that rely on water handling systems (e.g., oil and gas production, water

desalination; Moghadasi et al., 2006; Rahardianto et al., 2008), the precipitation of calcium sulfate phases leads to the deposition of minerals in pipes, filters and heat exchangers, forming mineral scales. Cleaning or removing such mineral scales is costly and undesirable and affects the efficiency and lifetime of processing technologies (e.g., Mi and Elimelech, 2010).

In order to reduce or mitigate calcium sulfate scaling, various simple anti-scaling approaches have been suggested, the most common being the use of inorganic (e.g., Mg^{2+}; Guan et al., 2010) or organic additives (e.g., sulfonic, phosphonic or carboxylic compounds; Shakkthivel and Vasudevan, 2006; Prisciandaro et al., 2005; Akyol et al., 2009). The main requirements for an effective additive are that (1) it is readily available; (2) it is effective at low concentrations; (3) it is cheap and its addition will not significantly affect production costs; (4) ideally it is biodegradable or non-toxic to the environment; and (5) it reduces mineral formation or prevents nucleated phases from adhering to surfaces of crucial production apparatus. Among additives fulfilling many of the above requirements are carboxylic acids (Hasson et al., 2011; Cao et al., 2014). To date, studies that tested the effects of carboxylic acids on calcium sulfate precipitation have primarily evaluated changes in precipitation onset or the effect of high temperatures (Prisciandaro et al., 2005; Senthilmurugan et al., 2010; Ling et al., 2012; Amjad and Koutsoukos, 2014). Missing is a mechanistic understanding of the effects of variable concentrations of carboxylic acid and / or various carboxylic acid moieties.

To address this gap results are presented here on the effects of three P- and N- free carboxylic acids with low molecular chain, different functional group numbers and different molecular structure (citric, maleic and tartaric) at variable additive concentrations (0-20 ppm) on the kinetics and phase morphologies that develop during homogeneous calcium sulfate formation reactions and derive a more mechanistic understanding of the processes.

4.2. Experimental methods

Inhibitor-free calcium sulfate precipitates (termed 'pure $CaSO_4$' hereafter) were produced by mixing equal volumes of a 100 mM $CaCl_2 \cdot 2H_2O$ solution and a 100 mM Na_2SO_4 solution (99 % purity, VWR) at room temperature (21 ˚C) and under constant and continuous stirring. The mixed solutions were supersaturated with respect to gypsum (saturation index SI_{Gyp} = ~ 0.5) but undersaturated with respect to bassanite (SI_{Bas} = ~ -0.37). The saturation indices (as the logarithm of the ion activity product over the solubility product) and the related solubility products ($K_{sp,bassanite} = 10^{-3.66}$ and $K_{sp,gypsum} = 10^{-4.53}$) were calculated by means of the geochemical computer code PHREEQC using the LLNL database (Parkhurst and Appelo, 1999).

In order to prevent the complexation with Ca^{2+} which may delay the onset of crystallisation, carboxylic acids (citric, maleic or tartaric acid; 99-100 %, VWR) were added to the initial sodium sulfate solution at concentrations between 5 and 20 ppm. In all experiments, prior to mixing, the pH of the initial solutions was adjusted to 7, with 0.1 M NaOH.

The kinetics of the reactions in the absence and presence of carboxylic acids was monitored through the development of turbidity in the mixed solutions as measured using a UV-VIS spectrophotometer (Uvikon XL) at 520 nm. Reactions were followed in triplicate at room temperatures for up to 4 hours and the variations in the turbidity onset from the three repeats are reported in minutes. At intermediate time steps and at the end of each experiment the solutions were quench-filtered (0.2 µm) under vacuum with isopropanol and the solids retrieved. These solids were characterized mineralogically using powder X-ray diffraction (XRD; Bruker D8 diffractometer; CuKα1; 2θ range 5-30˚; 0.105˚ / step), while the morphology of the phases formed was imaged using a field emission gun scanning electron microscope (FEG-SEM, FEI Quanta 650, 3 kV).

4.3. Results

Turbidity developed in all experiments but the onset of turbidity occurred after different periods of time (induction times) that were dependent on additive type and concentration. Comparing the turbidity curve from the pure $CaSO_4$ experiment with equivalent curves from experiments where 20 ppm of the 3 carboxylic acids were added (Figure 4.1), revealed a carboxylic acid-dependent increase in induction time. In the pure $CaSO_4$ system, the first increase in turbidity was observed after 6±1 min and the increase in absorbance took ~ 60 min to reach a steady value on a plateau. In the presence of 20 ppm carboxylic acids the induction times increased to 9±1 min, 16±1 min and 25±1 min for tartaric, maleic acid and citric acid, respectively, and specifically in the case of added citric acid the reaction curve took much longer to reach a plateau (~ 200 min; Figure 4.1). Furthermore, the slope of the linear part of the turbidity graphs decreased from 5 (% . min^{-1}) in the additive-free system to 4.3 ± 0.1, 3.9 ± 0.1 and 1.5 ± 0.1 (% . min^{-1}) in the presence of 20 ppm tartaric, maleic and citric acids, respectively. The half crystallisation time ($t_{50\%}$) in the additive-free systems was also 25 ± 1 min which in the presence of 20 ppm tartaric, maleic and citric acids occurred at longer times of 33 ± 1, 41 ± 1 and 68 ± 1 min respectively.

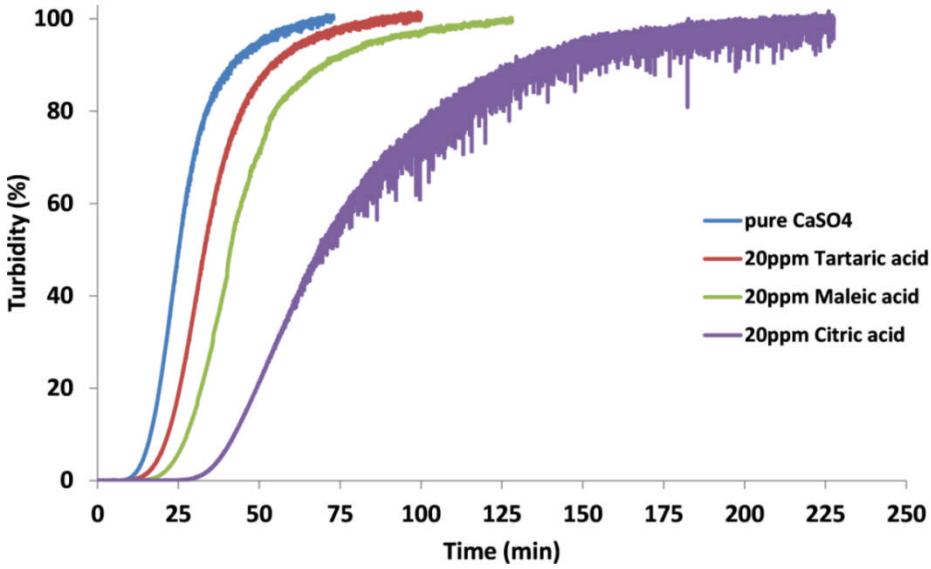

Figure 4.1.The effect of adding 20 ppm tartaric, maleic or citric acid on the development of turbidity compared to the pure $CaSO_4$ system.

Testing variable concentrations of citric acid (5, 10, 20 ppm) showed a proportional increase in induction time with increasing additive concentration (Figure 4.2). The 6±1 min induction time observed in the pure $CaSO_4$ system almost doubled in the presence of 5 ppm citric acid (10±1 min), tripled with 10 ppm (17±1 min) and at 20 ppm citric acid led to an induction time four times greater than that for the pure $CaSO_4$ system (25±1 min). Quadrupling the citric acid concentration from 5 ppm to 20 ppm, increased the half crystallisation time ($t_{50\%}$) from 45 ± 1 minutes to 68 ± 1 minutes and decreased the slope of the turbidity graphs from 2 ± 1 to 1.3 ± 1,

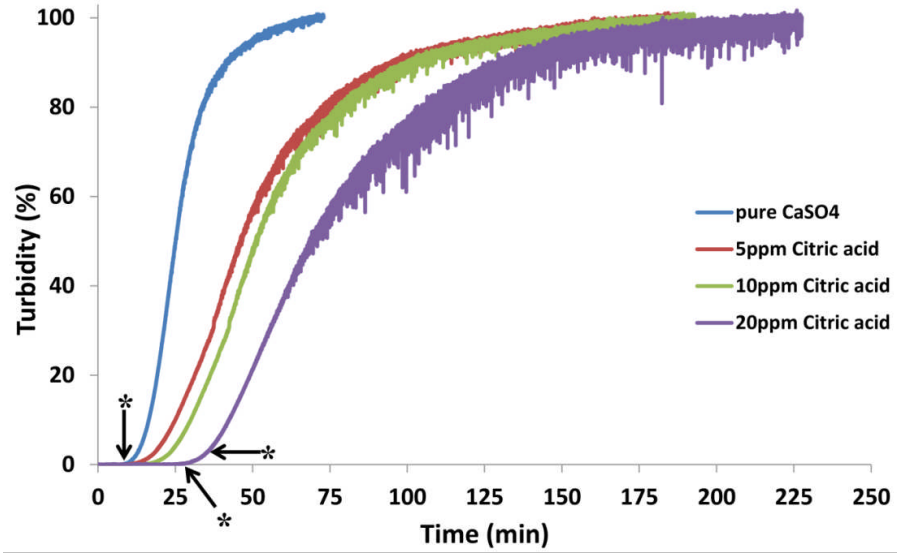

Figure 4.2.The effect of variable concentrations of citric acid (5, 10, 20 ppm) on the development of turbidity. * indicates the absolute times (~ 7 min in the pure system and 28 and 35 min, respectively, in the 20 ppm citric acid system) when solids were removed and analysed. Data are shown in Figure 4.3 a, c and d and 4.4 a and c.

The XRD analyses of the solids recovered at the end of each reaction (in both the pure and carboxylic acid-amended experiments) revealed that the sole mineral end-product was gypsum. However, samples filter-quenched just after the onset of turbidity in the pure and citric acid system (e.g., after 30 sec in the pure system and after 3 and 10 min in the presence of 20 ppm citric acid; marked with ***** in Figure 4.2 and corresponding to ~ 7, 26 and 35 min in absolute time, respectively) showed in the XRD patterns the presence of bassanite coexisting with gypsum (Figure 4.3 a,c). In both cases with time, the proportion of bassanite decreased (bassanite peaks decreased in intensity or disappeared completely) showing that bassanite was an intermediate phase (Figure 4.3 d) but that in both systems the final product was pure gypsum (Figure 4.3 b,e). As mentioned above, an increase in induction time prior to the onset of turbidity was also observed in the presence of the other two carboxylic acids (maleic and tartaric; Figure 4.1). Although the shape and slope of the turbidity curves hint at a similar process, we do not have equivalent time-resolved XRD evidence that these additives also stabilized bassanite (but see below and Figure 4.4 e,f).

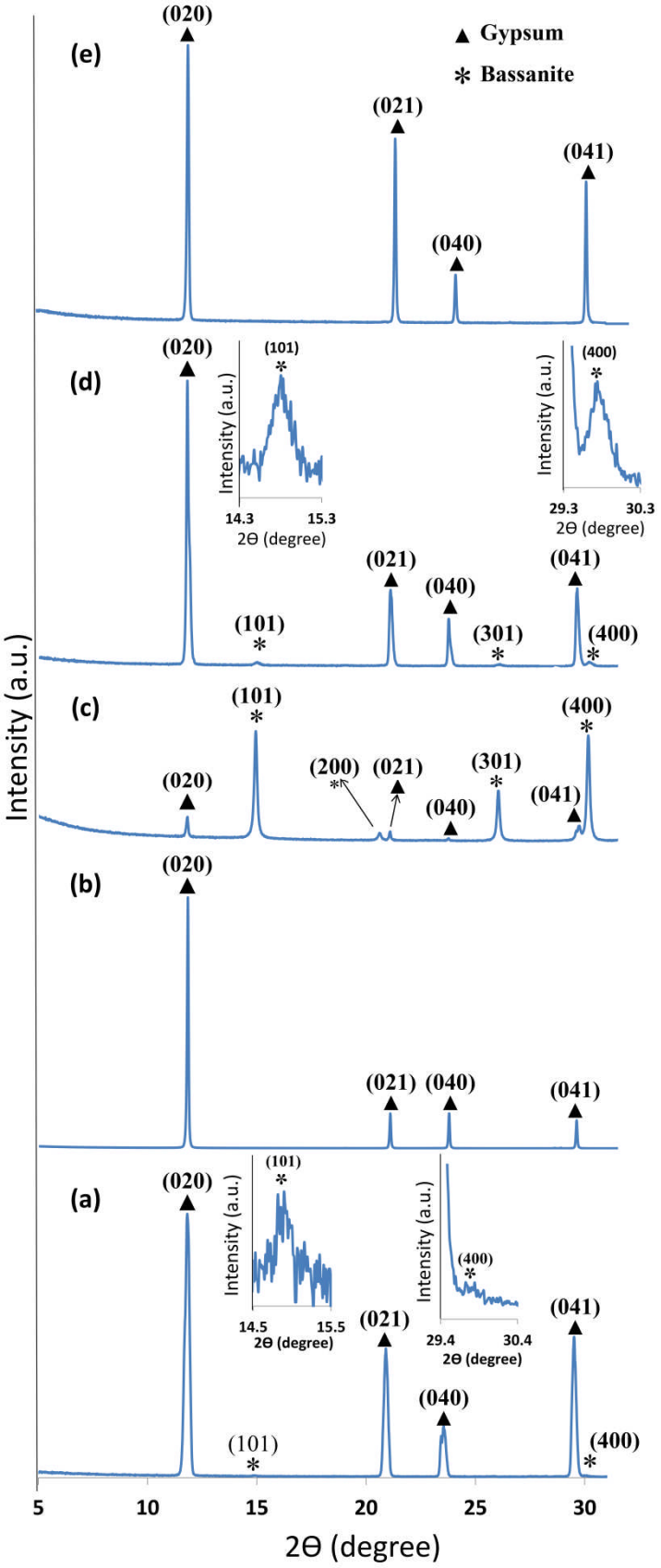

Figure 4.3.XRD patterns of precipitated materials from (a) the pure $CaSO_4$ system removed from the reaction solution 30 seconds after turbidity onset (absolute time is ~ 7 min) with stars marking bassanite

peaks of low intensity that are seen more easily in the insets, where the low intensity (101) and (400) bassanite peaks are highlighted; (b) same system but 63 min after turbidity onset (absolute time = 70 min) when the transformation to gypsum was complete and no bassanite remained; (c-e) XRD patterns from the system with 20 ppm citric acid added; (c) 3 min after turbidity onset (absolute time = 28 min) showing all four distinct and very intense bassanite peaks ((101), (200), (301) and (400) all marked with a star); (d) 10 min after turbidity onset (absolute time = 35 min) showing smaller bassanite peaks; and (e) 175 min after turbidity onset (absolute time = 200 min) where only gypsum peaks remain and all bassanite has been transformed.

Photomicrographs of the intermediate (~ 7 min, or 30 seconds after onset of turbidity) and end-product (after 70 min of total reaction) materials in the pure $CaSO_4$ system revealed that bassanite was present at the beginning of the reaction only as elongated nanorods (up to ~ 200 nm long) while at the end of the experiment only gypsum was present as larger (up to ~ µm size), thin, needle-like crystals, partly twinned (Figure 4.4 a and b). These morphologies and sizes are equivalent with those reported by Van Driessche et al. (2012) and Wang et al. (2013) and the presence of bassanite in our samples had already been documented through XRD (Figure 4.3 a,c). At the end of the pure system crystallization reaction (Figure 4.4 b) all bassanite had transformed and only large, elongated (between 5-50 µm) needle-like and twinned gypsum crystals were present, again confirming the XRD data (Figure 4.3 b). In the presence of 20 ppm citric acid, after the onset of turbidity (3 min, 28 min after mixing of the initial solutions) the bassanite identified by XRD (Figure 4.3 c) was present as very small but almost isometric nanoparticles (< ~ 90 nm; Figure 4.4 c) that occurred together with larger gypsum crystals. At the end of the reaction, when the turbidity curve reached a plateau (after 200 minutes; Figure 4.4 d) only gypsum was present. It was striking that, compared to the pure $CaSO_4$ system both the bassanite and gypsum in the citrate system did not exhibit the typical bassanite nanorod or gypsum needle-like habits, but rather far more isomeric (bassanite; Figure 4.4 c) and distinctly platy (gypsum; Figure 4.4 d) habits. Although we have no XRD evidence of bassanite stabilization in the presence of maleic and tartaric acid, photomicrographs of samples removed a few minutes after the onset of turbidity in the 20 ppm experiments with these carbocyclic acids present revealed equivalent nanorod (particles < 200 nm) morphologies that are inferred here to be bassanite. These occurred together with longer,

needle-like crystals inferred to be gypsum (Figure 4.4 e and f). In contrary to the citric acid system however, in the presence of 20 ppm tartaric or maleic acid the shape, size or habit of the intermediate bassanite and end-product gypsum were the same as in the pure $CaSO_4$ experiment, although a slight ‘thinning’ of the gypsum needles was observed.

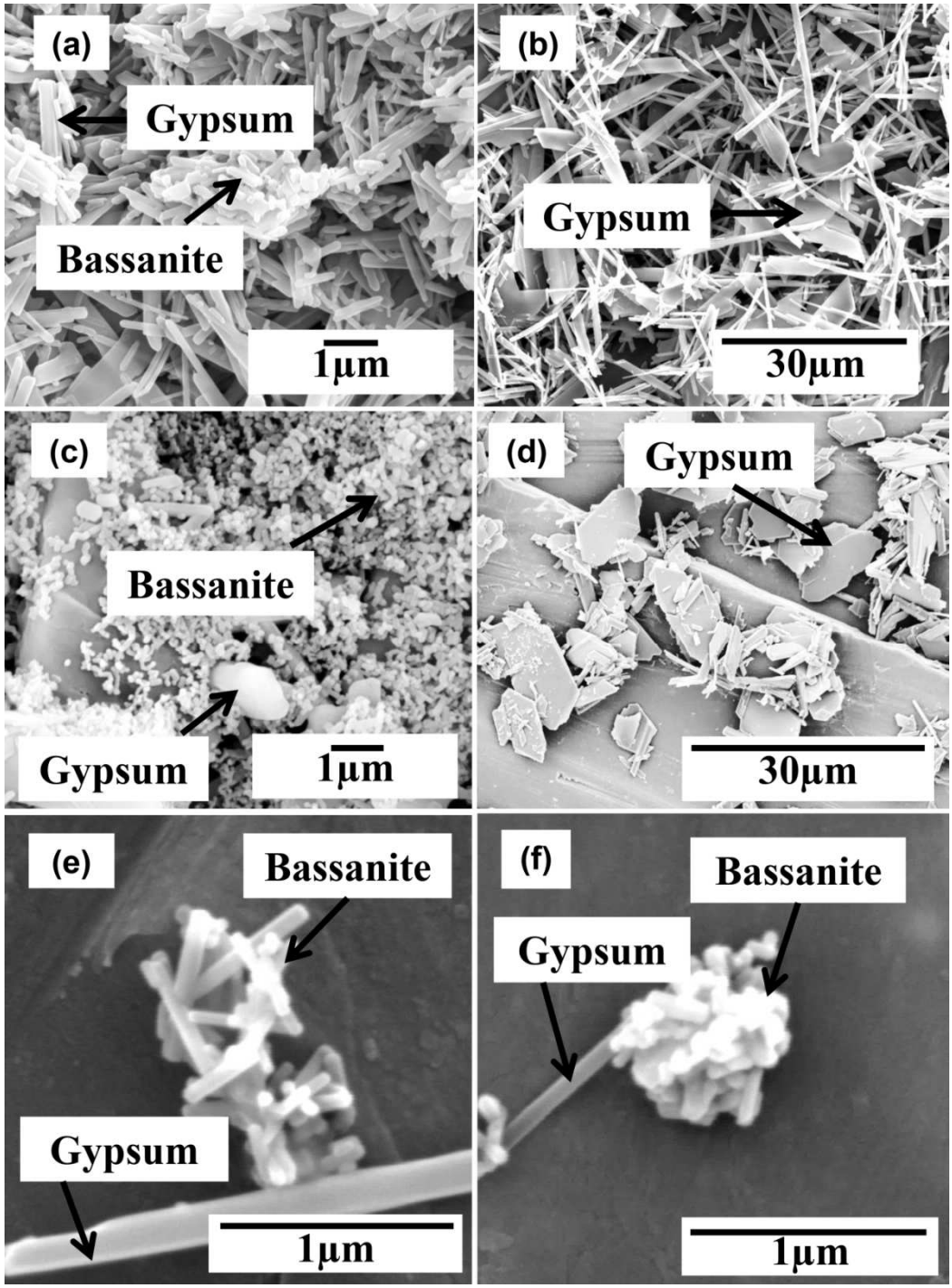

Figure 4.4.SEM image of precipitated materials from experiments in; (a) the pure $CaSO_4$ system 30 seconds after turbidity onset showing bassanite nanorods and gypsum needles; (b) the pure $CaSO_4$ system 63 min after turbidity onset (70 min total time) showing only variably sized gypsum needles; (c) tiny bassanite nanoparticles formed in the presence of 20 ppm citric acid 3 min after turbidity onset together with some larger gypsum crystals; (d) plate-like gypsum crystals formed in the presence of 20 ppm citric acid after 200 min of total reaction; (e) bassanite nanorods and single larger gypsum needle collected a few minutes after the onset of turbidity in the 20 ppm maleic acid experiment; (f) bassanite nanorods and single larger gypsum needle collected a few minutes after the onset of turbidity in the 20 ppm tartaric acid experiment.

4.4. Discussion

Measuring turbidity and estimating induction times in the absence and presence of additives is one of the most common methods of evaluating the efficiency of additives as a mechanism to delay the nucleation and growth of sparingly soluble scale minerals.

Additives that are biodegradable, such as the carboxylic acids used in the current study, and that delay dramatically the nucleation and or growth of a phase at low concentrations, are considered to be effective and are often referred to as 'inhibitors' although they do not inhibit nucleation and growth but most often just delay or change the reaction progress.

Our data revealed that the turbidity graphs in this study had similar development shapes confirmed the similarity in mechanisms governed the nucleation and growth inhibition of gypsum crystals. The inhibitors also did not inhibit the gypsum nucleation (turbidity occurred) and just decreased the growth kinetics (slope of the turbidity graphs). Therefore, the carboxylic acids in this study are classified as growth inhibitors.

Furthermore, at equal concentrations (20 ppm), among the three additives tested, citric acid increased the induction time and decreased the slope of the turbidity curve more than either the tartaric and maleic acid, inferring that citric acid is inherently a better inhibitor. If we also consider the differences in molar concentrations of the carboxylic acids used(C_{cit} = 1.01 µM, C_{tart}= 1.33 µM *vs.* C_{mal}= 1.72 µM), these further support the fact that citric acid is the most effective inhibitor even though it is present in the lowest molar concentration. The reasons for its greater effectiveness are not yet clear but probably stem from the variations in molecular geometries and sorption capacities between these three carboxylic acids.

Additives can affect the nucleation and growth of scale minerals, e.g., by forming complexes or chelating agents with the active ions in the nucleating solutions (equation 1; where x = 2 for maleic / tartaric acids or 3 for citric acid) or by sorbing to active crystal sites and inhibiting mineral growth (e.g., Crabtree et al., 1999; Badens et al., 1999; Ersen et al., 2006; Magallanes-Rivera et al., 2009).

$$R(COOH)_x + Ca^{2+} \rightarrow R(COOCa)_x + xH^+ \quad (4.1)$$

In the case of the carboxylic acids tested, complexation with calcium is well known (Bazin et al., 1995) but sorption and growth inhibition also seems to play important roles. All carboxylic acids delayed the onset of nucleation (increased induction time compared to the pure system, Figure 4.1 and 4.2). The citric acid additive also affected the growth of the scale mineral, however, in that both bassanite and gypsum exhibited different habits compared to the additive-free phases (Figure 4.4). Finally, of interest for mineral-scale formation and inhibition is the fact that, compared to the pure system, even low concentrations of citric acid stabilized the bassanite phase for much longer periods.

In additive experiments one of the fundamental parameters that controls 'inhibition' either through complexation with the active ions (in this case Ca^{2+}) or sorption to active growth sites is the speciation and degree of protonation of the additive used. All our experiments with or without additives were carried out with the initial solutions adjusted to pH 7. At this pH value all carboxylic acids are deprotonated to the largest extent (Table 1).

Table 4.1. Dissociation constants of carboxylic acids used (from Lide, 1988)

Carboxylic acid moiety	**pK_{a1}**	**pK_{a2}**	**pK_{a3}**
Citric acid	3.13	4.76	6.40
Maleic acid	1.92	6.23	
Tartaric acid	3.03	4.34	

The delay in precipitation, indicated by the increased induction time, is probably due in part to Ca^{2+} complexation with these deprotonated species through the reduction of Ca^{2+} supersaturation. Of the carboxylic acids tested, citric acid at pH 7 is the most deprotonated and may, therefore, acts as the most efficient inhibitor, as reflected in the longest induction time. Nevertheless, the nucleation barrier in the presence of all additives is overcome and bassanite nucleates and eventually transforms to gypsum.

Moreover, the stronger inhibitory effect of maleic acid than tartaric acid could be related to the molecular configuration differences between these two carboxylic acids. The

double bond in the maleic acid back bone holds the two carboxylic acid moieties in an orientation that is favouring further chelation the free calcium ions. In contrast, in tartaric acid, two carboxylic acid functional groups can rotate around a single bond, which reduces its chelation efficiency (Furia, 1973; Pomogailo et al., 2010). However, a detail molecular configuration role of the tested carboxylic acids needs further studies.

The delay in precipitation in the presence of the carboxylic acid may also be attributed to sorption onto bassanite and gypsum growth sites. Badens et al. (1999) and Ersen et al. (2006) found that adsorption of citrate onto active growth faces of both bassanite and gypsum inhibited growth in those directions more than other carboxylic acid (e.g., tartaric or malic). This suggests that with citric acid, both bassanite and gypsum grew with different habits from those in the pure $CaSO_4$ system, as our imaging data in the present study also confirmed (Figure 4.4 a,b). Citric acid seems to have inhibited growth along the *c* axis and prevented the formation of typical long, needle-like habits. Instead, the growth of gypsum was favoured in the *a* and *b* directions, leading to platy crystal habits (Figure 4.4). Similar morphological changes in gypsum habits in the presence of carboxylic acids have been reported by others (Li et al., 2007; Magallanes-Rivera et al., 2009), but a molecular level understanding of the process is still lacking.

For gypsum formed in the presence of citric acid, Prisciandaro et al. (2005) showed that the increase in induction time was due to a dramatic change in interfacial tension compared to an additive-free system. Although the present study confirmed these findings, bassanite was also shown to be a metastable intermediate forming prior to gypsum not just in the pure $CaSO_4$ system (Wang et al., 2012; Van Driessche et al., 2012) but also in the presence of carboxylic acids. In the pure system, bassanite forms below its thermodynamic bulk solubility and its transformation to gypsum is through hydration and self-assembly via a process controlled by a particle-size dependent surface energy (Van Driessche et al., 2012). This is different to non-classical nucleation, growth and dehydration pathways suggested for calcium carbonates (Rodriguez-Blanco et al., 2011; Bots et al., 2012) or calcium phosphates

(Combes and Rey, 2010). The current study shows, however, that in the presence of even low concentrations of carboxylic acid: (1) the onset of the precipitation reaction is delayed; (2) bassanite is stabilized and its transformation to gypsum slowed; and (3) citric acid changes the shape and habit of the bassanite and gypsum formed.

If citric acid inhibitors are used in an industrial fluid handling system (where $CaSO_4$ scale minerals are a problem) they can substantially retard nucleation and growth even at low concentrations. Importantly, citric acid may not just stabilize a nanoparticulate phase such as bassanite and thus reduce clogging of filters, but the size effect may also prevent adherence to pipe surfaces. However, this latter process and further growth of $CaSO_4$ phases on surfaces is still under study.

Acknowledgements

This study was supported by the Marie Curie grant from the European Commission in the framework of the MINSC ITN (Initial Training Research network), Project number 290040. The authors thank the Cohen Laboratories in the School of Earth and Environment, and the Leeds Electron Microscopy and Spectroscopy Centre (LEMAS) for help and access to instruments during the course of this study. They also thank three reviewers and the associate editor for their constructive comments, which helped improve the paper.

4.5. References

Akyol, E., Öner, M., Barouda, E. & Demadis, K. D., 2009. Systematic Structural Determinants of the Effects of Tetraphosphonates on Gypsum Crystallization. *Crystal Growth & Design,* 9**,** 5145-5154.

Amjad, Z. & Koutsoukos, P. G., 2014. Evaluation of maleic acid based polymers as scale inhibitors and dispersants for industrial water applications. *Desalination,* 335**,** 55-63.

Badens, E., Veesler, S. & Boistelle, R., 1999. Crystallization of gypsum from hemihydrate in presence of additives. *Journal of Crystal Growth,* 198**,** 704-709.

Bazin, H., Descotes, G., Bouchu, A. & Petit-Ramel, M., 1995. Comparison of calcium complexation of some carboxylic acids derived from Dglucose and D-fructose. *Canadian journal of chemistry,* 73**,** 1338-1347.

Bots, P., Benning, L. G., Rodriguez-Blanco, J.-D., Roncal-Herrero, T. & Shaw, S., 2012. Mechanistic insights into the crystallization of amorphous calcium carbonate (ACC). *Crystal Growth & Design,* 12**,** 3806-3814.

Camarini, G. & De Milito, J. A., 2011. Gypsum hemihydrate–cement blends to improve renderings durability. *Construction and Building Materials,* 25**,** 4121-4125.

Cao, K., Zhou, Y., Liu, G., Wang, H. & Sun, W., 2014. Preparation and properties of a polyether- based polycarboxylate as an antiscalant for gypsum. *Journal of Applied Polymer Science,* 131**,** 1-9.

Combes, C. & Rey, C., 2010. Amorphous calcium phosphates: synthesis, properties and uses in biomaterials. *Acta Biomaterialia,* 6**,** 3362-3378.

Crabtree, M., Eslinger, D., Fletcher, P., Miller, M., Johnson, A. & King, G., 1999. Fighting scale—removal and prevention. *Oilfield Review,* 11**,** 30-45.

Ersen, A., Smith, A. & Chotard, T., 2006. Effect of malic and citric acid on the crystallisation of gypsum investigated by coupled acoustic emission and electrical conductivity techniques. *Journal of Materials Science,* 41**,** 7210-7217.

Freyer, D. & Voigt, W., 2003. Crystallization and Phase Stability of CaSO4 and CaSO4 - Based Salts. *Monatshefte fur Chemie / Chemical Monthly,* 134**,** 693-719.

Furia, T. E., 1973. *CRC handbook of food additives*, CRC press.

Guan, B., Yang, L. & Wu, Z., 2010. Effect of Mg2+ ions on the nucleation kinetics of calcium sulfate in concentrated calcium chloride solutions. *Industrial & Engineering Chemistry Research,* 49**,** 5569-5574.

Hasson, D., Shemer, H. & Sher, A., 2011. State of the art of friendly "green" scale control inhibitors: a review article. *Industrial & Engineering Chemistry Research,* 50**,** 7601-7607.

Kinsman, D. J., 1969. Modes of formation, sedimentary associations, and diagnostic features of shallow-water and supratidal evaporites. *AAPG Bulletin,* 53**,** 830-840.

Li, J., Li, G. & Yu, Y., 2007. The influences of gypsum water-proofing additive on gypsum crystal growth. *Materials letters,* 61**,** 872-876.

Lide, D. R., 1988. CRC handbook of chemistry and physics. CRC press.

Ling, L., Zhou, Y., Huang, J., Yao, Q., Liu, G., Zhang, P., Sun, W. & Wu, W., 2012. Carboxylate-terminated double-hydrophilic block copolymer as an effective and environmental inhibitor in cooling water systems. *Desalination,* 304**,** 33-40.

Magallanes-Rivera, R. X., Escalante-García, J. I. & Gorokhovsky, A., 2009. Hydration reactions and microstructural characteristics of hemihydrate with citric and malic acid. *Construction and Building Materials,* 23**,** 1298-1305.

Mi, B. & Elimelech, M., 2010. Gypsum scaling and cleaning in forward osmosis: measurements and mechanisms. *Environmental science & technology,* 44**,** 2022-2028.

Moghadasi, J., Sharif, A., Müuller- Steinhagen, H. & Jamialahmadi, M., 2006. Prediction of scale formation problems in oil reservoirs and production equipment due to injection of incompatible waters. *Developments in Chemical Engineering and Mineral Processing,* 14**,** 545-566.

Parkhurst, D. L. & Appelo, C., 1999. User's guide to PHREEQC (Version 2): A computer program for speciation, batch-reaction, one-dimensional transport, and inverse geochemical calculations.

Pomogailo, A. D., Dzhardimalieva, G. I. & Kestel′man, V. N., 2010. *Macromolecular metal carboxylates and their nanocomposites*, Springer Science & Business Media.

Prisciandaro, M., Santucci, A., Lancia, A. & Musmarra, D., 2005. Role of Citric Acid in Delaying Gypsum Precipitation. *The Canadian Journal of Chemical Engineering,* 83**,** 586-592.

Rahardianto, A., McCool, B. C. & Cohen, Y., 2008. Reverse osmosis desalting of inland brackish water of high gypsum scaling propensity: kinetics and mitigation of membrane mineral scaling. *Environmental science & technology,* 42**,** 4292-4297.

Rodriguez-Blanco, J. D., Shaw, S. & Benning, L. G., 2011. The kinetics and mechanisms of amorphous calcium carbonate (ACC) crystallization to calcite, via vaterite. *Nanoscale,* 3**,** 265-271.

Senthilmurugan, B., Ghosh, B., Kundu, S., Haroun, M. & Kameshwari, B., 2010. Maleic acid based scale inhibitors for calcium sulfate scale inhibition in high temperature application. *journal of Petroleum Science and Engineering,* 75**,** 189-195.

Shakkthivel, P. & Vasudevan, T., 2006. Acrylic acid-diphenylamine sulphonic acid copolymer threshold inhibitor for sulphate and carbonate scales in cooling water systems. *Desalination,* 197**,** 179-189.

Van Driessche, A., Benning, L., Rodriguez-Blanco, J., Ossorio, M., Bots, P. & García-Ruiz, J., 2012. The role and implications of bassanite as a stable precursor phase to gypsum precipitation. *Science,* 336**,** 69-72.

Wang, Y. W., Christenson, H. K. & Meldrum, F. C., 2013. Confinement leads to control over calcium sulfate polymorph. *Advanced Functional Materials,* 23**,** 5615-5623.

Wang, Y. W., Kim, Y.-Y., Christenson, H. K. & Meldrum, F. C., 2012. A new precipitation pathway for calcium sulfate dihydrate (gypsum) via amorphous and hemihydrate intermediates. *Chemical Communications,* 48**,** 504-506.

This chapter has been published in *Crystal Growth & Design*. It has been modified and reformatted for this PhD thesis, in response to both the reviewers' comments and to the requests from the two thesis examiners.

Chapter 5. The effects of inorganic additives on the nucleation and growth kinetics of calcium sulfate dihydrate crystals

Taher Rabizadeh[1*], Tomasz M. Stawski [1,2], David J. Morgan[3], Caroline L. Peacock[1], Liane G. Benning[1,2,4*]

1- Cohen Geochemistry Laboratory, School of Earth and Environment, University of Leeds, Leeds, LS2 9JT, United Kingdom

2- GFZ, German Research Centre for Geosciences, Telegrafenberg, 14473 Potsdam, Germany

3- Cardiff Catalysis Institute, School of Chemistry, Cardiff University, Cardiff, CF10 3AT, United Kingdom

4- Department of Earth Sciences, Free University of Berlin, 12249 Berlin, Germany

* Correspondence to: Taher Rabizadeh (eetr@leeds.ac.uk) and Liane G. Benning (Benning@gfz-potsdam.de)

Abstract

The effects that 50-500 mM aqueous Li^+, Na^+, K^+, and Mg^{2+} have on the crystallization kinetics of calcium sulfate dihydrate (gypsum; $CaSO_4 \cdot 2H_2O$) were determined by *in situ* and time-resolved UV-VIS spectrophotometry. The mechanisms of surface or structural associations between these additives and the end-product gypsum crystals were evaluated through a combination of inductively coupled plasma mass and / or optical emission spectrometric analyses of digested end-products and X-ray photoelectron spectroscopy (XPS)

of the surface of the solids. Furthermore, X-ray diffraction (XRD) and scanning electron microscopy (SEM) were utilized for determining any changes in phase composition and growth morphologies of the formed crystals. Our results revealed that Mg^{2+}, even at low concentrations, decreased the nucleation and growth kinetics 5-10 fold more than Li^{+}, Na^{+} and K^{+}. In all cases, the additives also changed the shapes and sizes of the formed crystals, with Mg^{2+} and Li^{+} resulting in longer and narrower crystals compared to the additive-free system. In addition, we show that, regardless of concentration, Mg^{2+}, Li^{+} and K^{+} only adsorb to the newly forming surfaces of the growing gypsum crystals, while ~ 25% of Na^{+} becomes incorporated into the synthesized crystals.

Keywords: crystallisation, calcium sulfate dihydrate, kinetics, surface adsorption, X-ray photoelectron spectroscopy.

5.1. Introduction

Gypsum is one of the main evaporitic minerals forming at Earth surface conditions (Freyer et al., 1999). In addition, gypsum is a crucial mineral extensively used in various industries for construction, medical or agricultural applications (Liu et al., 2016; Ossorio et al., 2014; Gupta et al., 2016).

It is well known that both inorganic (Akyol et al., 2009; Abdel-Aal et al., 2015) and organic additives (Rabizadeh et al., 2014; Prisciandaro et al., 2012) affect the nucleation, crystallisation and morphologies of gypsum crystals. To date, primarily the role that elements like Cr^{3+}, Cu^{3+}, Cr^{6+} Al^{3+} and Fe^{3+} have on gypsum growth from solution have been studied (Hamdona and Al Hadad, 2007; Sayan et al., 2007; Kruger et al., 2001; Morales et al., 2016). In contrast, a mechanistic understanding of the effect that major ions in, for example, brines or formation waters (e.g., Na^{+}, K^{+}, Li^{+}, Cl^{-} or Mg^{2+}) has on gypsum crystallisation is still lacking. Existing data from studies that address the crystallisation of calcium sulfate phases in the presence of these ions are highly discrepant and whether these ions become structurally

incorporated or only surface adsorbed into the growing gypsum is still debated. For example, Na^+ has been shown to incorporate into the calcium sulfate hemihydrate ($CaSO_4 \cdot 0.5\ H_2O$; bassanite) (Mao et al., 2014) but not into gypsum (Ben Ahmed et al., 2014). On the other hand, Mg^{2+} was suggested to only incorporate into gypsum (Ben Ahmed et al., 2014). However, lacking so far is a quantitative and molecular level understanding of the processes that lead either to these ions becoming adsorbed onto or incorporated into growing gypsum crystal structures. Lacking is also a mechanistic pathway explaining the role that these crucial ions in brines have on the nucleation, growth and crystallisation of gypsum.

To fill this gap, we have in this work elucidated the effects that variable concentrations (50-500 mM) of aqueous Li^+, Na^+, K^+ and Mg^{2+} ions have on the nucleation and growth kinetics, as well as the morphology of gypsum crystals forming from supersaturated aqueous solutions. We followed the processes by combining analyses of the solution and solid end-products and determined the mechanisms that control the way these alkali and alkaline earth cations became associated with growing gypsum crystals. We show, in contrast to previous studies that Li^+, K^+ and Mg^{2+} do not incorporate into the gypsum structures, while ~ 25% of Na^+ becomes incorporated. However, the major effect that all ions have is in delaying the nucleation and growth through adsorption onto the growing mineral surfaces. In the case of Mg^{2+} and Li^+, this interaction also leads to a change in the resulting crystal growth morphologies.

5.2. Experimental methods

Calcium and sulfate stock solutions were prepared from dissolving analytical grade $CaCl_2 \cdot 2H_2O$ (≥99-100 %; AnalaR Normapour; VWR) and diluting concentrated H_2SO_4 (93-98 % v/vol, AnalaR Normapour; VWR) in 18 $M\Omega cm^{-1}$ ultra-pure Milli-Q water to reach concentrations of 200 mM. The effects of inorganic metal ions on gypsum crystallisation were evaluated by adding Li^+, Na^+, K^+ and Mg^{2+} to separate $CaCl_2 \cdot 2H_2O$ stock solutions, using analytical grade LiCl (puriss. p.a., anhydrous, ≥99.0 %; Sigma-Aldrich), NaCl (≥99.9 %;

Fisher), KCl (puriss. p.a., anhydrous, ≥99-100 %; Sigma-Aldrich) and $MgCl_2 \cdot 6H_2O$ (≥99-100 %; AnalaR Normapour; VWR). Precipitates were produced by mixing 1 ml of $CaCl_2 \cdot 2H_2O$ with or without the additives with 1 ml H_2SO_4 in 4 ml polystyrene cuvettes at room temperature (21 ˚C) and under constant stirring. The mixing led to a solution with a pH of ~ 2 and initial Ca^{2+} and SO_4^{2-} concentrations of 100 mM. The initial concentration of additives in the crystallisation solutions (after mixing) was varied between 50 and 500 mM. Once mixed, all solutions were supersaturated with respect to gypsum as indicated by the saturation indices (as the logarithm of the ion activity product over the solubility product) calculated with the geochemical computer code PhreeqC 3.3.3 and using the PITZER database (Parkhurst and Appelo, 2013).

Changes in the mixed solutions were monitored by measuring the increase in absorbance using a UV-VIS spectrophotometer (Uvikon XL) at λ = 520 nm with an angle between the incident beam and detector of 180˚. The reactions were followed at room temperature for up to 200 minutes with UV-VIS data collected every second and each experimental set was carried out five times. The absorbance data are plotted as the normalized change in solution turbidity. At the end of each turbidity experiment, the contents of each cuvette were vacuum-filtered through 0.2 μm polycarbonate filters, dried and preserved for further analyses (for additional details see Appendix A; Figure A.1).

In all experiments, regardless if additives were present or not, the solid end-products were always gypsum as determined by powder X-ray diffraction (XRD; Bruker D8 diffractometer; CuKα1; 2θ range 5 - 35˚; resolution 0.105˚ / step; counting time 1 s / step) with XRD patterns analyzed with the EVA software (version 3) and the PDF-2-1996 database (see Figure A.2). To accurately determine the d-spacing in all samples, each gypsum end-product powder was mixed with a silicon standard reference material prior to the XRD analysis.

The growth morphologies (different from equilibrium morphologies; Aquilano et al., 2016) of the resulting gypsum crystals were imaged using a field emission gun scanning electron microscope (FEG-SEM, FEI Quanta 650, 5 kV) and the dimensions of the crystals were

evaluated by measuring the lengths and widths of 200 crystals in each sample using the ImageJ v. 1.49 software (Abràmoff et al., 2004).

To evaluate the association between the additives and the formed gypsum, aliquots of the precipitated end-products were dissolved in 2 % nitric acid (69 % AnalaR NORMAPUR analytical reagent) and the resulting solutions were analyzed for their Li^+, Na^+, K^+, Mg^{2+}, and Ca^{2+} contents by inductively coupled plasma mass spectrometry (ICP-MS; Thermo Scientific iCAPQc) and inductively coupled plasma optical emission spectrometer (ICP-OES; Thermo Scientific iCAP 7400); for limit of detection and uncertainties see Table A.1). To differentiate between the potentially surface adsorbed and the structurally incorporated fractions of the additives, in each case a 0.5 g aliquots of an end-product gypsum sample was suspended in 25 ml of a saturated gypsum solution and filtered. Subsequently, the gypsum on filter was then filter-rinsed 6 times with 25 ml of saturated gypsum solutions (total rinsing time of ~ 10 minutes) to desorb any potentially surface adsorbed additives. The saturated gypsum solution was prepared by equilibrating gypsum (puriss, 99.0-101.0 %, Sigma-Aldrich) in 18 $M\Omega cm^{-1}$ ultra-pure Milli-Q water at pH ~ 2 for 24 hours and filtering through 0.2 µm syringe filters prior to desorption. After this desorption step the remaining solids were digested in 2% nitric acid and the digestion solutions were analyzed as described above. The concentrations of additives associated with the end-product gypsum crystals (association amount; C_A) before and after desorption were calculated from the moles of cation measured in the full digestion solution divided by the moles of total dissolved gypsum crystals.

Finally, to determine the nature of the surface interactions between the various ions and the formed precipitates, we employed X-ray photoelectron spectroscopy (XPS) with a detection limit of 0.1 at.% (which is roughly 1 ppth or 10^{19} atoms/cm^3). On both the as-formed and the desorbed end-product solids, XPS was used to determine whether and how additives were associated with the mineral surfaces or the crystal structures. XPS spectra were acquired from the top 8-10 nm of end-product gypsum crystals using a Kratos Axis Ultra-DLD spectrometer with a monochromatic Al Kα X-ray source (144 W) and analyzer pass energies

of either 160 eV (survey scans) or 40 eV (high resolution scans). The base pressure during analysis was ca. 6×10^{-7} Pa. All data were referenced to the C (1s) signal of adventitious carbon at 284.8 eV and quantified as atomic percentage using CasaXPS™ (Version 2.3.15) using elemental sensitivity factors supplied by the manufacturer.

5.3. Results

5.3.1. The effects of additives on the crystallisation process

In the additive-free experiments, the turbidity started to develop after 3±1 minutes (induction time) and it took ~ 30 minutes for the turbidity to reach a steady value on a plateau (Figure 5.1 a). In contrast, in each of the additive-containing experiments (Figure 5.1 a and b), the induction times and the time to reach a plateau were markedly longer. At the highest concentration (500 mM) of monovalent cations (Li^+, Na^+ and K^+), the induction time increased in the order of $K^+ < Na^+ < Li^+$ by 2 fold, 4 fold and almost 5 fold, respectively (Table A.2). The slope of the linear part of the turbidity graphs decreased from 6.2 ± 0.1 (% . min^{-1}) in the additive-free system to 5.3 ± 0.1, 4.4 ± 0.1 and 3.8 ± 0.1 (% . min^{-1}) in the presence of 500 mM of K^+, Na^+ and Li^+, respectively and the crystallisation end-plateaus were reached significantly later than in the additive-free system in the same order (K^+ ~ 37 minutes, Na^+ ~ 48 minutes and Li^+ ~ 60 minutes; Figure 5.1 a). Moreover, the half crystallisation time ($t_{50\%}$) in the additive-free systems was 17 ± 1 minutes while the $t_{50\%}$ in the presence of 500 mM K^+, Na^+ and Li^+, it increased to 22 ± 1, 29 ± 1 and 37 ± 1 minutes, respectively. It is also worth mentioning that exponential part of the turbidity graphs in the additive-free systems terminated at turbidity of 8 % (after 11 minutes) but in the presence of 500 mM K^+, Na^+ and Li^+, it terminated at the turbidity of 12 % (after 15 minutes), 15 % (after 22 minutes) and 18 % (after 28 minutes). This is akin to an apparent Langmuir-type behavior where a change in slope may indicate a change in adsorption mechanism (Sparks, 2003). However, in the current study we show that specifically for Na^+ the mechanism of association between the ions and the

newly forming gypsum crystals is dominated by incorporation. The turbidity development was even more affected by the presence of Mg^{2+}. Even at a low additive concentration (e.g., 100 mM; Figure 5.1 a) the induction time was much longer than for all monovalent cations at 500 mM. Quadrupling the Mg^{2+} concentration from 50 mM to 200 mM, increased the induction time exponentially (Figure 5.1 b, Table A.2) and decreased the slope of the turbidity graph from 4.5 ± 0.1 to 1.3 ± 0.1 (% . min^{-1}) whilst, the half crystallisation time increased from 30 minutes to 105 minutes. Moreover, the exponential part of the turbidity graph in the presence of 50 mM Mg^{2+} terminated at the turbidity of 12 % and after 24 minutes which increased to 100 minutes at the turbidity of 24 % in the presence of 200 mM Mg^{2+}. Furthermore, for Mg^{2+} at 300 and 500 mM even after 200 minutes of reaction no change in turbidity was observed indicating total inhibition of the reaction under these experimental conditions. For all additives with increasing cation concentrations the induction time increased linearly (Figure 5.1 c), but the effect was markedly larger for the divalent Mg^{2+} compared to the monovalent Li^+, Na^+ and K^+ (Figure 5.1 c).

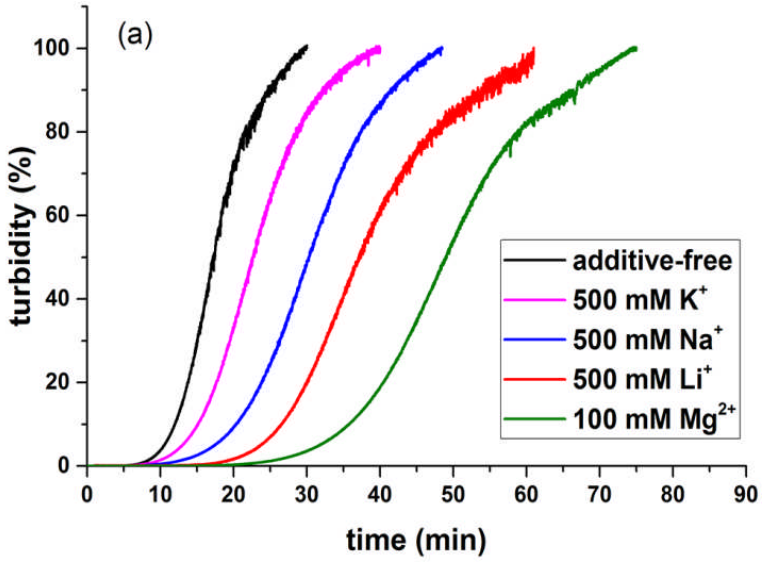

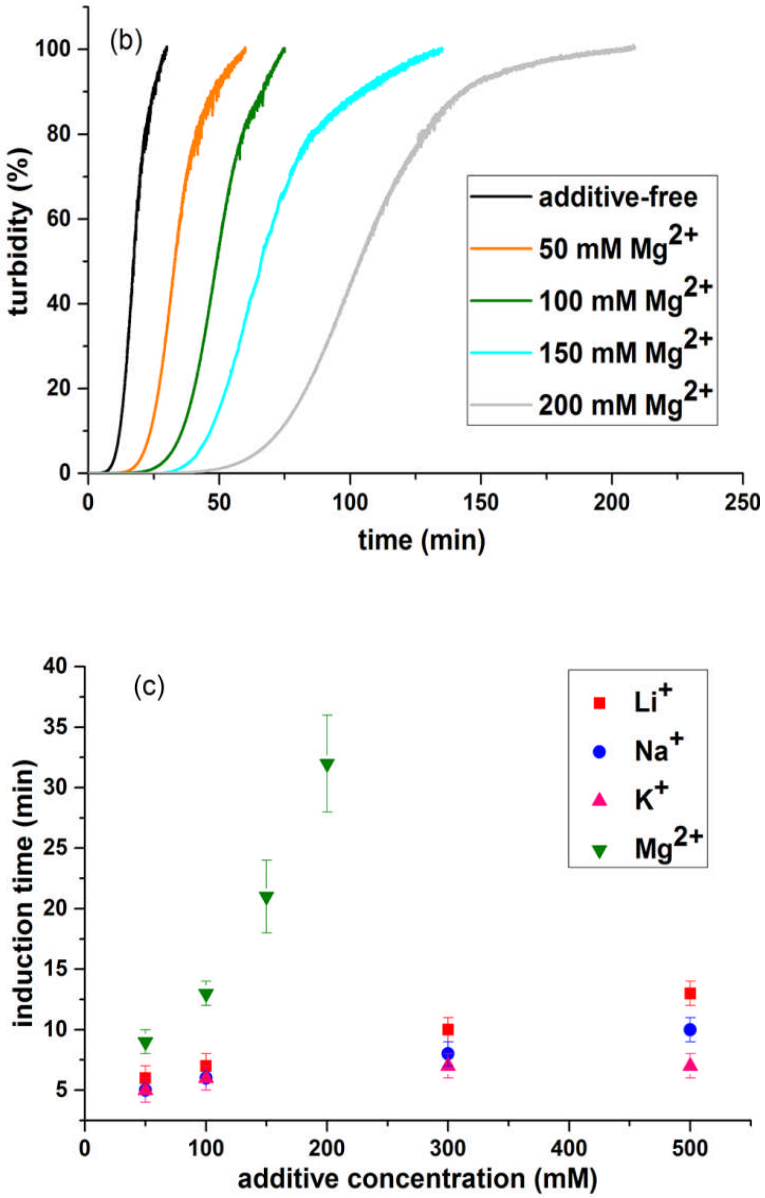

Figure 5.1.Turbidity curves plotted as a function of time; (a) in the absence and presence of high concentrations of additives (note that Mg^{2+} is only 100 mM while all monovalent ions are 500 mM); (b) at variable concentrations of Mg^{2+}; (c) changes in induction times as a function of additive concentrations.

5.3.2. The association between additives and gypsum crystals

For all additive ions, increasing additive concentration in solution was mirrored by an increase in associated ion concentration (C_A) in the solids formed (Figure 5.2 a-d). For example, for monovalent additive concentrations between 50 and 500 mM, C_{A,Li^+} increased ~ 5 times, while C_{A,Na^+} and C_{A,K^+} increased ~ 4 and ~ 3 times, respectively (Figure 5.2 a-c). For Mg^{2+} at concentrations up to 200 mM, the $C_{A,Mg^{2+}}$ increased ~ 4 times (Figure 5.2 d) and reached a

value almost equivalent to the highest value obtained for the C_A of Li^+ at 500 mM. Comparing the association amounts at a fixed additive concentration (100 mM), mirrors the trend observed for the increase in induction time, namely $K^+ < Na^+ < Li^+ < Mg^{2+}$.

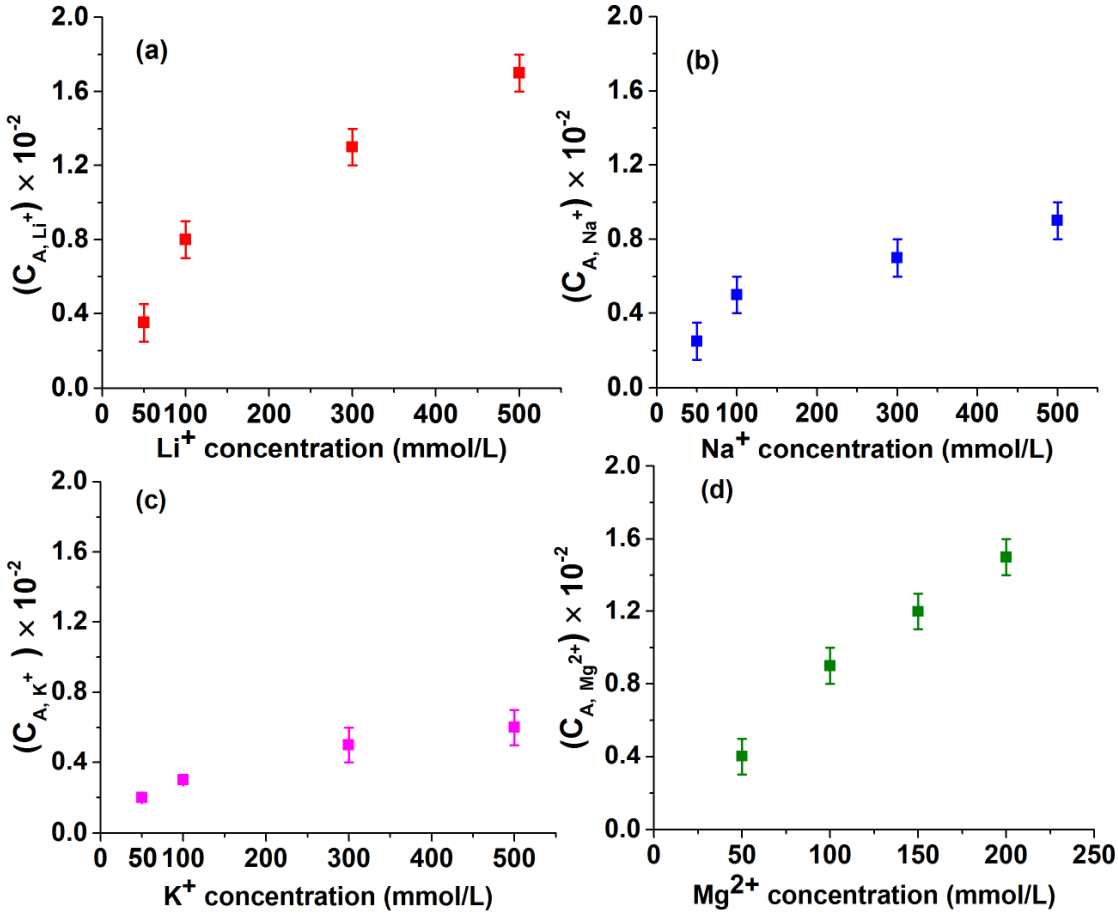

Figure 5.2.Variations in cation association at different concentrations of (a) Li^+; (b) Na^+; (c) K^+; and (d) Mg^{2+}. The error bars represent the standard deviations measured in five replicate samples.

When we evaluated the partitioning of additives between crystal surfaces (adsorption) or crystal matrixes (structural incorporation), our data revealed that the C_A for Li^+, K^+ and Mg^{2+} in the post-desorption digested samples were below detection limits. This clearly indicated that these cations were only adsorbed to the surfaces of the growing gypsum crystals with insignificant or no incorporation into the crystal structures. In contrast, at the highest additive concentrations (500 mM), up to 25% of the associated Na^+ ($C_{A,500\ mM}$ = 0.002 out of 0.009) became incorporated into the gypsum structure (Figure A.3). The additive ion adsorption was also confirmed by XPS surface analyses of as-formed and desorbed gypsum crystals (Figure

5.3). The XPS spectra confirmed that the Li 1s (55.8 eV), K $2p_{3/2}$ (292.9 eV) and Mg 2s (89.8 eV) peaks were present in all as-formed samples but absent in the post-desorbed ones confirming that these ions were solely surface adsorbed and not incorporated into the gypsum structure (Figure 5.3 a, c and d). On the other hand, for Na^+ the 1s peak at 1071.6 eV was present in both the as-formed and desorbed gypsum spectra, again corroborating our C_A data (Figure 5.3 b) that a fraction of the associated Na^+ became sequestered into the gypsum crystal structure. The surface elemental compositions (in atomic percentage) of the as-produced and desorbed gypsum crystals illustrated that Li^+ had the highest adsorption affinity (1.5 at. %) followed by Mg^{2+} (1.1 at. %), Na^+ (0.4 at. %), and K^+ (0.4 at. %) (Table 5.1). However, unlike Li^+, K^+ and Mg^{2+}, Na^+ remained associated with the gypsum crystals post-desorption (0.1 at.%) confirming its structural incorporation. Note the signal of lithium is low due to its small ionization cross-section and in part covered by the large satellite peak visible in Figure 5.3.

Together with the adsorbed ions, in all as-formed but not the desorbed samples, the XPS spectra revealed the presence of Cl^- 2p peaks confirming that Cl^- also became co-adsorbed to the gypsum surfaces (Figure A.4). Furthermore, the Ca to S at.% ratio was close to 1:1 but the O to Ca or S ratio was higher than 4:1, likely related to gypsum structural water (Table 5.1).

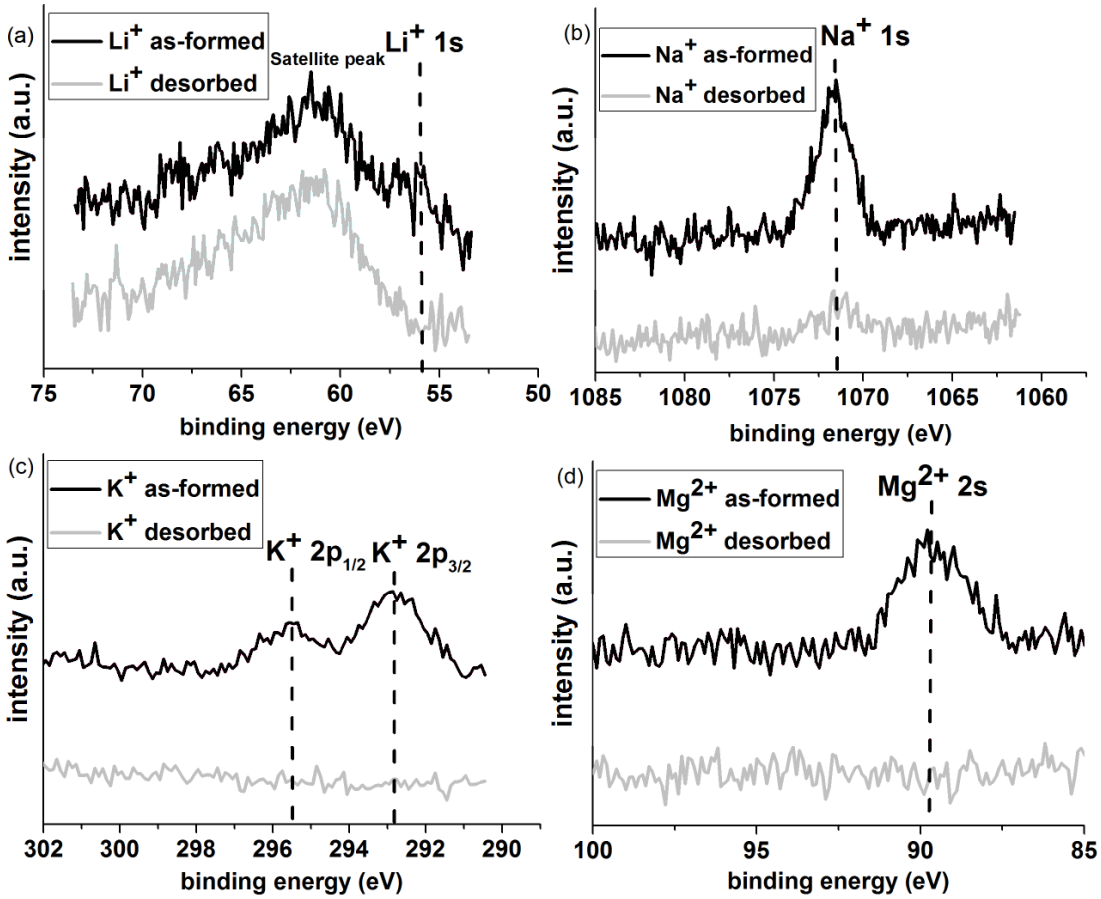

Figure 5.3.XPS spectra for the as-formed and desorbed gypsum crystals containing additive cations. Note that the peak intensities are in arbitrary units and do not represent the concentration of the elements on the surface.

Table 5.1. Surface composition of the precipitated gypsum crystals detected by XPS (at. %)

	Ca	S	O	Li	Na	K	Mg	Cl	C[1]
Additive-free (as-formed)	11.5	12.0	58.3	-	-	-	-	-	18.2
Additive-free (desorbed)	11.6	12.0	58.3	-	-	-	-	-	18.1
Li^+-500 mM (as-formed)	9.6	10.0	52.3	1.5	-	-	-	1.7	24.9
Li^+-500 mM (desorbed)	12.0	12.7	57.3	-	-	-	-	-	18.0
Na^+-500 mM (as-formed)	12.6	13.1	59.5	-	0.5	-	-	0.1	14.2
Na^+-500 mM (desorbed)	12.3	13.0	59.4	-	0.1	-	-	-	15.2
K^+-500 mM (as-formed)	12.2	12.7	58.8	-	-	0.4	-	0.1	15.8
K^+-500 mM (desorbed)	12.3	13.1	59.9	-	-	-	-	-	14.7
Mg^{2+}-200 mM (as-formed)	10.2	10.9	48.9	-	-	-	1.1	1	27.9
Mg^{2+}-200 mM (desorbed)	12.3	12.9	57.9	-	-	-	-	-	16.9

1 adventitious carbon

5.3.3. The effects of additives on the morphology of gypsum

Micrographs of the formed gypsum crystals revealed that in the additive-free system, short (4-6 μm) and narrow (2-2.5 μm) gypsum crystals formed (Figures 5.4 a, 5.5 a,b and A.6 a,b). In contrast, the crystals from the additive-containing solutions were markedly longer and narrower (Figures 5.4 b, 5.5 b and A.6 a,b). For example, in the presence of 500 mM Li^+ the end-product gypsum crystals were ~ 200% longer and ~ 50% narrower compared with the additive-free crystals.

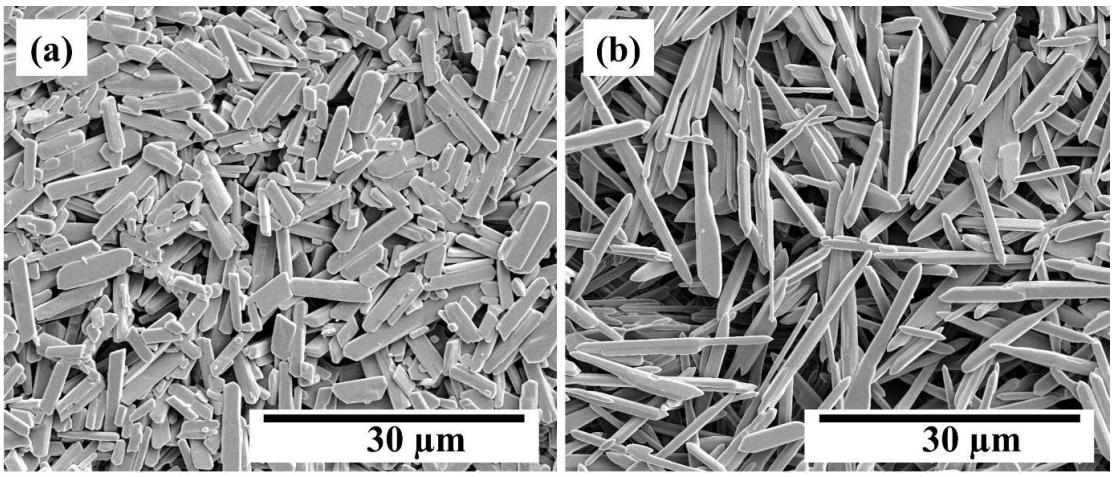

Figure 5.4.SEM micrographs of the end-product gypsum crystals in (a) the additive-free system; (b) the presence of 500 mM Li^+ (for morphologies of gypsum crystals precipitated in the presence of K^+, Na^+ and Mg^{2+} see Figures A.5).

This is clearly visible that in the presence of Li^+ and Mg^{2+} the length of the resulting crystals almost doubled, while the width slightly decreased compared to the additive-free system (Figures 5.5 a,b and A.6 a,b).

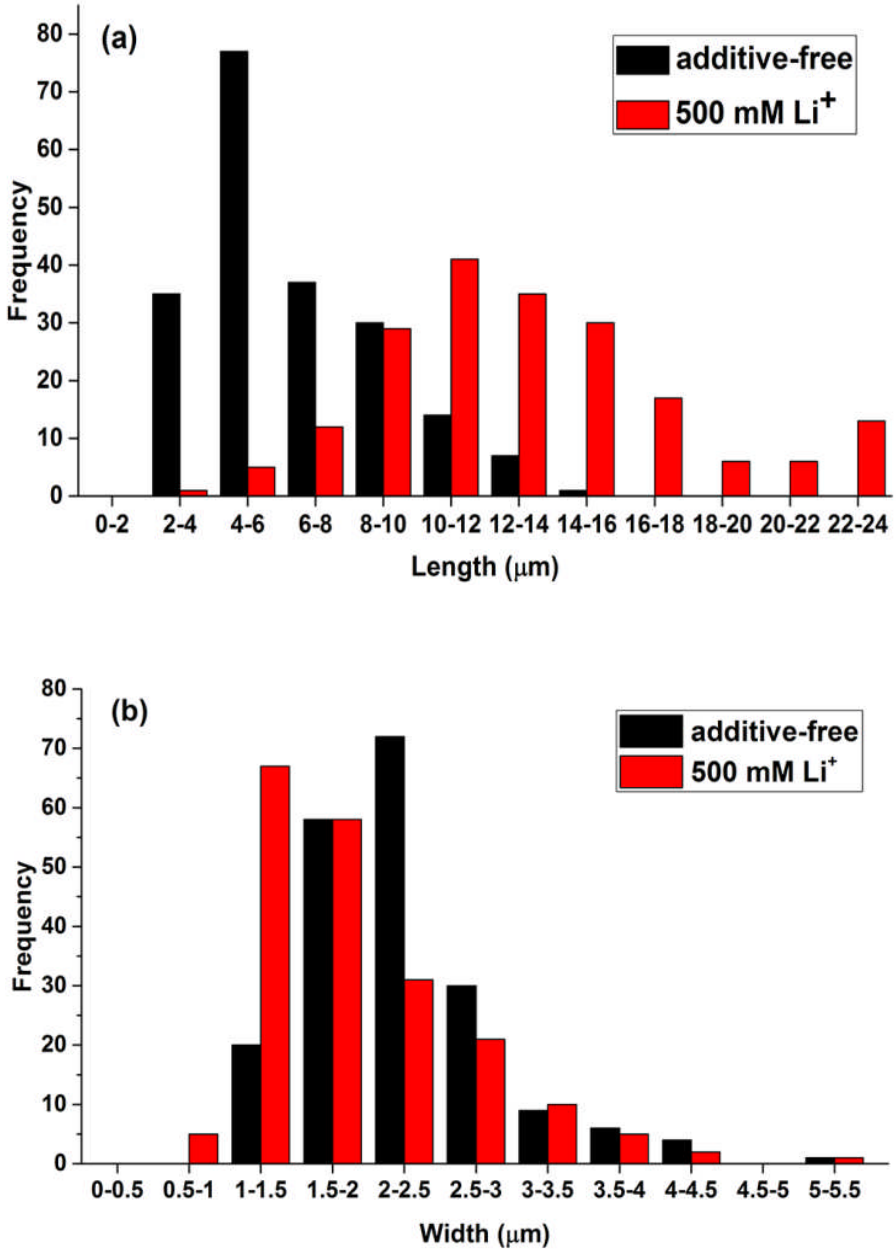

Figure 5.5.Particle size analysis of gypsum crystals precipitated from solution containing 500 mM Li^+ after 200 minutes; (a) length of the crystals; (b) width of the crystals (the particle size analysis of the gypsum crystals precipitated in the presence of 500 mM K^+, 500 mM Na^+ and 200 mM Mg^{2+} are in Figure A.6 a,b).

In addition, the tips of the growing gypsum crystals differed (Figures 5.6 a-e and A.7-10), with the additive-free crystals having dominantly flat tips. For example, in the presence of Li^+ the tips were broader and thicker and in these crystals small spiral growth and steps were also obvious (Figures 5.6 b and A.7 c). Similarly, the gypsum crystals precipitated in the presence of 500 mM Na^+ (Figures 5.6 c and A.8) and K^+ (Figures 5.6 d and A.9) had uneven tips also

with small steps while the Mg^{2+} modified gypsum crystals had curved tips (Figures 5.6 e and A.10).

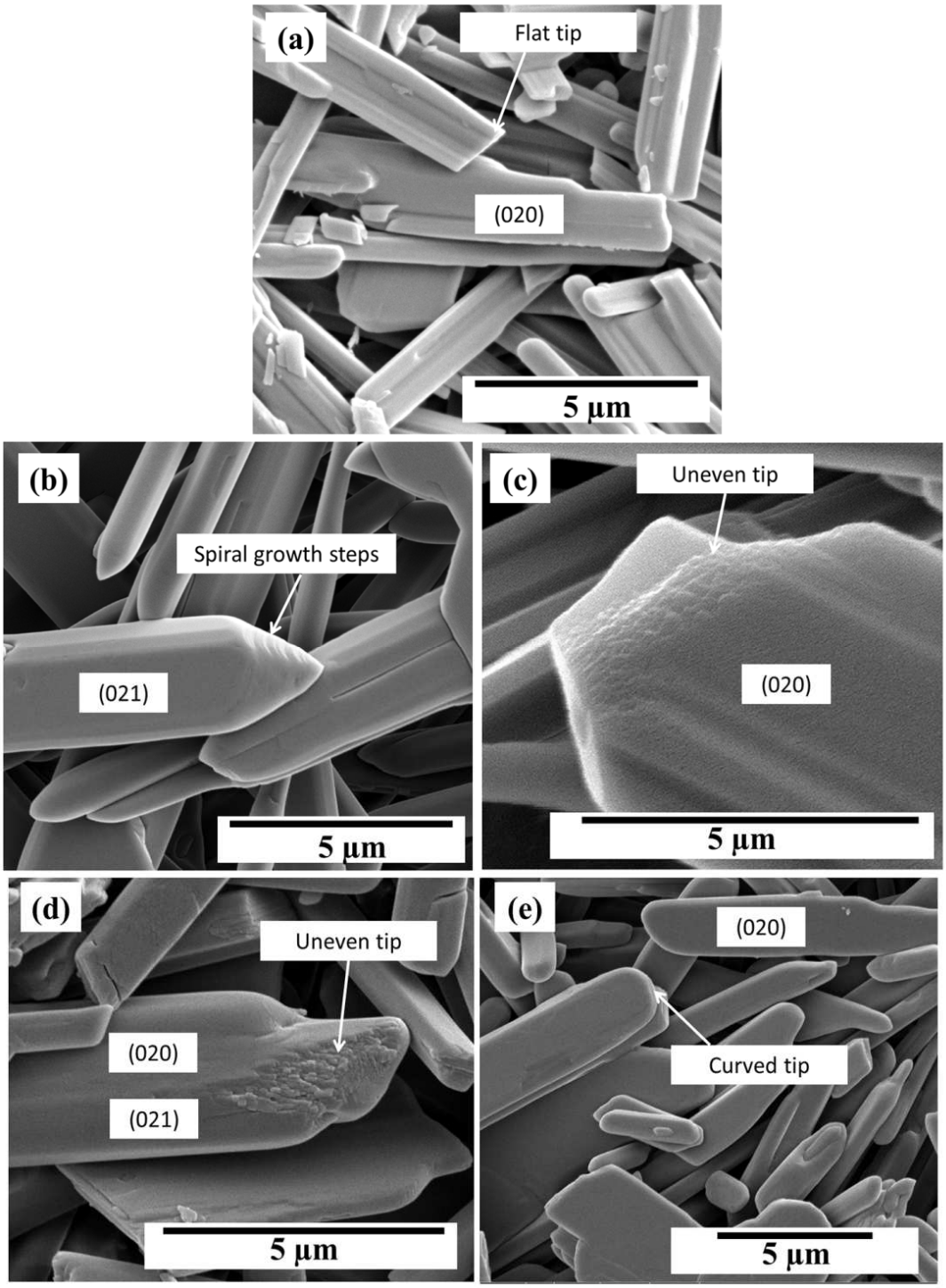

Figure 5.6.SEM micrograph of end-product gypsum tips from systems with (a) no additive; (b) 500 mM Li^+; (c) 500 mM Na^+; (d) 500 mM K^+; (e) 200 mM Mg^{2+}. Note indexed faces of the crystals formed in the presence of the additives are tentatively assigned, because rounds shapes are difficult to index based on SEM images alone.

5.4. Discussion

5.4.1. Crystallisation kinetics: role of additives

We used the change in turbidity induction times in the absence and presence of the additives as a proxy to evaluate the effects they have on the nucleation and growth of gypsum. Our data showed a clear increase in induction time with increasing additive concentrations, and a decreased in nucleation and growth kinetics in the order of $K^+ < Na^+ < Li^+ < Mg^{2+}$ (Figure 5.1 a-c).

The turbidity graphs in this study had similar shapes and development trends confirmed the similarity in mechanisms governed the nucleation and growth inhibition of gypsum crystals. Although it is not possible to separate the nucleation from the growth part on a turbidity graph (Chen et al., 2004), it can be seen that gypsum crystals in this study nucleated (turbidity occurred) and just their growth kinetics were modified by the additives. Therefore, the alkali and alkaline earth metals acted as growth inhibitors. However, this classification is not absolute and depends on the concentration of the additives or the experimental conditions because for example at very high additive concentrations (e.g., 2-5 M) gypsum may not nucleate therefore these additives will be considered as nucleation inhibitors.

To fully understand the interaction, we also assessed how the crystallisation process (i.e., nucleation and growth) was affected by the presence of the additives.

The increase in ionic strength (IS) with increasing the additive concentrations from 50 mM to 500 mM, invariably resulted in a decrease in the activities of $SO_4^{2-}$and Ca^{2+} and this affected the solubility of gypsum and delayed its precipitation (Figure 5.1 a-c). This is a well-known process in the $CaSO_4$ system (Sun et al., 2015; Sverjensky et al., 1997; Tanji, 1969; Zhang et al., 2013). Specially, at high ion concentrations, and thus high ionic strengths (IS = 1 M and 1.1 M for 500 mM monovalent cations and 200 mM Mg^{2+} containing solutions, respectively), additives can be present as ion pairs or charged complexes (Jiang et al., 2013).

Such complexes further decrease the activity of free SO_4^{2-} and $CaSO_4^0$ ion pairs. In our study, the additive-sulfate ion-paring strength increased in the order of $K^+ < Na^+ < Li^+ < Mg^{2+}$ ($[KSO_4]^- < [NaSO_4]^- < [LiSO_4]^- < [MgSO_4^0]$) (Elgquist and Wedborg, 1978; Jiang et al., 2013; Reardon, 1975; Leaist and Goldik, 2001). As such this likely explains our observation that Mg^{2+} decreased the nucleation rate and increased the solubility of the gypsum crystals more than the monovalent cations. However, it is important to note that the observed order in which these ions affected the induction time and crystallisation kinetics ($K^+ < Na^+ < Li^+ < Mg^{2+}$) is different to what was predicted from the saturation indices calculated by PhreeqC ($Na^+ < Li^+ < K^+ < Mg^{2+}$; Table A.3).

Once nucleation is overcome, most often the rate-limiting step for crystal growth is determined by cation desolvation (Dove and Czank, 1995). The increase in hydration enthalpy for $K^+ < Na^+ < Li^+ < Mg^{2+}$ reveals that in our system the divalent Mg^{2+} ion with the highest hydration enthalpy and water residence time (Kerisit and Parker, 2004), by far outcompetes the monovalent ions as it limits crystal growth more effectively. Among the monovalent ions, Li^+ retained its water longer than Na^+ and K^+ (Sakuma and Kawamura, 2011).

This is similar to the inhibitory order for the precipitation of calcium oxalate monohydrate (Farmanesh et al., 2015) or for barium sulfate (Kowacz et al., 2007).

5.4.2. Surface adsorption and / or structural incorporation

Our results (Figures 5.2, 5.3 and A.3) revealed that all the tested inorganic additives adsorbed onto the surfaces of the gypsum crystals and that among them the cations with more negative hydration enthalpies (Li^+ and Mg^{2+}) had the highest surface adsorption affinity (Table 5.1). This behavior can be explained by the water “structure making-structure breaking” model (Gierst et al., 1966). According to this model, an ion and a surface exerting similar structural effects on their surrounding water, are attracted entropically to each other. Gypsum has a negative heat of hydration (Singh and Middendorf, 2007) and retains H_2O molecules in the vicinity of its surface and fits therefore to the structure-making model. These H_2O molecules

may thus act as anchoring points for the stronger adsorption of Li^+ and Mg^{2+}, which are structure-making ions compared to Na^+ and K^+. In addition, equivalent adsorption (in atomic percentage) of Mg^{2+} and Li^+ (Table 5.1), despite the more than 2 fold lower concentration of Mg^{2+} (200 mM) than Li^+ (500 mM), further supports this mechanism. Similar behaviors (i.e., higher surface adsorption of Li^+ than Na^+ and K^+) have been reported for TiO_2 (Bourikas et al., 2001), α-Al_2O_3 (Johnson et al., 1999). Moreover, it has been suggested that gypsum crystals might have negative surface charges (Salopek et al., 1992). Therefore, it can be concluded that the cations adsorbed via electrostatic interactions.

Our data (Table 5.1 and Figure A.4) also showed a high adsorption affinity of Cl^- on the as-formed gypsum crystals precipitated in the presence of Li^+ and Mg^{2+} but only trace amount of Cl^- on the gypsum crystals formed in the presence of Na^+ and K^+. Sakuma and Kawamura (2011) used molecular dynamics modeling and suggested that cations co-adsorbed with chloride on muscovite surfaces. In addition, Rahnemaie et al. (2006) documented that in the goethite-solution double layer Cl^- was closer to the surface than the other ions, and that Li^+ and Na^+ were at the intermediate position of the double layer and K^+ was at the largest distance.

Our observations are in agreement with these previous reports for the monovalent ions Li^+, Na^+ and K^+, but we evidenced further the role of Li^+ and Mg^{2+} in co-adsorbing the chloride ion. This is further supported by the fact that, neither on the surfaces of the as-formed additive-free gypsum crystals nor in all the post desorption gypsum crystals Cl^- was detected by XPS (Table 5.1 and Figure A.4). This was despite the fact that in all initial solutions used for precipitating gypsum crystals in these additive-free experiments, calcium chloride was the major source of Cl^- (200 mM). Moreover, in the samples where Li^+ and Mg^{2+} ions and chloride were determined to be adsorbed to the gypsum surfaces (Table 5.1), the atomic percentage of the adsorbed Cl^- was in a ratio close to 1:1 with the adsorbed Li^+ and Mg^{2+}. This suggest that Li^+ and Mg^{2+} likely adsorbed onto the gypsum surfaces as chloride ion-pairs or complexes such as $LiCl(H_2O)_4$ for Li^+ and $[MgCl(H_2O)_M]^+$ for Mg^{2+} (Sobolewski and

Domcke, 2005; Siokou et al., 2003). For Li^+ this is supported by the fact that the binding energies for Li 1s and Cl^- 2p at 55.8 eV and 198.5 eV, are the same as the binding energies of these two ions in LiCl (Naumkin et al., 2012).

It is also worth mentioning that compared with the additive-free gypsum crystals, the Li^+ and Mg^{2+} surface adsorption via sulfate binding shifted the S $2p_{3/2}$ toward higher binding energies by 0.2 eV and 0.5 eV for Li^+ and Mg^{2+}, respectively (Figure A.11). This shift was not observed for the adsorbed Na^+ or K^+, which indicates their low surface adsorption. Hou et al. (2014) reported S $2p_{3/2}$ binding energy variations related to Mg^{2+} association with hydrothermally synthesized calcium sulfate hemihydrate crystals. They attributed this shift to the partial substitution of Ca^{2+} with Mg^{2+} in the calcium sulfate hemihydrate (bassanite) structure and the higher electronegativity of Mg^{2+} (1.39) with respect to Ca^{2+} (1.00), which explained the higher binding energy between Mg^{2+} and S compared to those between Ca^{2+} and S.

Analyzing the post-desorption gypsum crystals revealed that only Na^+ became partly (max. 25%) incorporated into the gypsum structure. Such an incorporation likely happened through substitution of Na^+ for Ca^{2+} specially as Na^+ has the closest ionic radius (1.16 Å) to Ca^{2+} (1.12 Å) compared to the other studied cations (Li^+ = 0.92 Å, K^+ = 1.52 Å and Mg^{2+} = 0.89 Å). Therefore, in gypsum it is likely that Ca^{2+} became substituted by 2 Na^+ ions with one of the Na^+ ions occupying the interstitial positions in the water layer (Freyer et al., 1999; Kushnir, 1980). Another possibility is the sulfate vacancy formation for charge compensation similar to the carbonate vacancy creation during the substitution of Na^+ into Ca^{2+} sites in the lattice structures of calcium carbonate phases (e.g., calcite and aragonite) (Yoshimura et al., 2016)

We are the first to show that when gypsum crystals grown in solutions containing low to high concentrations of monovalent and divalent ions, the prime interaction is through adsorption and that structural incorporation is only a minor effect for Na^+. Kushnir (1982) reported that Sr^{2+}, Mg^{2+}, Na^+, and K^+ ions present in seawater brines became partitioned into

growing gypsum crystals, but no determination whether the partitioning was because of the surface adsorption or structural incorporation is available. Recently, Wang and Meldrum (2012) showed that gypsum crystals synthesized from experimental solutions containing 200 mM Mg^{2+} contained a small, but measurable amount (0.4% mol) of Mg^{2+} in their structure. Similarly, Ben Ahmed et al. (2014) suggested that a shift in d-spacing of the gypsum (020) peak, indicates that Mg^{2+} became incorporated into the structure and suggested that this occurred by Mg^{2+} substituting for Ca^{2+}. Based on the same approach they suggested that Na^{+} did not incorporate into the gypsum structure. In our current work, although we observed a similar shift towards lower diffraction angles in the gypsum (020) peak position as a function of Mg^{2+} concentration (Figure A.12), we assert that this is more a function of inherent differences in crystallisation paths and not due to the presence of the magnesium ion during gypsum growth. This is because we clearly documented, by two complementary approaches (ICP-MS / ICP-OES analyses of pre- and post-desorption digests and XPS analyses of pre- and post-desorption crystal surfaces), that only less than ~ 25% of Na^{+} became incorporated into the gypsum structure, while all other ions, even at high concentrations, were solely adsorbed to the growing gypsum crystal surfaces. There, they affected both the growth kinetics and the shapes of the resulting gypsum crystals.

5.4.3. Morphological modification

The selective adsorption of additives onto the growing gypsum crystals inhibited their growth along specific directions and thus modified their shapes (Figure 5.4 and A.5). It is not surprising that such inhibition most often affects particular crystal faces as this depends on the attachment energies of each crystal face (Schmidt and Ulrich, 2012). Recently, Massaro et al. (2011) demonstrated theoretically that for gypsum, there is a higher site density (Ca^{2+} and SO_4^{2-}) on the (021) faces compared to the fully hydrated (020) faces. Thus, it is likely that because of the higher surface energy of the (021) face compared to the (020) face adsorption will be more dominant on the (021) face. This is in line with our observations that adsorption

preferentially occurred on the (021) faces and this favored growth along the (020) faces and this led to an elongation in the *c* axis direction (van der Voort and Hartman, 1991) (Figures 5.4, A.5 and A.13). In the presence of additives (specially Li^+ and Mg^{2+}), the resulting elongated gypsum crystals were accompanied by a corresponding decrease in the crystal widths (Figures 5.5 and A.6). The observed spiral growth we have observed for gypsum crystals grown in the presence of additives, together with the uneven crystal tips and the presence of growth steps on the crystal surfaces (Figures 5.6 and A.7-10) suggests that indeed the additives played an important role in the growth of the gypsum crystals in our experiments.. Such observations have not been reported before for mono and divalent ions but similar growth steps have been reported for gypsum crystals grown in the presence of acrylic polymers (Montagnino et al., 2011). On the other hand, it is also well-known that any changes in supersaturation can have a distinct effect on growth morphology (Prywer, 2006; Yang et al., 2006) and this should be investigated in future studies.

The current study shows the potential of alkali and alkaline earth metals to be used as gypsum formation inhibitors and retarders in different industries such as construction and medical. These elements can also cause gypsum elongation which will clog the membranes in different industries such as water desalination. Therefore, the presence of alkali and alkaline earth metals in the system should be considered while evaluating the mineral scaling potential of the system. Furthermore, gypsum can be used in pollution sites to remove the contaminants such as Li^+ by surface adsorption mechanism. Moreover, in agricultural industries this mineral can provide alkali and alkaline earth metals to soil.

5.5. Conclusion

With this study, we documented quantitatively the effects that alkali and alkaline earth metals have on the crystallisation of gypsum. The additives increased the time needed for its precipitation to be initiated in the order of $K^+ < Na^+ < Li^+ < Mg^{2+}$. In all cases, gypsum was the sole precipitated phase after 200 minutes and the additives did not cause any phase

transformation even at high salt concentrations. The combination of ICP-MS / ICP-OES of digested as-formed and post-desorbed digested gypsum crystals together with XPS analyses of the surfaces of these solids revealed that Li^+, K^+ and Mg^{2+} only adsorbed on the surfaces of the gypsum crystals, while small fraction of associated Na^+ (max. 25%) became structurally incorporated. Growing in the presence of all additives resulted in elongated gypsum crystals, with the change in aspect ratio compared to the additive-free system being most prominent in the presence of Li^+ and Mg^{2+} because of their higher surface adsorption affinities.

Acknowledgments

This study was supported by a Marie Curie grant from the European Commission in the framework of the MINSC ITN (Initial Training Research network), Project number 290040. The authors would like to thank the Cohen Laboratories in the School of Earth and Environment, and the Leeds Electron Microscopy and Spectroscopy Centre (LEMAS) for help and access to instruments during the course of this study.

5.6. References

Abdel-Aal, E., Abdel-Ghafar, H. & El Anadouli, B., 2015. New Findings about Nucleation and Crystal Growth of Reverse Osmosis Desalination Scales with and without Inhibitor. *Crystal Growth & Design,* 15**,** 5133-5137.

Abràmoff, M. D., Magalhães, P. J. & Ram, S. J., 2004. Image processing with ImageJ. *Biophotonics international,* 11**,** 36-42.

Akyol, E., Öner, M., Barouda, E. & Demadis, K. D., 2009. Systematic Structural Determinants of the Effects of Tetraphosphonates on Gypsum Crystallization. *Crystal Growth & Design,* 9**,** 5145-5154.

Aquilano, D., Otálora, F., Pastero, L. & García-Ruiz, J. M., 2016. Three study cases of growth morphology in minerals: Halite, calcite and gypsum. *Progress in Crystal Growth and Characterization of Materials,* 62**,** 227-251.

Ben Ahmed, S., Tlili, M. M., Amami, M. & Ben Amor, M., 2014. Gypsum Precipitation Kinetics and Solubility in the NaCl–MgCl2–CaSO4–H2O System. *Industrial & Engineering Chemistry Research,* 53**,** 9554-9560.

Bourikas, K., Hiemstra, T. & Van Riemsdijk, W., 2001. Ion pair formation and primary charging behavior of titanium oxide (anatase and rutile). *Langmuir,* 17**,** 749-756.

Chen, T., Neville, A. & Yuan, M., Effect of PPCA and DETPMP inhibitor blends on CaCO3 scale formation. SPE International Symposium on Oilfield Scale, 2004. Society of Petroleum Engineers.

Dove, P. M. & Czank, C. A., 1995. Crystal chemical controls on the dissolution kinetics of the isostructural sulfates: Celestite, anglesite, and barite. *Geochimica et Cosmochimica Acta,* 59**,** 1907-1915.

Elgquist, B. & Wedborg, M., 1978. Stability constants of NaSO 4−, MgSO 4, MgF+, MgCl+ ion pairs at the ionic strength of seawater by potentiometry. *Marine Chemistry,* 6**,** 243-252.

Farmanesh, S., Alamani, B. G. & Rimer, J. D., 2015. Identifying alkali metal inhibitors of crystal growth: a selection criterion based on ion pair hydration energy. *Chemical Communications,* 51**,** 13964-13967.

Freyer, D., Reck, G., Bremer, M. & Voigt, W., 1999. Thermal behaviour and crystal structure of sodium-containing hemihydrates of calcium sulfate. *Monatshefte für Chemie/Chemical Monthly,* 130**,** 1179-1193.

Gierst, L., Vandenberghen, L., Nicolas, E. & Fraboni, A., 1966. Ion pairing mechanisms in electrode processes. *Journal of The Electrochemical Society,* 113**,** 1025-1036.

Gupta, K., Singh, S. & Rao, M. R., 2016. Direct and Facile Room-Temperature Synthesis of Nanocrystalline Calcium Sulfate Dihydrate (Gypsum). *Crystal Growth & Design,* 16**,** 3256-3261.

Hamdona, S. K. & Al Hadad, U. A., 2007. Crystallization of calcium sulfate dihydrate in the presence of some metal ions. *Journal of Crystal Growth,* 299**,** 146-151.

Hou, S., Wang, J., Wang, X., Chen, H. & Xiang, L., 2014. Effect of Mg2+ on hydrothermal formation of α-CaSO4· 0.5 H2O whiskers with high aspect ratios. *Langmuir,* 30**,** 9804-9810.

Jiang, G., Fu, H., Savino, K., Qian, J., Wu, Z. & Guan, B., 2013. Nonlattice Cation-SO42–Ion Pairs in Calcium Sulfate Hemihydrate Nucleation. *Crystal Growth & Design,* 13**,** 5128-5134.

Johnson, S. B., Scales, P. J. & Healy, T. W., 1999. The binding of monovalent electrolyte ions on α-alumina. I. Electroacoustic studies at high electrolyte concentrations. *Langmuir,* 15**,** 2836-2843.

Kerisit, S. & Parker, S. C., 2004. Free energy of adsorption of water and metal ions on the {1014} calcite surface. *Journal of the American Chemical Society,* 126**,** 10152-10161.

Kowacz, M., Putnis, C. & Putnis, A., 2007. The effect of cation: anion ratio in solution on the mechanism of barite growth at constant supersaturation: role of the desolvation process on the growth kinetics. *Geochimica et Cosmochimica Acta,* 71**,** 5168-5179.

Kruger, A., Focke, W. W., Kwela, Z. & Fowles, R., 2001. Effect of ionic impurities on the crystallization of gypsum in Wet-Process Phosphoric Acid. *Industrial & Engineering Chemistry Research,* 40**,** 1364-1369.

Kushnir, J., 1980. The coprecipitation of strontium, magnesium, sodium, potassium and chloride ions with gypsum. An experimental study. *Geochimica et Cosmochimica Acta,* 44**,** 1471-1482.

Kushnir, J., 1982. The partitioning of seawater cations during the transformation of gypsum to anhydrite. *Geochimica et Cosmochimica Acta,* 46**,** 433-446.

Leaist, D. G. & Goldik, J., 2001. Diffusion and ion association in concentrated solutions of aqueous lithium, sodium, and potassium sulfates. *Journal of solution chemistry,* 30**,** 103-118.

Liu, H., Bu, Y., Nazari, A., Sanjayan, J. G. & Shen, Z., 2016. Low elastic modulus and expansive well cement system: The application of gypsum microsphere. *Construction and Building Materials,* 106**,** 27-34.

Mao, X., Song, X., Lu, G., Sun, Y., Xu, Y. & Yu, J., 2014. Effects of Metal Ions on Crystal Morphology and Size of Calcium Sulfate Whiskers in Aqueous HCl Solutions. *Industrial & Engineering Chemistry Research,* 53**,** 17625-17635.

Massaro, F. R., Rubbo, M. & Aquilano, D., 2011. Theoretical equilibrium morphology of gypsum (CaSO4· 2H2O). 2. The stepped faces of the main [001] zone. *Crystal Growth & Design,* 11**,** 1607-1614.

Montagnino, D., Costa, E., Massaro, F., Artioli, G. & Aquilano, D., 2011. Growth morphology of gypsum in the presence of copolymers. *Crystal Research and Technology,* 46**,** 1010-1018.

Morales, J., Astilleros, J. M., Matesanz, E. & Fernández-Díaz, L., 2016. The Growth of Gypsum in the Presence of Hexavalent Chromium: A Multiscale Study. *Minerals,* 6**,** 22.

Naumkin, A. V., Kraut-Vass, Gaarenstroom, S. W. & Powell, C. J., 2012. *NIST X-ray Photoelectron Spectroscopy Database, Version 4.1 (National Institute of Standards and Technology, Gaithersburg, 2012)* [Online]. Available: http://srdata.nist.gov/xps/.

Ossorio, M., Van Driessche, A., Pérez, P. & García-Ruiz, J., 2014. The gypsum–anhydrite paradox revisited. *Chemical Geology,* 386**,** 16-21.

Parkhurst, D. L. & Appelo, C., 2013. Description of input and examples for PHREEQC version 3—a computer program for speciation, batch-reaction, one-dimensional transport, and inverse geochemical calculations. *US geological survey techniques and methods, book,* 6**,** 497.

Prisciandaro, M., Olivieri, E., Lancia, A. & Musmarra, D., 2012. PBTC as an Antiscalant for Gypsum Precipitation: Interfacial Tension and Activation Energy Estimation. *Industrial & Engineering Chemistry Research,* 51**,** 12844-12851.

Prywer, J., 2006. Effect of supersaturation on evolution of crystal faces—theoretical analysis. *Journal of crystal growth,* 289**,** 630-638.

Rabizadeh, T., Peacock, C. L. & Benning, L. G., 2014. Carboxylic acids: effective inhibitors for calcium sulfate precipitation? *Mineralogical Magazine,* 78**,** 1465-1472.

Rahnemaie, R., Hiemstra, T. & van Riemsdijk, W. H., 2006. A new surface structural approach to ion adsorption: Tracing the location of electrolyte ions. *Journal of colloid and interface science,* 293**,** 312-321.

Reardon, E., 1975. Dissociation constants of some monovalent sulfate ion pairs at 25. deg. from stoichiometric activity coefficients. *The Journal of Physical Chemistry,* 79**,** 422-425.

Sakuma, H. & Kawamura, K., 2011. Structure and dynamics of water on Li+-, Na+-, K+-, Cs+-, H 3 O+-exchanged muscovite surfaces: a molecular dynamics study. *Geochimica et Cosmochimica Acta,* 75**,** 63-81.

Salopek, B., Krasić, D. & Filipović, S., 1992. *Measurement and application of zeta-potential,* Rudarsko-geološko-naftni fakultet.

Sayan, P., Titiz- Sargut, S. & Avcı, B., 2007. Effect of trace metals on reactive crystallization of gypsum. *Crystal Research and Technology,* 42**,** 961-970.

Schmidt, C. & Ulrich, J., 2012. Morphology prediction of crystals grown in the presence of impurities and solvents—an evaluation of the state of the art. *Journal of Crystal Growth,* 353**,** 168-173.

Singh, N. & Middendorf, B., 2007. Calcium sulphate hemihydrate hydration leading to gypsum crystallization. *Progress in Crystal Growth and Characterization of Materials,* 53**,** 57-77.

Siokou, A., Kefalas, D. & Ntais, S., 2003. XPS study of hydrated MgCl 2 impregnated on flat SiO 2/Si (100) Mo and Au substrates. *Surface science,* 532**,** 472-477.

Sobolewski, A. L. & Domcke, W., 2005. Photochemistry of MCl (H 2 O) 4, M= H, Li, Na clusters: finite-size models of the photodetachment of the chloride anion in salt solutions. *Physical Chemistry Chemical Physics,* 7**,** 970-974.

Sparks, D. L., 2003. *Environmental soil chemistry,* Academic press.

Sun, J., Wang, L. & Yu, G., 2015. Effects of Na, Ca, Mg, and Al Chloride Salts on Dissolution and Phase Stability of Calcium Sulfate Dihydrate in Aqueous Solutions at 278.15 K to 308.15 K. *Journal of Chemical & Engineering Data,* 60**,** 2559-2566.

Sverjensky, D., Shock, E. & Helgeson, H., 1997. Prediction of the thermodynamic properties of aqueous metal complexes to 1000 C and 5 kb. *Geochimica et Cosmochimica Acta,* 61**,** 1359-1412.

Tanji, K. K., 1969. Solubility of gypsum in aqueous electrolytes as affected by ion association and ionic strengths up to 0.15 M and at 25. deg. *Environmental Science & Technology,* 3**,** 656-661.

van der Voort, E. & Hartman, P., 1991. The habit of gypsum and solvent interaction. *Journal of crystal growth,* 112**,** 445-450.

Wang, Y. W. & Meldrum, F. C., 2012. Additives stabilize calcium sulfate hemihydrate (bassanite) in solution. *Journal of Materials Chemistry,* 22**,** 22055-22062.

Yang, G., Kubota, N., Sha, Z., Louhi-Kultanen, M. & Wang, J., 2006. Crystal shape control by manipulating supersaturation in batch cooling crystallization. *Crystal growth & design,* 6**,** 2799-2803.

Yoshimura, T., Tamenori, Y., Suzuki, A., Kawahata, H., Iwasaki, N., Hasegawa, H., Nguyen, L. T., Kuroyanagi, A., Yamazaki, T. & Kuroda, J., 2016. Altervalent substitution of sodium for calcium in biogenic calcite and aragonite. *Geochimica et Cosmochimica Acta***,** In Press.

Zhang, Y., Yang, Z., Guo, D., Geng, H. & Dong, C., 2013. Effect of chloride salts and bicarbonate on solubility of CaSO 4 in aqueous solutions at 37 C. *Procedia Environmental Sciences,* 18**,** 84-91.

This chapter is in preparation for submission to the *Journal of Crystal Growth*.

Chapter 6. Comparative performance of biodegradable *vs.* poly(acrylic acid) antiscalants on calcium sulfate dihydrate crystallisation

Taher Rabizadeh[1*], David J. Morgan[2], Caroline L. Peacock[1], Liane G. Benning[1,3,4*]

1-Cohen Geochemistry Laboratory, School of Earth and Environment, University of Leeds, Leeds, LS2 9JT, United Kingdom

2- Cardiff Catalysis Institute, School of Chemistry, Cardiff University, Cardiff, CF10 3AT, United Kingdom

3- GFZ, German Research Centre for Geosciences, Telegrafenberg, 14473 Potsdam, Germany

4- Department of Earth Sciences, Free University of Berlin, 12249 Berlin, Germany

* Correspondence to: Taher Rabizadeh (eetr@leeds.ac.uk) and Liane G. Benning (Benning@gfz-potsdam.de)

Abstract

The effects that 20 ppm poly(epoxysuccinic acid) (PESA), poly(aspartic acid) (PASP) and two poly(acrylic acid) (PAA) compounds with molecular weights between ~ 2000 and ~100000, have on the crystallisation of gypsum were evaluated by *in situ* UV-VIS spectrophotometry. X-ray diffraction (XRD) and scanning electron microscopy (SEM) were utilised for phase and morphological studies, while the way these additives are associated with the final gypsum crystals was evaluated by X-ray photoelectron spectroscopy (XPS). The comparison showed that PASP performed far better than the other antiscalants and it completely inhibited the

formation of gypsum. Our data show that PAA with the low molecular weight increased the induction time (~ 80 times) and decreased the crystallisation kinetics greater than the larger molecular weight PAA. When the pH in the reacting solution was switched from ~ 4 to ~ 7, the efficiency of the low molecular weight PAA in inhibiting gypsum formation increased, while it resulted in an adverse effect on the performance of PAA with higher molecular weight by forming a "net-structure" in the solution. Turbidity plots revealed a depletion of additives from the crystallisation solution as a result of their surface adsorption. The XPS analysis further confirmed the surface adsorption of additives which caused changes in the morphology of the gypsum crystals.

Keywords: crystallisation; calcium sulfate dihydrate; biodegradable polymers; poly(acrylic acid); X-ray Photoelectron Spectroscopy.

6.1. Introduction

In many industrial processes that rely on water handling systems (e.g., oil and gas production, water desalination, water treatment, cooling systems, etc.), the formation of mineral scales such as gypsum mineral scale in pipes, filters and heat exchangers has detrimental consequences to process efficiency (Amjad and Demadis, 2015).

A number of methods have been proposed to inhibit or prevent the formation of calcium sulfate scales. Among them, the addition of inhibitors or antiscalants, is economical and more efficient than acid washing or mechanical cleaning (Crabtree et al., 1999; Olajire, 2015).

Industrial inhibitors are generally divided into nonpolymeric (e.g., hexametaphosphates, phosphonates; Ketrane et al., 2009) and polymeric (e.g., polycarboxylates; Al-Roomi and Hussain, 2015), and their application and effects on mineral scaling have been extensively studied (e.g., Amjad, 1996), but a molecular level understanding of the effects is still lacking. In addition, the post-reaction disposal of such additives

containing phosphorous and nitrogen leads to pollution of the environment and when such P and N containing compounds reach the water ways, they play a key role in eutrophication which can cause major ecological damage (Du et al., 2009; Nederlof et al., 2005). Therefore, the concept of "Green Chemistry" was proposed and scale inhibitors that are not detrimental to our environment have become a recent focus for inhibiting industrial scale formation (Belarbi et al., 2014).

Among green inhibitors, poly(epoxysuccinic acid) (PESA) and poly(aspartic acid) (PASP) are the most common and promising environmentally friendly polycarboxylate antiscalants. They are both highly biodegradabile and non-toxic (Liu et al., 2012), two of the main criteria of a 'green' inhibitor. They have both been extensively used in various industrial applications (Gao et al., 2015). However, to date, studies that evaluate the effects of different poly(carboxylic acid) inhibitors on calcium sulfate precipitation have primarily focused on changes in precipitation onset, or the effect of high temperatures (Prisciandaro et al., 2005; Senthilmurugan et al., 2010; Ling et al., 2012; Amjad and Koutsoukos, 2014). A mechanistic understanding of the effects that different poly(carboxylic acids), particularly the green ones, have on gypsum formation is still lacking. How these inhibitors operate, and how they can be further optimised to inhibit scale formation, is poorly understood. Indeed, in some cases, it is still unclear whether the commonly used conventional non-green polycarboxylic inhibitors (e.g., polyacrylic acid) can be replaced by greener equivalents.

To address these gaps in our knowledge, we present here results from a study on the effects of three common industrial poly(carboxylic acids) on the formation kinetics and phase morphologies of gypsum. We tested two green inhibitors (PESA and PASP) and a common non-green inhibitor (PAA) and derived a mechanistic understanding of the inhibition processes. At first we investigated the effects of four industrial inhibitors at pH ~ 7 which was close to the gypsum scaling conditions in different industries. Then, we studied the effects of molecular weight of two inhibitors on their inhibitory performance at pH ~ 4 and pH ~ 7. We document important differences in the crystallisation trends in the presence of the different

inhibitors, and demonstrate that the additives adsorb onto the surface of the newly forming gypsum crystals and change the shapes and sizes of resulting crystals. We also demonstrate the significant impact of the molecular weight of polymeric antiscalants on gypsum inhibition efficiencies and illustrate the potential of PESA and PASP as an adequate replacement for the environmentally unfriendly PAA antiscalant to prevent gypsum formation.

6.2. Experimental methods

Calcium sulfate crystallisation solutions were produced by mixing equal volumes of a 200 mM $CaCl_2 \cdot 2H_2O$ solution (100 % AnalaR Normapour VWR) and a 200 mM Na_2SO_4 solution (100 % AnalaR Normapour VWR) in a 1 L reactor at room temperature (21 ˚C) and under constant and continuous stirring.

Polyepoxysuccinic acid sodium salt with M_w ~ 400-1500 Da ($PESA_{<1.5K}$), polyaspartic acid sodium salt with M_w ~ 1000-5000 Da ($PASP_{<5K}$), provided by Shandong Taihe Water Treatment Technologies Company, and two polyacrylic acids (Sigma-Aldrich) with M_w ~ 2000 Da (PAA_{2K}) and ~ 100000 Da (PAA_{100K}) were added to the initial sodium sulfate solution at a concentration of 40 ppm. This was done prior to mixing of this stock solution with the calcium chloride stock solution. Therefore, there were 100 mM Ca^{2+}, 100 mM SO_4^{2-} and 20 ppm additive, initially, after mixing solutions. In all experiments, the pH of the mixed solutions was adjusted to pH to ~ 4 or ~ 7, with NaOH and / or HCl. Once mixed, all solutions were supersaturated with respect to gypsum as indicated by the saturation indices (as the logarithm of the ion activity product over the solubility product) calculated with the geochemical computer code PhreeqC 3.3.3 and using the LLNL database (Parkhurst and Appelo, 2013).

Changes in the mixed solutions were monitored by measuring the increase in absorbance using a UV-VIS spectrophotometer (Uvikon XL) at λ = 520 nm with the angle between the incident beam and detector of 180˚. The reactions were followed at room temperature for up to 300 minutes by measuring the absorbance of 3 mL aliquots taken from

the mixed solutions. Each experimental set was carried out in triplicate. The absorbance data is plotted as the normalised change in solution turbidity over 300 minutes.

At the end of each experiment, the solutions were quench-filtered (0.2 μm) under vacuum and the solids retrieved. These solids were characterised for their mineralogy using powder X-ray diffraction (XRD; Bruker D8 diffractometer; CuKα1; 2θ range 5-30°; 0.105° / step), while the morphology of the formed phases was imaged using a field emission gun scanning electron microscope (FEG-SEM, FEI Quanta 650, 5 kV). The sizes and shapes of the resulting crystals were evaluated using the ImageJ v. 1.49 software (Abràmoff et al., 2004).

Finally, to determine the nature of the surface interactions between the inhibitors and the gypsum end-products, we employed X-ray photoelectron spectroscopy (XPS) with a detection limit of 0.1 at. % (which is roughly 1ppth or 10^{19} atoms/cm^3). XPS spectra were acquired from the top 8-10 nm of gypsum crystals using a Kratos Axis Ultra-DLD spectrometer with a monochromatic Al K_α X-ray source (144 W) and analyser pass energies of 40 eV (high resolution scans). The base pressure during analysis was ca. 6×10^{-7} Pa. All data were referenced to the C (1s) signal at 284.8 eV and quantified using CasaXPS™ (Version 2.3.15) using elemental sensitivity factors supplied by the manufacturer.

6.3. Results

In the additive-free experiments at either pH ~ 4 or pH ~ 7, the solution became turbid after ~ 30 seconds (induction time) and it took ~ 30 minutes to reach 100 % turbidity (Figure 6.1, black data points). However, the addition of the inhibitors at pH ~ 7 affected the induction times and the time to reach a maximum turbidity plateau. In the presence of $PESA_{<1.5K}$, the induction time increased 3 fold (to ~ 90 seconds) and it took ~ 90 minutes reach 100% turbidity (Figure 6.1, red data points). In contrary, the presence of PAA_{100K} actually accelerated the onset of turbidity, with first turbidity appearing after ~ 10 seconds. However, only a small increase in total turbidity was reached after which the turbidity remained supressed up to ~ 40 minutes. Only in a second stage did the turbidity start to increase again

reaching 100 % within the following ~ 30 minutes with a slope similar to the slope of the turbidity development in the additive-free solution (Figure 6.1, blue data points). Using the lower molecular weight additive, PAA_{2K} dramatically increased the induction time (~ 80 fold, to ~ 40 minutes) and in addition the slope of the turbidity curve also decreased. Yet, the turbidity continued to only gradually increase and it did not reach 100 % even after 300 minutes (Figure 6.1, magenta data points). The most noticeable effect was observed in the presence of $PASP_{<5K}$, where no change in turbidity were noticeable even after 300 minutes (Figure 6.1, olive data points). The overall order for inhibition effectiveness was therefore $PESA_{<1.5K} < PAA_{100K} < PAA_{2K} < PASP_{<5K}$.

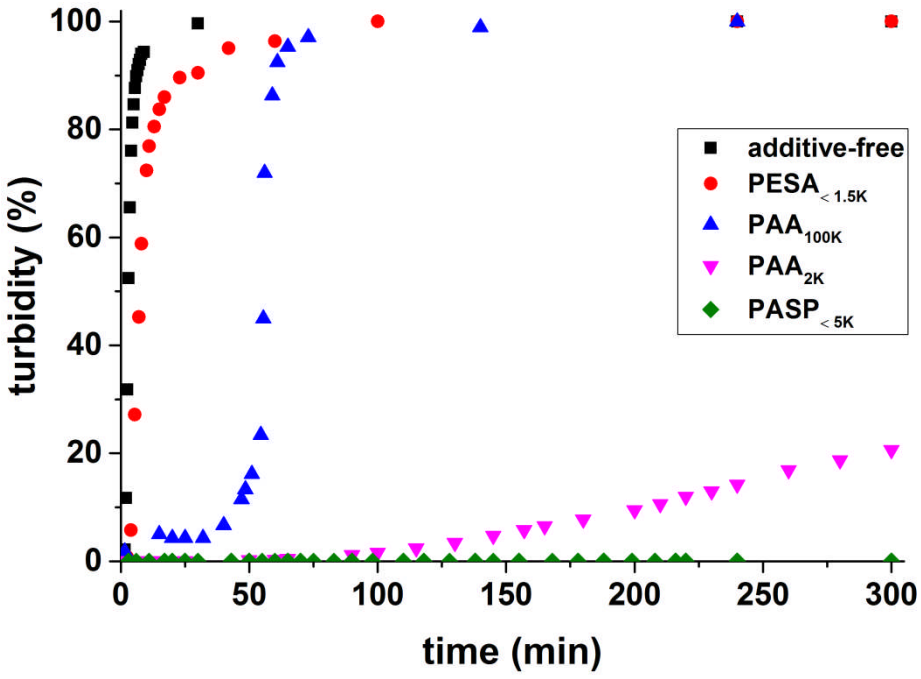

Figure 6.1.The effect of adding 20 ppm $PESA_{<1.5K}$, PAA_{100K}, PAA_{2K} or $PASP_{<5K}$ at pH ~ 7 on the development of solution turbidity compared to the additive-free gypsum crystallisation.

The effects of PAA_{100K} and PAA_{2K} on the onset and the development of turbidity is also pH dependent (Figure 6.2). At pH ~ 4, with $PAA_{100K,}$ the results show that in contrast to the data from pH ~ 7 (Figure 6.1), the onset of turbidity was the same as that in the additive-free system (~ 30 seconds). However, the subsequent development of the turbidity was slower and

followed a different trend than the additive-free and PAA_{100K} at pH ~ 7 systems (Figure 6.2, black *vs.* blue *vs.* orange data points). Specifically, at pH ~ 4 the turbidity remained at a constant ~ 2% for ~ 50 minutes, after which within the next ~ 70 minutes it increased slowly but exponentially until reaching ~ 50%. After this point (~ 130 minutes), the turbidity abruptly increased and reached a plateau within the next ~ 10 minutes with a slope similar to the slope of the turbidity development in the additive-free system (~ 140 minutes after onset). Comparing the behaviour of the PAA_{100K} as a function of pH indicates that it is a more effective inhibitor at pH ~ 4 than ~ 7. On the other hand, for PAA_{2K} at pH ~ 4 the onset of turbidity was faster and developed more quickly than at pH ~7. Specifically, the first change in turbidity was measured after ~ 25 minutes (in comparison to the induction time at pH ~7 and additive-free experiments of ~ 40 minutes and ~ 30 seconds, respectively). Subsequently, the turbidity increased moderately and exponentially for the next ~ 210 minutes (green points in Figure 6.2 showing turbidity of ~ 60 % at ~ 235 minutes). In the final stage the turbidity then sharply increased and levelled off after ~ 255 minutes with a slope similar to the slope of the turbidity development in the additive-free system (Figure 6.2, green data points). These results indicate that PAA_{2K} is a more effective inhibitor at pH ~ 7.

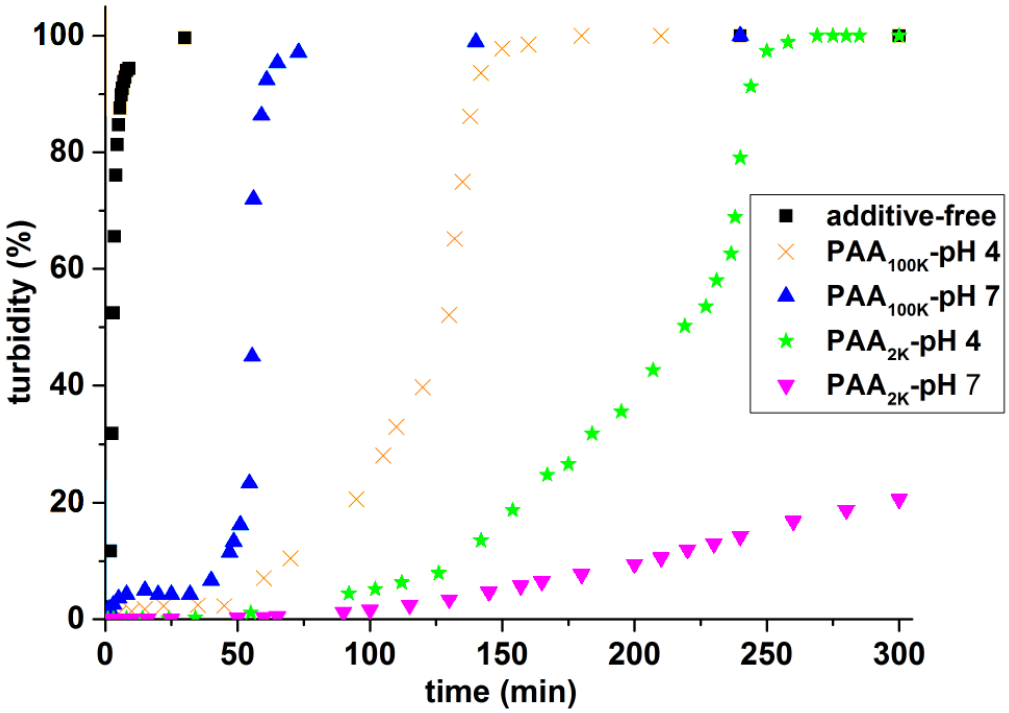

Figure 6.2.The effect of 20 ppm PAA_{2K} and PAA_{100K} on the development of turbidity at pH of ~ 4 and ~ 7. Note that because of the fast turbidity development, the turbidity plots of the additive-free system at either pH ~ 4 or ~ 7 were similar.

To obtain further insights into the role of the additives in inhibiting gypsum crystallisation, the atomic composition of the topmost surface layers of the as-formed gypsum crystals precipitated from the additive-free and the 20 ppm PAA_{2K} amended samples at pH ~ 7 were characterised by XPS analysis for C1s (Figure 6.3). The C1s envelope could be deconvoluted into three distinct peaks of C-C bonds, C–O–C functional groups and ester (–COOR) groups.

In the additive-free sample, two main groups of C-C bonds at 284.7 eV and C–O–C functional groups at 286.3 eV were evident. In contrast, in the PAA_{2K} amended sample two functional groups of C-C and C–O–C together with remarkably COOR were detected at 284.6 eV, 285.5 eV, and 288.3 eV, respectively.

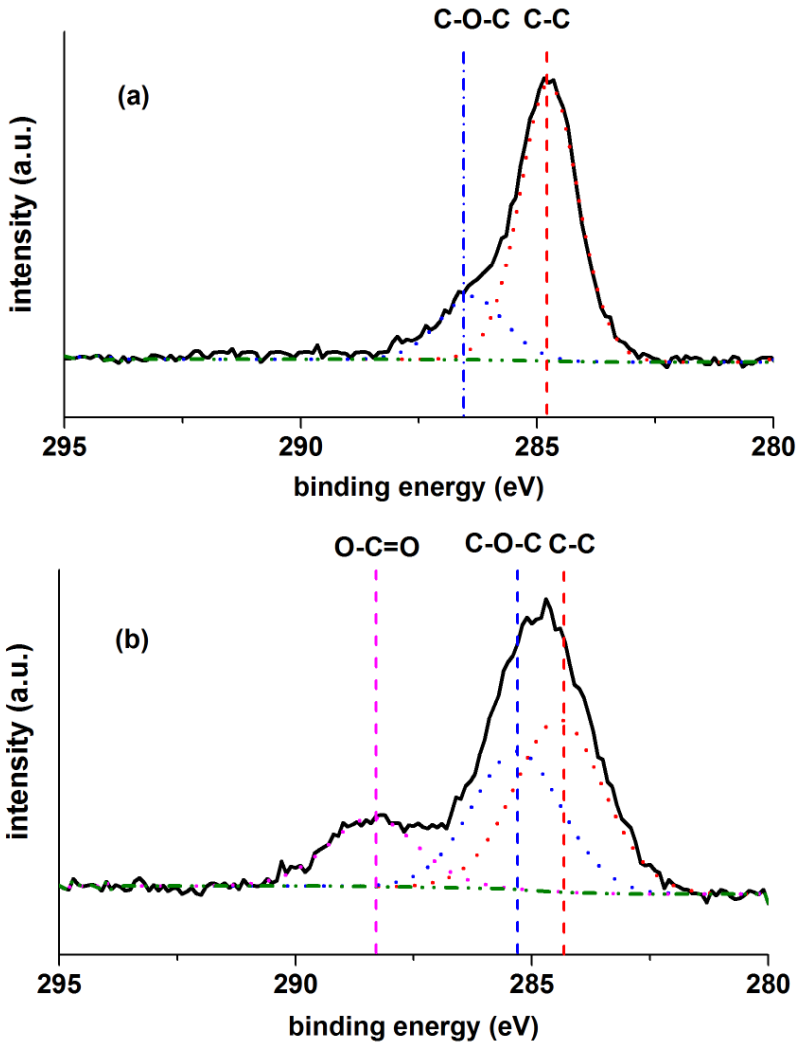

Figure 6.3.XPS spectra for gypsum crystals obtained from (a) additive-free; (b) 20 ppm PAA_{2K} solution at pH ~ 7 after 300 minutes; the individual contributions to the fitted envelope of different functional groups are represented with dotted lines.

Morphological changes of gypsum crystals that formed during growth from the additive-free and inhibitor amended solutions were characterised by SEM (Figure 6.4). The gypsum crystals that formed in the additive-free system were mostly large and thin twin crystals (Figure 6.4 a). The crystals precipitated in the presence of 20 ppm $PESA_{<1.5K}$ and PAA_{100K} at pH ~ 7 were similar to those in the additive-free system (Figure 6.4 b, and d respectively). In contrast, adding 20 ppm of PAA_{100K} at pH ~ 4 modified the morphology of the gypsum crystals into small irregular particles (Figure 6.4 c). The most profound effect on gypsum crystal morphology and size was observed when PAA_{2K} was used as an inhibitor. At pH ~ 4,

relatively small but blocky crystals of sizes ranging between 2-10 µm (Figure 6.4 e), contrasted to loose, tiny crystals with a size range of 20 nm to 5 µm at pH ~ 7 (Figure 6.4 f).

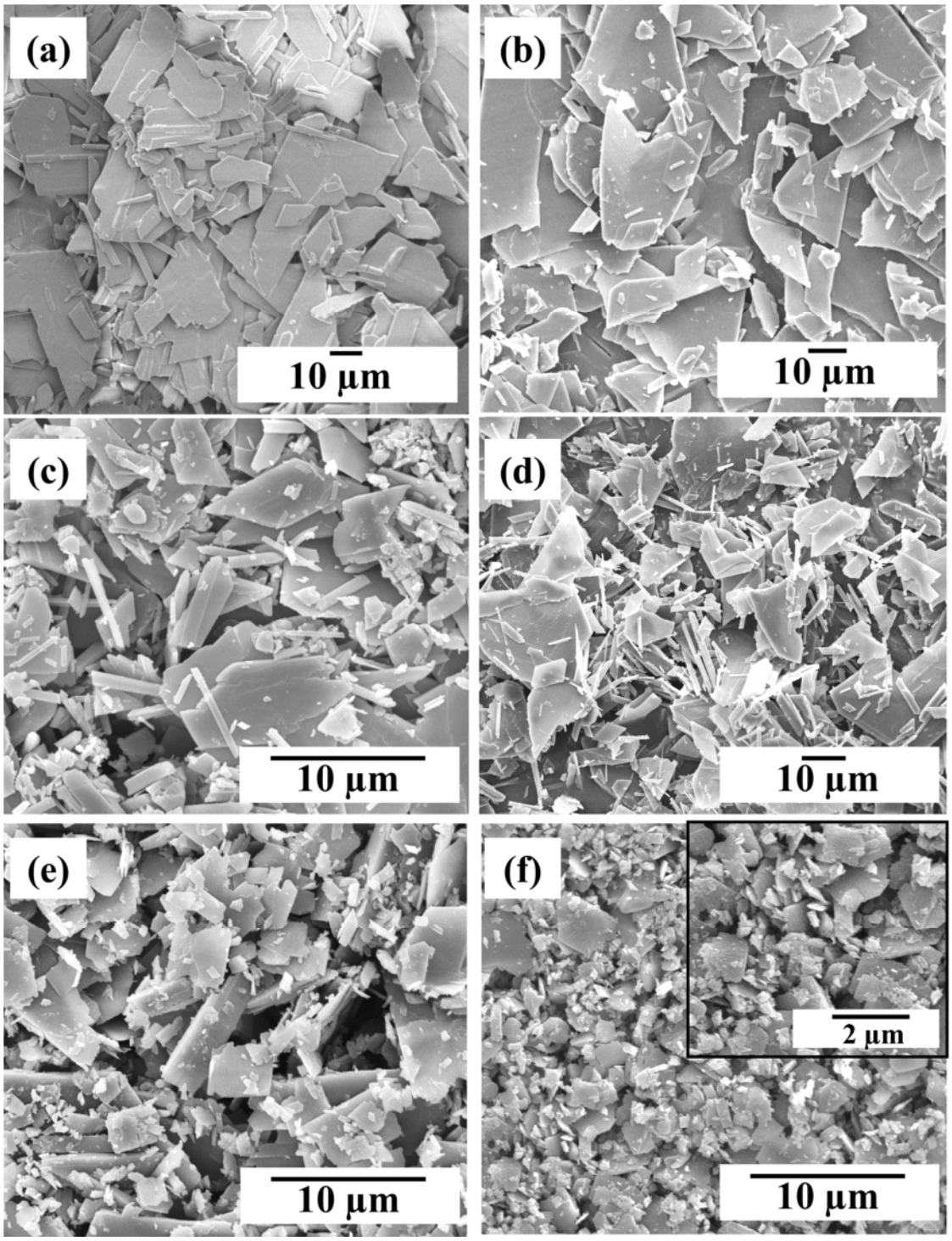

Figure 6.4.SEM micrograph of gypsum crystals collected after 300 minutes; (a) additive-free at pH ~ 7; (b) 20 ppm PESA at pH ~ 7; (c) 20 ppm PAA_{100K} at pH ~ 4; (d) 20 ppm PAA_{100K} at pH ~ 7; (e) 20 ppm PAA_{2K} at pH ~ 4; (f) 20 ppm PAA_{2K} at pH ~ 7; note that no gypsum crystals precipitated from solutions containing 20 ppm $PASP_{<5K}$ at pH ~ 7 (see Figure 6.1).

6.4. Discussion

Measuring turbidity and estimating induction times in the absence and presence of additives is one of the most common methods of evaluating the efficiency of antiscalants in delaying the nucleation and growth of sparingly soluble scale minerals. Our turbidity measurements (Figure 6.1) revealed that at equal concentrations of 20 ppm, among the three polymers tested, $PASP_{<5K}$ increased the induction time and decreased the slope of turbidity curve more than $PESA_{<1.5K}$ and compared to the two PAA polymers. Thus, $PASP_{<5K}$ is inherently a better gypsum nucleation and growth inhibitor.

The scale inhibitors are also classified as “nucleation” and “growth” inhibitors (Amjad and Demadis, 2015). It can be seen in Figure 6.1 that no gypsum crystal nucleated in the presence of the $PASP_{<5K}$ (no turbidity occurred), therefore this inhibitor can be considered as a nucleating inhibitor. Whilst, in the presence PESA and PAA, the gypsum crystals nucleated (an increase in turbidity) and just their growth was modified which was reflected by a decrease in the slope of the turbidity graphs. Hence, PESA and PAA can be classified as growth inhibitors. However, this classification is not absolute and depends on the concentration of the inhibitors or the experimental conditions because for example at lower $PASP_{<5K}$ concentration (e.g., 0-10 ppm) gypsum might nucleate and just its growth may be inhibited which will make the $PASP_{<5K}$ a growth inhibitor.

Furthermore, the turbidity graphs in this study developed with different trends than the turbidity graphs reported in our previous studies (i.e., Rabizadeh et al., 2014; Rabizadeh et al., 2017). This could be because of some different mechanisms by which the additives affected the gypsum crystallisation.

The reasons behind these observations are linked to type and conformation of active functional groups, the molecular structure, and molecular weight of the polyelectrolytes together with the pH of the reacting solutions. Some of these mechanisms are discussed below in relation to our data.

It is well-known that polymeric additives can prevent gypsum scale formation by different mechanisms, such as through dispersing scale minerals, adsorbing onto scale mineral surfaces, and by sequestration or chelation of the key scale mineral ions in the reacting solution (e.g., Lioliou et al., 2006). In our experiments, the COO^- functional groups of the polymeric additives retarded gypsum crystallisation by chelation with Ca^{2+} ions which decreased the activity of free Ca^{2+}, and therefore $CaSO_4^0$ ion pairs (Sun et al., 2015). On the other hand, deprotonated COO^- groups of polycarboxylates can also adsorb onto the growing crystal surfaces by binding to Ca^{2+} (surface adsorption) (Wang et al., 2015).

Calcium ions in gypsum structure have high hydration energy therefore they are highly shielded by water molecules, either the structural water molecule or the surrounding solution (Weijnen and Van Rosmalen, 1986). Furthermore, it has been suggested that gypsum crystals have negative surface charge over the pH ranges of this study (above pH ~ 2) (e.g.,Weijnen et al., 1987). Therefore, it implies that carboxylic functional groups did not adsorb onto the gypsum crystals via electrostatic interaction (physisorption) but their adsorption was by an irreversible chemisorption mechanism called “ligand-exchange” mechanism (also known as “specific adsorption” or “coordination adsorption”), during which the carboxylic functional groups replace the hydroxyl groups linked to the Ca^{2+} ions (Zhang and Yu, 1997). Similarly, the negatively charged phosphonate bonding to the calcium ions of the gypsum structure by substituting the water molecules of the hydrated calcium ions in a process called “calcium-phosphonate interaction” has been proposed (Akyol et al., 2009).The adsorption of anions onto the hydrated minerals (e.g., α-alumina; Zarbakhsh et al., 2013) via ligand exchange mechanism has also been documented.

The effectiveness of polycarboxylic additives in inhibiting gypsum crystallisation is therefore controlled by the solution pH (because the speciation of the carboxylic groups is highly pH dependent) and the molecular weight of the additives (which governs the number and conformation of the carboxylic groups).

At pH ~ 7 the carboxylic functional groups of all three tested additives are largely deprontonated ($PASP_{<5K}$: pK 3.25, 4.25 (Kokufuta et al., 1977); $PESA_{<1.5K}$: pK 4.68, 4.92 (Zhang et al., 2008); PAA: pK 4.9 (De Giglio et al., 2007)) but $PASP_{<5K}$ has a higher molecular weight than $PESA_{<1.5K}$ and PAA_{2K} and therefore provides a greater number of deprotonated carboxylic groups to inhibit gypsum formation by complexing Ca^{2+} (Figure 6.1). This agrees with Liu et al. (2011) who reported that PASP is a highly effective inhibitor of calcium carbonate formation.

The effectiveness of PAA as an inhibitor can be explained by considering the fact that PAA is a weak polyelectrolyte and its structure is pH-responsive and undergoes conformational changes that are also dependent on pH and molecular weight. These aid to increase the inhibition of gypsum crystallisation in the presence of PAA_{2K} from pH ~ 4 to ~ 7 (Figure 6.2). Upon PAA addition into solution, an acidic solution of uncharged polymers with a highly coiled structure is produced, as a result of extensive intermolecular hydrogen bonding. With increasing pH, the carboxylic groups are deprotonated and a high amount of negative charge densities are produced, and the polymer chains become extended as a result of electrostatic repulsion (Mountrichas and Pispas, 2006). These extended polymer chains are then better able to complex with Ca^{2+} in solution or on the crystal surfaces (stronger surface adsorption). Indeed, this feature of PAA has been successfully exploited to disperse nanoparticles (e.g., carbon nanotube) at high pH (e.g., Grunlan et al., 2006).

However, comparing the efficiency of PAA_{100K} with PAA_{2K} at constant pH of ~ 4, shows that as PAA increases in molecular weight, its ability to complex Ca^{2+} and thus inhibit gypsum crystallisation decreases. At higher molecular weight, it might become more difficult for PAA_{100K} to stretch its polymer chains into an extended configuration (Laguecir et al., 2006) resulting in more loops and tails in the solution and on the crystal surface for complexation of Ca^{2+} (Amjad and Koutsoukos, 2014; Liufu et al., 2005).

For PAA_{100K} increasing the pH from ~ 4 to ~ 7, also decreased the inhibition of gypsum formation (Figure 6.2). At pH ~ 7, upon mixing the sodium sulfate solution

containing PAA_{100K} with the calcium chloride solution, some Ca^{2+} ions link the extended polymer chains to each other and build a "net-like" structure which decreases the efficiency of the inhibitor, makes the solution slightly turbid and prevents the polymer to adsorb onto the nucleating and growing crystals. As a result, by losing the efficiency of the inhibitor, gypsum crystals can easily nucleate and grow (due to presence of the excess Ca^{2+} ions which did not attend in forming the "net-structure" and sulfate ions). However, at pH ~ 4, Ca^{2+} ions do not make a "net-structure" with the PAA_{100K} with a coiled configuration, therefore the coiled PAA_{100K} can adsorb onto the nucleating and growing gypsum crystals. In other words, despite an extended configuration and an abundance of deprotonated carboxylic groups for complexation with Ca^{2+}, high molecular weight PAA in an extended state might form complex "net-like" structures with Ca^{2+} which are actually less effective at chelating Ca^{2+} than PAA in a coiled, un-extended state, and also less able to adsorption to the growing gypsum surfaces (Figure 6.4). Indeed, the role of Ca^{2+} in cross-linking PAA polymers and alginates and forming a net-like structure (hydrogels) has been reported also for calcium carbonates (Rianasari et al., 2016; Wan et al., 2008).

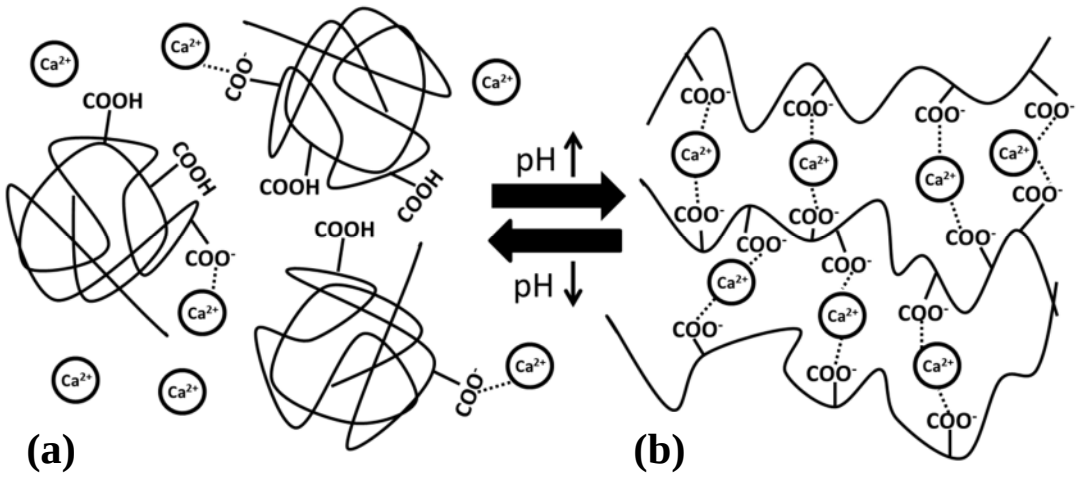

Figure 6.5.Schematic illustration of the effect of pH on the conformation of PAA_{100K}; (a) PAA_{100K} molecules at pH ~ 4 are only minimally deprotonated and randomly coiled; (b) at pH ~ 7 despite being deprotonated and in their extended conformation, PAA_{100K} molecules form a "net-structure" in the presence of Ca^{2+}; this prevents further Ca^{2+} complexation and attachment of the PAA_{100K} molecules to the crystal surfaces.

It is also worth mentioning that the abrupt increase in turbidity in the presence of PAA_{2K} at pH ~ 4 (Figure 6.2; turbidity of ~ 60 %; ~ 235 minutes) and PAA_{100K} at pH ~ 4 (Figure 6.2; turbidity of ~ 50 %; ~ 130 minutes) could be attributed to a depletion of the inhibitors from the reacting solution due to surface adsorption via a ligand exchange mechanism during the gypsum growth. That means, as the turbidity increases in the mixing solution, nucleation and growth of a new phase occurred and the carboxylic functional groups strongly bonded onto the new surfaces and therefore their concentration gradually decreases in solution. This continued over time until at certain point bulk gypsum crystals easily nucleated and grew, as mirrored by the abrupt increase in the turbidity (Figure 6.2).

Our assertion that surface absorption plays a major role is supported by our XPS analysis which confirmed the surface adsorption of the additives. The variation in C1s chemical states, especially comparing the O-C=O binding energy and its peak area (Figure 6.3) with the additive-free gypsum crystals helped assess the association between the polymers and the surface of gypsum crystals. In the absence of additive, no O-C=O peak was detected but in the presence of PAA_{2K} at pH ~ 7, a significant O-C=O peak was measured which made up 18% of the total C 1s peak area. The presence of O-C=O peak can also be due to the adventurous carbon contamination (Naumkin et al., 2012). However, here we attributed it to the surface adsorption of PAA_{2K} because O-C=O was not detected on the surface of the additive-free sample. Similarly, the occurrence of the O-C=O peak on the PAA modified hydroxyapatite powders was reported (Shen et al., 2011).

The inhibitors also changed the morphology and size of the precipitated gypsum crystals and we ascribe this to the surface adsorption of polymers (Figure 6.4). It has been demonstrated that the antiscalants with high surface binding are effective gypsum inhibitors (Ling et al., 2012).

In comparison to the additive-free gypsum crystals, PESA did not cause any morphological changes, which was due to the low molecular weight and lack of surface adsorption on the fast growing gypsum crystals (Figure 6.4 b). Interestingly, morphological changes as a result of

adsorption of PESA on calcium oxalate has been previously observed (Zhang et al., 2015) but for gypsum this effect was less prominent (Figure 6.4 b). It is also worth mentioning that the morphology of the gypsum crystals formed in the absence of additives (irregular twinned crystals) was different than the morphology of the additive-free gypsum crystals (needle shaped crystals) that I have also reported in our previous studies (i.e., Rabizadeh et al., 2014; Rabizadeh et al., 2017). The change in shape is likely due to the higher supersaturation of the solution (0.84 *vs.* 0.55) and the larger volume of the crystallisation solution (1 litre *vs.* 2 ml). However, investigating the effects of the supersaturation and the solution volume on gypsum crystallisation was out of the scope of this study.

At pH ~ 4, both PAA_{100K} and PAA_{2K} were present in solution in a coiled conformation, but because of higher steric hindrance between coils, the larger molecular weight additive exhibited very limited adsorption and this resulted in less surface modification (Figure 6.4 c) compared to the effects observed at the same condition with PAA_{2K} (Figure 6.4 e). At pH ~ 7, the "net-like-structure" of PAA_{100K} decreased the available of monomers for surface adsorption, and thus the morphologies (Figure 6.4 d) remained similar to those in the additive-free system (Figure 6.4 a). In contrast, at pH ~7, PAA_{2K} with a flat configuration and higher deprotonation state is highly adsorbed (Figure 6.3) and this led to the formation of much smaller crystals (Figure 6.4 f) compared to the non-additive or PAA_{100K} systems. It is also noteworthy that in Figure 6.4 (c-e) two different crystal morphologies are visible. A combination of few, thin needle crystals ate visible among the big twinned gypsum crystals. However, in this study just the end-products of the crystallization reaction were evaluated and there is not enough evidence to determine if the formation and growth process of each morphology and size range based on the turbidity graphs is a continuum. Figure 6.6 schematically illustrates the effects of pH on PAA_{2K} confirmation and its adsorption. Similar gypsum morphology modification in the presence of water soluble polymers (e.g., 5 ppm acrylic acid-allylpolyethoxy maleic carboxylate) have been reported (Cao et al., 2014). The adsorption of PAA on the other minerals such as barium sulfate (Li et al., 2016) and calcium

carbonate (Ouhenia et al., 2008) which caused crystal morphology deformation has also been observed.

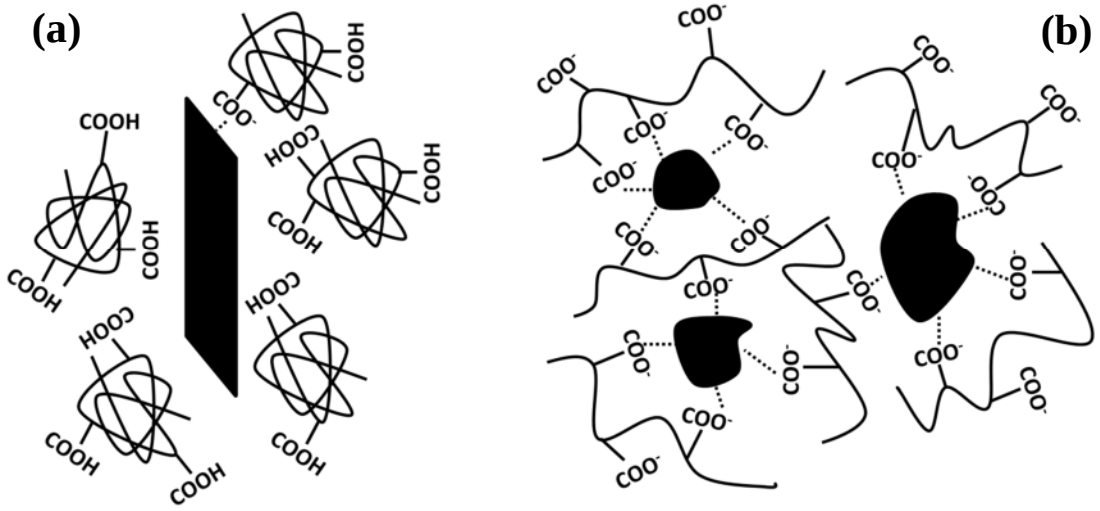

Figure 6.6.A schematic showing the change in gypsum microstructure because of PAA_{2K} conformation and its deprotonation; (a) the PAA_{2K} molecules are randomly coiled at pH ~ 4 and had limited adsorption on gypsum crystals; (b) deprotonated PAA_{2K} molecules are in their extended conformation at pH ~ 7, deformed the gypsum crystals and prevented the growth of tiny crystals.

The current study shows the potential of the green polycarboxylic type inhibitors as an efficient additive to replace the non-biodegradable polycarboxylic inhibitors in reducing or even preventing gypsum formation. Furthermore, the molecular weight of the polymeric inhibitors is an important factor which has to be considered when choosing an effective antiscalant. If the green inhibitors are used in an industrial fluid handling system (where gypsum scale minerals are a problem) they can substantially retard nucleation and growth even at low concentrations. The green inhibitors can reduce clogging of filters by gypsum, but the size effect may also prevent adherence to pipe surfaces.

6.5. Conclusion

With this study, we documented the effects that polycarboxylic antiscalants have on the nucleation and growth kinetics of gypsum crystals and illustrated the potential of biodegradable PASP and PESA to replace the non-biodegradable PAA additives. 20 ppm of

additives affected gypsum formation with the other of (PESA < PAA < PASP) which reveals, among tested additives, PASP performed far better and completely inhibited the gypsum crystallisation. Comparing the efficiency of PAA_{2K} and PAA_{100K}, showed that PAA with low molecular weight increased the induction time and decreased the crystallisation kinetics greater than the PAA with high molecular weight. The increase in pH of the solution from ~ 4 to ~ 7, had a positive effect on the efficiency of the PAA_{2K} while it decreased the efficiency of PAA_{100K} due to a "net-structure" formation in the presence of PAA_{100K}. Combination of XPS and turbidity plots revealed the depletion of additives from the crystallisation solution as a result of their surface adsorption which caused changes in the morphology of the gypsum crystals.

Acknowledgement

This study was supported by a Marie Curie grant from the European Commission in the framework of the MINSC ITN (Initial Training Research network), Project number 290040. The authors would like to thank the Cohen Laboratories in the School of Earth and Environment, and the Leeds Electron Microscopy and Spectroscopy Centre (LEMAS) for help and access to instruments during the course of this study.

6.6. References

Abràmoff, M. D., Magalhães, P. J. & Ram, S. J., 2004. Image processing with ImageJ. *Biophotonics international,* 11**,** 36-42.

Akyol, E., Öner, M., Barouda, E. & Demadis, K. D., 2009. Systematic Structural Determinants of the Effects of Tetraphosphonates on Gypsum Crystallization. *Crystal Growth & Design,* 9**,** 5145-5154.

Al-Roomi, Y. M. & Hussain, K. F., 2015. Application and evaluation of novel acrylic based CaSO 4 inhibitors for pipes. *Desalination,* 355**,** 33-44.

Amjad, Z., Scale inhibition in desalination applications: an overview. Corrosion, NACE, 1996 Huston (TX). 96-230.

Amjad, Z. & Demadis, K. D., 2015. *Mineral Scales and Deposits: Scientific and Technological Approaches*, Elsevier.

Amjad, Z. & Koutsoukos, P. G., 2014. Evaluation of maleic acid based polymers as scale inhibitors and dispersants for industrial water applications. *Desalination,* 335**,** 55-63.

Belarbi, Z., Gamby, J., Makhloufi, L., Sotta, B. & Tribollet, B., 2014. Inhibition of calcium carbonate precipitation by aqueous extract of Paronychia argentea. *Journal of Crystal Growth,* 386**,** 208-214.

Cao, K., Zhou, Y., Liu, G., Wang, H. & Sun, W., 2014. Preparation and properties of a polyether- based polycarboxylate as an antiscalant for gypsum. *Journal of Applied Polymer Science,* 131**,** 1-9.

Crabtree, M., Eslinger, D., Fletcher, P., Miller, M., Johnson, A. & King, G., 1999. Fighting scale—removal and prevention. *Oilfield Review,* 11**,** 30-45.

De Giglio, E., Cometa, S., Cioffi, N., Torsi, L. & Sabbatini, L., 2007. Analytical investigations of poly (acrylic acid) coatings electrodeposited on titanium-based implants: a versatile approach to biocompatibility enhancement. *Analytical and bioanalytical chemistry,* 389**,** 2055-2063.

Du, K., Zhou, Y., Wang, L. & Wang, Y., 2009. Fluorescent- tagged no phosphate and nitrogen free calcium phosphate scale inhibitor for cooling water systems. *Journal of applied polymer science,* 113**,** 1966-1974.

Gao, Y., Fan, L., Ward, L. & Liu, Z., 2015. Synthesis of polyaspartic acid derivative and evaluation of its corrosion and scale inhibition performance in seawater utilization. *Desalination,* 365**,** 220-226.

Grunlan, J. C., Liu, L. & Kim, Y. S., 2006. Tunable single-walled carbon nanotube microstructure in the liquid and solid states using poly (acrylic acid). *Nano letters,* 6**,** 911-915.

Ketrane, R., Saidani, B., Gil, O., Leleyter, L. & Baraud, F., 2009. Efficiency of five scale inhibitors on calcium carbonate precipitation from hard water: effect of temperature and concentration. *Desalination,* 249**,** 1397-1404.

Kokufuta, E., Suzuki, S. & Harada, K., 1977. Potentiometric titration behavior of polyaspartic acid prepared by thermal polycondensation. *BioSystems,* 9**,** 211-214.

Laguecir, A., Ulrich, S., Labille, J., Fatin-Rouge, N., Stoll, S. & Buffle, J., 2006. Size and pH effect on electrical and conformational behavior of poly (acrylic acid): Simulation and experiment. *European polymer journal,* 42**,** 1135-1144.

Li, J., Liu, D., Jiang, H., Wang, J., Jing, X., Chen, R., Zhu, W., Han, S., Li, W. & Wei, H., 2016. Effects of polyacrylic acid additive on barium sulfate particle morphology. *Materials Chemistry and Physics,* 175**,** 180-187.

Ling, L., Zhou, Y., Huang, J., Yao, Q., Liu, G., Zhang, P., Sun, W. & Wu, W., 2012. Carboxylate-terminated double-hydrophilic block copolymer as an effective and environmental inhibitor in cooling water systems. *Desalination,* 304**,** 33-40.

Lioliou, M. G., Paraskeva, C. A., Koutsoukos, P. G. & Payatakes, A. C., 2006. Calcium sulfate precipitation in the presence of water-soluble polymers. *J Colloid Interface Sci,* 303**,** 164-70.

Liu, D., Dong, W., Li, F., Hui, F. & Lédion, J., 2012. Comparative performance of polyepoxysuccinic acid and polyaspartic acid on scaling inhibition by static and rapid controlled precipitation methods. *Desalination,* 304**,** 1-10.

Liu, Z., Sun, Y., Zhou, X., Wu, T., Tian, Y. & Wang, Y., 2011. Synthesis and scale inhibitor performance of polyaspartic acid. *Journal of Environmental Sciences,* 23**,** S153-S155.

Liufu, S., Xiao, H. & Li, Y., 2005. Adsorption of poly (acrylic acid) onto the surface of titanium dioxide and the colloidal stability of aqueous suspension. *Journal of Colloid and Interface Science,* 281**,** 155-163.

Mountrichas, G. & Pispas, S., 2006. Synthesis and pH responsive self-assembly of new double hydrophilic block copolymers. *Macromolecules,* 39**,** 4767-4774.

Naumkin, A. V., Kraut-Vass, Gaarenstroom, S. W. & Powell, C. J., 2012. *NIST X-ray Photoelectron Spectroscopy Database, Version 4.1 (National Institute of Standards and Technology, Gaithersburg, 2012)* [Online]. Available: http://srdata.nist.gov/xps/.

Nederlof, M., Van Paassen, J. & Jong, R., 2005. Nanofiltration concentrate disposal: experiences in The Netherlands. *Desalination,* 178**,** 303-312.

Olajire, A. A., 2015. A review of oilfield scale management technology for oil and gas production. *Journal of Petroleum Science and Engineering,* 135**,** 723-737.

Ouhenia, S., Chateigner, D., Belkhir, M., Guilmeau, E. & Krauss, C., 2008. Synthesis of calcium carbonate polymorphs in the presence of polyacrylic acid. *Journal of Crystal Growth,* 310**,** 2832-2841.

Parkhurst, D. L. & Appelo, C., 2013. Description of input and examples for PHREEQC version 3—a computer program for speciation, batch-reaction, one-dimensional transport, and inverse geochemical calculations. *US geological survey techniques and methods, book,* 6**,** 497.

Prisciandaro, M., Santucci, A., Lancia, A. & Musmarra, D., 2005. Role of Citric Acid in Delaying Gypsum Precipitation. *The Canadian Journal of Chemical Engineering,* 83**,** 586-592.

Rabizadeh, T., Peacock, C. L. & Benning, L. G., 2014. Carboxylic acids: effective inhibitors for calcium sulfate precipitation? *Mineralogical Magazine,* 78**,** 1465-1472.

Rabizadeh, T., Stawski, T. M., Morgan, D. J., Peacock, C. L. & Benning, L. G., 2017. The effects of inorganic additives on the nucleation and growth kinetics of calcium sulfate dihydrate crystals. *Crystal Growth & Design,* 17**,** 582-589.

Rianasari, I., Benyettou, F., Sharma, S. K., Blanton, T., Kirmizialtin, S. & Jagannathan, R., 2016. A Chemical Template for Synthesis of Molecular Sheets of Calcium Carbonate. *Scientific reports,* 6.

Senthilmurugan, B., Ghosh, B., Kundu, S. S., Haroun, M. & Kameshwari, B., 2010. Maleic acid based scale inhibitors for calcium sulfate scale inhibition in high temperature application. *Journal of Petroleum Science and Engineering,* 75**,** 189-195.

Shen, D., Fang, L., Chen, X. & Tang, Y., 2011. Structure and properties of polyacrylic acid modified hydroxyapatite/liquid crystal polymer composite. *Journal of Reinforced Plastics and Composites,* 30**,** 1155-1163.

Sun, X., Zhang, J., Yin, C., Zhang, J. & Han, J., 2015. Poly (aspartic acid)–tryptophan grafted copolymer and its scale- inhibition performance. *Journal of Applied Polymer Science,* 132**,** 1-8.

Wan, L. Q., Jiang, J., Arnold, D. E., Guo, X. E., Lu, H. H. & Mow, V. C., 2008. Calcium concentration effects on the mechanical and biochemical properties of chondrocyte-alginate constructs. *Cellular and molecular bioengineering,* 1**,** 93-102.

Wang, H., Liu, G., Huang, J., Zhou, Y., Yao, Q., Ma, S., Cao, K., Liu, Y., Wu, W. & Sun, W., 2015. Performance of an environmentally friendly anti-scalant in CaSO4 scale inhibition. *Desalination and Water Treatment,* 53**,** 8-14.

Weijnen, M., Van der Leeden, M. & Rosmalen, G., 1987. Influence of the molecular structure of phosphonate inhibitors on various aspects of barite and gypsum crystallization. *Geochemistry of the Earth's surface and Mineral formation***,** 753-76.

Weijnen, M. & Van Rosmalen, G., 1986. Adsorption of phosphonates on gypsum crystals. *Journal of Crystal Growth,* 79**,** 157-168.

Zarbakhsh, A., Lee, S., Welbourn, R., Clarke, S., Skoda, M. & Clifton, L., 2013. Adsorption of sodium hexanoate on a-alumina. *Journal of Colloid and Interface Science*.

Zhang, G. & Yu, T., 1997. Coordination adsorption of anions. *In:* Yu, T. (ed.) *Chemistry of Variable Charge Soils. Oxford Univ. Press, New York.* Oxford University Press.

Zhang, L., Zhu, Z., Qiu, Y., Zhang, R. & Zhao, J., 2008. Determination of the dissociation constants of polyepoxysuccinic acid. *Frontiers of Environmental Science & Engineering in China,* 2**,** 505-508.

Zhang, Y., Tang, Y., Xu, J., Zhang, D., Lu, G. & Jing, W., 2015. Modulation of polyepoxysuccinic acid on crystallization of calcium oxalate. *Journal of Solid State Chemistry,* 231**,** 7-12.

This chapter is in preparation for submission to *Langmuir*.

Chapter 7. Investigating the effects of phosphonate inhibitors on the nucleation and growth kinetics of calcium sulfate dihydrate crystals

Taher Rabizadeh[1*], David J. Morgan[2], Caroline L. Peacock[1], Liane G. Benning[1,3,4*]

1-Cohen Geochemistry Laboratory, School of Earth and Environment, University of Leeds, Leeds, LS2 9JT, United Kingdom

2- Cardiff Catalysis Institute, School of Chemistry, Cardiff University, Cardiff, CF10 3AT, United Kingdom

3- GFZ, German Research Centre for Geosciences, Telegrafenberg, 14473 Potsdam, Germany

4- Department of Earth Sciences, Free University of Berlin, 12249 Berlin, Germany

* Correspondence to: Taher Rabizadeh (eetr@leeds.ac.uk) and Liane G. Benning (Benning@gfz-potsdam.de)

Abstract

The effects of 20 ppm 1-Hydroxy Ethylidene-1,1-Diphosphonic Acid (HEDP), Amino Trimethylene Phosphonic Acid (ATMP), Polyamino Polyether Methylene Phosphonic Acid (PAPEMP), Diethylene Triamine Penta (Methylene Phosphonic Acid) (DTPMPA) and Bis(HexaMethylene Triamine Penta (Methylene Phosphonic Acid)) (BHMTPMPA) on the crystallisation of gypsum were evaluated by *in situ* UV-VIS spectrophotometry. Concentration variations of the additives during the crystallisation of gypsum together with surface or

structural associations between these additives and the end-product gypsum crystals were evaluated by inductively coupled plasma optical emission spectrometry (ICP-OES). X-ray diffraction (XRD) and scanning electron microscopy (SEM) were utilised for phase and morphological studies of the formed crystals, respectively. Furthermore, the surface composition of the final products was evaluated by X-ray photoelectron spectroscopy (XPS). Comparison between the additive-containing and additive-free experiments showed that BHMTPMPA performed far better than the other antiscalants by completely inhibiting crystallisation. Due to the chain length of the BHMTPMPA molecule, the crystallisation kinetics decreased to a larger extent than DTPMPA. The increase in pH of the solution from ~ 4 to ~ 7, had a positive effect on the efficiency of the phosphonates in inhibiting crystallisation. In some experiments, a sudden and sharp increase in turbidity plots was observed which could be because of depletion of additives from the crystallisation solution as a result of their surface adsorption and / or structural incorporation. Our results revealed that partially deprotonated phosphonate additives were strongly associated with gypsum crystals potentially taken up into the crystal matrix. Phosphonate additives altered the thin, twinned gypsum crystals into thick needles and this morphological modification was severe in the presence of PAPEMP and DTPMPA.

Keywords: crystallisation; calcium sulfate dihydrate; antiscalants; phosphonates; desorption; X-ray Photoelectron Spectroscopy.

7.1. Introduction

In different industries, inhibitors are added to the system to remove the mineral scales such as gypsum (Amjad and Demadis, 2015). Commonly used industrial inhibitors are generally divided into nonpolymeric (e.g., hexametaphosphates, phosphonates; Ketrane et al., 2009) and polymeric (e.g., poly(citric acid); Zhao et al., 2016) inhibitors, and their effects on mineral scaling have been extensively studied (Amjad and Demadis, 2015). However, a fundamental

understanding of how industrial inhibitors operate is slowly emerging and the operation and efficiency of phosphonate antiscalants, in particular, is still not clearly understood. With regard to the calcium sulfate scale system, studies that evaluate the effects of different phosphonate inhibitors on calcium sulfate precipitation have primarily focused on changes in the precipitation onset (Prisciandaro et al., 2006). While in other scale systems, studies that attempt to provide a more mechanistic understanding of the operation of phosphonate antiscalants still leave many unanswered questions; for example, in the calcite scale system, molecular modelling has shown that among phosphonate additives (e.g., HEDP and monophosphonates), just monophosphonates incorporate into the calcite structure (Ojo et al., 2002), while HEDP associates by interacting with the calcite surface or at step sites (Nygren et al., 1998). It is also not well-understood why the inhibitory efficiency of Diethylene Triamine Penta (Methylene Phosphonic Acid) (DTPMPA) on barite (Mavredaki et al., 2011) and calcite (Sousa and Bertran, 2014) scale formation is lower than that of the poly-phosphino carboxyllic acid (PPCA). Overall, a mechanistic understanding of the effects of different phosphonates on calcium sulfate scale formation is still lacking, and therefore how these inhibitors operate, interact or change the way calcium sulfate crystals form and how they can be further optimised to reduce or inhibit scale formation, is poorly understood.

To address these gaps in knowledge, we present results from a study where we assessed the effects of five industrial phosphonate antiscalants on the nucleation and growth kinetics of gypsum, as well as the morphology of gypsum crystals forming from supersaturated aqueous solutions. We followed the processes by combining analyses of both the reacting solution and the forming solids simultaneously and determined the mechanisms that control the way these antiscalants became associated with the growing gypsum crystals. For the first time, we quantify the different trends in the kinetics of gypsum crystallisation and demonstrate the surface adsorption and / or structural incorporation of the antiscalants using a combination of XPS and ICP-OES analyses. Our results show the significant impact of antiscalant functional group characteristics on the efficiency of the inhibitor in delaying

gypsum nucleation and growth. Furthermore, we document how this interaction also leads to a change in the resulting gypsum crystal morphologies.

7.2. Experimental methods

Calcium sulfate crystallisation solutions were produced by mixing equal volumes of a 200 mM $CaCl_2 \cdot 2H_2O$ solution (100 % AnalaR Normapour VWR) and a 200 mM Na_2SO_4 solution (100 % AnalaR Normapour; VWR) in a 1 L reactor at room temperature (21 ˚C) and under constant and continuous stirring.

1-Hydroxy Ethylidene-1,1-Diphosphonic Acid (HEDP), Amino Trimethylene Phosphonic Acid (ATMP), Polyamino Polyether Methylene Phosphonic Acid (PAPEMP), Diethylene Triamine Penta (Methylene Phosphonic Acid) (DTPMPA) and Bis(HexaMethylene Triamine Penta (Methylene Phosphonic Acid)) (BHMTPMPA) provided by Shandong Taihe Water Treatment Technologies Company were added to the initial sodium sulfate solution at a concentration of 10 ppm or 40 ppm prior to the addition of the calcium chloride solution. Therefore, there were 100 mM Ca^{2+}, 100 mM SO_4^{2-} and 5 ppm or 20 ppm additive initially after mixing solutions. In all experiments, the pH of the mixed solutions was adjusted to pH to ~ 4 or ~ 7, with NaOH and / or HCl. Once mixed, all solutions were supersaturated with respect to gypsum as indicated by the saturation indices (as the logarithm of the ion activity product over the solubility product) calculated with the geochemical computer code PhreeqC 3.3.3 and using the LLNL database (Parkhurst and Appelo, 2013).

Changes in the mixed solutions were monitored by measuring the increase in absorbance using a UV-VIS spectrophotometer (Uvikon XL) at λ = 520 nm with an angle between the incident beam and detector of 180˚. The reactions were followed at room temperature for up to 240 minutes by measuring the absorbance of 3 mL aliquots taken from the mixed solutions, and each experimental set was carried out in triplicate. The absorbance data is plotted as the normalised change in solution turbidity over 240 minutes.

In all experiments, regardless whether additives were present or not, the solid end-products were always gypsum as determined by powder X-ray diffraction (XRD; Bruker D8 diffractometer; CuKα1; 2θ range 5 - 35°; resolution 0.105° / step; counting time 1 s / step) with XRD patterns analysed with the EVA software (version 3) and the PDF-2-1996 database. The morphology of the formed phases was imaged using a field emission gun scanning electron microscope (FEG-SEM, FEI Quanta 650, 5 kV).

To quantify the association between the additives and the formed gypsum, aliquots of the precipitated end-products were dissolved in 2% nitric acid (69% AnalaR Normapour analytical reagent) and the resulting solutions together with aliquots taken from the crystallisation solution after 10 seconds (initial concentration) and 240 minutes (end concentration) were analysed for their Ca and P contents by inductively coupled plasma optical emission spectrometry (ICP-OES; Thermo Scientific iCAP 7400; with a limit of detection of 0.007 ppm and uncertainties of 3.78%). To differentiate between the potentially surface adsorbed and the structurally incorporated fractions of the additives, 1.5 grams of the end-product gypsum samples were suspended in a 200 ml saturated gypsum solution for 2 hours under continuous stirring to desorb any potentially surface adsorbed additives. The saturated gypsum solution was prepared by equilibrating gypsum (puriss, 99.0-101.0%, Sigma-Aldrich) in 18 MΩcm^{-1} ultra-pure Milli-Q water at pH ~ 9 and filtering through 0.2 µm syringe filters prior to desorption. After this desorption step the remaining solids were digested in 2% nitric acid and the digestion solutions were analysed for P concentration as described above. The concentrations of the inhibitors associated with the end-product gypsum crystals (association amount; $C_{A,inhibitor}$) before and after desorption were calculated from the concentration of inhibitor (ppm) (calculated based on the phosphorous element concentration measured in the full digestion solutions) divided by the total dissolved gypsum crystals (ppm).

Finally, to determine the nature of the surface interactions between the inhibitors and the formed precipitates, we subjected the end-product solids to X-ray photoelectron spectroscopy (XPS) with a detection limit of 0.1 at. % (which is roughly 1ppth or 10^{19}

atoms/cm^3). XPS spectra were acquired from the top 8-10 nm of the gypsum crystals using a Kratos Axis Ultra-DLD spectrometer with a monochromatic Al K_α X-ray source (144 W) and analyzer pass energies of 40 eV (high resolution scans). The base pressure during analysis was ca. 6×10^{-7} Pa. All data were referenced to the C (1s) signal at 284.8 eV and quantified as atomic percentage using CasaXPS™ (Version 2.3.15) using elemental sensitivity factors supplied by the manufacturer.

7.3. Results

In the additive-free experiments, at either pH ~ 4 or ~ 7, the solution became turbid after ~ 30 seconds (induction time) and it took ~ 30 minutes to reach 100% turbidity (Figure 7.1). In contrast, in each of the additive-containing experiments and at pH ~ 4, the induction times and the time to reach a maximum turbidity plateau were longer. At a constant concentration (20 ppm) of antiscalants and pH ~ 4, the induction time increased 4 fold (to ~ 2 minutes), 36 fold (to ~ 18 minutes), 60 fold (to ~ 30 minutes), and 140 fold (to ~ 70 minutes) in the presence of HEDP, ATMP, PAPEMP and DTPMPA, respectively. The slope of the turbidity curves decreased and the crystallisation end-plateaus were reached only in the presence of HEDP (after ~ 65 minutes) and ATMP (after ~ 100 minutes). The most noticeable effect was observed in the presence of BHMTPMP, where no change in turbidity was noticeable even after long time periods.

At a higher pH (~ 7), the effects of 20 ppm additive were less marked and no change in turbidity was observed except for HEDP. In the presence of HEDP the elapsed time before the onset of turbidity was ~ 30 minutes (15 times longer than in the pH ~ 4 experiments at equivalent concentration). However, noticeable also is the fact that the turbidity developed with a different trend than in the additive-free system (Figure B.1) in that up to ~ 75 minutes the turbidity increased with a constant slope until it reached ~ 3 %. At this point, the turbidity curve sharply increased and reached a plateau within the next ~ 50 minutes (after ~ 130

minutes from beginning). A similar trend was observed for 5 ppm BHMTPMPA at an unadjusted pH of ~ 4.7 (Figure B.2).

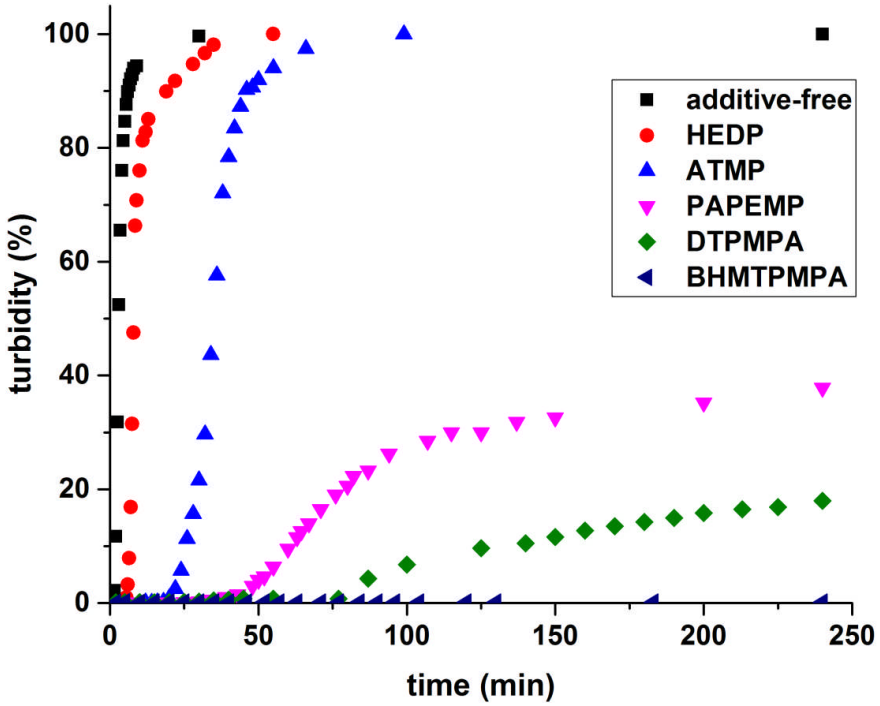

Figure 7.1.Turbidity curves plotted as a function of time in the absence and presence of 20 ppm HEDP, ATMP, PAPEMP, DTPMPA and BHMTPMP at pH ~ 4.

Changes in concentration of the antiscalants during gypsum crystallisation were analysed by measuring their initial (after ~ 10 seconds; ~ 20 ppm inhibitor) and end concentrations (after 240 minutes) of reaction (Figure 7.2). At pH ~ 4, no decrease in the HEDP and BHMTPMP concentrations were measured, but the concentrations of ATMP, PAPEMP and DTPMPA decreased by 18 ppm, 10 ppm and 7 ppm. At pH ~ 7, no decrease in the inhibitors' concentrations were observed even after 240 minutes, except for HEDP which decreased by 20 ppm. This decrease in HEDP inhibitor concentration was mirrored by a reverse trend in the turbidity plot (Figure 7.3).

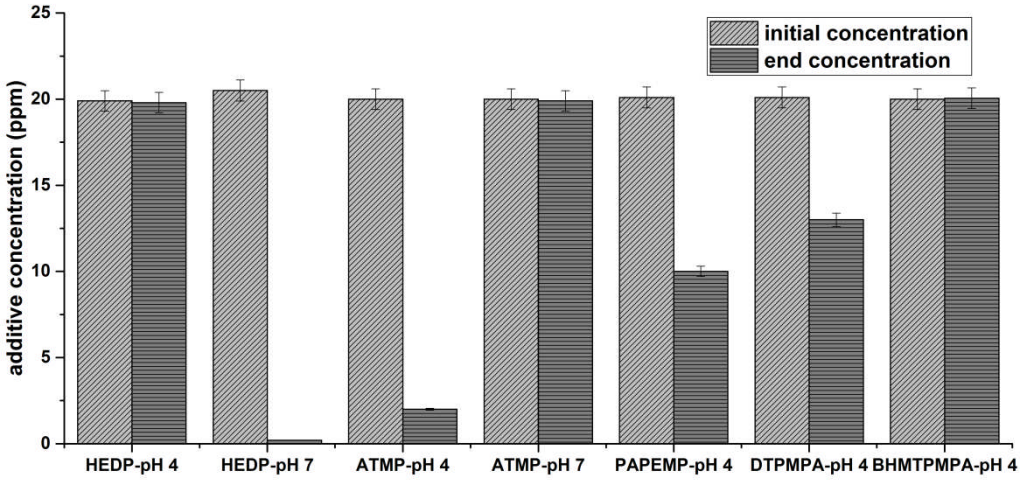

Figure 7.2.Initial and end concentrations of HEDP, ATMP, PAPEMP, DTPMPA and BHMTPMP in the experimental solutions at pH ~ 4 and ~ 7.

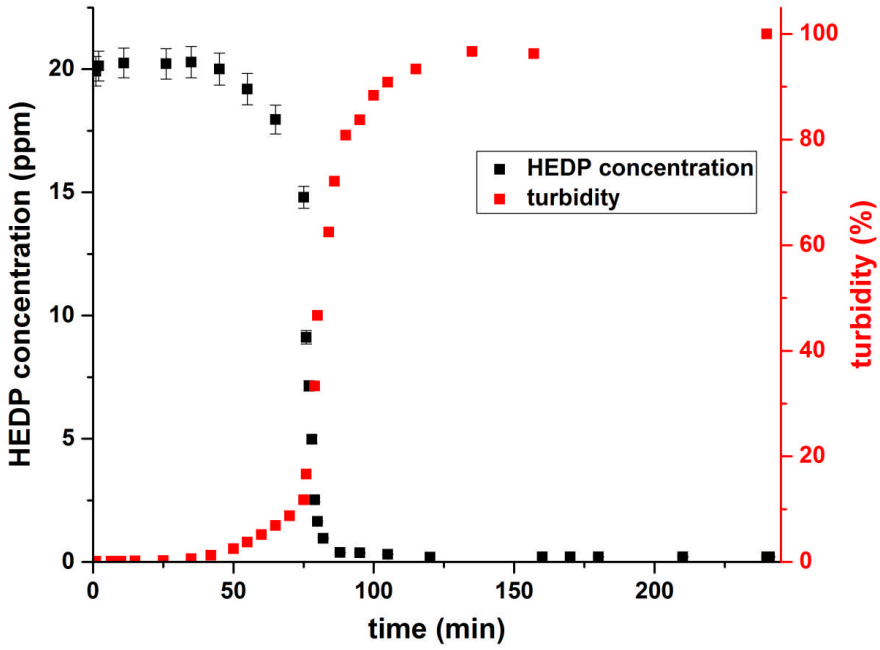

Figure 7.3.Changes in turbidity and HEDP concentration in the gypsum crystallisation solution carried out in the presence of 20 ppm HEDP over 240 minutes at pH ~ 7.

To shed light on the role of these phosphorous containing additives in inhibiting gypsum crystallisation, the amount of inhibitors taken up by the as-formed and desorbed gypsum crystals was quantified (Figure 7.4). For the as-formed crystals at pH ~ 4, the amount of inhibitor associated with the solid crystals ($C_{A,inhibitor}$) was lowest for the HEDP system (below the detection limit of our analytical method (ICP-OES)), and highest for the ATMP system

with a $C_{A,inhibitor}$ of ~ 0.0013. In the PAPEMP and DTPMPA systems the $C_{A,inhibitor}$ was ~ 40% and ~ 45% lower than that for the ATMP additive, respectively. For the as-formed crystals at pH ~ 7, the highest $C_{A,inhibitor}$ (~ 0.0015) was measured for the HEDP system; this was also the highest uptake amount overall. After desorption our data revealed that only ~ 10% of the associated additives were desorbed (i.e., ~ 90% of the associated inhibitors were not readily desorbed into the desorption solution).

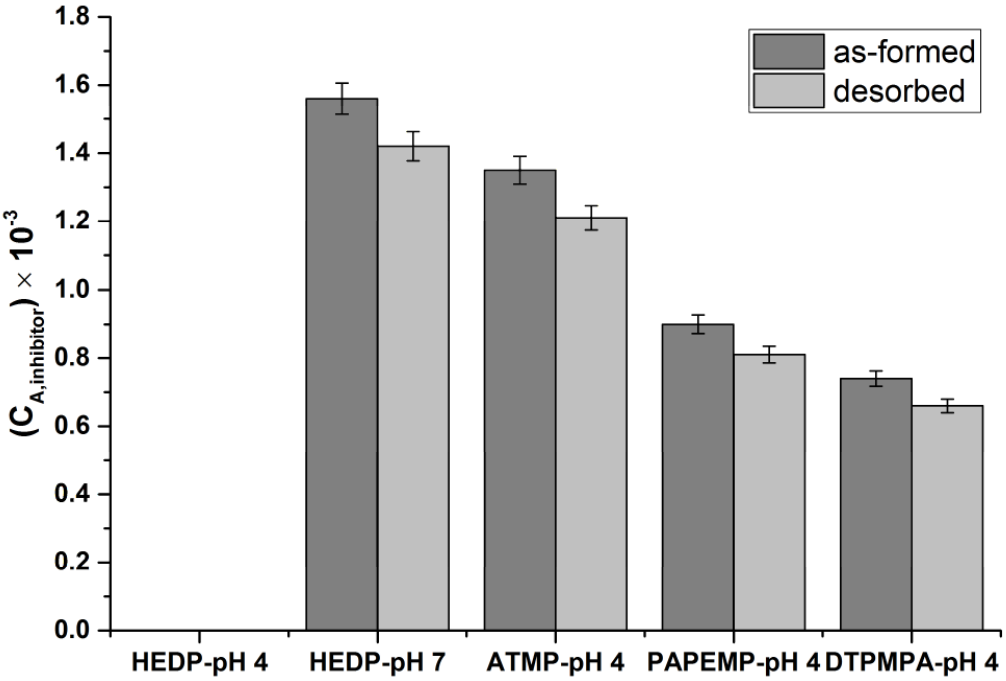

Figure 7.4.Inhibitors' association with end-product gypsumcrystals in the presence of 20ppm HEDP, ATMP, PAPEMP and DTPMPA at pH ~ 4 or ~ 7. Note that no gypsum crystals were obtained in the BHMTMPMA amended experiments (see Figure 7.1).

The atomic composition of the topmost surface layers of the gypsum crystals synthesised from a solution containing 20 ppm DTPMPA at pH ~ 4 were probed by XPS analysis (Figure 7.5). Besides Ca 2p (12.59 at.%), S 2p (12.8 at.%) and O 1s (58.87 at.%) the XPS spectra revealed the presence of Na 1s (0.24 at.%) and Cl 2p (0.15 at.%), and P 2p (0.87 at.%) and N 1s (0.28 at. %) at the gypsum surface. The Na and Cl spectral signatures are related to the presence of NaCl, while P and N signals correspond to the phosphonate antiscalant DTPMPA.

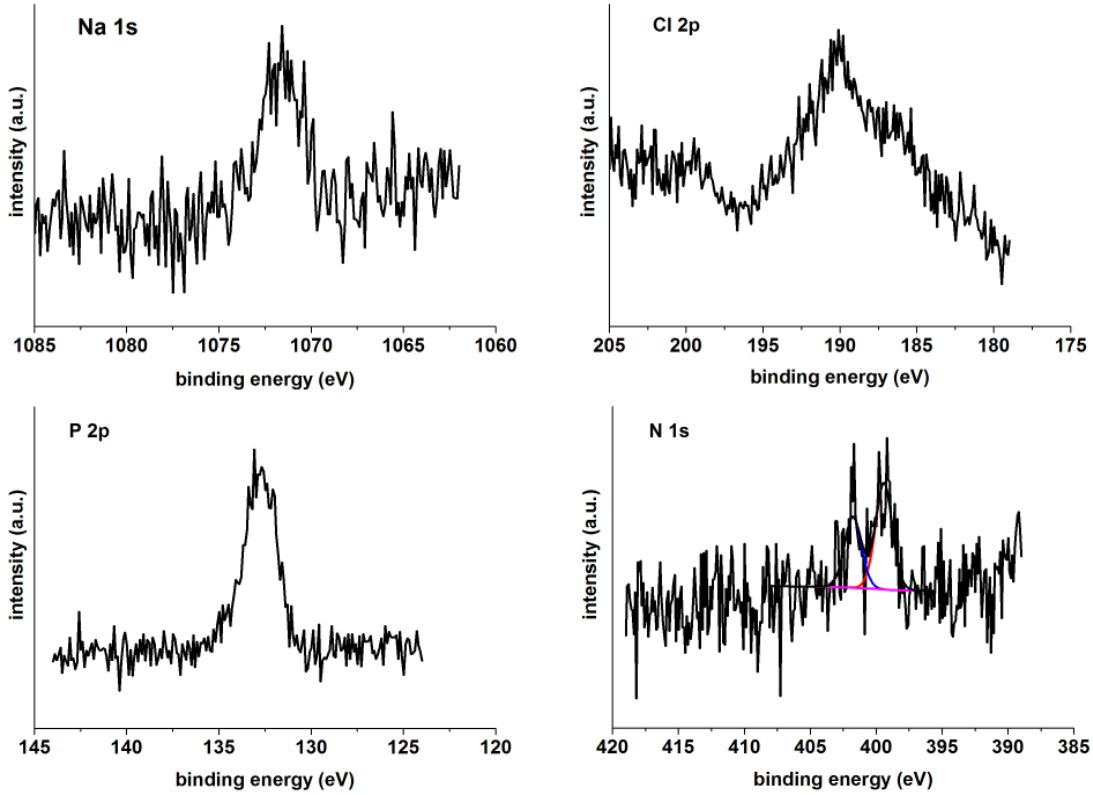

Figure 7.5.XPS spectra for the as-formed gypsum crystals precipitated in the presence of 20 ppm DTPMPA at pH ~ 4. Note that the peak intensities are in arbitrary units and do not represent the concentration of the elements on the surface.

The morphology of the gypsum crystals grown from supersaturated solutions with or without additives were characterised by SEM (Figure 7.6). In the absence of inhibitors almost exclusively large and thin twin crystals were produced (Figure 7.6 a). This was similar to the crystals formed in the presence of HEDP at pH ~ 4 (Figure 7.6 b). However, both HEDP at pH ~ 7 and ATMP at pH ~ 4 dramatically modified the morphology of the forming gypsum crystals and this resulted in thick needle shaped particles (Figure 7.6 c and 7.6 d). The other additives, PAPEMP and DTPMPA, also had profound effects on the morphology and size of the formed gypsum crystals with PAPEMP at pH ~ 4 yielding a mixture of long “dendritic” needles with thick short crystals (Figure 7.6 e), and DTPMPA at pH ~ 4 resulting in thick and short crystals together with some long dendritic crystals covered by tiny crystal fragments (Figure 7.6 f).

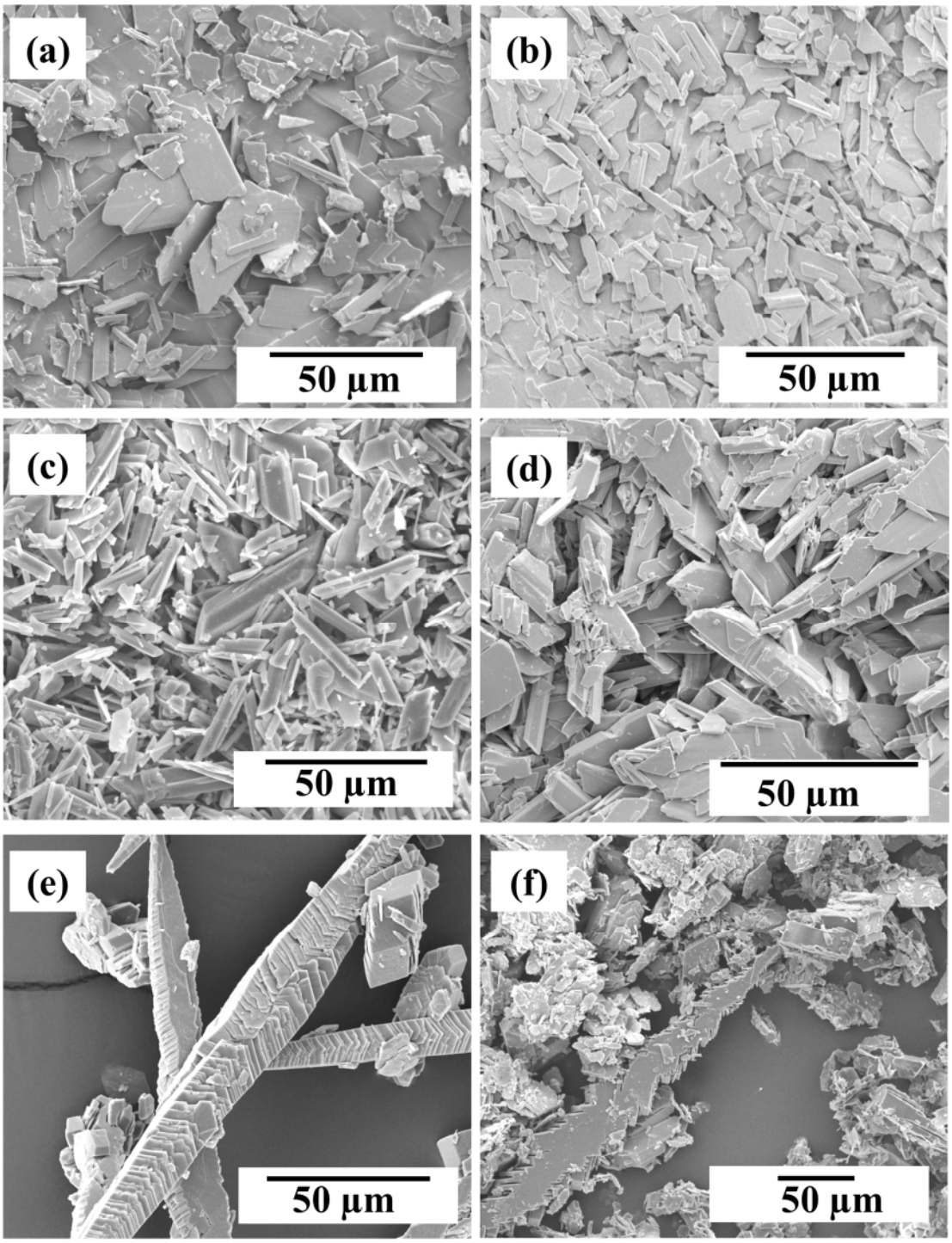

Figure 7.6.SEM micrograph of gypsum crystals gathered after 240 minutes from experiments in (a) additive-free at pH ~ 7; (b) 20 ppm HEDP at pH ~ 4; (c) 20 ppm HEDP at pH ~ 7; (d) 20 ppm ATMP at pH 4; (e) 20 ppm PAPEMP at pH ~ 4; (f) 20 ppm DTPMPA at pH ~ 4; note that no gypsum crystals precipitated from a solution containing 20 ppm BHMTPMPA at pH ~ 4.

7.4. Discussion

We used the change in induction times in turbidity curves in the absence and presence of P – containing antiscalants as a proxy to evaluate the effects they have on the nucleation and growth of gypsum. Our data at pH ~ 4 showed a clear increase in induction time and a decrease in nucleation and growth kinetics in the presence of 20 ppm additives following the order HEDP < ATMP < PAPEMP < DTPMPA < BHMTPMPA (Figure 7.1). Although it is not possible to separate the nucleation from the growth part on a turbidity graph (Chen et al., 2004), it can be seen in Figure 7.1 that no gypsum crystal nucleated in the presence of the BHMTPMPA (no turbidity occurred), therefore this inhibitor can be considered as a nucleating inhibitor. However, in the presence HEDP, ATMP, PAPEMP and DTPMPA, the gypsum crystals nucleated (an increase in turbidity) and just their growth was decreased which was reflected by a decrease in the sloped of the turbidity graphs. Hence, HEDP, ATMP, PAPEMP and DTPMPA can be considered as growth inhibitors. However, this classification is not absolute and depends on the concentration of the inhibitors or the experimental conditions because for example at lower BHMTPMPA concentration (e.g., 0-10 ppm) gypsum might nucleate and just its growth may be inhibited which will make the BHMTPMPA a growth inhibitor.

Furthermore, the turbidity graphs in this study developed with different trends than the turbidity graphs reported in our previous studies (i.e., Rabizadeh et al., 2014; Rabizadeh et al., 2017). It could be because of different mechanisms by which the phosphonate additives affected the gypsum crystallisation. Moreover, in this research, the phosphonate inhibitors, themselves, yielded different turbidity development trends (Figure 7.1, B.1-3). The graphs obtained from both HEDP and ATMP at pH ~ 4 amended solutions, had similar development trends inferring similarity in gypsum nucleation and growth mechanisms. However, in the presence of PAPEMP, DTPMPA at pH ~ 4 and HEDP at pH ~ 7, the turbidity developed differently, For example, in the presence of PAPEMP at pH ~ 4, the turbidity graph changed its development trend 65 minutes after turbidity induction (at 30 % turbidity) and increased

with lower slope which could be due to the changes in the PAPEMP interaction with gypsum crystals and gypsum formation mechanism. However, the detail reasons for these changes in mechanisms are still unclear.

The reasons behind these observations are linked to some parameters such as functional groups, molecular structure, and molecular weight of antiscalants together with the pH of the solution are among the main factors affecting the performance and efficiency of these antiscalants (Amjad and Demadis, 2015). We, therefore, considered these to help understand each inhibitor's performance. It is well-known that antiscalants can prevent scale formation by different mechanisms, such as through sequestration or chelation of the ions in solution that are required for precipitation, increasing the interfacial tension between nuclei and the solution, dispersing scale mineral crystals, and / or adsorbing to the scale mineral surfaces (Lioliou et al., 2006; Prisciandaro et al., 2006). Some of these mechanisms are discussed below in relation to our data.

Sequestration or chelation: Phosphonate antiscalants are known to retard crystallisation by chelating with active ions in the precipitation solutions (Prisciandaro et al., 2006). In our case, complexation with Ca^{2+} ions would result in a decrease in the activity of free Ca^{2+} and $CaSO_4^0$ ion pairs, which is likely reflected by the delay in gypsum crystallisation kinetics (Figures 7.1, 7.3 and B.1-3). Furthermore, the role of pH is also fundamental because phosphonate inhibitors deprotonate at higher pH and further complex with Ca^{2+}, and therefore hinder the crystallisation which was also demonstrated in this study (Figure B.3). Table 7.1 further illustrates the chelation effect of the studied inhibitors. It can be seen that in the additive-free system 72 ± 1.4 mM of Ca^{2+} was consumed. However, in the presence of 20 ppm of the strongest inhibitor (BHMTPMPA; at pH ~ 4), no Ca^{2+} ion was depleted from the crystallisation solution revealing the strong complexation between the phosphonate functional groups and Ca^{2+}. Moreover, by increasing the pH of the ATMP amended crystallisation solution from ~ 4 to ~ 7, the Ca^{2+} consumption was stopped which reveals the effect of deprotonation of an inhibitor on sequestration of the active ions in the crystallisation solution.

These results confirm our turbidity measurements where for example no gypsum formation was observed in the presence of BHMTPMPA at pH ~ 4 and ATMP at pH ~ 7.

Table 7.1. Difference between calcium ion concentration at the beginning and end of the gypsum crystallisation process (after 240 minutes) in the presence and absence of inhibitors at different pH.

	Additive-free	HEDP - pH 4	HEDP - pH 7	ATMP - pH 4	ATMP - pH 7	PAPEMP- pH 4	DTPMPA- pH 4	BHMTPMPA- pH 4
$\Delta_{Ca^{2+}}$(mM)	72 ± 1.4	69 ± 1.3	60 ± 1.2	52± 1	0	48 ± 0.9	44 ± 0.8	0

Molecular structure: We note that there is a direct relation between the number of functional groups in the phosphonate inhibitor structure and the decrease in gypsum crystallisation kinetics (Figure 7.1). In this regard, it is likely that DTPMPA and BHMTPMPA each with five phosphonate functional groups more effectively complexed with Ca^{2+} than PAPEMP, ATMP and HEDP with four, three and two functional groups, respectively, and thus more effectively inhibited gypsum crystallisation (i.e., DTPMPA and BHMTPMPA showed the longest induction times; Figure 7.1). A more effective inhibition of calcite crystallisation by the five phosphonate functional group DTPMPA compared to the tetraphosphonate inhibitors is also reported elsewhere and similarly attributed to a more effective complexation of phosphonate functional groups by DTPMPA (Xia and Chen, 2015).

With regard to BHMTPMPA, at constant concentration of 20 ppm (29.2 µM) BHMTPMPA, no induction was detected, indicating an even higher inhibitory efficiency of this additive than 20 ppm (34.9 µM) DTPMPA (Figure 7.1). Because the pK of DTPMPA and BHMTPMPA are very similar, we suggest that the differences in inhibitory efficiency are related to differences in the molecular structure of these two antiscalants, i.e. the backbone chain length where DTPMPA and BHMTPMPA contain 4 and 12 methylene groups in their backbone connecting the N atoms, respectively. Akyol et al (2009) showed that a tetraphosphonate antiscalant with a longer backbone chain had a greater gypsum inhibitory efficiency than tetraphosphonate antiscalants with shorter backbone chains and as such we also attribute the greater inhibitory efficiency of BHMTPMPA compared to DTPMPA to this

molecular structure effect. Recent work by Shi et al (2013) focused on this molecular structure phenomenon and used a molecular modelling approach to show that there is an optimum PAPEMP molecular length for increased anhydrite inhibition and among the PAPEMP antiscalants with different methylene groups (n = 1-7), the PAPEMP with 3 methylene groups had higher adsorption on anhydrite. The Shi et al. (2013) results, however, are contrary to similar molecular modelling for calcite which showed that because of steric hindrance effects, the tetraphosphonate inhibitors with longer back bone chains resulted in a weaker inhibition of calcite crystallisation (Xia and Chen, 2015).

Surface adsorption / structural incorporation: In this research, the deprotonation state of the additives in the crystallisation solutions can directly affect the concentration variation of the additives during the crystallisation experiments, and the association of the additives with the forming gypsum crystals (Figures 7.2-4). It is well-known that antiscalants with deprotonated functional groups adsorb onto developing nuclei and / or growing crystals by binding onto active growth sites (i.e., steps and kink sites). During this process just a few percent of a crystal surface (e.g., 5 % in the barite system) needs to be covered to totally block crystal growth (Leung and Nancollas, 1978).

Adsorption of inhibitors also affects the thermodynamic stability of nuclei by keeping them at subcritical size and dissolving the nuclei before their further growth. Then, the inhibitors are available for repeated adsorption (Liu and Nancollas, 1975). It is also worth mentioning that impurities can trap within the growing gypsum crystal structure and association of foreign ions with gypsum crystals increases with increasing the crystal growth rate (Kushnir, 1980).

Here, HEDP at pH ~ 4 is only weakly deprotonated and therefore it is likely that this additive did not adsorb on the gypsum crystal surfaces or become trapped in the rapidly growing gypsum crystals (Figure 7.1 and 7.2). This is evident in the fact that the HEDP concentration did not decrease during the experiment (Figure 7.2). Overall, with no HEDP association with the gypsum crystals there was no gypsum inhibition (Figure 7.1). In contrast,

HEDP at pH ~ 7 and ATMP at pH ~ 4 were deprotonated and therefore likely adsorbed and became trapped in the fast growing gypsum crystals, resulting in significant gypsum inhibition (Figure 7.1 and 7.3). PAPEMP and DTPMPA at pH ~ 4 were partially deprotonated and thus likely just partially adsorbed and became trapped into the growing gypsum crystals, and ≥ 50 % of these additives remained in the crystallisation solution after 240 minutes.

To shed light on the surface adsorption *vs.* structural incorporation of our additives with gypsum, we performed desorption experiments. Evaluating the association of additives with as-formed gypsum crystals after 2 hours of desorption revealed that just ~ 10% of associated inhibitors desorbed and a high fraction of it (~ 90%) remained associated either with the surface (strong binding and no desorption) and / or incorporated into the structure (Figure 7.4).

Furthermore, it is well-known that the surface charge of the adsorbent (here gypsum) and the nature of the adsorbate (e.g., phosphonate additives) affects the extent of the adsorption. Calcium ions in the gypsum structure have high hydration energy therefore they are highly shielded by water molecules, either the structural water molecule or the surrounding solution (Weijnen and Van Rosmalen, 1986). A negative surface charge over the pH ranges of this study (above pH ~ 2) has also been reported for gypsum (e.g.,Weijnen et al., 1987). Therefore, it implies that phosphonate functional groups did not adsorb onto the gypsum crystals via electrostatic interaction (physisorption) but their adsorption was by an irreversible chemisorption mechanism called “ligand-exchange” mechanism (also known as “specific adsorption” or “coordination adsorption”) during which the phosphonate functional groups replaced the hydroxyl groups linked to the Ca^{2+} ions (Zhang and Yu, 1997). The adsorption of anions onto the hydrated minerals (e.g., α-alumina; Zarbakhsh et al., 2013) via ligand exchange mechanism has also been documented.

This agrees with Weijnen and Van Rosmalen (1986) who observed the adsorption of HEDP on the negatively surface charged gypsum crystals and could not measure any desorbed HEDP even after several days suspending the gypsum crystals in a supersaturated gypsum

solution. These authors, therefore, suggested that the strong surface adsorption of HEDP onto gypsum is irreversible. In this regard, Akyol et al. (2009) proposed that negatively charged phosphonates bind to the calcium ions of the gypsum structure by substituting the water molecules of the hydrated calcium ions in a process called “calcium-phosphonate interaction”. Indeed, precipitation of a calcium-phosphonate layer on calcium based cement grains in the presence of ATMP has been similarly proposed (Bishop et al., 2003), and the formation of calcium phosphonate compounds (Ca-DTPMPA) on calcite surfaces have also been identified (Kan et al., 2005). Furthermore, in the presence of an orthophosphoric acid, phosphate adsorption on calcite was observed to be irreversible which was due to its incorporation into the calcite structure (Suzuki et al., 1986). The structural incorporation of HEDP into hydroxyapatite at high temperature and after long reaction times has also been reported (Daniels et al., 2015).

XPS analysis of as-formed gypsum crystals precipitated from 20 ppm DTPMPA amended solution at pH ~ 4, further confirmed the association of this additive with the gypsum crystal surface (Figure 7.5). Besides the Na 1s at 1072 eV and Cl^- 2p at 193 eV peaks which originated from adsorption of Na^+ and Cl^-, the P 2p peak located at a binding energy of 133.4 eV is attributed to the ($–PO(OH)_2$) functional group of the antiscalant (Zhang et al., 2015). Jonasson et al. (1996) related the XPS phosphorous peak to a thin calcium phosphonate layer formed on the calcite surface as a result of surface adsorption and surface reaction / precipitation during the calcite inhibition process in the presence of DTPMPA. Moreover, it has been suggested that in acidic solutions, nitrogen atoms of amino groups in DTPMPA can be protonated and adsorb to the negatively charged sites of a mirabilite crystal (Ruiz-Agudo et al., 2006; Vavouraki and Koutsoukos, 2016). Therefore, the N 1s peak with two components located at binding energies of 399.4 eV and 401.7 eV has been assigned to amino groups and protonated nitrogen (NH^{3+}) on the gypsum surface, respectively (Qian et al., 2013).

Morphological effects: As our morphological investigations show, selective adsorption and structural incorporation of additives onto and into the growing gypsum crystals

inhibited their growth along specific directions and thus modified their shapes (Figure 7.6 and B.4-9). This is a common phenomenon, but our imaging data confirmed that with phosphonate additives, gypsum crystals change their habits compared to those in the additive-free system. It is also worth mentioning that the morphology of the gypsum crystals formed in the absence of the additives in this study (irregular twinned crystals) was different than the morphology of the additive-free gypsum crystals reported in our previous studies (needle shape) (i.e., Rabizadeh et al., 2014; Rabizadeh et al., 2017). It can be due to the higher supersaturation of the gypsum crystallisation solution (0.84 *vs.* 0.55) and the larger volume of the crystallisation solution (1 litre *vs.* 2 ml) in this study. However, investigating the effects of the supersaturation and the solution volume on gypsum crystallisation was out of the scope of this study.

HEDP at pH ~ 4 was likely not deprotonated enough to interact with the growing gypsum crystals and so did not associate and therefore did not cause any morphological changes. On the other hand, HEDP at at pH ~ 7 yielded gypsum crystals with different morphologies. This additive at pH ~ 7 inhibited the growth along the *c* axis and favoured the growth of gypsum in the *a* and *b* directions, leading to dominantly thick crystal habits instead of thin twin crystals. This morphological change was further demonstrated by changes in XRD peak intensity ratios where the (020) to (021) peak intensity ratio in the HEDP amended system at pH ~ 7 was smaller (~ 0.69) than the corresponding ratio at pH ~ 4 (~ 2.6). Considering the typical gypsum unit cell (Rubbo et al., 2011), this variation in peak intensity ratio is attributed to the increase in thickness of the crystal accompanied by an increase in (021) peak intensity. A similar change in XRD peak intensity ratio, and associated morphological changes, as a result of a carboxylic acid adsorption onto another calcium sulfate phase (bassanite; $CaSO_4 \cdot 0.5H_2O$) has been reported (Li et al., 2013).

Furthermore, a few twin and thin needle gypsum crystals were present among the thick ones (Figure B.4). This variation in morphology can be related to two step nucleation and growth mechanism of gypsum crystals (step 1: a constant increase in turbidity until ~ 3 %

and step 2: a sharp increase in turbidity from this point; Figure B.1). However, in this study the SEM images were just obtained from the end-products and no SEM data are available from the growing gypsum crystals, therefore it is not possible to link the turbidity graph to the SEM images and determine the formation step of each morphology type.

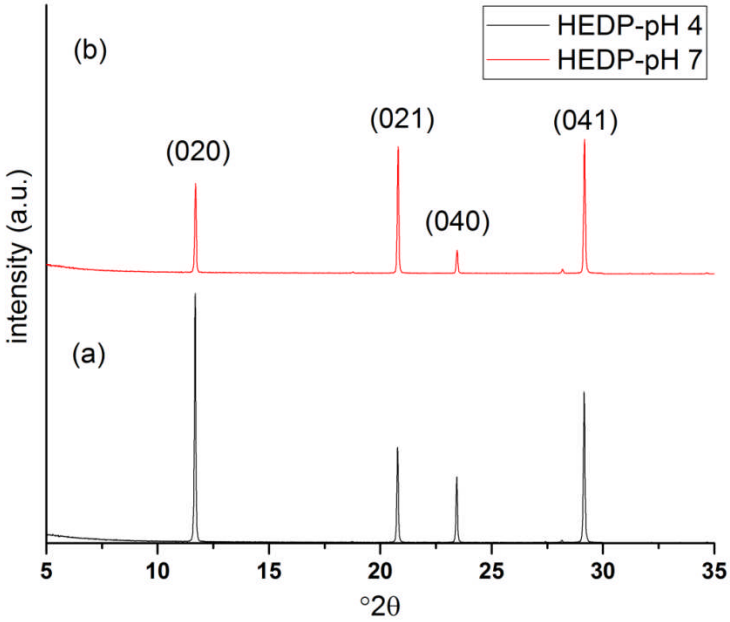

Figure 7.7.The effects of HEDP on gypsum (020) to (021) peak intensity ratio at two different pH of ~ 4 and ~ 7.

Thicker needle gypsum crystals were also observed as a consequence of ATMP association at pH ~ 4, while stronger association of PAPEMP and DTPMPA containing four and five phosphonate functional groups at pH ~ 4 yielded gypsum crystals that were shorter and thicker (Figure 7.6 e,f, B.6 and B.7). However, PAPEMP and DTPMPA at pH ~ 4 produced long dendritic gypsum crystals as well which can be related to their long molecular structure. Here, we again emphasise due to the lack of SEM images from forming gypsum crystals during turbidity development process, it is not possible to determine at what turbidity development step these two morphologies (“short, thick” and “long, dendritic”) precipitated. But, formation of long dendritic gypsum crystals can probably be related to the long molecular structure of PAPEMP and DTPMPA. These long molecules are flexible and capable of bending which may allow these additives to interact with calcium or sulfate ions in different crystal faces via

deprotonated phosphonates and protonated amino groups (Akyol et al., 2009). This phenomenon might have inhibited growth along the *c* direction yielding long "dendritic" crystals. Similarly, adsorption of flexible deprotonated DTPMPA resulted in gypsum morphology variations from thin twin crystals obtained in the presence of 5 ppm DTPMPA at pH ~ 4 to long dendritic needles precipitated from 5 ppm DTPMPA at pH ~ 7 (Figures B.8 and B.9). However, a detailed molecular level understanding of the process is still outstanding.

Considering the efficiency of the tested inhibitors and the morphology of precipitated gypsum crystals, BHMTMPA is the most suitable phosphonate inhibitor to be used in different industries. Moreover, we emphasise that the phosphonate additives should be added at high enough concentration to the gypsum crystallisation solution to prevent the nucleation and growth of gypsum crystals, otherwise thick and long dendritic needle crystals will form which might clog pipelines and membranes and again cause problems in some industries such as reverse osmosis water desalination.

7.5. Conclusion

With this study, we documented the effects that industrial phosphonate containing antiscalants have on the nucleation and growth kinetics of gypsum crystals. The presence of additives led to inhibition of gypsum formation because they increased the time needed for gypsum precipitation in the order of increasing number of phosphonate functional groups in the antiscalant additive as follows: HEDP < ATMP < PAPEMP < DTPMPA < BHMTPMPA. Gypsum was the sole mineral phase after 240 minutes and the additives did not cause any phase transformation. Combination of ICP-OES and XPS analyses revealed that highly deprotonated antiscalants associated with gypsum crystals through surface adsorption and / or structural incorporation. This was accompanied by a decrease in additive's concentration in the crystallisation solution during gypsum growth. Just ~ 10 % of the associated additives were adsorbed to the surface while the remainder was either strongly sorbed or structurally incorporated. Growing in the presence of additives affected the morphology of gypsum

crystals. Thin and twin gypsum crystals precipitated from additive-free solutions compared to short and thick crystals in the presence of HEDP at pH ~ 7 and ATMP at pH ~ 4. This was in contrast to gypsum growth in the presence of PAPEMP and DTPMPA at pH ~ 4, where short and thick crystals and long dendritic needles were obtained.

Acknowledgement

This study was supported by a Marie Curie grant from the European Commission in the framework of the MINSC ITN (Initial Training Research network), Project number 290040. The authors would like to thank the Cohen Laboratories in the School of Earth and Environment, and the Leeds Electron Microscopy and Spectroscopy Centre (LEMAS) for help and access to instruments during the course of this study.

7.6. References

Akyol, E., Öner, M., Barouda, E. & Demadis, K. D., 2009. Systematic Structural Determinants of the Effects of Tetraphosphonates on Gypsum Crystallization. *Crystal Growth & Design,* 9**,** 5145-5154.

Amjad, Z. & Demadis, K. D., 2015. *Mineral Scales and Deposits: Scientific and Technological Approaches*, Elsevier.

Bishop, M., Bott, S. G. & Barron, A. R., 2003. A new mechanism for cement hydration inhibition: solid-state chemistry of calcium nitrilotris (methylene) triphosphonate. *Chemistry of materials,* 15**,** 3074-3088.

Chen, T., Neville, A. & Yuan, M., Effect of PPCA and DETPMP inhibitor blends on CaCO3 scale formation. SPE International Symposium on Oilfield Scale, 2004. Society of Petroleum Engineers.

Daniels, Y., Lyczko, N., Nzihou, A. & Alexandratos, S. D., 2015. Modification of Hydroxyapatite with Ion-Selective Complexants: 1-Hydroxyethane-1, 1-diphosphonic Acid. *Industrial & engineering chemistry research,* 54**,** 585-596.

Jonasson, R. G., Rispler, K., Wiwchar, B. & Gunter, W. D., 1996. Effect of phosphonate inhibitors on calcite nucleation kinetics as a function of temperature using light scattering in an autoclave. *Chemical geology,* 132**,** 215-225.

Kan, A. T., Fu, G. & Tomson, M. B., 2005. Adsorption and precipitation of an aminoalkylphosphonate onto calcite. *Journal of colloid and interface science,* 281**,** 275-284.

Ketrane, R., Saidani, B., Gil, O., Leleyter, L. & Baraud, F., 2009. Efficiency of five scale inhibitors on calcium carbonate precipitation from hard water: effect of temperature and concentration. *Desalination,* 249**,** 1397-1404.

Kushnir, J., 1980. The coprecipitation of strontium, magnesium, sodium, potassium and chloride ions with gypsum. An experimental study. *Geochimica et Cosmochimica Acta,* 44**,** 1471-1482.

Leung, W. H. & Nancollas, G. H., 1978. Nitrilotri (methylenephosphonic acid) adsorption on Barium Sulfate crystals and its influence on crystal growth. *Journal of Crystal Growth,* 44**,** 163-167.

Li, F., Liu, J., Yang, G., Pan, Z., Ni, X., Xu, H. & Huang, Q., 2013. Effect of pH and succinic acid on the morphology of α-calcium sulfate hemihydrate synthesized by a salt solution method. *Journal of Crystal Growth,* 374**,** 31-36.

Lioliou, M. G., Paraskeva, C. A., Koutsoukos, P. G. & Payatakes, A. C., 2006. Calcium sulfate precipitation in the presence of water-soluble polymers. *J Colloid Interface Sci,* 303**,** 164-70.

Liu, S. & Nancollas, G., 1975. A kinetic and morphological study of the seeded growth of calcium sulfate dihydrate in the presence of additives. *Journal of Colloid and Interface Science,* 52**,** 593-601.

Mavredaki, E., Neville, A. & Sorbie, K. S., 2011. Initial stages of barium sulfate formation at surfaces in the presence of inhibitors. *Crystal Growth & Design,* 11**,** 4751-4758.

Nygren, M. A., Gay, D. H., Catlow, C. R. A., Wilson, M. P. & Rohl, A. L., 1998. Incorporation of growth-inhibiting diphosphonates into steps on the calcite cleavage plane surface. *Journal of the Chemical Society, Faraday Transactions,* 94**,** 3685-3693.

Ojo, S. A., Slater, B. & Catlow, C., 2002. Computer simulation of calcite growth inhibition: A study of monophosphonate interaction with calcite. *Molecular Simulation,* 28**,** 591-606.

Parkhurst, D. L. & Appelo, C., 2013. Description of input and examples for PHREEQC version 3—a computer program for speciation, batch-reaction, one-dimensional transport, and inverse geochemical calculations. *US geological survey techniques and methods, book,* 6**,** 497.

Prisciandaro, M., Olivieri, E., Lancia, A. & Musmarra, D., 2006. Gypsum Precipitation from an Aqueous Solution in the Presence of

Nitrilotrimethylenephosphonic Acid. *Industrial & Engineering Chemistry Research,* 45**,** 2070-2076.

Qian, B., Wang, J., Zheng, M. & Hou, B., 2013. Synergistic effect of polyaspartic acid and iodide ion on corrosion inhibition of mild steel in H 2 SO 4. *Corrosion Science,* 75**,** 184-192.

Rabizadeh, T., Peacock, C. L. & Benning, L. G., 2014. Carboxylic acids: effective inhibitors for calcium sulfate precipitation? *Mineralogical Magazine,* 78**,** 1465-1472.

Rabizadeh, T., Stawski, T. M., Morgan, D. J., Peacock, C. L. & Benning, L. G., 2017. The effects of inorganic additives on the nucleation and growth kinetics of calcium sulfate dihydrate crystals. *Crystal Growth & Design,* 17**,** 582-589.

Rubbo, M., Massaro, F., Aquilano, D. & Vanzetti, W., 2011. Morphology of gypsum: a case study. *Crystal Research and Technology,* 46**,** 779.

Ruiz-Agudo, E., Rodriguez-Navarro, C. & Sebastián-Pardo, E., 2006. Sodium sulfate crystallization in the presence of phosphonates: Implications in ornamental stone conservation. *Crystal growth & design,* 6**,** 1575-1583.

Shi, W., Xia, M., Lei, W. & Wang, F., 2013. Molecular dynamics study of polyether polyamino methylene phosphonates as an inhibitor of anhydrite crystal. *Desalination,* 322**,** 137-143.

Sousa, M. F. & Bertran, C. A., 2014. New methodology based on static light scattering measurements for evaluation of inhibitors for in bulk CaCO 3 crystallization. *Journal of colloid and interface science,* 420**,** 57-64.

Suzuki, T., Inomata, S. & Sawada, K., 1986. Adsorption of phosphate on calcite. *Journal of the Chemical Society, Faraday Transactions 1: Physical Chemistry in Condensed Phases,* 82**,** 1733-1743.

Vavouraki, A. & Koutsoukos, P., 2016. The inhibition of crystal growth of mirabilite in aqueous solutions in the presence of phosphonates. *Journal of Crystal Growth,* 436**,** 92-98.

Weijnen, M., Van der Leeden, M. & Rosmalen, G., 1987. Influence of the molecular structure of phosphonate inhibitors on various aspects of barite and gypsum crystallization. *Geochemistry of the Earth's surface and Mineral formation***,** 753-76.

Weijnen, M. & Van Rosmalen, G., 1986. Adsorption of phosphonates on gypsum crystals. *Journal of Crystal Growth,* 79**,** 157-168.

Xia, M. & Chen, C., 2015. Probing the Inhibitory Mechanism of Calcite Precipitation by Organic Phosphonates in Industrial Water Cooling System. *International Journal of Environmental Science and Development,* 6**,** 300.

Zarbakhsh, A., Lee, S., Welbourn, R., Clarke, S., Skoda, M. & Clifton, L., 2013. Adsorption of sodium hexanoate on a-alumina. *Journal of Colloid and Interface Science*.

Zhang, B., He, C., Wang, C., Sun, P., Li, F. & Lin, Y., 2015. Synergistic corrosion inhibition of environment-friendly inhibitors on the corrosion of carbon steel in soft water. *Corrosion Science,* 94**,** 6-20.

Zhang, G. & Yu, T., 1997. Coordination adsorption of anions. *In:* Yu, T. (ed.) *Chemistry of Variable Charge Soils. Oxford Univ. Press, New York.* Oxford University Press.

Zhao, Y., Jia, L., Liu, K., Gao, P., Ge, H. & Fu, L., 2016. Inhibition of calcium sulfate scale by poly (citric acid). *Desalination,* 392**,** 1-7.

Chapter 8. Conclusions and outlook

8.1. Conclusions

In this thesis, I describe the work I have carried out in order to investigate the effects of different types of antiscalants on the crystallisation kinetics and formation mechanism of calcium sulfate phases, specifically gypsum. I tested a variety of inhibitors (carboxylic acids, alkali / alkaline earth metal cations, polycarboxylic acids and phosphonates) and used a combination of techniques to fill our knowledge gaps about the kinetic pathways and mechanisms by which inhibitors affect the formation of calcium sulfate mineral scales.

In all my experiments the solid end-products were gypsum and in all cases the additives delayed its crystallisation to various degrees. This was documented through an increase in induction time and slope of the solution turbidity graphs. The observed delays were dependent on additive type, additive molecular structure, additive concentration and solution pH. All these factors changed not just the rates and mechanisms of gypsum formation but in some cases the morphology of the resulting gypsum crystals was also modified.

I illustrate that using antiscalant additives can inhibit or even prevent scale formation and that this happens through different mechanisms. These include adsorption of ions to gypsum surfaces, their incorporating into the gypsum structure, or the chelation of the ions with calcium or sulfate ions that are required for gypsum precipitation. Below, I will briefly summarise and link the findings described in chapters 4 to 7.

Monitoring the effects of 0-20 ppm carboxylic acids at pH 7, revealed that at equivalent concentrations citric acid with three carboxylic functional group numbers performed far better than tartaric and maleic acids with two carboxylic functional group

numbers (Chapter 4). Maleic acid showed slightly higher inhibitory effect than tartaric acid which could be due to differences in their molecular structure and the presence of a double bond in the maleic acid back bone. The turbidity graphs in this chapter had similar development shapes which confirm that a similar mechanism governed the nucleation and growth inhibition of gypsum crystals in the presence of carboxylic acids. Citric acid changed the final gypsum habit from typical needle-like crystals in the additive-free system to plates in the citrate additive experiments. Moreover, in all cases, first bassanite (the calcium sulfate hemihydrate) formed, yet with time it transformed to gypsum.

In the work with the alkali and alkaline earth metals, I used a wide concentration range (50-500 mM) to mimic concentrations of the major ions in natural fluids (e.g., sea water, brines or formation waters). The turbidity graphs in this chapter which had similar development shapes revealed that these ions delayed the nucleation and growth kinetics of gypsum with almost similar mechanism and in the order $K^+ < Na^+ < Li^+ < Mg^{2+}$ (chapter 5). The additives absorbed via electrostatic interactions and an apparent Langmuir adsorption isotherm was observed for the tested additives. The solution analyses of the digested as-formed and post-desorbed digested gypsum crystals, together with the surface analyses of the solid end-products, showed that Li^+, K^+ and Mg^{2+} only adsorbed onto the surfaces of the gypsum crystals, while a small fraction of Na^+ (max 25%) became structurally incorporated. Because of their higher surface adsorption affinities, Li^+ and Mg^{2+} also modified the gypsum crystals more prominently than Na^+ and K^+.

Comparing the efficiency of 20 ppm PESA and PASP as biodegradable polycarboxylic inhibitors with 20 ppm non-biodegradable PAA additives helped me illustrate the potential of a green polycarboxylic type inhibitor as an efficient additive to replace the non-biodegradable polycarboxylic inhibitors in reducing or even preventing gypsum formation (chapter 6). The comparison between these two types of additives showed that PASP was the most efficient of the tested antiscalants as it completely inhibited the formation of gypsum. The turbidity plots in this chapter had different development trends than the observed turbidity

plots in chapters 4 and 5 which could be due to the differences in the mechanisms by which the polycarboxylic additives inhibited gypsum formation. The XPS analysis revealed the adsorption of the inhibitors on gypsum crystals which resulted in the depletion of the additives from the crystallisation solution and was reflected in the turbidity plots by an abrupt and sudden increase. Furthermore, the data showed that the molecular weight of the polymeric inhibitors was an important factor which has to be considered when choosing an effective antiscalant. My investigations revealed that a low molecular weight PAA (~ 2000) has superior gypsum inhibitory effect compared with a PAA with a higher molecular weight (~100000). At pH ~ 7, calcium ions bridged the PAA_{100K} monomers and formed a "net-like" structure which decreased the efficiency of this inhibitor. In this chapter, because of changes in experimental conditions (e.g., supersaturation of the solution, larger volume of the crystallisation solution, etc.), the gypsum crystals precipitated in the absence of additives had thinner and twinned morphologies which were different than the morphology of the gypsum crystals in chapters 4 and 5. The additives modified the morphology of the gypsum crystals and in the presence of for example PAA_{2K} at pH ~ 7, loose, tiny crystals with a size range of 20 nm to 5 µm precipitated.

When I tested the effects of phosphonate inhibitors, my results demonstrated that they all also inhibited gypsum formation and that the time needed for gypsum precipitation increased in the order HEDP < ATMP < PAPEMP < DTPMPA < BHMTPMPA. This is because the inhibition order matches the increasing the number of phosphonate functional groups in the structure of the additives (chapter 7). Indeed, BHMTPMPA completely inhibited the formation of gypsum. The turbidity plots in this chapter had different development trends than the observed turbidity plots in chapters 4, 5 and 6 which could be due to the differences in the mechanisms by which the phosphonate additives inhibited gypsum formation. Changes in the solution composition and gypsum surface analyses revealed that depending on the additive type and its deprotonation state, phosphonate antiscalants were depleted from the crystallisation solution as a result of their surface adsorption and / or structural incorporation

into the growing gypsum, which was evidenced by a sudden and sharp increase in turbidity during the reaction (e.g., in the presence of HEDP at pH ~ 7). The XPS analysis illustrated the surface adsorption of the phosphonate inhibitors. Digesting the precipitated gypsum crystals before and after the desorption experiments revealed the structural incorporation of the phosphonate additives or their strong irreversible surface adsorption via a ligand-exchange mechanism. Thin and twin gypsum crystals precipitated from the additive-free solution and this contrasted with the short and thick crystals that formed in the presence of HEDP at pH ~ 7 and ATMP at pH ~ 4. These also contrasted with gypsum growth in the presence of PAPEMP and DTPMPA at pH ~ 4, in which both short and thick crystals and long dendritic needles were obtained. However, based on the obtained morphologies I concluded that none of the phosphonate antiscalants except BHMTPMPA are suitable to be used in many industries (e.g., those with membranes such as water desalination) because, short and thick crystals and long dendritic gypsum needles would block such membranes.

From all these studies I can conclude that all the additives were gypsum growth inhibitors except PASP and BHMTPMPA which were nucleation inhibitors. Furthermore, gypsum inhibition occurs with all tested additives, following the inhibition order: alkali / alkaline earth metal cations < carboxylic acids < polycarboxylic acids ≤ phosphonates and I also highlight the potential of biodegradable inhibitors to replace phosphonate inhibitors.

8.2. Outlook

There are still some knowledge gaps in terms of understanding the mechanisms by which the antiscalants affect the nucleation and growth of gypsum which need further investigation. I suggest below some potential future experimental and theoretical approaches, which might help to gain better insights into gypsum scaling:

- Molecular modelling to understand the surface adsorption mechanism of antiscalants with gypsum crystals. Such a study may illustrate the configuration of the adsorbed additives on gypsum crystals.
- Investigating the interaction of antiscalants with gypsum crystals grown in the presence of other mineral scales or grown from solutions with different background electrolytes. This may help quantify the effect of background electrolyte on the efficiency of antiscalants in inhibiting gypsum scaling.
- Further investigating the adsorption of the additives and inhibitors on gypsum crystals by different adsorption isotherms.
- Utilising other molecular-level and *in-situ* approaches (e.g., Atomic Force Microscopy, microfluidic cells, etc.) to follow the interaction between antiscalants and growing gypsum crystals.
- Preparing cross sections of gypsum crystals synthesised in the presence of, for example, phosphonates (e.g., by FIB), and analysing with high-resolution micro-spectroscopy (e.g., EELS) to reveal the association mechanism between the additives and the forming gypsum crystals.
- Designing a set-up to study the heterogeneous nucleation and surface growth mechanisms of gypsum crystals. Such a study will help elucidate the effect of substrate type (e.g., steel, brass), surface roughness, and hydrodynamic factors (e.g. fluid flow velocity) on the nucleation and growth of gypsum crystals. Such a study should also be designed with a view to mimic gypsum precipitation on, for example, heat exchangers, in pipelines, and in water desalination plants (membrane blockage).

Appendix A Supporting Information for chapter 5

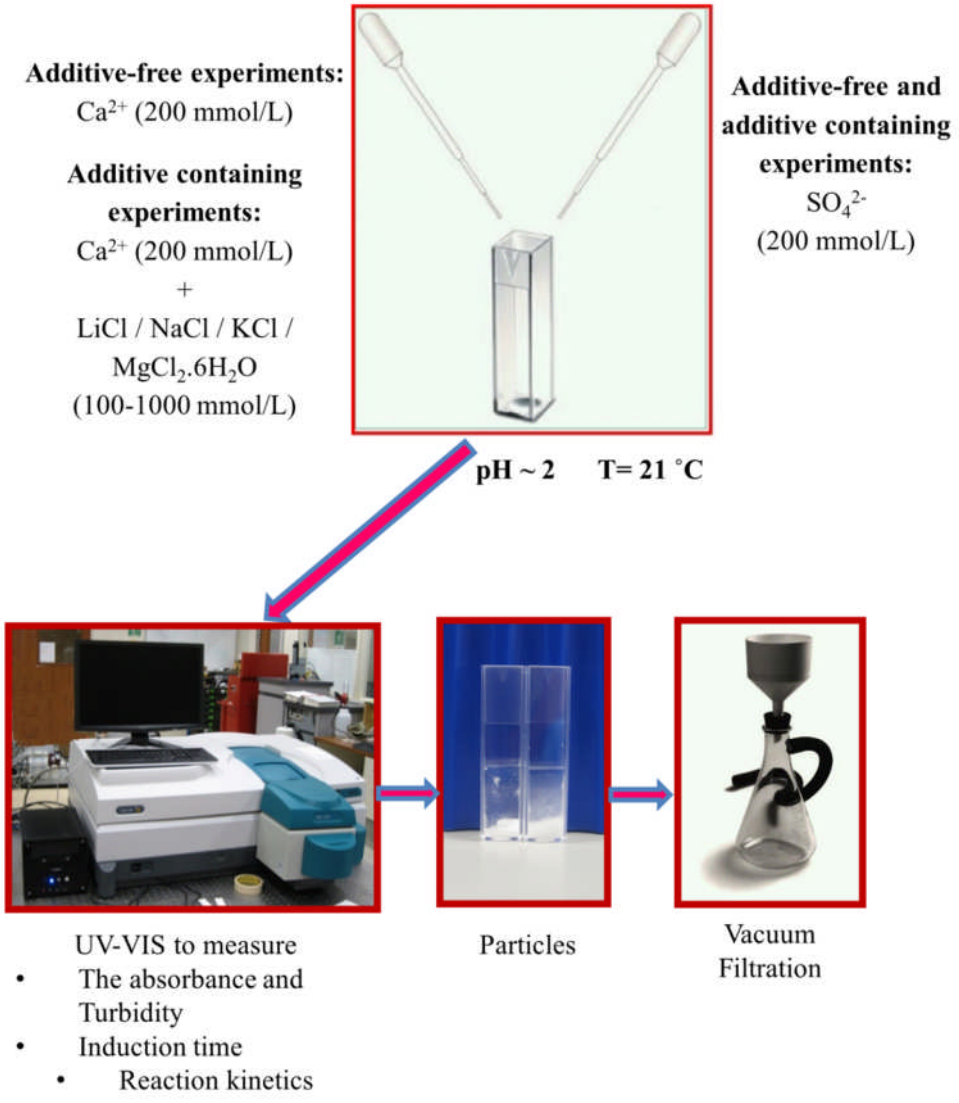

Figure A.1.The schematic of producing calcium sulfate dihydrate in the presence and absence of additives.

Table A.1.The limit of detection and uncertainty of ICP-MS / ICP-OES measurements.

	Li	Na	K	Mg	Ca
Limit of detection /ppm	3.35×10^{-4}	1.88×10^{-3}	4.07×10^{-3}	1.30×10^{-3}	4.50×10^{-3}
% uncertainty	1.62	2.02	2.08	1.38	2.09

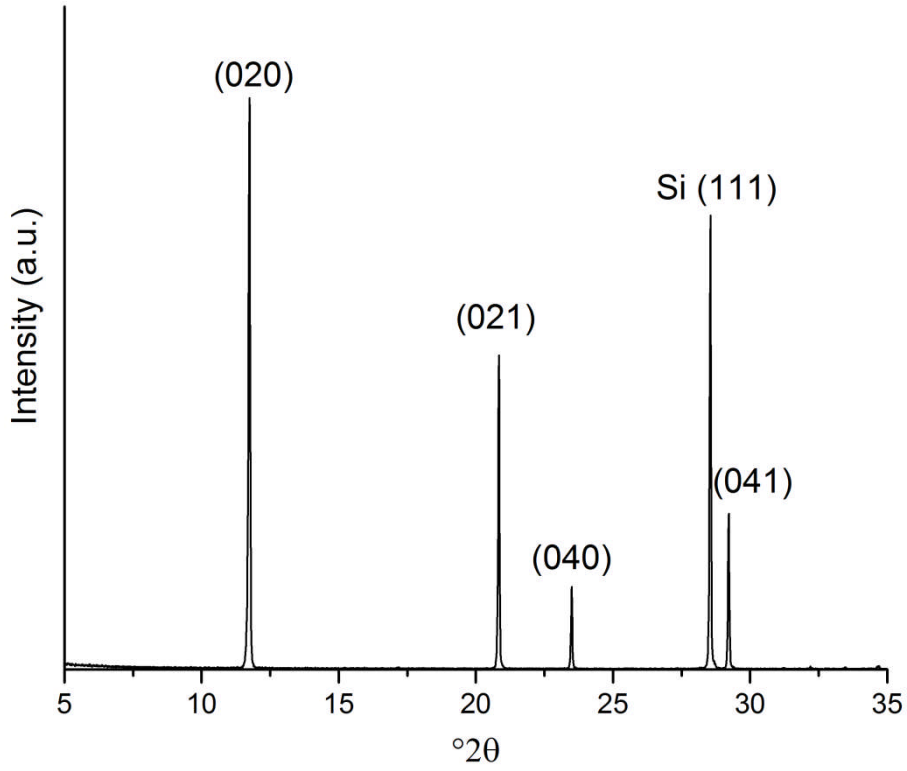

Figure A.2.XRD pattern with marked Bragg peaks representative of crystals synthesized in the absence of additives confirming that the end-product was gypsum; Si (111) was used to determine the d-spacing precisely.

Table A.2.Changes in induction time as a function of additive concentrations. Note that the induction time in the additive-free system was 3±1 minutes.

		Li^+		
concentration (mM)	50	100	300	500
induction time (min)	6±1	7±1	10±1	13±1
		Na^+		
concentration (mM)	50	100	300	500
induction time (min)	5±1	6±1	8±1	10±1
		K^+		
concentration (mM)	50	100	300	500
induction time (min)	5±1	6±1	7±1	8±1
		Mg^{2+}		
concentration (mM)	50	100	150	200
induction time (min)	9±1	17±1	23±3	32±4

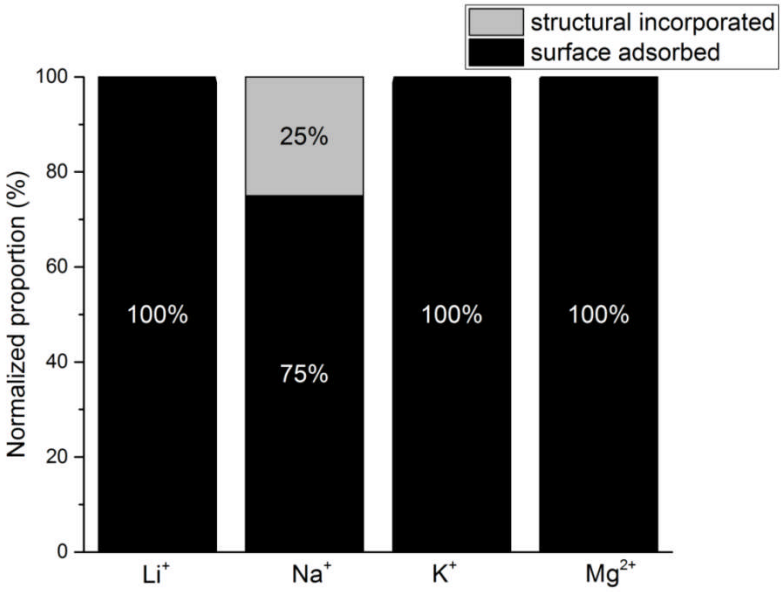

Figure A.3.Partitioning of cations between gypsum crystal surfaces (adsorption) or crystal matrixes (structural incorporation).

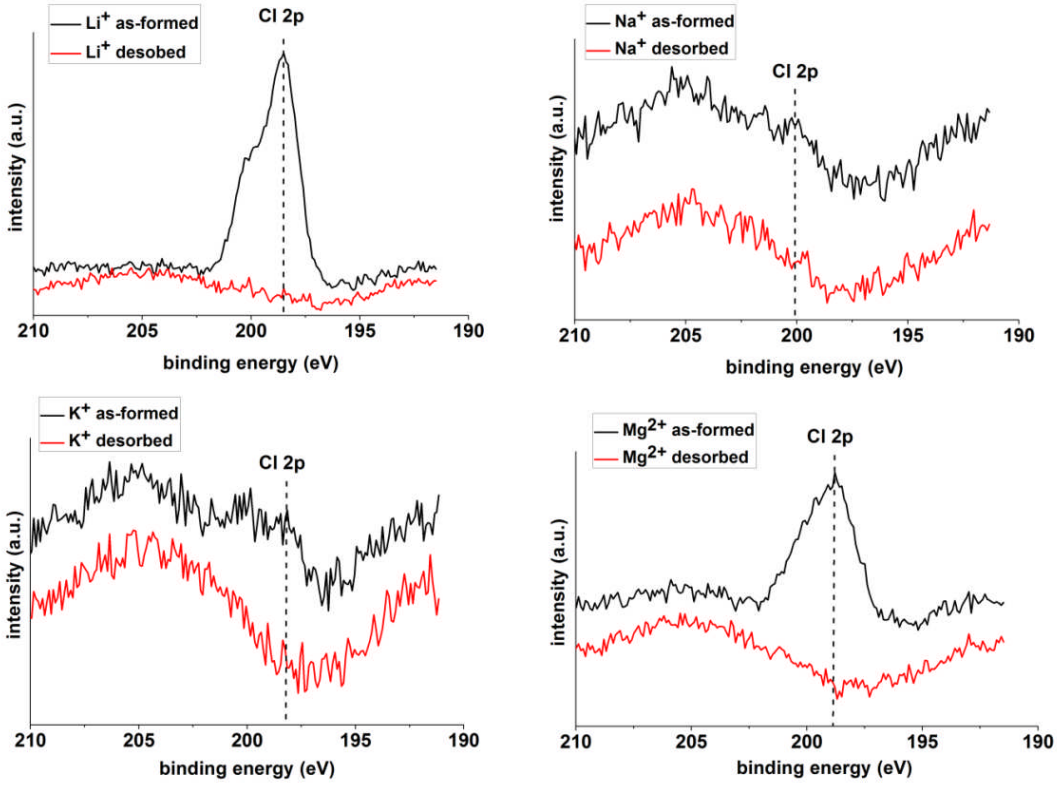

Figure A.4.XPS spectra for Cl^- indicating that Cl^- was associated with the as-formed gypsum end-products (black patterns). Cl^- was removed during desorption (red patterns) for all tested ions.

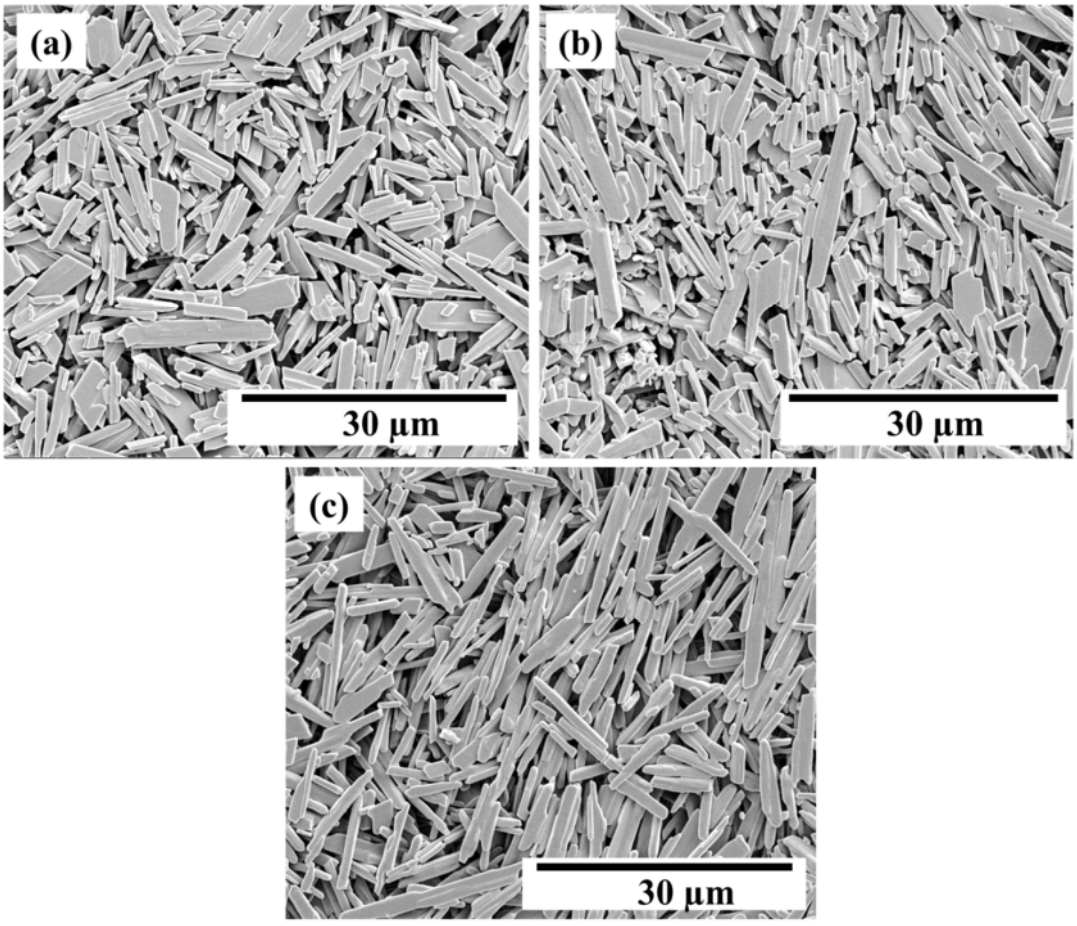

Figure A.5.SEM morphology the gypsum crystals obtained after 200 minutes in the presence of (a) 500 mM Na^{+}; (b) 500 mM K^{+}; and (c) 200 mM Mg^{2+}.

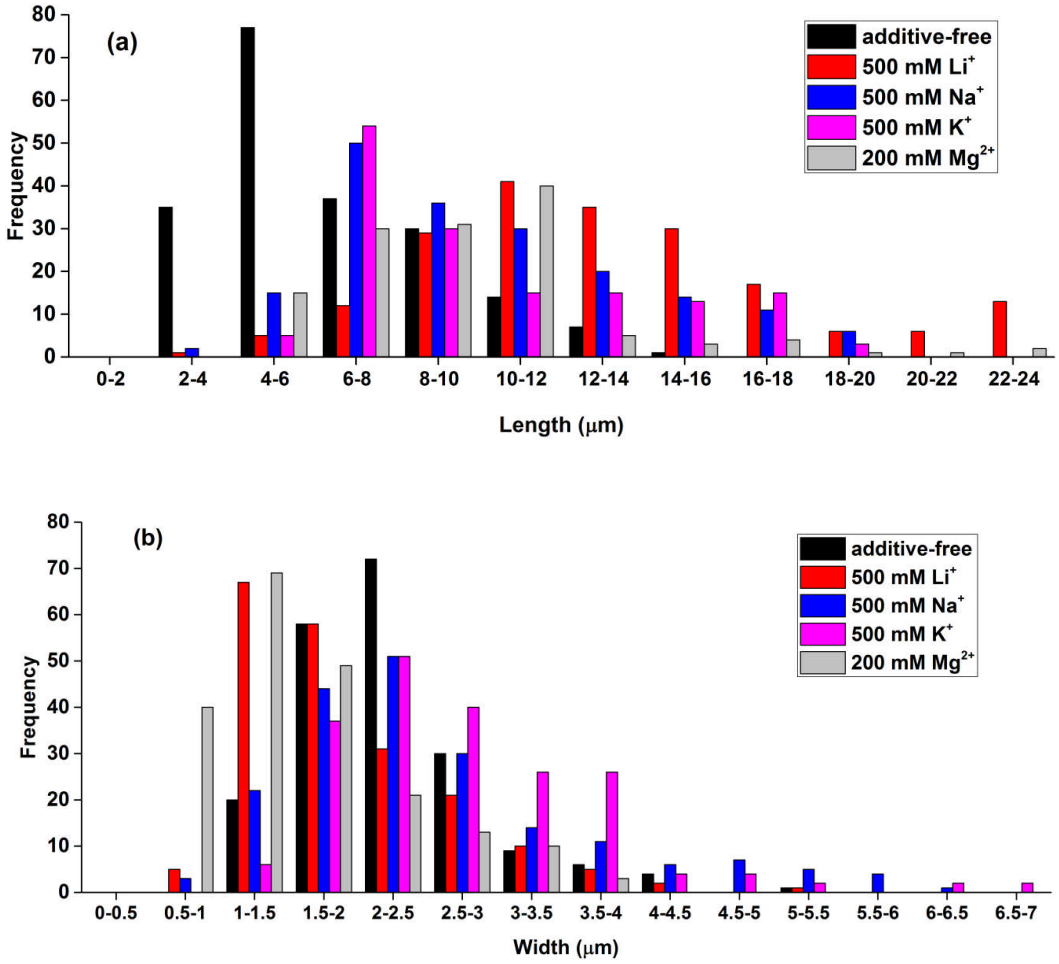

Figure A.6.(a) Length and (b) width distribution of gypsum end-products precipitated in the presence and absence of additives.

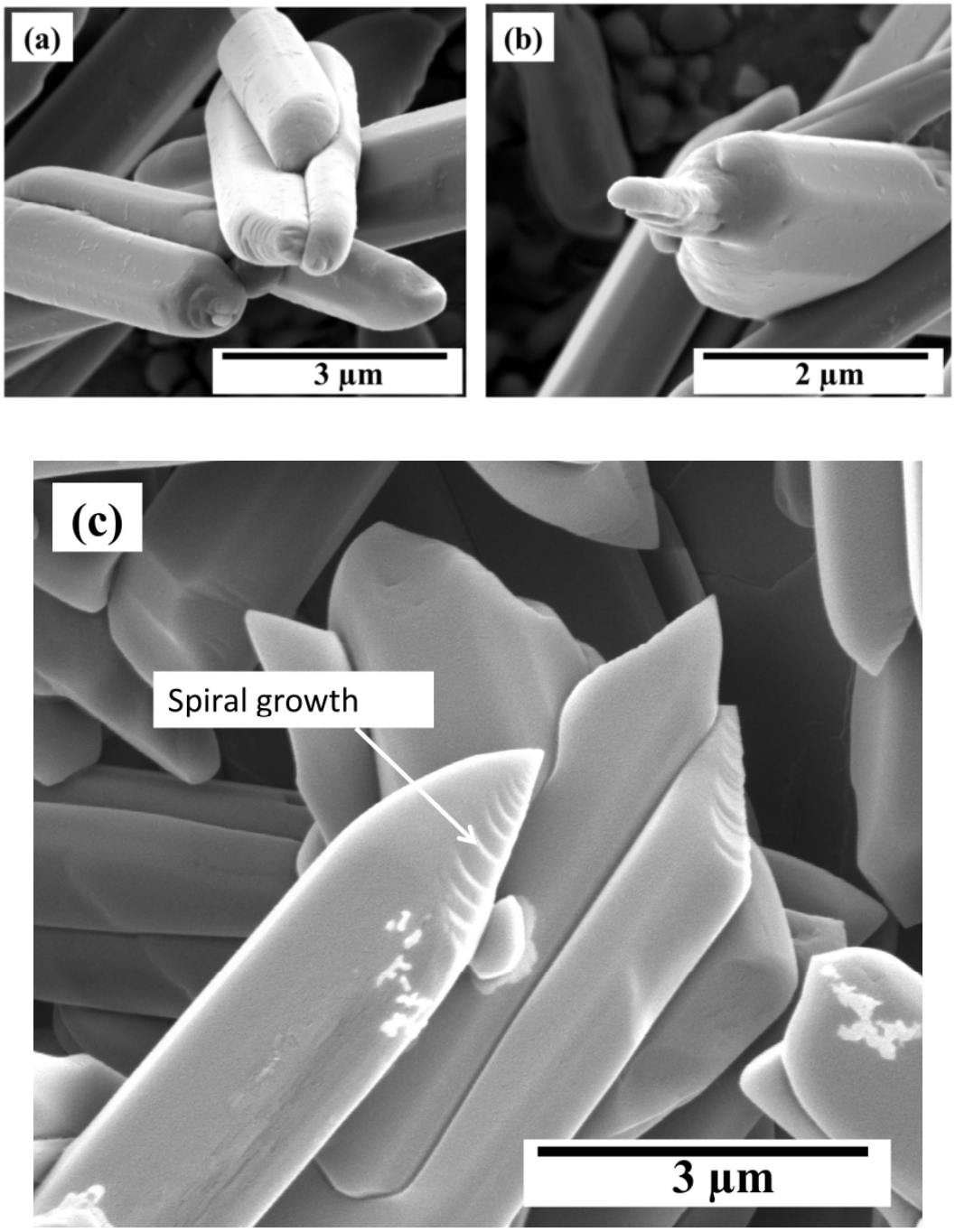

Figure A.7.(a-c) SEM micrograph of gypsum crystals obtained after 200 minutes in the presence of 500 mM Li^+ illustrating the growth steps and the spiral growth mode visible at the crystals tips.

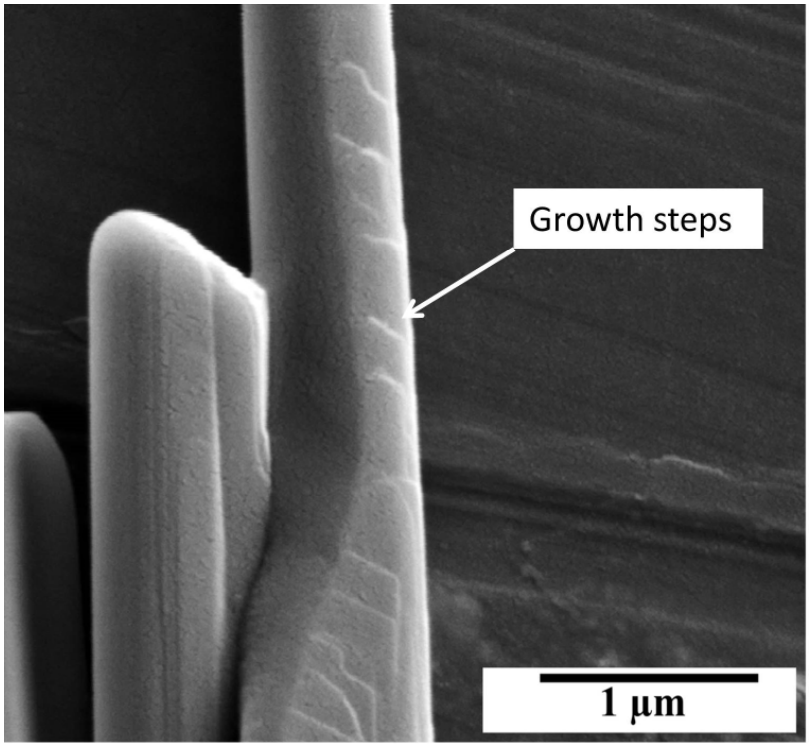

Figure A.8.SEM micrograph of gypsum crystals obtained after 200 minutes in the presence of 500 mM Na^+ illustrating the uneven growth mode and growth steps.

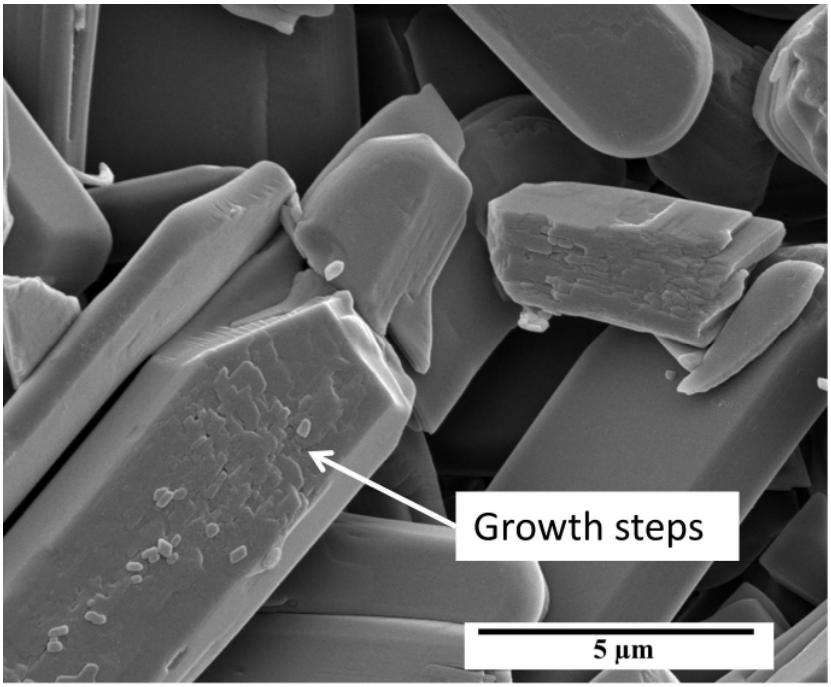

Figure A.9.SEM micrograph from gypsum crystals obtained after 200 minutes in the presence of 500 mM K^+ illustrating the presence of growth steps.

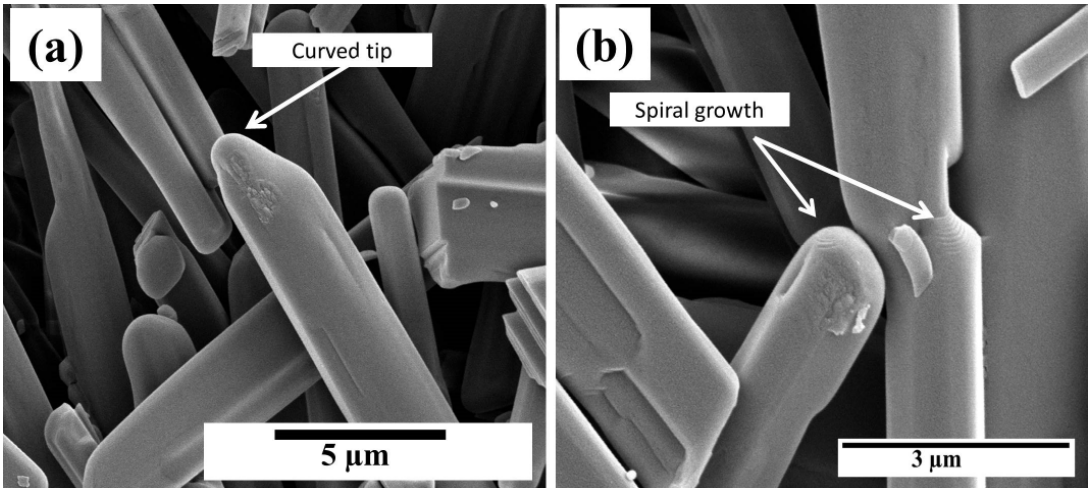

Figure A.10.SEM micrograph from gypsum crystals obtained after 200 minutes in the presence of 200 mM Mg^{2+} illustrating the presence of spiral growth and curved tips.

Table A.3.Predicted saturation indices of gypsum crystals as a function of additive concentrations calculated by PhreeqC software. Note that the saturation index of gypsum in the additive-free system was 0.55.

		Li^+		
concentration (mM)	50	100	300	500
saturation index	0.53	0.51	0.43	0.37
		Na^+		
concentration (mM)	50	100	300	500
saturation index	0.53	0.51	0.43	0.38
		K^+		
concentration (mM)	50	100	300	500
saturation index	0.52	0.49	0.4	0.33
		Mg^{2+}		
concentration (mM)	50	100	150	200
saturation index	0.48	0.43	0.38	0.34

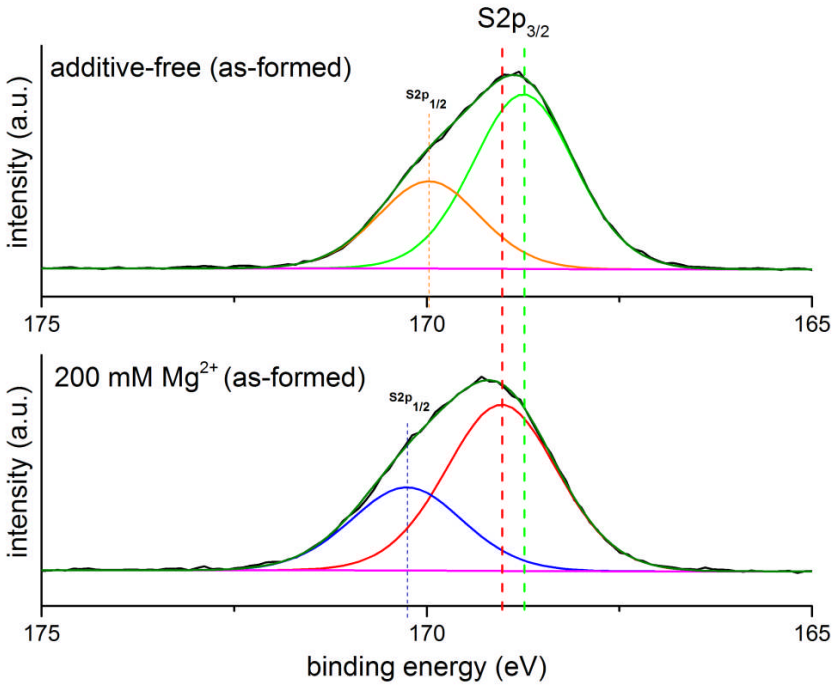

Figure A.11.Mg^{2+} surface adsorption caused a 0.5 eV shift in S $2p_{3/2}$ binding energy towards higher binding energy.

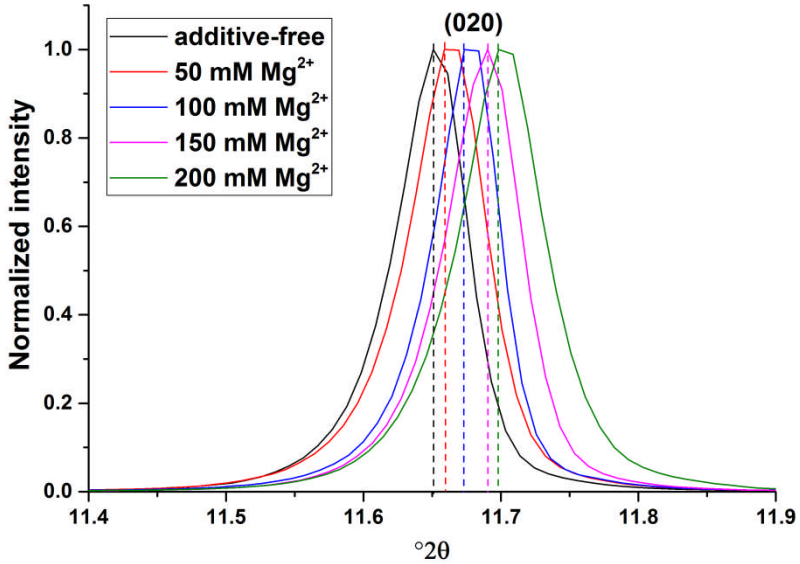

Figure A.12.Shift towards lower diffraction angles in the gypsum (020) peak position as a function of Mg^{2+} concentration.

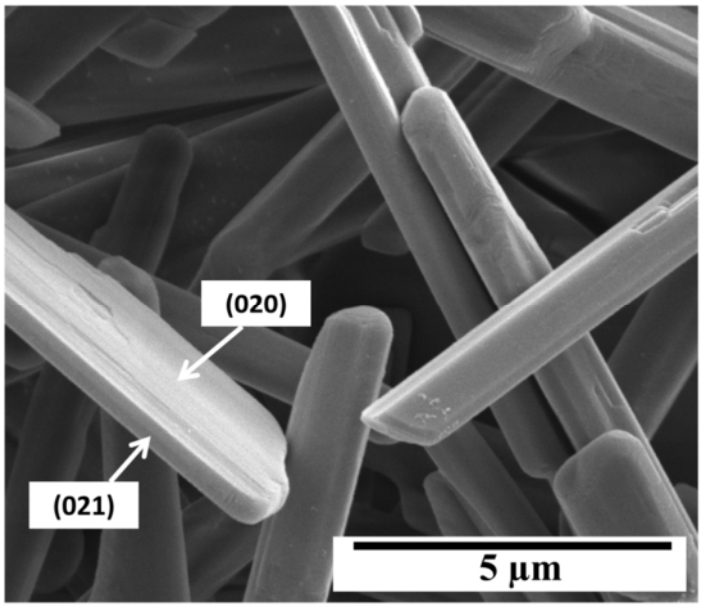

Figure A.13.(020) and (021) faces of a gypsum crystal synthesised in the presence of 500 mM Na^+.

Appendix B Supporting Information for chapter 7

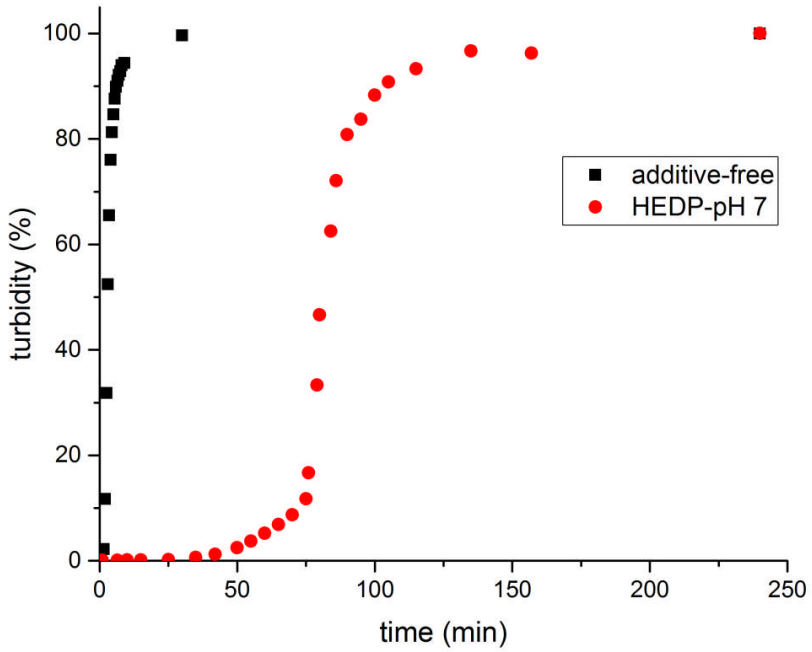

Figure B.1.Turbidity curves plotted as a function of time in the absence and presence of 20 ppm HEDP at pH ~ 7.

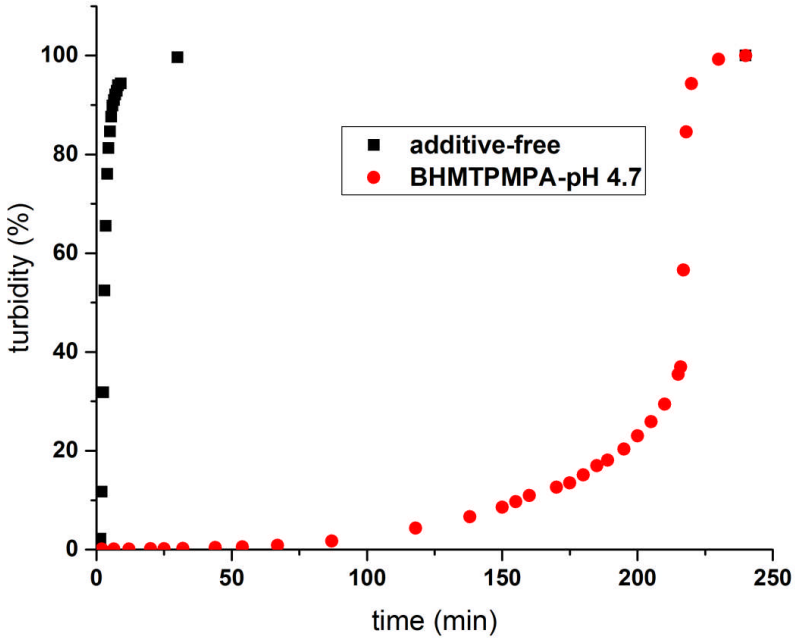

Figure B.2.Turbidity curves plotted as a function of time in the absence and presence of 5 ppm BHMTPMPA at unadjusted pH of ~ 4.7.

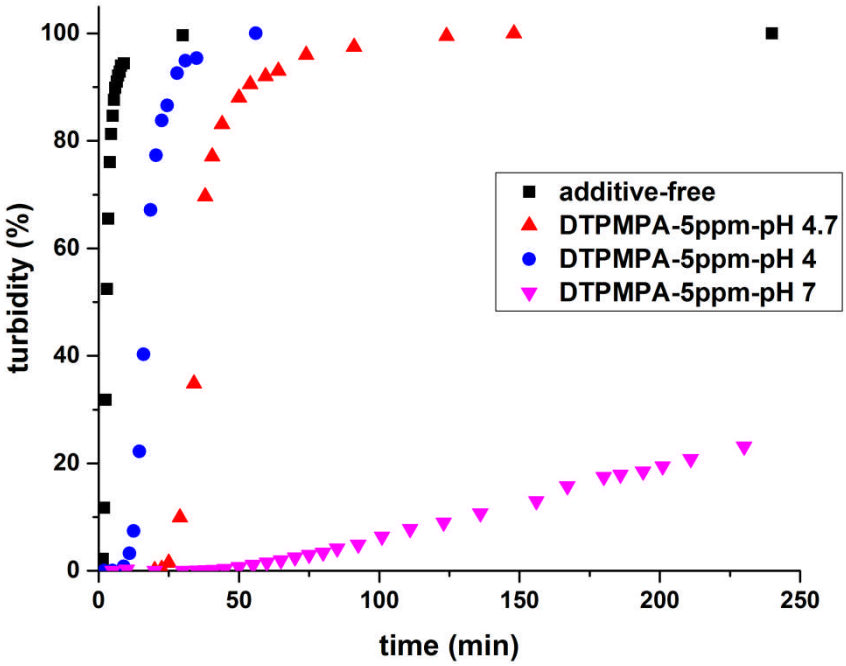

Figure B.3.Turbidity curves plotted as a function of time in the absence and presence of 5 ppm DTPMPA at different pH of ~ 4 and ~ 7 and unadjusted pH of ~ 4.7.

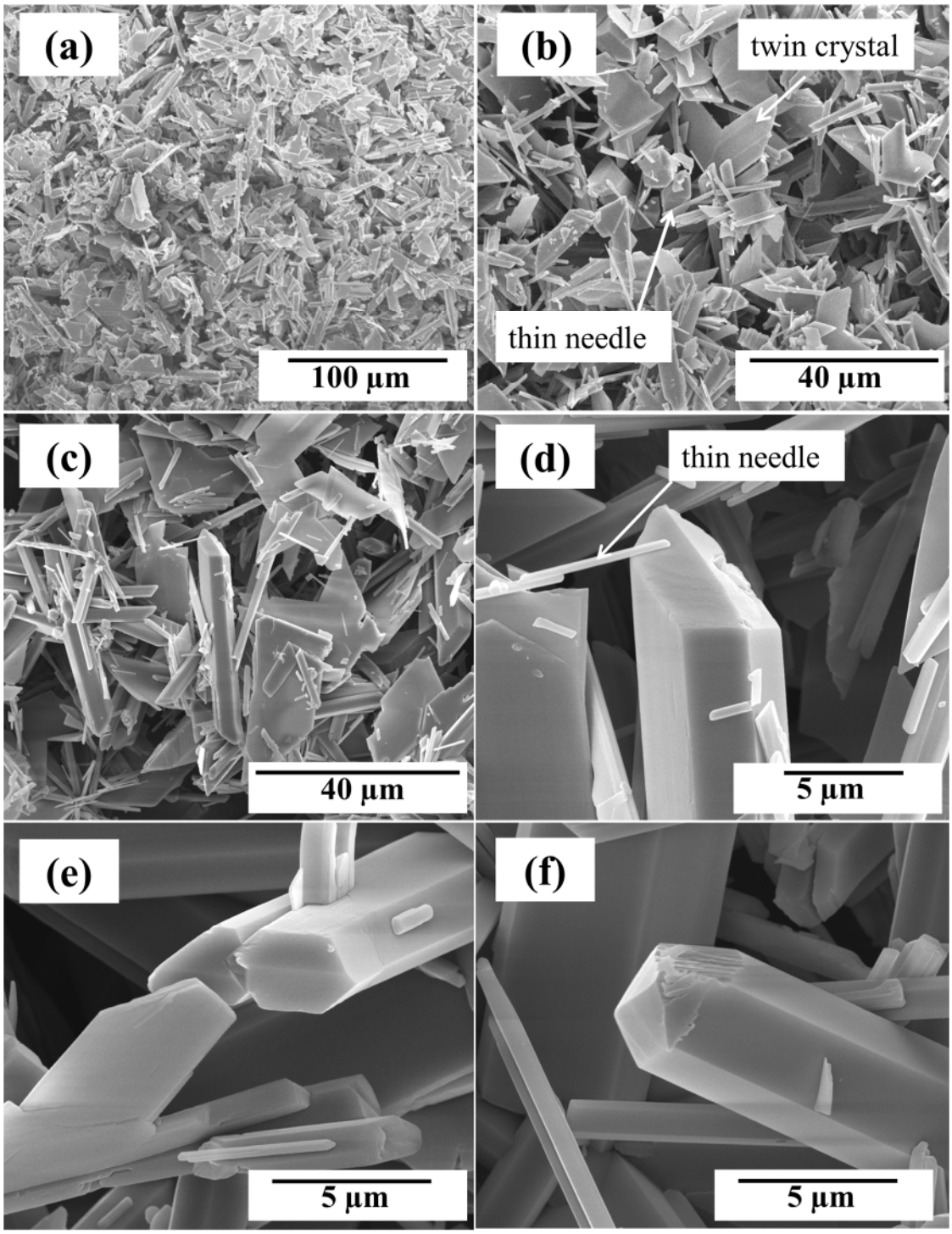

Figure B.4.SEM micrograph of gypsum crystals gathered after 240 minutes from experiments in 20 ppm HEDP at pH ~ 7.

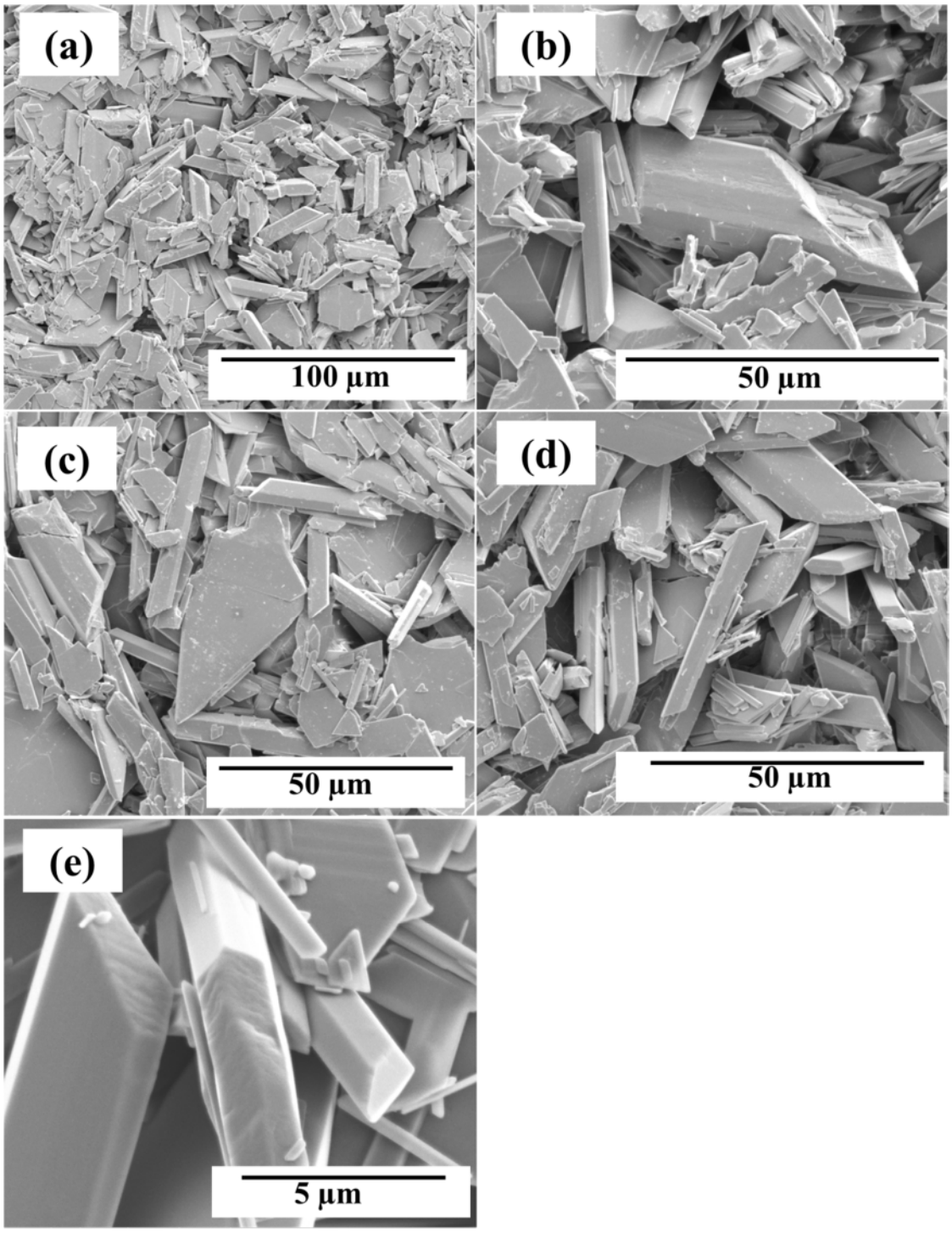

Figure B.5.SEM micrograph of gypsum crystals gathered after 240 minutes from experiments in 20 ppm ATMP at pH ~ 4.

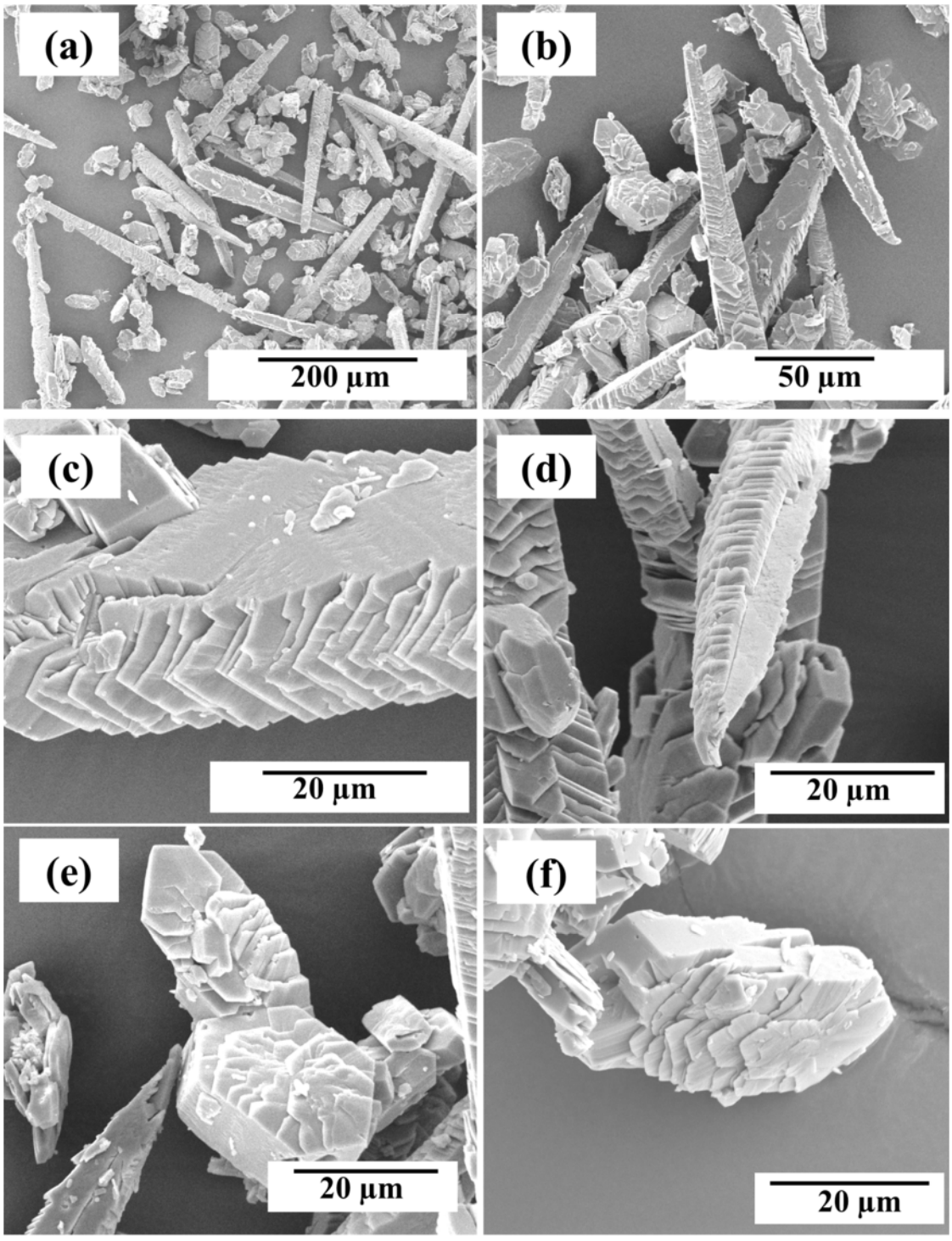

Figure B.6.SEM micrograph of gypsum crystals gathered after 240 minutes from experiments 20 ppm PAPEMP at pH ~ 4.

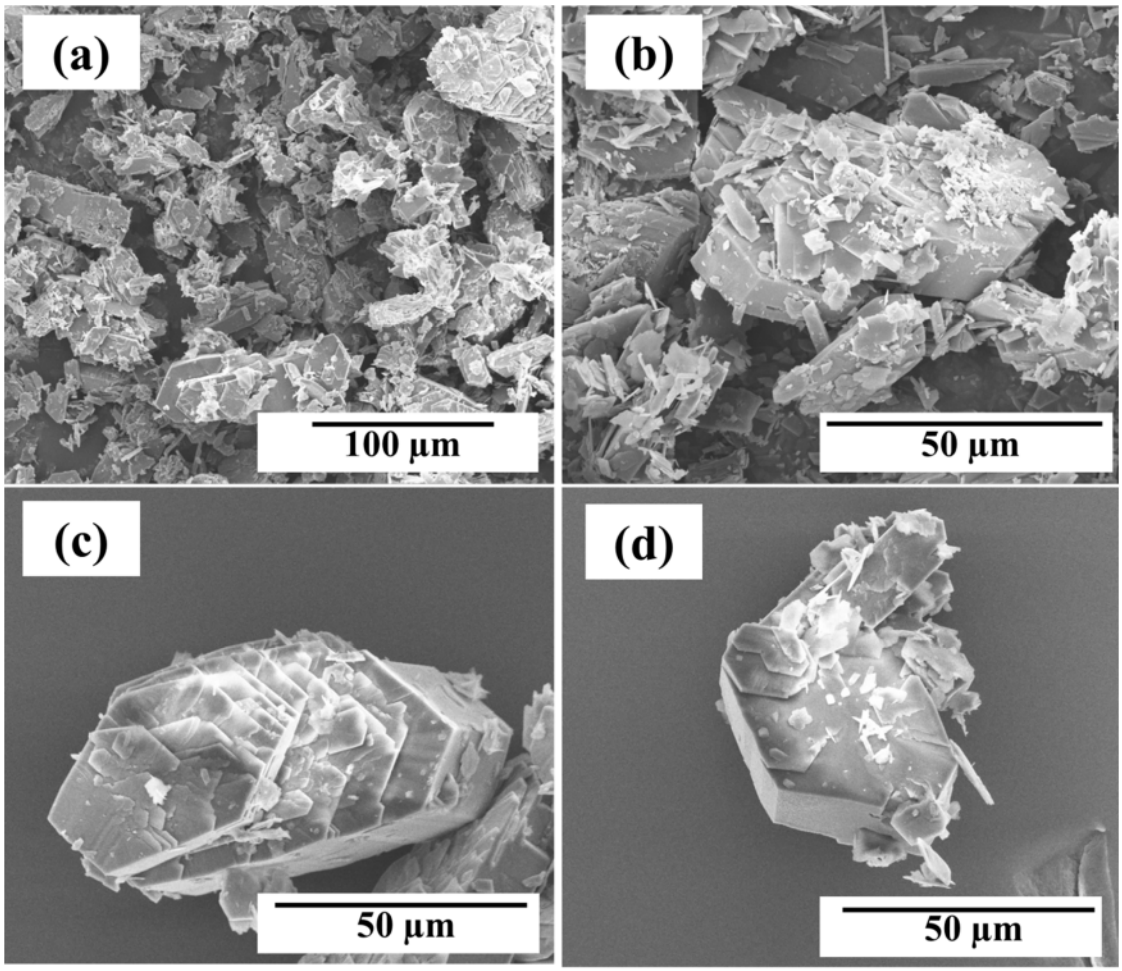

Figure B.7.SEM micrograph of gypsum crystals gathered after 240 minutes from experiments in 20 ppm DTPMPA at pH ~ 4.

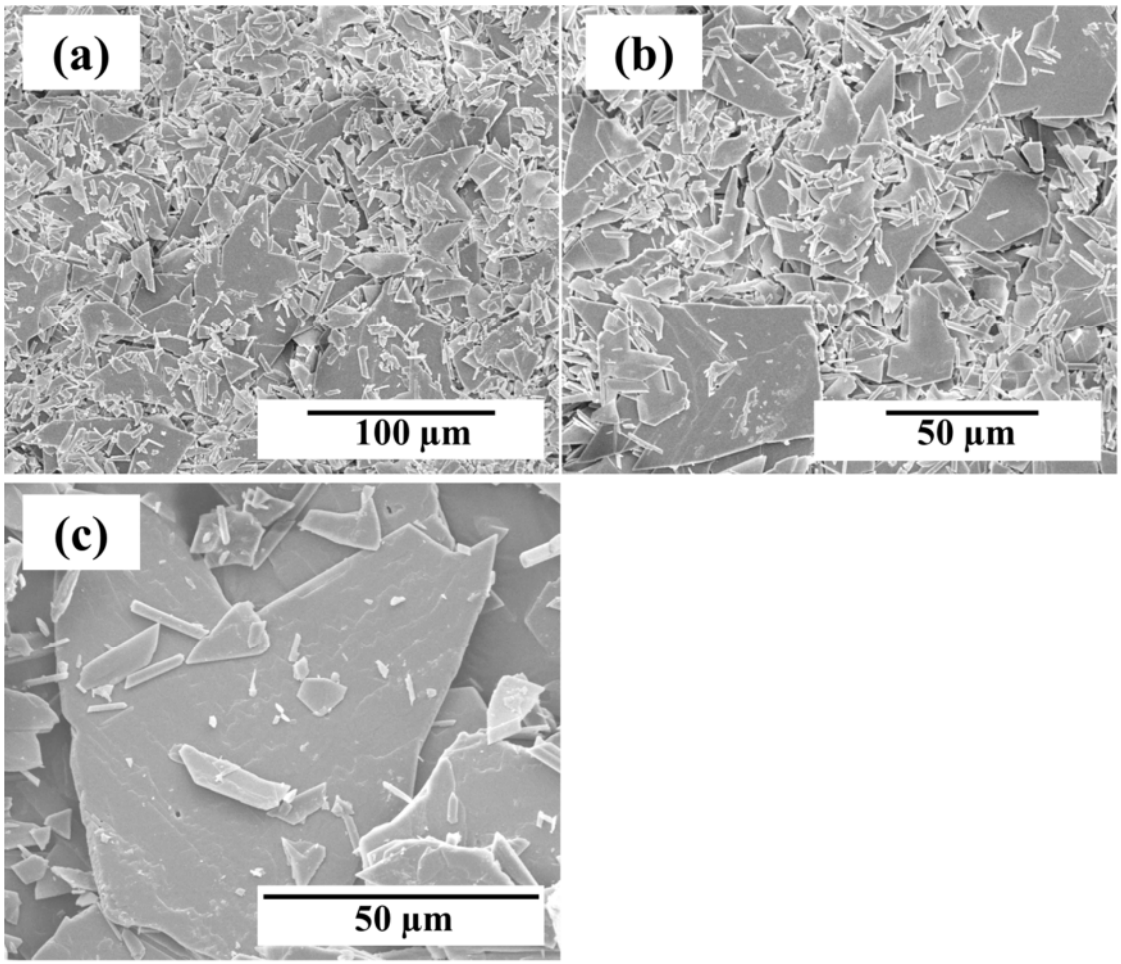

Figure B.8.SEM micrograph of gypsum crystals gathered after 240 minutes from experiments in 5 ppm DTPMPA at pH ~ 4.

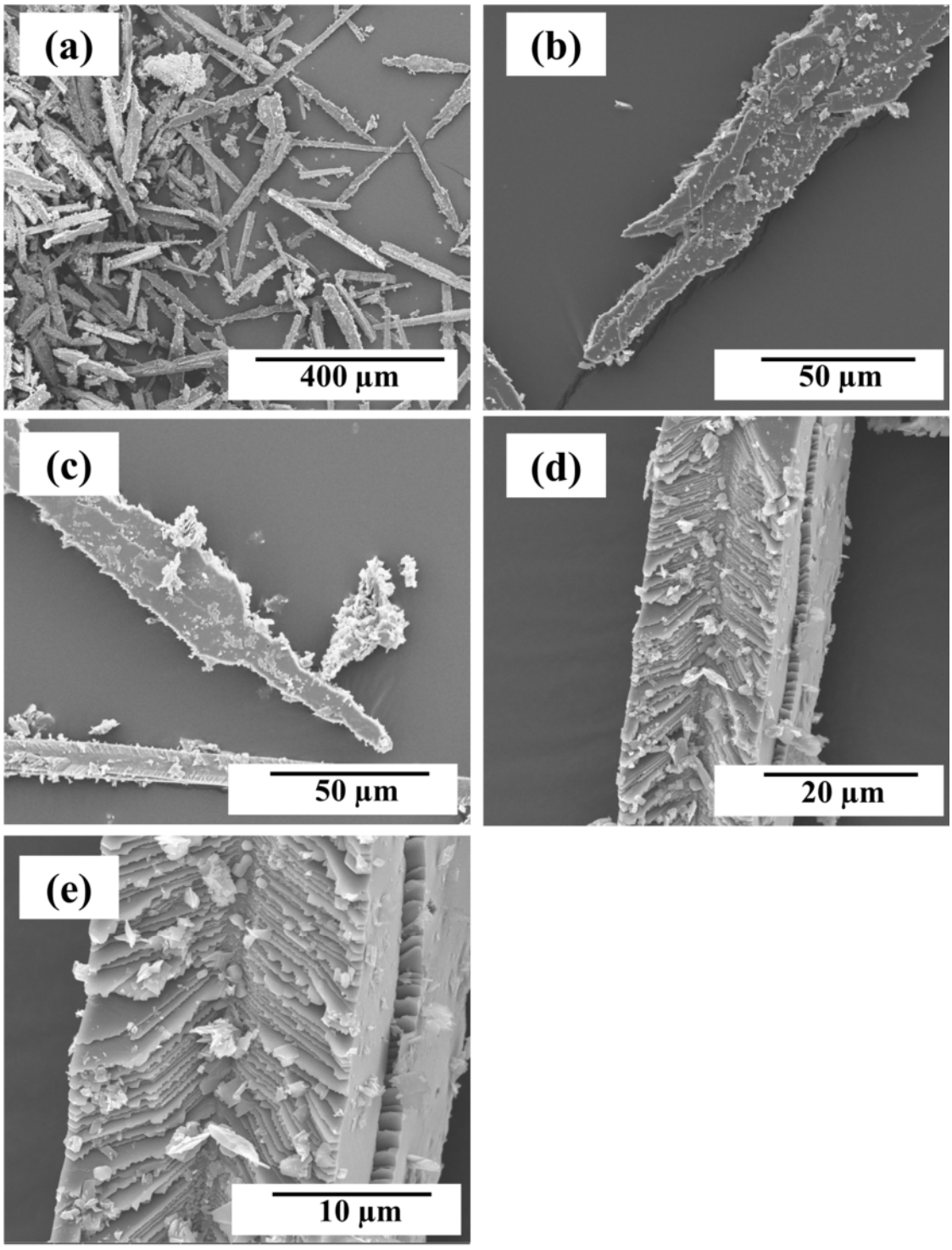

Figure B.9.SEM micrograph of gypsum crystals gathered after 240 minutes from experiments in 5 ppm DTPMPA at pH ~ 7.

Appendix C A Report on an investigation of the effects of a commercial additive on for crystallinity, shapes and sizes of pure and mixed PbS and ZnS particles

As part of collaboration between my supervisor and Clariant Oil Services UK Ltd, it was planned initially to investigate the effects of an antiscalant developed by the company, on lead and zinc sulfide mineral scale formation. After this initial investigation, however, we realised that a mechanistic understanding of the problem would be beyond the scope of this thesis. Therefore, I ultimately finished this report but then focused on the calcium sulfate system alone.

In this report, I summarised in brief the findings from the evaluations done on the samples provided by Clariant Oil Services UK Ltd.

C.1. Introduction

Following the meeting with Dr. Jamie Kerr and Dr. Adam Savin from Clariant Oil Services UK Ltd Company, 15 samples were received for analyses. These were sealed in glass jars and labelled as in Tables C.1-C.3 according to their chemical composition and the additive concentrations. The purpose of this report is to document the work carried out in Leeds that aimed to characterise the precipitates in these samples using X-ray diffraction (XRD) and transmission electron microscopy (TEM) and to analyse the resulting data in order to provide

enough data for a possible abstract to a conference and to develop a view for possible future work. As mentioned above the work did not continue beyond this report.

Table C.1.Details about the pure Pb-S systems (in all cases excess H_2S was added).

Jar number	Solution colour	Aspect	$[Pb^{2+}]$ mM	$[Zn^{2+}]$ mM	Additive concentration (ppm)
10	Black	Precipitated	2	0	0
2	Black	Precipitated	2	0	500
5	Black	Precipitated	2	0	1000
9	Black	Suspended	2	0	5000
11	Black	Suspended	2	0	10000

Table C.2.Details about the pure Zn-S systems (in all cases excess H_2S was added).

Jar number	Solution colour	Aspect	$[Pb^{2+}]$ mM	$[Zn^{2+}]$ mM	Additive concentration (ppm)
15	White	Precipitated	0	2	0
6	White	Precipitated	0	2	500
7	White	Precipitated	0	2	1000
12	White	Suspended	0	2	5000
13	White	Suspended	0	2	10000

Table C.3.Details about the mixed Pb-S / Zn-S systems (in all cases excess H_2S was added).

Jar number	Solution colour	Aspect	$[Pb^{2+}]$ mM	$[Zn^{2+}]$ mM	Additive concentration (ppm)
14	Black	Precipitated	1	1	0
8	Black	Precipitated	1	1	500
3	Black	Precipitated	1	1	1000
4	Black	Suspended	1	1	5000
1	Black	Suspended	1	1	10000

C.2. Experimental methods

All jars were visually inspected prior to sample preparation to investigate the additive concentration effect on degree of solution suspension. Samples that were not precipitated but in suspension, were also centrifuged for 10 minutes at 4000 rpm using an Eppendorf 5810 centrifuge to evaluate if the samples with suspended particles could easily be separated. This procedure indicated that the samples that were in suspension, were stable.

Therefore, to prepare samples for X-ray diffraction (XRD) and transmission electron microscopy (TEM) analysis, vacuum-filtration was used. All solutions were filtered through 0.2 µm polycarbonate filter papers followed by washing with Milli-Q water and isopropanol to remove all salts and dry the samples.

The mineralogical characterisation was carried out using powder X-ray diffraction (XRD, Bruker D8 diffractometer; Cu $K_{\alpha 1}$). Patterns were collected from 10 to 80º ($2\theta^{\circ}$), at a rate of 0.0105° / step. The resulting patterns were analysed with the EVA (version 3) software and PDF-2-1996 database to identify the phases, while the Bruker TOPAS (version 4.2) software was used to determine the proportion of phases in the precipitated materials through Rietveld refinement analyses. Furthermore, crystallite sizes were calculated from the Bragg peak full-width half-maximum (FWHM) of the main peaks using the Scherrer equation.

The microstructure of the samples from the Pb-S, Zn-S and Pb-S / Zn-S systems in the presence of the highest concentration of additive and without additives (samples No. 10, 11, 15, 13, 14 and 1) were investigated by transmission electron microscopy (TEM, JEM1400; samples were imaged at 120k eV after being deposited on holey carbon coated AGAR copper grids). Following TEM imaging, the particle sizes of the precipitates were evaluated by measuring the length and width of 100 particles each using the Image J software.

C.3. Results and discussion

Figure C.1 (a,d) shows the visual aspect of the jars as received. It is obvious that the addition of 5000 and 10000 ppm additive to the Pb-S, Zn-S and Pb-S / Zn-S systems caused the

particles to remain suspended (Figure C.1 b,d) while at additive concentration below 5000 ppm all particles precipitated out of solution (Figure C.1 a,c). Adding 500 ppm and 1000 ppm additive to the mixed Pb-S / Zn-S system caused some of the particles to remain suspended in solution and / or stick to the jar surface. Increasing the additive concentration from 500 to 1000 intensified this phenomena (Jar No. 3 and 8; Figure C.2 a,b).

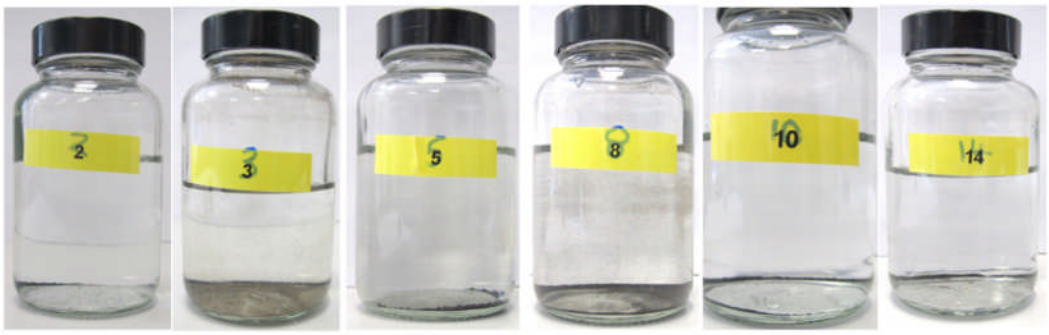

(a)

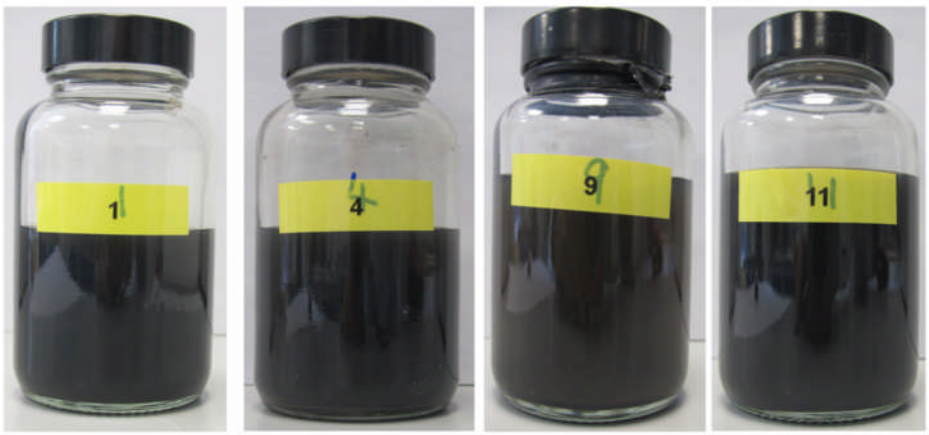

(b)

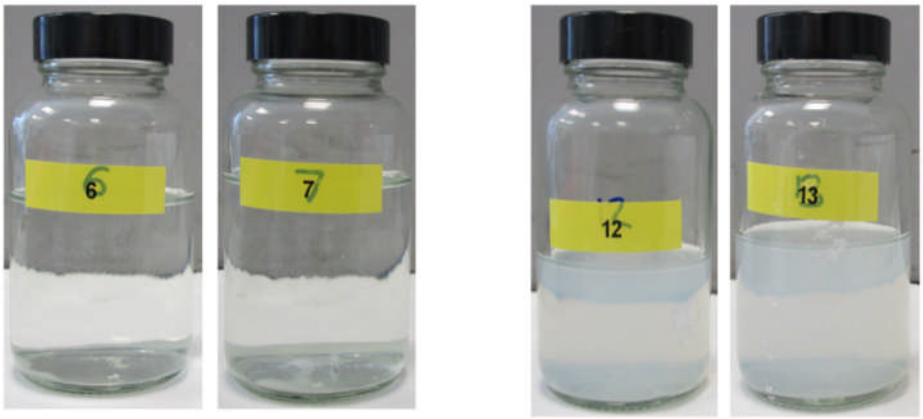

(c) (d)

Figure C.1.Visual aspects of the jars as received; (a) samples that were black in colour and that were precipitated; (b) Samples that were black in colour but that remained in suspension; (c) white, precipitates systems; (d) White systems but in suspension.

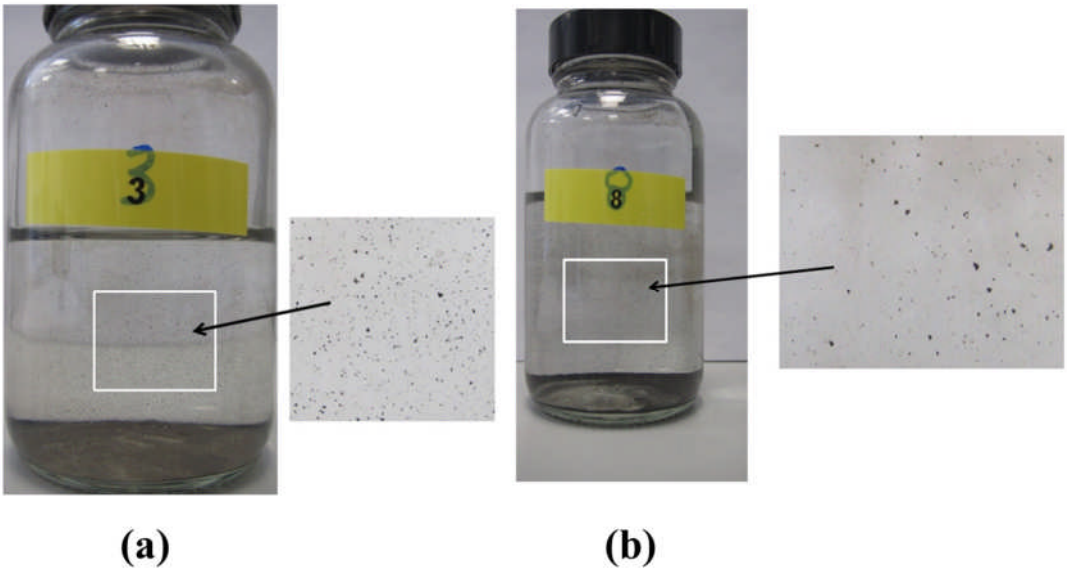

Figure C.2.The effect of additive concentration on the suspension behaviour of the Pb-S / Zn-S solution; (a) 1000 ppm; and (b) 500 ppm. Note that at higher additive concentration more black particles formed on the glass jars.

Figure C.3 shows a typical XRD pattern of powders obtained from a pure Pb^{2+} containing solution in the absence of additive (Jar No.10). The spectrum matches that of a pure PbS - Galena. All samples containing solely Pb^{2+} as a metal ion were made up of pure PbS particles, regardless of additive concentration. In Table C.4, the crystallite size calculations from all Pb-S system based on the Scherrer equation and the XRD peak (200) are presented. The data show a slight decrease in crystallite size with increasing additive concentration.

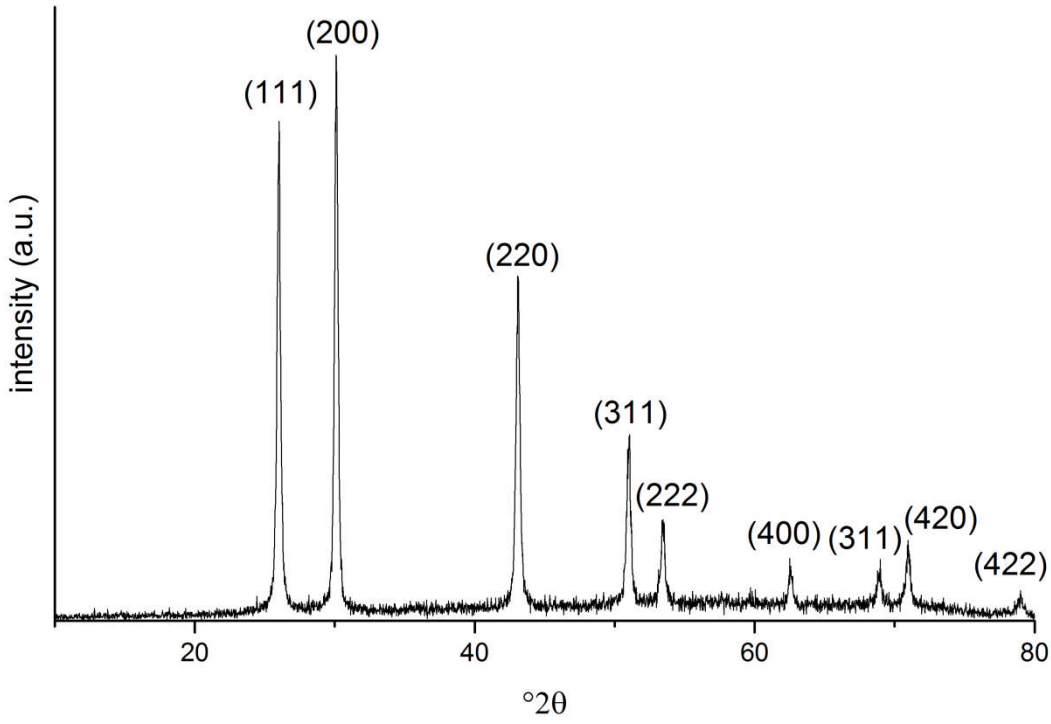

Figure C.3.A representative XRD pattern of powder obtained from the 2 mM Pb^{2+}, 0 mM Zn^{2+}, 0 ppm additive solution (sample No.10).

Table C.4.The crystallite size of the PbS (galena) powders.

Jar number	$[Pb^{2+}]$ mM	$[Zn^{2+}]$ mM	Additive concentration (ppm)	Crystallite size (nm)
10	2	0	0	29
2	2	0	500	22
5	2	0	1000	21
9	2	0	5000	19
11	2	0	10000	19

The additive-free Pb-S sample (Jar 10) and Pb-S sample with the highest additive concentration (Jar 11) were imaged and analysed with TEM. Representative TEM images of PbS particles in the absence and presence of additive together with their particle size distribution measurements are shown in Figures C.4 (a,b) and C.5 (a,b), respectively.

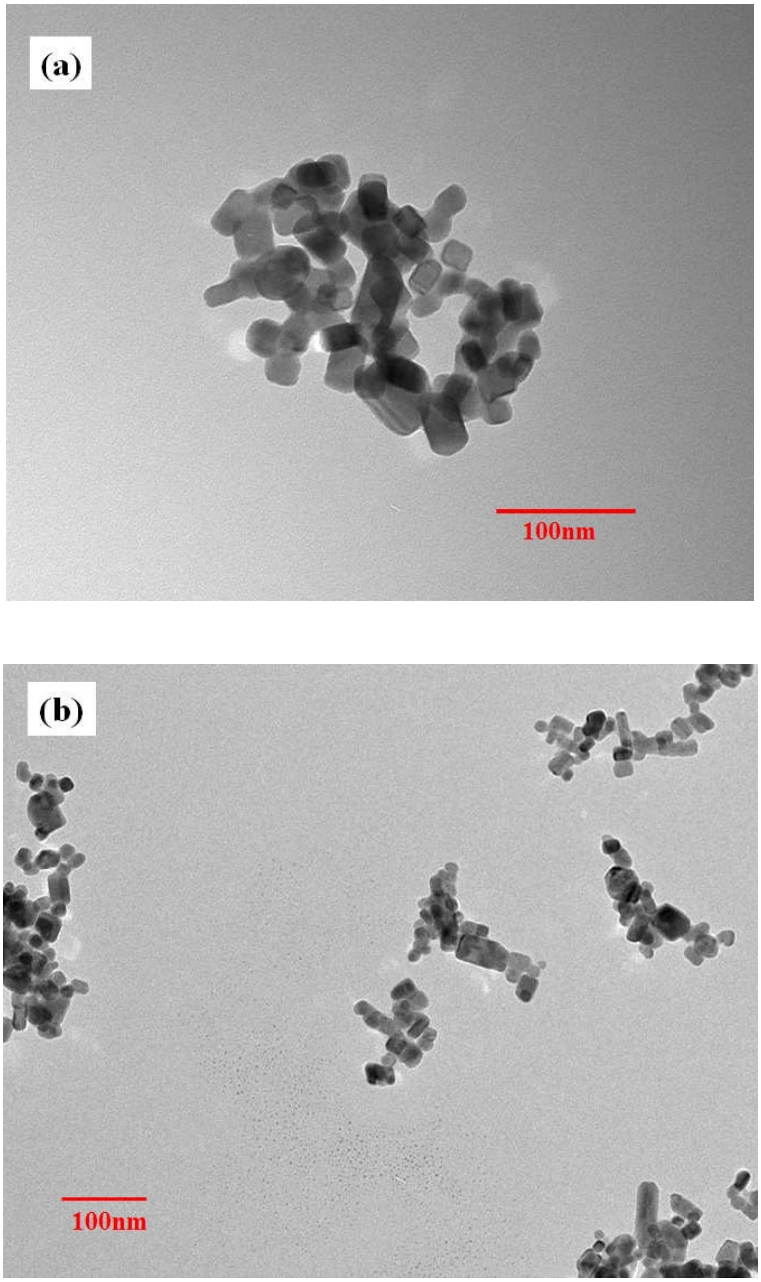

Figure C.4.TEM images of (a) the 2 mM Pb^{2+}, 0 mM Zn^{2+}, 0 ppm additive solution (sample No.10); and (b) the 2 mM Pb^{2+}, 0 mM Zn^{2+}, 10000 ppm additive solution (sample No.11).

It is obvious from the above images that the formed PbS particles were highly crystalline and mostly isometric in shape with only a slight elongation. In addition, the PbS particle sizes are smaller in the presence of the additive (Figure C.4 b) compared to the additive-free system (Figure C.4 a). The evaluation of aspect ratios of particles from the TEM images revealed that length and widths of the PbS particles in the additive Pb-S system were on average 15-20 nm

compared to the average of the additive-free PbS particles that reach median values of ~ 25-30 nm. Thus, the additive-free PbS particles were about 30-40 % larger (Figure C.5).

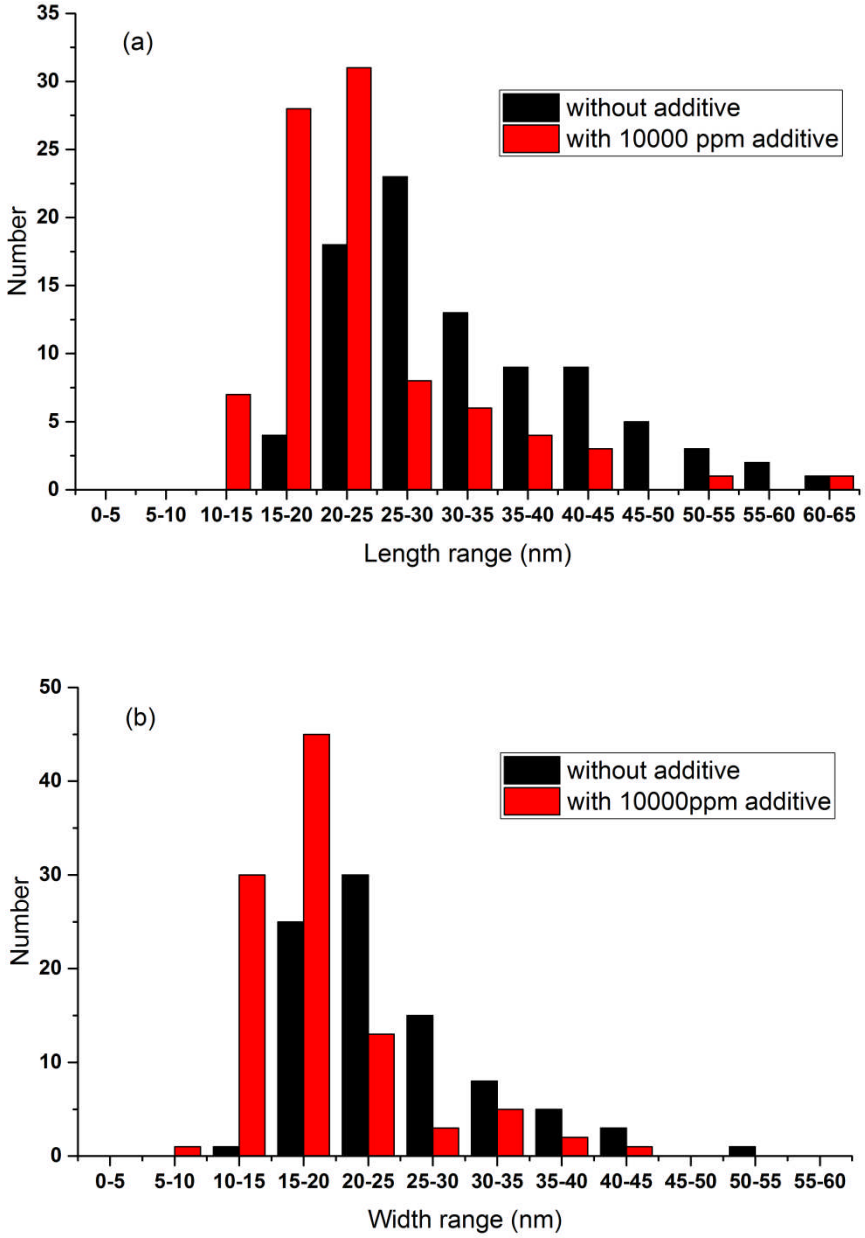

Figure C.5.Particle size analysis of the 2 mM Pb^{2+}, 0 mM Zn^{2+}, 0 ppm additive solution (sample No.10) and the 2mM Pb^{2+}, 0 mM Zn^{2+}, 10000 ppm additive solution (sample No.11); (a) length; and (b) width measurements.

The XRD pattern of powders obtained from the pure Zn^{2+} containing solution in the absence of additive is shown in Figure C.6. The spectrum matches that of the ZnS phase sphalerite. The calculated crystallite size of all powders formed in the Zn-S systems based on the Scherrer equation and the XRD peak (111) are presented in Table C.5. These data show that

the crystallite sizes of the ZnS (sphalerite) is in all cases around 7 nm and increasing the additive concentration did not seem to affect the size. However, at these small sizes the Scherer equation is also less precise but, by comparing the data from Table C.5 and C.4, it can be seen that the crystallite size in the samples of the Zn-S systems were far smaller than those of the Pb-S system.

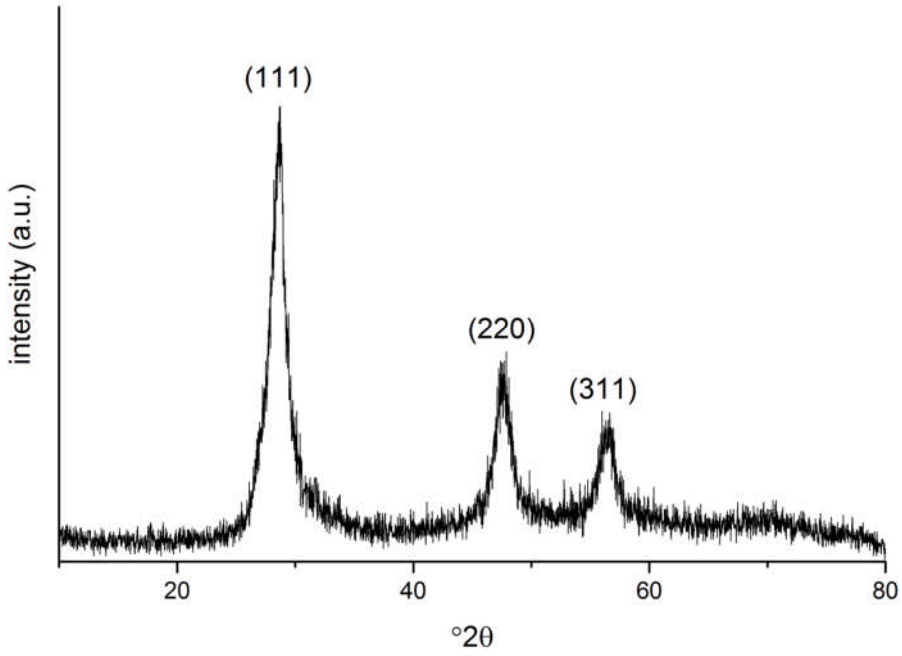

Figure C.6.The XRD pattern of powders gathered from the 0 mM Pb^{2+}, 2 mM Zn^{2+}, 0 ppm additive solution (sample No.15).

Table C.5.The crystallite size of ZnS powders.

Jar number	$[Pb^{2+}]$ mM	$[Zn^{2+}]$ mM	Additive concentration (ppm)	Crystallite size (nm)
15	0	2	0	6
6	0	2	500	7
7	0	2	1000	7
12	0	2	5000	7
13	0	2	10000	7

The TEM images of the ZnS particles in the absence and presence of highest concentration of additive together with their particle size measurements are shown in Figures C.7 (a,b), C.8 (a, b). The images reveal that the ZnS particles are smaller, less crystalline and that the resulting particles are spherical and seemingly highly porous and less dense compared to the PbS particles (Figure C.4).

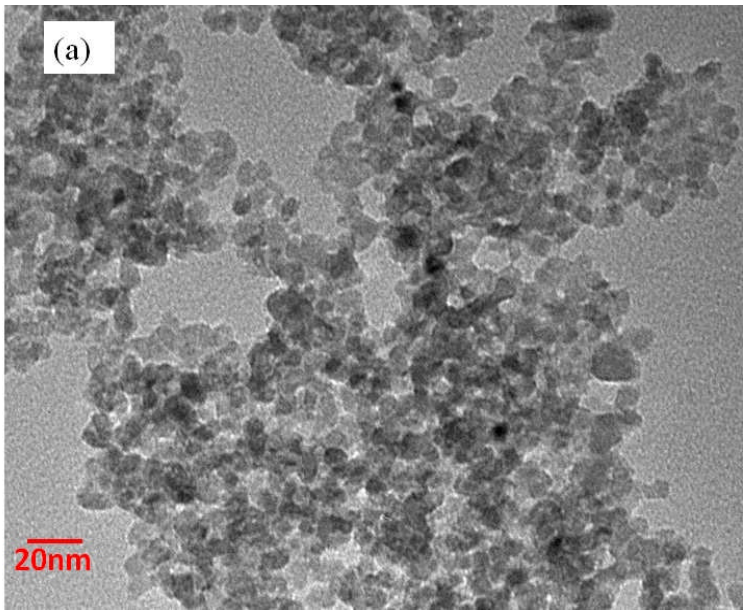

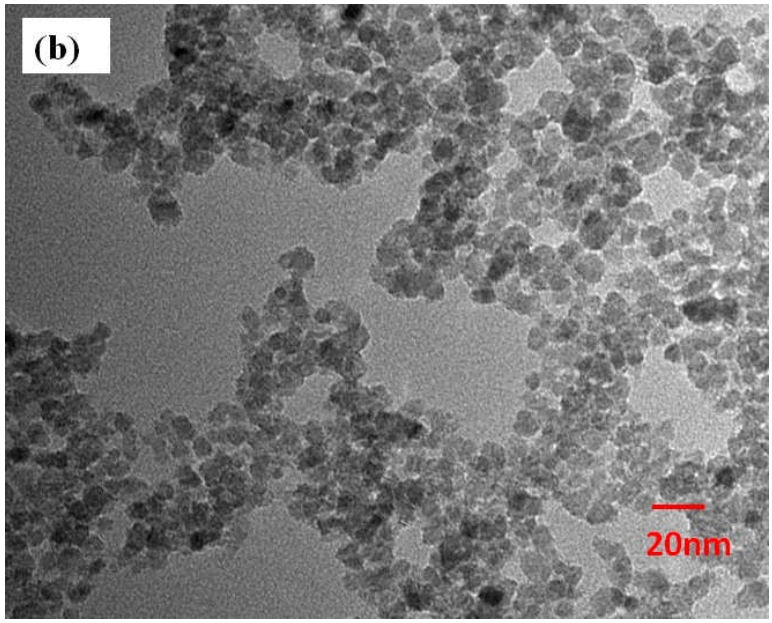

Figure C.7.TEM images of (a) sample 0 mM Pb^{2+}, 2 mM Zn^{2+}, 0 ppm additive solution (sample No.15); (b) 0 mM Pb^{2+}, 2mM Zn^{2+}, 10000 ppm additive solution (sample No.13).

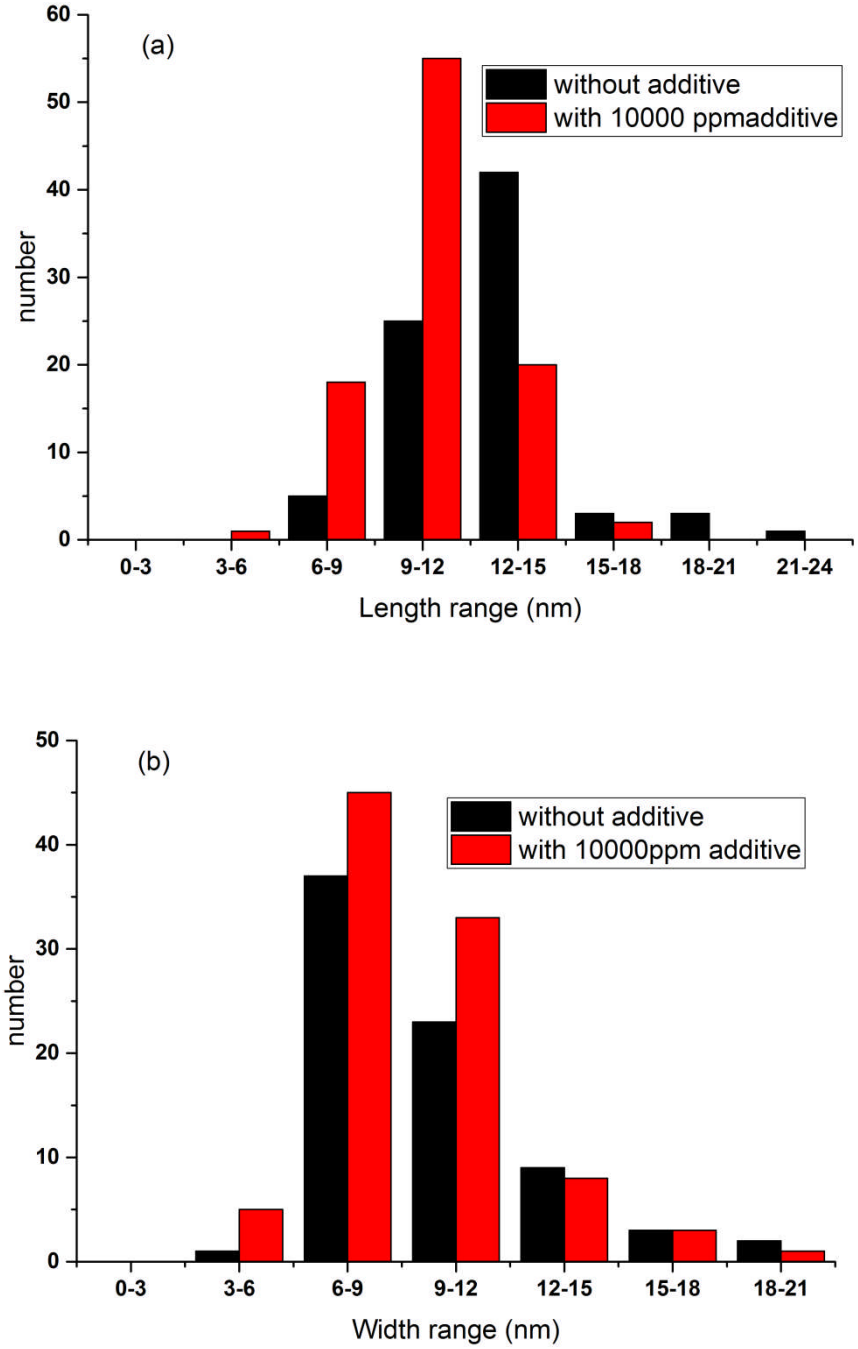

Figure C.8.Particle length; (a) and width (b) distribution of sample 15 (ZnS without additives) and sample 13 with the highest additive concentration (2 mM Zn^{2+}, 10000 ppm additive).

Overall, the particle size measurements in the Zn-S system revealed that in the presence of 10000 ppm additive, the resulting ZnS particles are marginally smaller compared with the additive-free system but this size difference is not significant.

Figure C.9 shows the XRD pattern of a powder obtained from mixed Pb-S / Zn-S system containing 10000 ppm additive. Both galena (PbS) and sphalerite (ZnS) are distinguishable

but the PbS peaks are far stronger. The ZnS peaks were extremely diffuse and weak indicating likely a lower amount or a smaller particle size and / or the less crystalline nature of the ZnS particles compared to the PbS particles. Interestingly, the Rietveld refinement revealed that in the sample with the highest concentration of additives a mixture of 71 % galena and 29 % sphalerite was obtained. In all mixed Pb-S / Zn-S system samples the proportions between precipitated galena (PbS) and sphalerite (ZnS) were similar (i.e., ~ 3 quarter PbS and 1 quarter ZnS; Table C.6). This is surprising, because all mixed Pb-S / Zn-S system samples (See Table 3) were produced from equimolar mixtures of Pb^{2+} and Zn^{2+} (1 mM each) with excess H_2S (7.8 mM Na_2S). Nevertheless, the diffraction patterns from the precipitates were dominated by the PbS signal, while imaging was dominated by ZnS particles. This reflects maybe the difference in solubility between PbS and ZnS but further work is needed to clarify this issue.

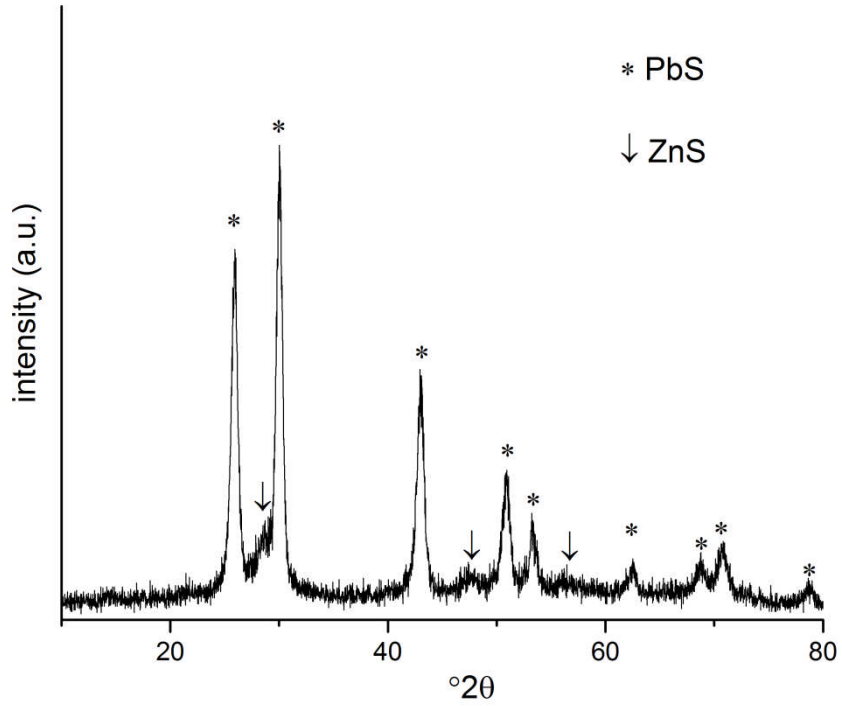

Figure C.9.The XRD pattern of powders obtained from solutions containing 1 mM Pb^{2+} and 1 mM Zn^{2+} with 10000 ppm additive (Jar No. 1).

Table C.6.% of PbS and ZnS phases in the powders from the mixed Pb-S / Zn-S system as evaluated by Rietveld refinement.

	Jar No.14 (no additive)	Jar No.8 (500 ppm)	Jar No.3 (1000 ppm)	Jar No.4 (5000 ppm)	Jar No.1 (10000 ppm)
% PbS	74	75	75	56	71
% ZnS	26	25	25	44*	29

*peak ratio is very poor thus numbers are totally unreliable

The microstructures of the powders from the mixed Pb-S / ZnS systems with 0 ppm or 10000 ppm additive are presented in Figure C.10 (a,b). By comparing the microstructure of the powders (Figure C.10 b) and the related XRD pattern (Figure C.9), it can be seen that although the peaks intensity of the PbS phase is higher than that of the ZnS phase, in the TEM images (Figure C.10 b) the ZnS particles are predominate. This is likely because of the larger particles and the more crystalline nature of the PbS phase in comparison to the ZnS phase. Interestingly, the PbS particles in the mixed PbS / ZnS systems with the highest additive concentration (Figure C.10 b) are much more elongated compared to the additive-free system, where the few available images indicate less elongates PbS crystals (Figure C.10 a). Additional work is needed to evaluate if this is an additive effect as the same behaviour (dramatic change in length) of the PbS crystals was not observed in the pure PbS system samples at high additive concentration (see Figure C.4 and C.5), yet there is a dramatic change in overall size of the crystallites and particles was observed.

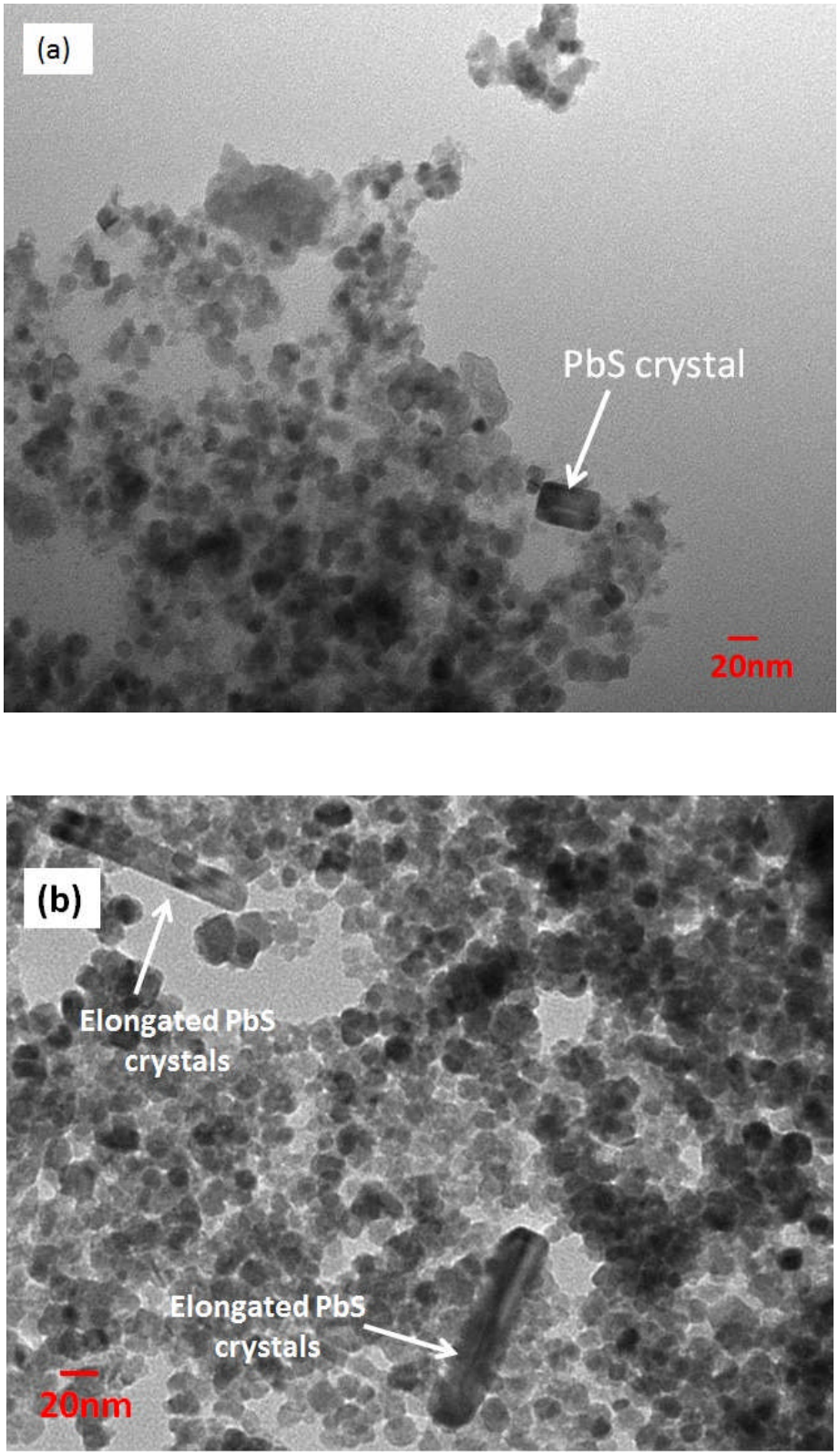

Figure C.10.TEM images of powders obtained from the mixed Pb-S / Zn-S systems containing (a) 0 ppm; and (b) 10000 ppm additive.

C.4. Conclusions

1- The visual observations show that 5000 ppm and 10000 ppm additives added to the Pb-S, Zn-S and Pb-S / Zn-S systems caused particles to remain suspended in solution.

2- The XRD pattern and phase analyses reveal that the phase precipitated in the Pb-S system was galena with crystallite sizes of around 30 nm in the absence of additive and just below 20 nm in the presence of 10000 ppm additive. The phase formed in the Zn-S system was sphalerite (ZnS) with crystallite sizes of 6 nm regardless if formed in the presence or absence of additives. The comparison of the XRD peaks intensity of PbS and ZnS phases reveal that because the PbS crystals are larger and much more crystalline, the Bragg peak intensity for PbS crystals is higher than for the ZnS crystals which exhibits more diffuse and weak Bragg peaks.

3- The TEM images of ZnS particles show that they have spherical in shape in comparison with PbS particles, which are more elongated.

4- In the case of particles obtained from Pb-S / Zn-S system, the marked between is in (1) the higher peak intensity of the PbS phase compared to ZnS and the associated larger PbS proportion from the Rietveld refinement evaluations; and (2) the visually larger proportion of ZnS particles in the TEM images compared to the PbS particles and the marked elongation in the presence of the additives. The 1st reason may be attributed to the higher crystallinity and larger sizes of PbS particles compared to the ZnS particles, while the 2nd reason may be due to a bias in images taken so far.

This report summarized in brief the findings from the evaluations done on the samples provided.